

THESE DE DOCTORAT DE L'UNIVERSITE PARIS-SUD XI

spécialité: Physique des solides

présentée par:

Luigi Frunzio

pour obtenir le grade de DOCTEUR de l'UNIVERSITE PARIS-SUD XI

Sujet de la thèse:

**Conception et fabrication de circuits supraconducteurs pour
l'amplification et le traitement de signaux quantiques**

soutenue le 18 mai 2006, devant le jury composé de MM.:

Michel Devoret

Daniel Esteve, President

Marc Gabay

Robert Schoelkopf

Rapporteurs scientifiques MM.:

Antonio Barone

Carlo Cosmelli

Table of content

List of Figures	vii
List of Symbols	ix
Acknowledgements	xvii
1. Outline of this work	1
2. Motivation: two breakthroughs of quantum physics	5
2.1. Quantum computation is possible	5
<i>2.1.1. Classical information</i>	<i>6</i>
<i>2.1.2. Quantum information unit: the qubit</i>	<i>7</i>
<i>2.1.3. Two new properties of qubits</i>	<i>8</i>
<i>2.1.4. Unique property of quantum information</i>	<i>10</i>
<i>2.1.5. Quantum algorithms</i>	<i>10</i>
<i>2.1.6. Quantum gates</i>	<i>11</i>
<i>2.1.7. Basic requirements for a quantum computer</i>	<i>12</i>
<i>2.1.8. Qubit decoherence</i>	<i>15</i>
<i>2.1.9. Quantum error correction codes</i>	<i>16</i>
2.2. Macroscopic quantum mechanics: a quantum theory of electrical circuits	17
<i>2.2.1. A natural test bed: superconducting electronics</i>	<i>18</i>
<i>2.2.2. Operational criteria for quantum circuits</i>	<i>19</i>

2.2.3. <i>Quantum harmonic LC oscillator</i>	19
2.2.4. <i>Limits of circuits with lumped elements: need for transmission line resonators</i>	22
2.2.5. <i>Hamiltonian of a classical electrical circuit</i>	24
2.2.6. <i>Quantum description of an electric circuit</i>	27
2.2.7. <i>Caldeira-Leggett model for dissipative elements</i>	27
2.2.8. <i>Beyond the harmonic oscillator: need for non-linearity</i>	29
3. A non-linear circuit element: the Josephson tunnel junction	31
3.1. A model for the Josephson tunnel junction	32
3.2. Josephson equations	33
3.3. Quantum Hamiltonian of an isolated Josephson tunnel junction	34
4. Superconducting circuits based on the Cooper Pair Box	37
4.1. Different competing implementations of quantum computers	37
4.2. The Cooper Pair box	38
4.3. Manipulation of the state of a Cooper Pair box	41
4.4. Brief summary on other superconducting quantum circuits	42
5. Read-out strategy with the Cooper Pair Box	47
5.1. Read-out requirements	47

5.2. Weakly coupled read-out of a Cooper Pair Box: charge strategy	49
5.3. Weakly coupled read-out of a Cooper Pair Box: loop current strategy	50
5.4. Dispersive read-out of Cooper Pair Box: non-linear inductive read-out in the RF-Quantronium architecture	53
5.5. Dispersive read-out of Cooper Pair Box: non-linear capacitive read-out in the Circuit QED architecture	57
5.6. Non-linear amplification of quantum signals: the Josephson Bifurcation Amplifier	60
6. Reprints of experimental and theoretical results on the Quantronium architecture with the JBA	63
7. Reprints of experimental and theoretical results on the Circuit QED architecture	89
8. Fabrication techniques used for this work	111
8.1. Substrates	111
8.2. Optical photolithography for resonator patterning	112
8.3. Capacitor fabrication	116
8.4. Dolan bridge technique to fabricate JTJ-based circuits	119
9. Conclusions and perspectives	125
Appendix: text and slides from the defense presentation	127
Bibliography	185

List of Figures

Figure 2.1.1. The Bloch sphere for a single qubit.

Figure 2.1.2. The collapse of the Bloch sphere at measurement.

Figure 2.2.1. Electrical circuit version of a harmonic oscillator.

Figure 2.2.2. Convention on the branch variables.

Figure 2.2.3. Caldeira-Leggett model for a dissipative element.

Figure 3.1. Josephson tunnel junction.

Figure 3.2. Josephson tunnel junction circuit model.

Figure 4.1. The Cooper Pair Box.

Figure 4.2. The split Cooper Pair Box.

Figure 5.1. The “Quantronium” architecture.

Figure 5.2. Dispersive read-out in the RF-Quantronium architecture.

Figure 5.3. The Circuit Quantum Electrodynamics architecture.

Figure 5.4. Dispersive read-out.

Figure 5.5. The Josephson Bifurcation Amplifier.

Figure 8.1. The double layer resist “mushroom”.

Figure 8.2. Aluminum profile after lift-off.

Figure 8.3. Edges of a Niobium resonator.

Figure 8.4. Josephson Bifurcation Amplifier capacitor fabrication.

Figure 8.5. Capacitors for a Quantronium circuit.

Figure 8.6. Resist bilayer patterned for a double angle deposition.

Figure 8.7. Undercut double layer resist.

Figure 8.8. Josephson tunnel junction fabricated by double angle evaporation.

List of Symbols

α, β	<i>Superposition coefficients</i>
γ	<i>Rotation angle between frames in a Bloch sphere</i>
γ	<i>Qubit depolarization rate in the cQED reprints</i>
$\hat{\gamma}$	<i>Gauge invariant phase difference operator</i>
Γ	<i>Decay rate of the excited state in a damped harmonic oscillator</i>
Γ_1	<i>Depolarization rate</i>
Γ_2	<i>Decoherence rate</i>
Γ_1^{ON}	<i>Depolarization rate in the ON state</i>
Γ_2^{OFF}	<i>Decoherence rate in the OFF state</i>
Γ_φ	<i>Dephasing rate</i>
δ	<i>Gauge invariant phase difference</i>
Δ	<i>Superconducting energy gap</i>
Δ	<i>Detuning between the qubit and the resonator frequency</i>
$\hat{\delta}$	<i>Gauge invariant phase difference operator for the split Cooper pair box</i>
$\hat{\delta}_i$	<i>Gauge invariant phase difference operator for a single junction</i>
$\Delta\hat{\delta}$	<i>Flux fluctuations</i>
ΔI_{01}	<i>Current difference between the qubit states</i>
ΔN_g	<i>Effective gate charge number change</i>
ΔU	<i>Barrier height in a JTJ</i>
ΔU_{01}	<i>Charge difference between the qubit states</i>
ε_o	<i>Vacuum dielectric permeability</i>
ε_r	<i>Relative dielectric permeability</i>
η, ξ, ζ	<i>Numerically determined constants</i>
η_o	<i>Electromagnetic wave impedance in vacuum</i>
θ	<i>Latitude on the Bloch sphere</i>

θ	<i>Phase difference between the two superconducting electrodes</i>
$\hat{\theta}$	<i>Phase difference operator</i>
κ	<i>Photon decay rate in a 1D transmission line resonator</i>
λ	<i>Wavelength</i>
λ_{cQED}	<i>Resonator-qubit coupling in circuit QED</i>
λ_{RF-Q}	<i>Resonator-qubit coupling in RF-Quantronium</i>
μ_o	<i>Vacuum magnetic permeability</i>
μ_r	<i>Relative magnetic permeability</i>
ν_{01}	<i>Qubit transition frequency</i>
ν_r	<i>Resonator frequency</i>
ν_{Rabi}	<i>Rabi frequency</i>
ν_{RF}	<i>Pulse frequency</i>
ν_s	<i>Spectroscopy tone frequency</i>
ρ_o	<i>Normal state resistivity of a metal</i>
$\rho(\omega, T)$	<i>Residual resistivity of a BCS superconductor</i>
$\hat{\sigma}_i$	<i>Pauli operators</i>
σ^+	<i>Spin creation operator</i>
σ^-	<i>Spin annihilation operator</i>
φ	<i>Longitude on the Bloch sphere</i>
Φ	<i>Magnetic field flux</i>
$\hat{\Phi}$	<i>Magnetic field flux operator</i>
Φ_0	<i>Superconducting magnetic flux quantum</i>
$\Phi_b(t)$	<i>Branch flux</i>
Φ_{ext}	<i>External magnetic flux</i>
$\tilde{\Phi}_l, \Phi_l$	<i>External flux bias through a loop</i>
$\Phi_n(t)$	<i>Node flux</i>
$\hat{\Phi}_{n,i}$	<i>Node flux operators</i>

Φ_m	<i>Intermediate node flux for the m-th oscillator</i>
$\Phi_j(t)$	<i>Josephson element branch flux</i>
$\chi, \chi(t)$	<i>Bias current normalized to the critical current in a JTJ</i>
$\psi, \psi\rangle$	<i>Arbitrary normalized superposition</i>
$\hat{\psi}$	<i>Unit norm state vector</i>
ω_{01}	<i>Transition angular frequency between the qubit states</i>
ω_o	<i>Resonant angular frequency of the oscillator</i>
ω_d	<i>Drive angular frequency</i>
ω_p	<i>Bare plasma angular frequency</i>
ω_r	<i>Resonator angular frequency</i>
ω_{Rabi}	<i>Rabi angular frequency</i>
ω_{Ramsey}	<i>Ramsey angular frequency</i>
ω_{RF}	<i>Angular frequency of an RF voltage signal</i>
ω_s	<i>Shifted resonant angular frequency of the oscillator</i>
“0”	<i>Classical zero state of bit</i>
“1”	<i>Classical one state of bit</i>
$ 0\rangle$	<i>Ground state of the qubit</i>
$ 1\rangle$	<i>Excited state of the qubit</i>
\hat{A}	<i>Generic operator</i>
\vec{a}	<i>Representative vector of the operator \hat{A}</i>
\hat{a}	<i>Photon annihilation operator</i>
\hat{a}^\dagger	<i>Photon creation operator</i>
a_i	<i>Components of \vec{a} in a reference frame</i>
b	<i>Branch</i>
\bar{c}	<i>Field propagation velocity in a medium</i>
C	<i>Capacitance</i>
C_Σ	<i>Cooper Pair Box total capacitance</i>

C_g	<i>Cooper Pair Box gate capacitance</i>
C_i	<i>Cooper Pair Box island capacitance</i>
C_J	<i>Josephson tunnel junction capacitance</i>
C_m	<i>Capacitive component of the m-th oscillator</i>
C_{TL}	<i>Transmission line total capacitance</i>
d	<i>Junction asymmetry coefficient</i>
D	<i>Number of dimensions</i>
\vec{dl}	<i>Line path element</i>
dt	<i>Infinitesimal time interval</i>
e	<i>Electron charge</i>
\vec{E}	<i>Electric field</i>
E_B	<i>Barrier Energy</i>
E_C	<i>Coulomb charging energy for one Cooper pair in a Cooper Pair Box</i>
E_C^d	<i>Detector junction charging energy</i>
E_{CJ}	<i>Coulomb charging energy for one Cooper pair in an isolated Josephson tunnel junction</i>
E_J	<i>Josephson energy</i>
E_J^*	<i>Effective Josephson energy of a symmetric split Cooper pair box</i>
E_J^d	<i>Detector junction Josephson energy</i>
E_L	<i>Inductive energy</i>
E_z	<i>Minimum energy splitting of the qubit states</i>
F	<i>Read-out fidelity or discriminating power</i>
g	<i>Photon-qubit coupling in the circuit QED Hamiltonian</i>
\vec{h}	<i>Representative vector of the Hamiltonian operator</i>
\hbar	<i>Planck constant divided by 2π</i>
\vec{H}	<i>Magnetic field</i>
\hat{H}_c	<i>Noise coupling Hamiltonian</i>

\hat{H}_{cQED}	<i>Circuit QED Hamiltonian</i>
\hat{H}_{cQED}^*	<i>Effective circuit QED Hamiltonian</i>
$\hat{H}_{cQED}^{\text{int}}$	<i>QND probe operator in circuit QED</i>
h_i	<i>Components of \vec{h} in a reference frame</i>
$h_J(t)$	<i>Energy stored in the Josephson element</i>
$\hat{h}_{J,SCP B}$	<i>Split Cooper Pair Box Hamiltonian operator</i>
\hat{H}_{JC}^*	<i>Jaynes-Cummings Hamiltonian operator</i>
\hat{h}_{JTJ}	<i>Isolated Josephson tunnel junction Hamiltonian operator</i>
\hat{H}_{qubit}	<i>Qubit Hamiltonian operator</i>
$\vec{h}_{R,TOT}$	<i>Representative vector of the total Hamiltonian operator in the rotating frame</i>
$\hat{H}_{RF}(t)$	<i>Time dependent Hamiltonian operator</i>
\hat{H}_{RF-Q}^*	<i>Effective RF-Quantronium Hamiltonian</i>
$\hat{H}_{RF-Q}^{\text{int}}$	<i>QND probe operator in RF-Quantronium</i>
$\vec{h}_{RF,R}$	<i>Representative vector of $\hat{H}_{RF}(t)$ in the rotating frame</i>
$\hat{H}_{RF-SQUID}$	<i>RF-SQUID Hamiltonian</i>
$h(X)$	<i>Energy stored in a component</i>
h_Y	<i>Hamiltonian of the admittance</i>
\hat{I}	<i>Identity operator</i>
\hat{I}	<i>Current operator</i>
$i_b(t)$	<i>Branch current</i>
I_c	<i>Josephson tunnel junction critical current</i>
i_n	<i>Node current</i>
$I_{rf}(t)$	<i>Current drive amplitude</i>

$i(t)$	<i>Current</i>
$I(t)$	<i>Current drive</i>
\hat{K}	<i>Tunneled Cooper pair number operator</i>
k_B	<i>Boltzmann constant</i>
L	<i>Inductance</i>
l	<i>Circuit component size</i>
l	<i>Loop</i>
L_J	<i>Phase-dependent Josephson inductance</i>
L_{J0}	<i>Josephson inductance</i>
L_m	<i>Inductive component of the m-th oscillator</i>
n	<i>Node</i>
n	<i>Number of photon in a resonator</i>
\hat{n}	<i>Number operator for photons in a harmonic oscillator</i>
\hat{N}	<i>Cooper pair number operator</i>
N_Φ	<i>Flux frustration</i>
N_{off}	<i>Residual offset number of Cooper pairs on the junction capacitor</i>
N_g	<i>Effective gate charge number</i>
$N(t)$	<i>Number of Cooper pairs having tunneled through a Josephson element</i>
O_{nb}	<i>Branch voltage orientation matrix elements</i>
\hat{p}	<i>Charge number operator</i>
$P_0(\psi\rangle)$	<i>Probability of measuring the “0” associated value with the qubit in state ψ</i>
$P_1(\psi\rangle)$	<i>Probability of measuring the “1” associated value with the qubit in state ψ</i>
q	<i>Charge</i>
\hat{q}	<i>Charge operator</i>
Q	<i>Quality factor for a parallel LC circuit</i>
Q_1	<i>Depolarization quality factor</i>
Q_2	<i>Decoherence quality factor</i>
$Q_b(t)$	<i>Branch charge</i>

$Q_c(t)$	Capacitor branch charge
$Q_J(t)$	Charge flowing through a Josephson element
q_m	Charge of the m -th oscillator
$Q_n(t)$	Node charge
\tilde{Q}_n	External charge bias at a node
$\hat{Q}_{n,i}$	Node charge operators
R	Resistance
R_N	Tunnel junction normal resistance
R_Q	Resistance quantum
$R_x(\vartheta)$	Rotation operator around \hat{x}
$R_y(\vartheta)$	Rotation operator around \hat{y}
S	Quantity of classical information
s	Circuit size
s_c	Connection size
$S_I(\omega)$	Power spectral density noise in a field along the I axis
S_{nb}	Branch current orientation matrix elements
S_q	Quantity of quantum information
t	Insulator thickness
T	Temperature
T_1	Depolarization time
T_2	Decoherence time
T_φ	Dephasing time
t_d	Dead time
t_m	Measurement time
U	Cubic approximation to the washboard potential in a JTJ
U_g	Cooper Pair Box gate voltage
\hat{V}	Island potential

$v_b(t)$	<i>Branch voltage</i>
v_n	<i>Node voltage</i>
$v(t)$	<i>Voltage</i>
W	<i>Number of configurations</i>
$\hat{x}, \hat{y}, \hat{z}$	<i>Unit vectors of the three orthogonal axis of the Bloch sphere</i>
$\hat{X}, \hat{Y}, \hat{Z}$	<i>Unit vectors of the three orthogonal axis of the eigenframe in a Bloch sphere</i>
X_c	<i>Magnitude of the qubit coupling in unit of E_z</i>
\hat{x}_R, \hat{z}_R	<i>Unit vectors of the rotating frame</i>
$Y(\omega)$	<i>Frequency dependent admittance</i>
Y_C	<i>Admittance of a capacitor</i>
y_{in}^C	<i>Open transmission line admittance</i>
y_o	<i>Transmission line characteristic admittance</i>
z_{in}^L	<i>Shorted transmission line impedance</i>
Z_L	<i>Impedance of an inductor</i>
z_o	<i>Transmission line characteristic impedance</i>
Z_o	<i>Harmonic oscillator characteristic impedance</i>

Acknowledgements

I would like to thank my thesis director Michel Devoret. I could not have asked for a better one. He has been supportive of my efforts, has encouraged my pursuits, when appropriate, and discouraged them, when appropriate. He has been an inexhaustible mine of knowledge and has continuously stimulated my thirst for more. He has been a friend to talk with of things other than science, from family and politics to art and history, and best of all as a French man, a true European French, the closest person I found as a Neapolitan, a true European Italian.

I would like to thank Rob Schoelkopf. I thought I had boundless energy and attention at details before bumping into him and realizing the difference between a Ferrari and a car.

I would like to thank Dan Prober, my first advisor as a post-doc here at Yale, he has always impressed me with his profound knowledge of physics and his ability to make me feel I could understand it and he has developed in me an appreciation for the practical aspects of science and for the continuous honest search for applications of whatever we think we do.

I worked with a number of graduate students directly or indirectly and I found in all of them sincere interest in science and in most of them friendship. Training some of them in the craft of superconducting electronics fabrication has given to me more than one reason to rejoice: Chris Wilson, David Schuster, Matthew Reese, Veronica Savu, Minghao Shen, Julie Wyatt Love, Joe Schreier. Each of them has added to my experience and knowledge at least as much as they believe they learned from me. Additional learning has been provided by interactions with Frederic Pierre, Lafe Spietz, Mike Metcalfe, Chad Rigetti, Simon Fissette. Developing new devices with and for Ken Segall, Thomas Stevenson, Liqun Li, Andreas Wallraff, Hannes Majer, Ben Turek, John Teufel, Daniel Santavicca, Etienne Boaknin, Rajamani Vijayaraghavan has been sometime a challenge and always a lot of fun. A special thank to Irfan Siddiqi with whom I shared seven years in the same Department and a lot more.

I would also like to acknowledge the “invisible” contribution to this work from our Department staff during the long time it took to be completed: Jayne Miller, Pam Patterson, Pat Brodka, Maria Gubitosi and Theresa Evangeliste.

I would like to thank my advisor at Orsay Marc Gabay, without his patience and reliable help this effort could not even have started.

I would like to thank Roberto Cristiano, my thesis advisor of sixteen years ago and then a beloved friend and colleague, and Settimo Termini, my Institute director at CNR in Pozzuoli, Naples, Italy, to support me in getting the leave of absence during which this work has been developed.

I would like to thank the other components of my thesis jury Antonio Barone, my first employer with an unjustified trust in my skills, Carlo Cosmelli, a friend and a colleague for more than ten years, and Daniel Esteve, whose friendship and guidance I am honored to acknowledge.

I would like to thank my parents for being always supportive for almost half a century, my parents-in-law for being patient with me in spite of stealing and exporting their daughter and my brother Paolo for encouraging me even when he had better things to do. I would like to thank the young Italian émigré community for the good time they always provide me with. I need to thank my children Carlo and Paola for not complaining for the many hours I subtracted from their playtime. Most of all, I need to thank my wonderful wife Giusy for still loving me in spite of altering her life and filling it with a lot of work during these first eight years, especially the last few months while writing this thesis. This work would not have been possible without her.

1. Outline of this work

Quantum mechanics has been developed more than eighty years ago as a revolutionary framework for understanding the atomic and subatomic world. It has repeatedly shown an exceptionally good agreement with experiments and its predictions have been confirmed in fields as varied as astrophysics, quantum optics, condensed matter physics, and chemistry. But for all these successes, it has not yet produced an application which we can properly call a quantum mechanical machine. It is true that many devices we intensively use in our daily life have been developed thanks to research in quantum physics: lasers, transistors, photo-detectors etc. However, the collective variables controlling the dynamics of these objects at the macroscopic level (current, voltage, electric and magnetic fields) are completely described by the equations of classical mechanics. In these equations, quantum mechanics is present only through the value of certain basic parameters like the material dependent work function, transition frequencies and the semiconductor energy gap, which involve the Planck constant and the electron mass and charge. These latter quantities appear in the Hamiltonian of those devices as consequences of fundamental aspect ratios of our Universe and they are in no way tunable by an engineer. Some of the readers may have had a chance to enjoy a beautiful series of books written in the 1940's by George Gamow [G40, G44]. There, the main character, a bank clerk called Mr. Tompkins, amazed by the progresses that physics had done in the previous forty years, dreamed of life experiences in a world where, time by time, either the Planck constant or the velocity of light in vacuum or the gravitational constant had completely different values. We would like to show that in some sense Mr. Tompkins' dreams were not completely meaningless and that in fact they may be realized by truly quantum machines, i.e. devices whose functions are entirely described by quantum mechanics and for which the quantum parameters are fully tunable. These quantum machines may indeed be thought as the product of the work of a new character: the quantum engineer.

In order to support this claim, we have to take a step back and consider two of the most important breakthroughs of quantum physics in the last thirty years: the idea of a

quantum computer and the extension of quantum mechanics to macroscopic degrees of freedom. In Chapter 2, we will briefly introduce these two subjects.

We will introduce the basic requirements for a quantum computer, which in this work plays the role of the ideal archetypal quantum machine. In order to realize it, we need as its elementary parts new quantum circuits with proper input and output ports. It will become clear that these new circuits will have to be operated at very low temperature with very low dissipation. Cryogenic engineering has developed quickly in the last twenty years but, at present, getting and keeping sensible volumes of matter cold in a relatively easy and cheap way is still only possible at temperatures down to about 10 mK. This implies that the scale of the energy level separation for a system that could exhibit quantum phenomena without being washed out by thermal fluctuations, is at least of the order of 10 μeV , which we can express also as a frequency of a few GHz. Even if nano-mechanical devices have been greatly developed in recent years, the natural choice for a low dissipation system in that frequency range is a superconducting electrical circuit. In Chapter 2, we will show that, indeed, superconducting electrical circuits may exhibit quantum behavior.

We will also find that in order to be able to easily access and observe these quantum phenomena we need to introduce some non-linearity in our circuits and in Chapter 3 we will show how to do this in a natural way with the help of Josephson tunnel junctions. In Chapter 4, we will show that the elementary parts of a quantum computer, the qubits, may be realized among other ways by a very simple circuit, the “elementary atom” of our quantum engineering, the so-called Cooper Pair Box (CPB). We will then describe the properties of this circuit.

In Chapter 5, we will present examples of the weak-coupling read-out strategies that have been realized for this simple electrical circuit in the past. We will then introduce a new strategy based on purely dispersive measurements of the qubit susceptibility. These measurements are realized by microwave irradiation of the read-out port of the circuit and then by probing the transmitted or reflected photons. One can think of the qubit as a nonlinear quantum system having a state-dependent admittance (capacitive or inductive), which changes between the ground and excited states. It is this change in polarizability which is measured in the dispersive measurement, which is also a quantum non-

demolition (QND) type of measurement because it does not modify the qubit state. This new strategy in two different configurations, with capacitive and inductive coupling to the CPB, has been the focus in the last four years of the groups involved in research on superconducting circuit for quantum information processing in the Departments of Applied Physics and Physics at Yale. We took part in this collective effort by principally contributing in the design and fabrication techniques of devices testing this strategy.

In Chapter 6 and 7, we reprint articles, already published by international scientific journals, containing the results obtained pursuing two different versions of this dispersive read-out strategy.

In Chapter 6, we reprint a published article presenting the RF version of the Quantronium architecture, which is the natural extension of what was developed in the Quantronics group at CEA in Saclay, France [VAC02]. This “RF-Quantronium” has been realized coupling the Quantronium circuit to a new amplifier for quantum measurement based on a nonlinear electrodynamic resonator with two metastable oscillation states: the Josephson Bifurcation Amplifier (JBA). The read-out is performed energizing with a microwave beam the JBA to a level where its oscillation state acts as a sensitive pointer of the qubit state, without generating any on-chip dissipation. This represents another valuable example of nonlinear dispersive measurements on a superconducting qubit circuit. The other published works reprinted in this Chapter focus on presenting the characteristic and properties as understood at the present stage of the development of this new amplifier.

In Chapter 7, we present the circuit quantum electrodynamics (QED) architecture [BHW04], which can be thought of as an electrical circuit version of the well-known cavity QED experiments [RBH01, MD02]. Of course, because we will be talking about frequencies in the range 2-50 GHz, we will have to take into serious consideration the need of realizing these superconducting electrical circuits out of distributed components rather than simple lumped components. In fact in the circuit QED, a one dimensional (1D) transmission line resonator consisting of a full-wave section of a superconducting coplanar waveguide plays the role of the cavity and is coupled within a simple circuit fabricated on a single chip to a superconducting CPB qubit that plays the role of the atom.

In Chapter 8, we describe in details our design considerations and the fabrication techniques to realize the various parts of the quantum circuits used in our work. These techniques together with the microwave engineering necessary to set up the measurements on these circuits represent the “nuts and bolts” of this new exciting field of scientific research.

In Chapter 9, we will conclude summarizing our results and presenting the perspectives for our new characters, the quantum engineers, of realizing quantum machines which will in turn generate new and even more exciting dreams in the next generations of Mr. Tompkins around the world.

In the final version of this manuscript, the text and the slides used for the defense presentation have been added in an Appendix.

2. Motivation: two breakthroughs of quantum physics

2.1. Quantum computation is possible

In the 1980's, Richard Feynman [F82, F85, F86, F96] demonstrated theoretically that the components of a computer could be reduced to individual atoms or even elementary particles, like electrons. The quantum uncertainty associated with non-commuting variables would not prevent such a computer from working properly. Even better, such a quantum computer would work with a minimal energy cost.

These results went essentially unnoticed outside a small community of theoretical physicists for at least two reasons: computers were much further than today from reaching the atomic scale and the message did not contradict mainstream views. In fact, that “miniaturization could just keep going on” was already part of the chipmakers gospel according to Moore.

However, a revolutionary discovery was made in 1994 by a Bell Labs computer scientist. Peter Shor [S94] discovered that a quantum computer would not just perform as well as a classical computer but would solve certain problems which were impossible tasks on a classical computer. He exhibited [S97] an algorithm for factoring numbers into prime ones in times which increased only polynomially with the number of digits. That was a formidable piece of mathematical physics. In fact, up until then, most computer scientists thought that the complexity of a problem was independent of the type of machine you could use. Some computers may run faster than others but the differences are only quantitative, not qualitative. The quantum computer was apparently able to do in a few hours what would take millions of years to do on a classical computer.

This discovery caused quite a sensation initially, but it was quickly dissipated when it was recognized that the computer had to operate in an almost perfect way in order to be useful. The quantum computer was infinitely superior, but also infinitely difficult to realize. Then in 1995, Peter Shor [S95], and at the same time independently Andrew Steane [St96, St98] at Oxford in UK, made an even more revolutionary discovery: they found that quantum error correction codes, which most physicists thought impossible, were in fact possible. This last invention is perhaps more profound than the first Shor's algorithm. It means that quantum machines, which have truly astounding properties, obey

the same construction principles than ordinary machines. The status of the construction of a quantum computer had suddenly shifted from being impossible to being extremely difficult.

The quantum computer has become the driving force of a new direction in quantum physics. Quantum mechanics does not only restrict the amount of information you can acquire on a system. On the contrary, by using subtle, but basic, quantum principles you could, in principle, build machines that treat this information faster and better than what classical mechanics allows.

2.1.1. Classical information

A classical binary information unit, a bit, is thought of as a binary digit, but it always consists of some physical system with two minimum energy states, “0” and “1”, separated by a tall barrier and with a lot of friction in order to make the bit insensitive to small perturbations. All implementations of this bit, either electric, magnetic or mechanical, are analogous to a bistable switch. In this latter case, the state variable is the position of the switch with some threshold to define either ON or OFF conditions. In a RAM computer memory, the state variable is a charge on a capacitor. In a magnetic disk-drive, the state variable is the magnetization of a little domain on the surface of the disk. The system is set to a particular state by some external force and then stays in that state. If we measure the system, submitting it to an external perturbation and measuring its response, we should find exactly the state that has been written in. In principle, if the bit is correctly constructed, the read-out operation reproduces the information stored during the write in operation. Copying is then always possible.

The quantity of information contained in set of N bits or N -register is $S = \log_2 W = N$, where $W = 2^N$ represents the number of configurations the N -register can have. The classical algorithms are executed using Boolean logical gates. Only one type of elementary gate, called the “universal” gate, is needed to perform all calculations: the NAND (or NOR) gate.

2.1.2. Quantum information unit: the qubit

The unit of quantum information, a quantum bit or qubit, has properties radically different from the classical bit [NC00]. Every bound microscopic particle has quantized energy levels. The electron in an atom has energy levels corresponding to different electronic orbitals. A single electron in a magnetic field has two energy levels corresponding to the two possible orientations of its spin with respect to the field. Usually these levels are not evenly separated. In fact, we do not want for quantum computation a system with regularly separated energy levels like a harmonic oscillator. The best situation for realizing a qubit is when two levels, for example the ground and first excited level, have a smaller separation than that between them and all the other levels.

These set of two levels forms the qubit. If the system is in the ground level the qubit is said to be in the $|0\rangle$ state, using Dirac's notation. Conversely, the first excited level corresponds to the $|1\rangle$ state.

The great difference from the classical bit is that, even if all the other energy states are forbidden, the quantum bit can be prepared in more than only these two states. It can be prepared in what is called a "normalized quantum superposition" of these two states, ψ :

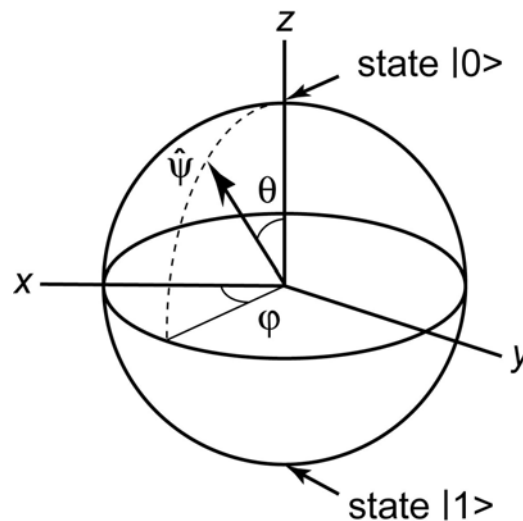


Figure 2.1.1. The Bloch sphere for a single qubit. The North Pole represents the ground state of the qubit or state $|0\rangle$, while the South Pole represents the excited state or state $|1\rangle$. Each point on the sphere represents a possible superposition of the two basis states and is characterized by latitude, θ , and a longitude, φ .

$$|\psi\rangle = \alpha|0\rangle + \beta|1\rangle$$

with $\alpha^2 + \beta^2 = 1$ or without losing any generality:

$$|\psi\rangle = \cos(\theta/2)e^{-i\varphi/2}|0\rangle + \sin(\theta/2)e^{i\varphi/2}|1\rangle$$

If we represent the two basis states as the South and North poles of a sphere, then all the possible superpositions can be mapped into points at the surface of this so-called Bloch sphere, as shown in Fig. 2.1.1. The latitude, θ , corresponds to the average energy of the state. The longitude, φ , is called the phase of the qubit. Each point on the sphere can be associated to a unit norm state vector centered in the sphere origin:

$$\hat{\psi} = \sin\theta\cos\varphi\hat{x} + \sin\theta\sin\varphi\hat{y} + \cos\theta\hat{z}$$

where \hat{x} , \hat{y} and \hat{z} are the unit vectors of the three orthogonal axis of the coordinate system of the Bloch sphere.

2.1.3. Two new properties of qubits

The first new and interesting property of a qubit consists of losing the mutual exclusion character of its states typical of the classical bit, since infinite intermediate possibilities between the classical results “0” and “1” exist.

The second surprising property of a qubit is that writing and reading its state are now completely asymmetric operations. By exciting the system with a force which oscillates at the transition frequency between the two states, and by adjusting the amplitude and duration of this excitation, we can prepare any superposition. We can thus write into the qubit a particular state with arbitrary accuracy.

The surprise comes when we measure the energy of the system, as represented in Fig. 2.1.2. We always find only one of two values: either the value associated with the state $|0\rangle$ or the one associated with the state $|1\rangle$. If we prepare the same superposition over and over again, each reading operation will find randomly the $|0\rangle$ value or the $|1\rangle$ value with probabilities corresponding to $P_0(|\psi\rangle) = \cos^2(\theta/2)$ and $P_1(|\psi\rangle) = \sin^2(\theta/2)$, respectively. The superposition appears to have collapsed either at the North or at the South Pole through the act of measurement.

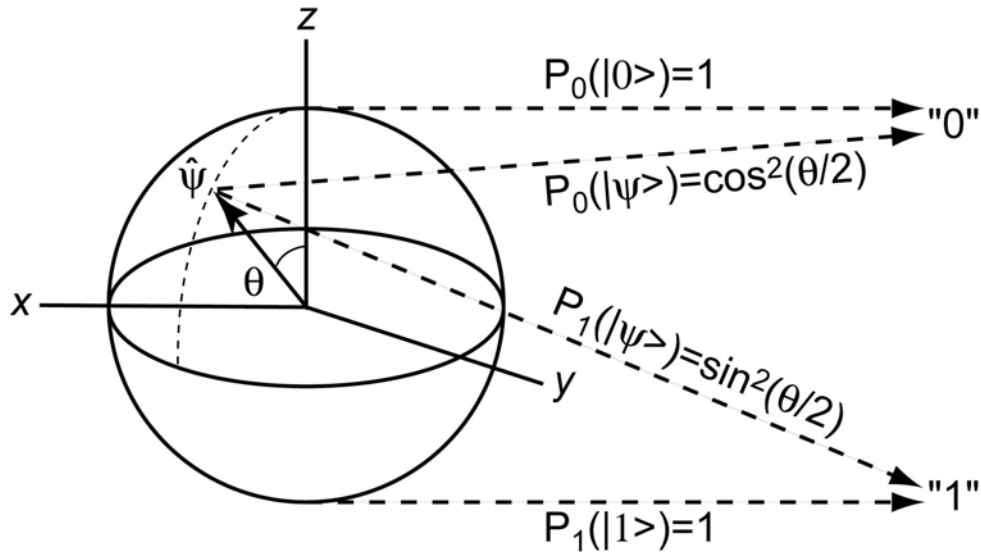


Figure 2.1.2. The collapse of the Bloch sphere at measurement. The result of an energy measurement on the qubit is always only one of two values: either the value associated with the state $|0\rangle$ or the one associated with the state $|1\rangle$. For each state on the Bloch sphere, that is superposition of the basis states, the result will be randomly the $|0\rangle$ value or the $|1\rangle$ value with probabilities corresponding to $P_0(|\psi\rangle) = \cos^2(\theta/2)$ and $P_1(|\psi\rangle) = \sin^2(\theta/2)$, respectively. Only the pure states $|0\rangle$ and $|1\rangle$ will be read-out as such with certainty.

One never measures an intermediate energy value, corresponding to one of the superposition states. The collapse prevents the read-out to be faithful. Only if we write the pure states $|0\rangle$ or $|1\rangle$, does the read-out give us back the initial information with certainty. It is, thus, impossible in general to copy quantum information. To copy we must read, which in general cannot be performed without destruction of the qubit state. Nevertheless, the information contained in the superposition exists. In fact, we can prepare an arbitrary superposition, and instead of reading it right away, we can rotate the sphere as a whole and bring the written state in the place of the pure $|0\rangle$ or $|1\rangle$ state. Then we can faithfully read the information. This is how we know that the information carried by arbitrary superpositions has some, albeit hard to fathom, existence.

2.1.4. Unique property of quantum information

A quantum register, like a classical register, is just a set of qubits. The quantum register generalizes the superposition phenomenon to an amazing degree: the general state of a quantum register is a superposition of all the possible configurations of the register. This means that whereas a classical N bit register store only one N digit number, an N qubit register can in a sense store all numbers between 0 and 2^N-1 , and we can do operations on all these numbers at once. This is truly massive parallelism!

In more mathematical terms, the state of the N -register is now a point on a hypersphere, whose number of dimensions, $D=2^{N+1}-2$, grows exponentially with the number of qubits in the register. If we have for instance 3 qubits, the hypersphere lives in a space with 14 dimensions. For 150 qubits, the number of dimensions of the hypersphere is greater than the total number of particles in the universe.

Since the surface of the Bloch hypersphere grows exponentially with the number of dimensions, the quantity of quantum information grows exponentially with the number of qubits, $S_q = \log_2 M^D \approx 2^{N+1} - 2$, where M is of order 10^4 based on considerations from error correction codes. This property confers tremendous advantage to quantum information over classical information. The quantity of information that can be stored grows exponentially with the resources, whereas classically it grows only linearly. If we want to double the amount of the quantum information carried by a quantum register, we just need to add only one qubit!

Until a decade ago, almost all physicists were somehow convinced that this prodigious amount of information was just a mirage. In fact, because of the collapse of the Bloch hypersphere in reading it, all this wonderful quantum information vanishes at measurement time and only one binary number is left in the register. The miracle of quantum mechanics, that Peter Shor was the first to witness, is that quantum information can still be put to practical use, despite its fragility.

2.1.5. Quantum algorithms

Certain problems, like answering the question “Is X a prime number?”, have a solution which contains very little information. In all the cases where the answer may

only be “Yes” or “No”, the solution has just one bit of information. David Deutsch [D85, D89], working at the University of Oxford, was the first to understand that for such problems, the collapse of quantum information, due to the read-out operation, was not such a severe limitation. The trick is not to perform any read-out until the very end of the computation. In the last stages, the information is “distilled” in such a way that the output register will not contain a superposition of answers, but is instead rotated so that “Yes” or “No” appears as pure state which can be read-out faithfully. Deutsch demonstrated that such distillation is possible on some very particular and not very interesting class of problems. Peter Shor [S97] was the first to show that the distillation was possible for an important practical problem, the decomposition of a number into prime factors. Moreover, he showed that such distillation could be performed in a way which is so efficient that all the parallel power of quantum computation is retained until the solution is reached.

2.1.6. Quantum gates

Quantum gates are rotations in a continuous complex vector space, unlike their classical counterparts which act in a discrete space. Nonetheless, it has been shown that a universal gate set consists of arbitrary one-qubit rotations plus a single two-qubit gate [NC00].

Using the Pauli operators, $\hat{\sigma}_x$, $\hat{\sigma}_y$, we introduce the 2x2 unitary matrices which represent the rotation operators around \hat{x} and \hat{y} :

$$R_x(\vartheta) = e^{-i\vartheta\hat{\sigma}_x/2} = \begin{pmatrix} \cos\frac{\vartheta}{2} & -i\sin\frac{\vartheta}{2} \\ -i\sin\frac{\vartheta}{2} & \cos\frac{\vartheta}{2} \end{pmatrix}$$

$$R_y(\vartheta) = e^{-i\vartheta\hat{\sigma}_y/2} = \begin{pmatrix} \cos\frac{\vartheta}{2} & -\sin\frac{\vartheta}{2} \\ \sin\frac{\vartheta}{2} & \cos\frac{\vartheta}{2} \end{pmatrix}$$

A general rotation for a two level system can then be executed as:

$$U = R_x(\alpha)R_y(\beta)R_x(\gamma)$$

and an example of a single two qubit gate is the so-called controlled-NOT or CNOT gate:

$$CNOT = \begin{pmatrix} 1 & 0 & 0 & 0 \\ 0 & 1 & 0 & 0 \\ 0 & 0 & 0 & 1 \\ 0 & 0 & 1 & 0 \end{pmatrix}$$

which performs a 180 degrees rotation on the target qubit if and only if the control qubit is in the “1” state. But be aware that this gate has a very strange property: it will take any quantum superposition of the four possible input configurations:

$$|\psi\rangle = \alpha|0_t, 0_c\rangle + \beta|1_t, 0_c\rangle + \gamma|0_t, 1_c\rangle + \delta|1_t, 1_c\rangle$$

and transform it into a superposition of the four possible output configurations:

$$CNOT|\psi\rangle = \alpha|0_t, 0_c\rangle + \beta|1_t, 0_c\rangle + \gamma|1_t, 1_c\rangle + \delta|0_t, 1_c\rangle.$$

There are experimental protocols [RBD05] for realizing universal gates in registers of superconducting qubits with fixed qubit coupling which employ irradiation of individual qubits with precisely tuned strength and duration.

2.1.7. Basic requirements for a quantum computer

Before describing specific possible implementations of the quantum computer, let us first establish the basic requirements that a system has to satisfy to be considered a good candidate for this task. In doing this, we will follow the indications expressed in a survey work by David DiVincenzo [Di95, Di00], at the IBM T.J. Watson Research Center in Yorktown Heights, NY. He pointed to four main basic requirements, which we have adapted here to our actual circuit implementations:

a) A scalable physical system with well characterized qubits

A well characterized qubit means that its physical parameters are accurately known. The first necessary step is to know the internal Hamiltonian of the qubit, which determines the two eigenstates or just states of the qubit. Knowing the Hamiltonian will also allow determining the existence of other possible states of the qubit and their coupling to the two basic states. In order to have a qubit, the transition frequency between state “0” and “1” must be sufficiently different from the transition between other eigenstates. This is what we previously called non-linearity or anharmonicity of

the system. The knowledge of the Hamiltonian may guide the understanding of how the qubits interact among themselves and how we may be able to manipulate their states by external fields. The scalability of the system is an important property if we want to realize registers of qubits in large enough numbers to be able to perform any non-trivial quantum computation. This implies that even if the effort to realize larger registers grows with the number of qubits, it has to do so in a way that would not throw away the advantage of quantum computation over the classical one.

b) A system with the ability to initialize and control the qubits

For any two level system, the three Pauli operators, $\hat{\sigma}_x$, $\hat{\sigma}_y$, $\hat{\sigma}_z$, and the identity operator, \hat{I} , represent a complete basis for the operators acting in a two dimensional Hilbert space. Any operator can be written as:

$$\hat{A} = -\frac{1}{2} \vec{a} \cdot \vec{\sigma} + \frac{1}{2} Tr\{\hat{A}\} \hat{I} = -\frac{1}{2} (a_x \hat{\sigma}_x + a_y \hat{\sigma}_y + a_z \hat{\sigma}_z) + \frac{1}{2} Tr\{\hat{A}\} \hat{I}$$

where the vector \vec{a} is the unique representative vector of the operator \hat{A} .

If we now limit ourselves to the two states of the qubit, we can in general write the qubit Hamiltonian as that of a pseudo-spin 1/2 particle:

$$\hat{H}_{qubit} = -\frac{E_z}{2} (\hat{\sigma}_z + X_c \hat{\sigma}_x)$$

where E_z represents the minimum energy splitting of the two states. The natural coupling variable for the qubit is what defines the x direction and X_c represents the magnitude of the coupling energy normalized to E_z . In Chapter 4, we will show that both E_z and X_c are functions of externally tunable parameters. We can now send signals in the form of NMR-type pulses through the control variable and prepare arbitrary superpositions of states. This operation will correspond to writing into the qubit. This same operation by itself or in association with some sort of cooling to the ground state also defines a possible initialization procedure for the qubit. The Hamiltonian also shows that at the ‘‘sweet spot’’ $X_c=0$, the qubit transition frequency is to first order insensitive to the noise of the control variable.

For the Hamiltonian introduced above, we have $\vec{h} = h_x \hat{x} + h_z \hat{z} = E_z X_c \hat{x} + E_z \hat{z}$.

We can always diagonalize the 2x2 matrix Hamiltonian and introduce a new reference frame for the Bloch sphere with \hat{Z} along the eigenvector with eigenvalue $-\hbar\omega_{01}/2$, where $\omega_{01} = E_c(1 + X_c^2)^{1/2}/\hbar$ is the transition angular frequency between the qubit states. This eigenframe is obtained considering a simple rotation of the axis such that: $\hat{Y} = \hat{y}$, $\hat{Z} = \sin\gamma \hat{x} + \cos\gamma \hat{z}$, with $\tan\gamma = X_c$, and $\hat{X} = \cos\gamma \hat{x} - \sin\gamma \hat{z}$. In this new reference frame the qubit Hamiltonian becomes:

$$\hat{H}_{qubit} = -\frac{\hbar\omega_{01}}{2} \hat{\sigma}_Z$$

and its representative vector is $\vec{h} = \hbar\omega_{01} \hat{Z}$, which represents a pseudo-magnetic field. This field produces a precession of the state unit vector around it with an angular frequency ω_{01} .

c) A system with the ability to read-out the qubits with high fidelity

For a system to be a valid candidate for quantum computer, it has to be able to read-out the information contained in the qubits. Then, we need to be able to open a coupling channel to the qubit for extracting information without at the same time submitting it to noise. An important quantity to optimize is the read-out fidelity. At the end of the read-out procedure, we should have reached one of the only two possible results. The read-out fidelity or discriminating power is defined as:

$$F = P_0(|0\rangle) + P_1(|1\rangle) - 1.$$

d) A system with a long decoherence time

For a system to be a valid candidate for quantum computer, it has to have states which do not lose coherence while the computation is running. Let us discuss this crucial point in more detail in the next section.

2.1.8. Qubit decoherence

A quantum computation is performed by first writing the input data, and then by running a sequence of gate operations. In this second stage, the quantum processor should be left undisturbed by parasitic influences which would either collapse the quantum information into classical information or alter irreversibly the superposition states in interactions with the degrees of freedom of the surrounding environment, including the read-out circuit. This fundamental alteration which reduces the description of a quantum system toward classical equations is called decoherence.

In general, these interactions generate an entanglement between the qubit and the environment. However if the interactions are weak, their effects on the qubit can be described in simpler terms. In the following we assume that this hypothesis is always verified in our case. As we said before, a generic quantum state of a qubit, $|\psi\rangle$, is represented by a unit vector $\hat{\psi}$ centered in the Bloch sphere origin and pointing to the sphere location with latitude θ and longitude φ . Let us assume the representative vector of our Hamiltonian is oriented along the Z axis.

Under the generic name of decoherence, there are two main classes of effects induced by the environmental degrees of freedom in the definition of the state. The first one corresponds to the tip of the unit vector diffusing in the latitude direction, which is the direction along the arc joining the two poles of the sphere. This process is called energy depolarization or state-mixing. In particular, the process is called relaxation if the unit vector is realigning with the ground state unit vector. It is called excitation if the unit vector is realigning with the excited state unit vector. The second class corresponds to the tip of the unit vector diffusing in the longitude direction, which is the direction perpendicular to the line joining the two poles. This process is called dephasing.

The depolarization process can be seen as resulting from unwanted transitions between the two qubit eigenstates induced by fluctuations in the effective fields along the X and Y axes. For weak fluctuations [ICJ05], we introduce the power spectral density noise of this fields, respectively $S_X(\omega)$ and $S_Y(\omega)$, and demonstrate using Fermi's Golden Rule that the depolarization time and rate are:

$$T_1^{-1} = \Gamma_1 = \frac{S_x(\omega_{01}) + S_x(-\omega_{01}) + S_y(\omega_{01}) + S_y(-\omega_{01})}{\hbar^2} .$$

A depolarization quality factor can be introduced $Q_1 = T_1 \omega_{01}$. $Q_1/2\pi$ indicates the average number of depolarization free precession turns.

The dephasing process, on the other hand, is induced by fluctuations in the effective field along the Z axis. If these fluctuations are Gaussian, with a power spectral density noise $S_Z(\omega)$ frequency independent up to frequencies of the order of several times the dephasing rate, we can show that dephasing time and rate are:

$$T_\varphi^{-1} = \Gamma_\varphi = \frac{S_Z(\omega \approx 0)}{\hbar^2}$$

In presence of a low frequency noise with a 1/f behavior, the formula is more complicated. If the environment producing the low frequency noise consists of many degrees of freedom, each of which is very weakly coupled to the qubit, then one is in presence of classical dephasing which, if slow enough, can in principle be fought using echo techniques. If, on the other hand, only a few degrees of freedom like magnetic spins or glassy two-level systems are dominating the low frequency dynamics, dephasing is quantum and not correctable, unless the transition frequencies of these few perturbing degrees of freedom are themselves very stable.

These two decoherence rates and times are related to the NMR spin decay rate and time:

$$\Gamma_2 = \Gamma_\varphi + \Gamma_1/2 = T_\varphi^{-1} + T_1^{-1}/2 = T_2^{-1}$$

which can be seen as the net decay time and rate of quantum information, including the influence of the decoherence processes. By analogy, a decoherence quality factor $Q_2 = T_2 \omega_{01}$ can be introduced. $Q_2/2\pi$ indicates the average number of decoherence free precession turns. Since a gate operation takes several precession turns to be performed ($m \sim 100$), Q_2/m indicates also the average number of such operations a qubit can undergo before quantum superpositions lose coherence.

2.1.9. Quantum error correction codes

A very beautiful and very important application of basic quantum gates is the correction of errors due to decoherence. Such processes were at first thought to be

impossible, since in order to correct, you first have to measure. Quantum error correction codes are based on redundancy and partial measurements. Many different versions had been proposed until 2002 when Daniel Gottesman [Go02], then at the California Institute of Technology, demonstrated that all possible one-qubit errors can be detected by encoding one logical qubit in five physical qubits at minimum. Interestingly, this detection leaves the quantum information untouched but reveals if an error has occurred or not. Furthermore, it allows you to know how the logical qubit has been altered and to correct it. However, the number of gate operations, which is needed to perform the entire routine for such error detection and correction, is of order of 10^4 . Once the gate operation time is taken into account, Q_2 's of order of about 10^6 are needed before attempting the construction of an actual quantum information processor.

2.2. Macroscopic quantum mechanics: a quantum theory of electrical circuits

Since the late 1970's, Anthony Leggett [L80], then at the University of Sussex in UK and few years after at the University of Illinois at Urbana-Champaign in USA, was looking for answers to the following questions:

- are macroscopic degrees of freedom governed by quantum mechanics?
- and if so, would it be possible to observe quantum phenomena, like tunneling, energy level quantization and coherent superpositions, before unavoidable interactions with the environment decoheres the macroscopic wavefunction of the system?
- can we obtain quantitative predictions for those phenomena, assuming a simple and general description of the environment as a source of energy dissipation?

Our experience tells us that a classical description of the everyday physical world appears to be completely satisfactory. We predict wonderfully well by classical mechanics the trajectories of the celestial bodies as well as that of billiard balls. The fall of a heavy rock and the Brownian motion of a speck of dust in a drop of water are all purely classical phenomena. While quantum mechanics appears to manifest itself at the macroscopic level through collective phenomena such as superfluidity, superconductivity, flux quantization

or the Josephson effect, these macroscopic quantum effects are in fact all generated by the classical cooperation of large numbers of microscopic degrees of freedom each governed by quantum mechanics. Leggett was instead looking for macroscopic quantum phenomena generated by a single macroscopic degree of freedom, i.e. a single collective variable. The minimum temperatures, which are relatively easily and cheaply available, are of the order of 10 mK. This consideration induced Leggett to look into electrical circuits to find the optimal candidate for answering his questions. At the same time, Leggett and others had realized that they could model the environment, in which such a circuit operates, by a very large number of microscopic degrees of freedom, behaving as a collection of harmonic oscillators. In general, their effect on the circuit can be represented by impedances with non zero real part inserted in appropriate branches of the circuit.

2.2.1. A natural test bed: superconducting electronics

For a circuit to behave quantum mechanically, the first requirement is the absence of internal dissipation. All metallic parts need to be made out of a material that has no resistance at the operating temperature and frequency. This is essential in order for electronic signals to be carried from one part of the quantum circuit to another without energy loss, a necessary but not sufficient condition for the preservation of quantum coherence. Superconductors are ideal for this task. Even if in principle any condensed electron phase with an energy gap could be used, the better understanding of dissipation in low temperature superconductors, like aluminum, tantalum and niobium, makes them the natural candidates in actual circuits. Superconducting circuits are built on substrates and their observations are made by means of leads connecting them to some sort of read-out device. Substrate, leads and read-out circuit have to be considered as part of the surrounding environment, which introduces dissipation in the quantum circuit.

In the last twenty years, using several different superconducting circuits, several groups have contributed to demonstrate experimentally that macroscopic degrees of freedom are governed by quantum mechanics and to improve and generalize the theory of the interaction with the environment in order to refine the agreement between predictions and observed phenomena such as macroscopic quantum tunneling [DMC85], macroscopic

energy level quantization [MDC85] and macroscopic quantum coherence [NPT99, FPC00].

2.2.2. Operational criteria for quantum circuits

In order to design and operate quantum circuits, we have to satisfy three criteria. The first criterion is that the typical energy of thermal fluctuations at the operating temperature has to be $k_B T \ll \hbar \omega_{01}$. For reasons which will become clear later, the energy level separation for superconducting circuits is in the 10-250 μeV range, which corresponds to transition frequency in the 2-50 GHz range. Therefore, the operating temperature must be around or below 20 mK. These temperatures may be readily obtained by cooling the quantum circuit with a dilution refrigerator. It is important to notice that the “electromagnetic temperature” of the leads allowing control and read-out of the quantum circuit has also to be small compared to $\hbar \omega_{01}$. This requires careful electromagnetic ultra-low noise filtering with techniques that have been developed in the last twenty years [MDC87]. Note that at low temperatures electromagnetic damping mechanisms are usually stronger than those originating from electron-phonon coupling. The second criterion is that the macroscopic degree of freedom has to be well decoupled from the environment so that the lifetime of the quantum states is longer than the characteristic time scale of the circuit.

The third criterion is that $\hbar \omega_{01} \ll \Delta$, where Δ is the energy gap of the superconducting material. In the fabrication of quantum circuits, this criterion implies that we have to use superconducting materials with energy gap of at least 100 μeV . The low temperature superconductors, we mentioned above, satisfy this requirement. In fact, the energy gap for niobium is $\Delta_{\text{Nb}}=1.52$ meV, for tantalum is $\Delta_{\text{Ta}}=700$ μeV and for aluminum is in the range $\Delta_{\text{Al}}=180\text{-}250$ μeV depending on the impurity content of the material.

2.2.3. Quantum harmonic LC oscillator

To illustrate the application of these criteria, we consider the simplest quantum circuit, the harmonic oscillator, as shown in the left side of Fig. 2.2.1, which consists of

an inductor with inductance L , connected in parallel with a capacitor with capacitance C , all metallic parts being superconducting. This simple quantum circuit is the lumped element version of a superconducting cavity or of a transmission line resonator. The magnetic flux Φ in the inductor plays the role of the position coordinate in the mechanical version of the harmonic oscillator. The charge q on the capacitor plays the role of its macroscopic conjugate momentum, such that as quantum operators they obey $[\hat{\Phi}, \hat{q}] = i\hbar$. The Hamiltonian of the isolated circuit is simply the sum of the energy stored in the two elements, expressed as a function of the pair of conjugated variables:

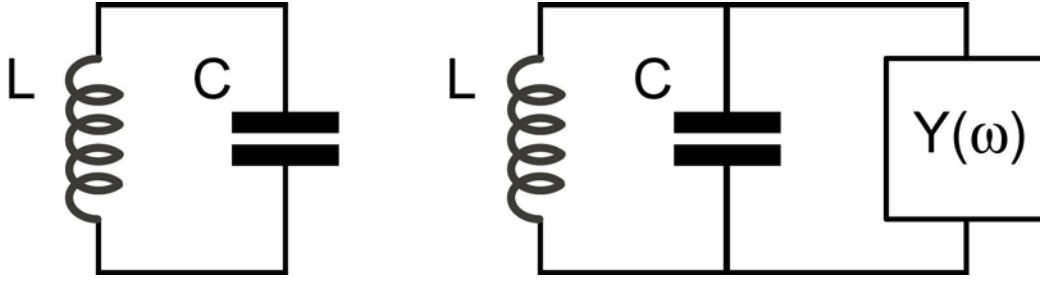


Figure 2.2.1. Electrical circuit version of a harmonic oscillator. Left: LC circuit. Right: LC circuit connected to an electromagnetic environment modeled by an admittance $Y(\omega)$ in parallel with the circuit.

$$\hat{H} = \frac{\hat{q}^2}{2C} + \frac{\hat{\Phi}^2}{2L}$$

If we introduce two operators defined as:

$$\hat{a} = \frac{1}{\sqrt{2\hbar Z_o}} (\hat{\Phi} + iZ_o \hat{q}) \quad \text{and} \quad \hat{a}^\dagger = \frac{1}{\sqrt{2\hbar Z_o}} (\hat{\Phi} - iZ_o \hat{q})$$

with $[\hat{a}, \hat{a}^\dagger] = 1$, where $Z_o = \sqrt{L/C}$ is the characteristic impedance of the circuit, we may define an operator \hat{n} that represents the number of photons in the oscillator as:

$$\hat{n} = \hat{a}^\dagger \hat{a}$$

Then, with some algebra, we can obtain the expression:

$$H = \hbar \omega_o \left(\hat{n} + \frac{1}{2} \right)$$

where $\omega_o = 1/\sqrt{LC}$ is the resonant angular frequency of the oscillator.

Observations of this circuit can only be made by leads that unavoidably couple it to the environment. The substrate on which the circuit has been realized is also coupling the circuit to a surrounding environment. Moreover, the circuit could also lose energy toward the environment by radiation. The combined effect of all these possible couplings to the environment can be described by a lumped element, whose frequency dependent admittance $Y(\omega)$ is in parallel with the LC circuit, see right side of Fig. 2.2.1. We now introduce the ratio of the energy stored in the unperturbed oscillator to the energy dissipated in one oscillation, the so called quality factor, $Q=1/\text{Re}\{Y(\omega_o)\}Z_o$. The Hamiltonian for the harmonic oscillator and the environment together can be written following the Caldeira-Leggett prescription, which we will briefly introduce in 2.2.7. We then obtain that, if $Q \gg 1/2$, the resonant angular frequency of the oscillator is shifted to:

$$\text{Re}\{\omega_s\} = \omega_o \left[-\frac{\text{Im}\{Y(\omega_o)\}Z_o}{2} + \sqrt{1 - \frac{1}{4Q^2} - \frac{(\text{Im}\{Y(\omega_o)\}Z_o)^2}{4}} \right]$$

and that the excited states have a decay rate:

$$\Gamma = \text{Im}\{\omega_s\} = \frac{\omega_o}{2Q}$$

These equations do not take in consideration terms higher than second order in $Y(\omega)$. When the admittance is purely real the quality factor becomes $Q=\omega_o RC$ and the two previous equations become:

$$\text{Re}\{\omega_s\} = \omega_o \sqrt{1 - \frac{1}{4Q^2}} \quad \text{and} \quad \Gamma = \frac{1}{2RC}$$

It is important to note that the parameters of the quantum system are not fundamental constants of Nature. They are engineerable quantities with a large range of possible values which can be modified easily by changing the dimensions of the elements in the electrical circuit.

To satisfy the three criteria introduced above defining a quantum circuit, we need:

- $\hbar\omega_o \gg k_b T$ which, for operating temperature of about 20 mK, implies $\omega_o/2\pi \geq 2$ GHz;

- $Z \gg Z_o$, which means that the circuit impedance has to be significantly larger than the characteristic impedance of the leads, whose typical value is 50 Ω ;

– $\hbar\omega_0 \ll \Delta$ which implies $\Delta > 100 \mu\text{eV}$.

This circuit may be fabricated using planar components with lateral dimensions around $10 \mu\text{m}$, giving values of L and C approximately 100 pH and 1 pF , respectively, and with $\omega_0/2\pi = 15.9 \text{ GHz}$ and $Z_o = 10 \Omega$. If we use aluminum, a good BCS superconductor with a transition temperature $T_c = 1.2 \text{ K}$ and an energy gap $\Delta \approx 190 \mu\text{eV}$, dissipation from the breaking of Cooper pairs will begin at a frequency $\omega \geq 2\Delta/\hbar = 88 \text{ GHz}$. According to the Mattis-Bardeen formula [MB58], the residual resistivity of a BCS superconductor is:

$$\rho(\omega, T) = \rho_o \hbar\omega / k_B T \exp(-\Delta / k_B T)$$

where ρ_o is the resistivity of the metal in the normal state and therefore the intrinsic losses of the superconductor at our operating temperature can be safely neglected.

2.2.4. Limits of circuits with lumped elements: need for transmission line resonators

Using the lumped element approximation carries some limitations. Any real component contains more than just one ideal lumped element. When we are dealing with non-static electromagnetic fields, the phase of the field change along the component if the scale of the component, l , is not much smaller than the wavelength of the field, λ . Even better, the total extension of the circuit, s , should be $s \ll \lambda$. Let us establish stricter conditions on the elements in the inductive and capacitive cases. For a lumped inductor with inductance L , the magnitude of the impedance is:

$$|Z_L| = \omega L \approx \frac{2\pi\bar{c}}{\lambda} \mu_o l = 2\pi \sqrt{\mu_r / \epsilon_r} \eta_o \frac{l}{\lambda}$$

where $\bar{c} = \sqrt{\mu_o \mu_r / \epsilon_o \epsilon_r}$ is the propagation velocity of the field in the inductor medium and $\eta_o = \sqrt{\mu_o / \epsilon_o} = 376.7 \Omega$ is the electromagnetic wave impedance in vacuum. Since we are in the lumped element approximation this implies an upper limit on the impedance amplitude beyond which the approximation breaks down:

$$\frac{l}{\lambda} = \frac{|Z_L|}{2\pi \sqrt{\mu_r / \epsilon_r} \eta_o} \ll 1$$

The same can be shown in the case of a lumped parallel plate capacitor, with capacitance C and insulator thickness t , where the amplitude of the admittance is:

$$|Y_C| = \omega C = \frac{2\pi\bar{c}}{\lambda} \epsilon_o \frac{l^2}{t} = 2\pi \sqrt{\mu_r/\epsilon_r} \eta_o^{-1} \frac{l}{\lambda}$$

that puts an upper limit on the admittance amplitude before the lumped element approximation breaks down and parasitic effects cannot be any longer neglected:

$$\frac{l}{\lambda} = \frac{|Y_C|}{2\pi \sqrt{\mu_r/\epsilon_r} \eta_o^{-1}} \ll 1.$$

In the frequency range of interest for this work, 2-50 GHz, which means $\lambda \sim 0.6-15$ cm in vacuum, we may be able to realize elements of sub-millimeter size, which we can describe as lumped element, or circuits of millimeter size, which we can model as transmission line, but we are going to face a technical challenge in dealing with connections among them or with the rest of the experimental set-up. For quasi-static fields the connections can be thought of as wires of negligible impedance, but this is not true anymore if we deal with connections, whose dimension, s_c , is comparable with the wavelength of the non-static field.

For instance, if we use a simple wire to connect the experimental set-up to a circuit which could be modeled as small impedance, we may treat the wire as an inductive connection realized by a shorted transmission line with characteristic impedance z_o :

$$z_{in}^L = jz_o \tan\left(2\pi \frac{s_c}{\lambda}\right)$$

Alternatively if the connected circuit could be modeled as small admittance, we may treat the wire as a capacitive connection realized by an open transmission line:

$$y_{in}^C = jy_o \tan\left(2\pi \frac{s_c}{\lambda}\right)$$

where z_o and y_o are the characteristic impedance and admittance of the transmission line. If we want to neglect respectively the impedance or the admittance of the wire respect to that of the connected element, even only for $d \ll \lambda$, we obtain in the two cases:

$$\frac{|z_{in}^L|}{z} = 2\pi \frac{z_o}{z} \frac{s_c}{\lambda} \ll 1 \qquad \frac{|y_{in}^C|}{y} = 2\pi \frac{y_o}{y} \frac{s_c}{\lambda} \ll 1$$

In both cases, these results put an even stronger constraint on the dimension of the connections since:

$$\frac{s_c}{\lambda} \ll \frac{z}{2\pi z_o} \qquad \frac{s_c}{\lambda} \ll \frac{y}{2\pi y_o}$$

In conclusion, we cannot in general neglect without consequences the parasitic elements of a lumped element circuit and it is then in general better to design them using the well-known transmission line and waveguides techniques bringing at the same time ease of fabrication and full understanding of the dynamics of the circuit. This strategy has been applied in the work described in Chapter 6.

2.2.5. Hamiltonian of a classical electrical circuit

For the harmonic *LC* oscillator, a straightforward application of the Hamiltonian formalism can easily be generalized to obtain a quantum description of the circuit. It is much less obvious how to do so in complicated circuits that may even include non-linear elements. We will briefly introduce a systematic procedure [YD84, De97] for setting up the Hamiltonian of an arbitrary electrical circuit.

An electrical circuit can be described as a network of branches connected at nodes. Several independent paths formed by a succession of branches can be found between nodes. The circuit can therefore contain one or several loops. Each branch consists of a two-terminal element, which we will consider as a lumped component. The element of each branch is characterized by two variables, see Fig. 2.2.2. One is the voltage across the branch defined as:

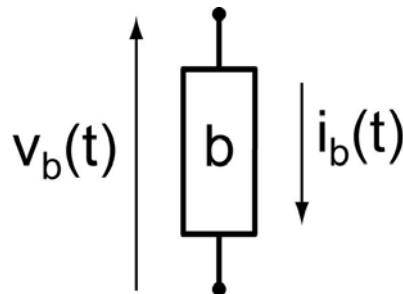


Figure 2.2.2. Convention on the branch variables. An arbitrary branch, *b*, of an electrical network circuit with the sign conventions for the voltage and the current associated to it.

$$v_b(t) = \int_{\text{beginning of } b}^{\text{end of } b} \vec{E}(t) \cdot d\vec{l}$$

where \vec{E} and $d\vec{l}$ are the electric field and a line path element inside the component. The other variable is the current flowing through the branch:

$$i_b(t) = \oint_{\text{around } b} \vec{H}(t) \cdot d\vec{l}$$

where \vec{H} and $d\vec{l}$ are the magnetic field and a line path element around the component. Because we consider lumped elements, we can make voltages and currents independent from the integration path once we impose for the line integral of the electric field to be outside the wire of the inductors and the loop integral of the magnetic induction field to be outside the dielectric of the capacitors.

A Hamiltonian description of an electrical circuit requires the definition of branch flux and branch charge as follows:

$$\Phi_b(t) = \int_{-\infty}^t v_b(t') dt'$$

$$Q_b(t) = \int_{-\infty}^t i_b(t') dt'$$

We have, of course, supposed that electric and magnetic fields have been adiabatically turned on starting at $t = -\infty$, so that there were no voltages or currents at that initial time. We have also to define a constitutive relation linking voltage and current for each element. A capacitive element will have a relation of the type $v_b = f(Q_b)$, where for a usual linear capacitor $f(Q_b) = Q_b / C$. An inductive element will have $i_b = g(\Phi_b)$, where for a usual linear inductor $g(\Phi_b) = \Phi_b / L$.

Since the power flowing into each branch is $v_b i_b = v_b \dot{Q}_b = i_b \dot{\Phi}_b$, we have that the energy stored in a capacitor is:

$$h(Q_b) = \int_0^{Q_b} \frac{Q}{C} dQ = \frac{Q_b^2}{2C},$$

while the energy stored in an inductor is:

$$h(\Phi_b) = \int_0^{\Phi_b} \frac{\Phi}{L} d\Phi = \frac{\Phi_b^2}{2L}.$$

The branch variables are not independent variables and must follow constraints imposed by the network topology. These constraints, called Kirchhoff's laws, state that the sum of the branch voltages around each loop, l , and the sum of the branch currents arriving at each node, n , should be zero as long as the flux through the loop, $\tilde{\Phi}_l$, imposed by external flux bias sources and the charge at the node, \tilde{Q}_n , imposed by charge bias sources are constant:

$$\sum_{\text{all } b \text{ around } l} \Phi_b = \tilde{\Phi}_l \qquad \sum_{\text{all } b \text{ arriving at } n} Q_b = \tilde{Q}_n$$

We have now to choose a set of independent variables corresponding to the degrees of freedom of the electrical circuit. In the following, we will use node variables because they are more adapted to treat circuits involving tunnel elements, like the ones we will be dealing with in the rest of this work. We could have instead used loop variables without losing any generality. Unlike branch variables, node variables depend on a particular description of the circuit topology. The one we will adopt is generated by the following procedure: one node of the circuit is first chosen as reference node or ground while the others are called active nodes. Then, from the ground, a loop-free set of branches called spanning tree is selected applying the following simple rule: each node of the circuit must be linked to the ground by one and only one path belonging to the tree. In general, inductors are preferred as branches of the tree but this is not necessary.

Once one of the many possible spanning tree is chosen, we associate to each node a node voltage, v_n , which is the algebraic sum of the branch voltages between ground and the node. The conjugate variable is the node current, i_n , which is the algebraic sum of all the branch currents flowing to the node through capacitors only. The dynamical variables appearing in the Hamiltonian of the electrical circuit are the node fluxes and node charges defined as:

$$\Phi_n(t) = \int_{-\infty}^t v_n(t') dt' = \sum_b \int_{-\infty}^t O_{nb} v_b(t') dt' = \sum_b O_{nb} \Phi_b(t)$$

where O_{nb} are matrix elements whose value is equal to 1 or -1 depending if the branch voltage has been considered with the right or the wrong orientation. It could also be equal to 0 if the branch does not belong to the path between ground and the node;

$$Q_n(t) = \int_{-\infty}^t i_n(t') dt' = \sum_b \int_{-\infty}^t S_{nb} i_b(t') dt' = \sum_b S_{nb} Q_b(t)$$

where S_{nb} are matrix elements whose value is equal to 1 or -1 depending if the branch current through the capacitor has been considered with the right or the wrong orientation. It could also be equal to 0 if the branch is either not connected to the node or does not contain a capacitor.

Using Kirchoff's laws, it is possible to express the flux and the charge of each branch as a linear combination of all the node fluxes and charges, respectively. In this inversion procedure, $\tilde{\Phi}_l$ and \tilde{Q}_n will appear.

If we now sum the energies of all branches of the circuit expressed in terms of node fluxes and charges, we will obtain the Hamiltonian of the circuit corresponding to the representation associated with that particular spanning tree. In this Hamiltonian, capacitor energies behave like kinetic terms while the inductor energies behave as potential terms. The Hamiltonian of the LC circuit, we have previously introduced, is an elementary example of this procedure.

2.2.6. Quantum description of an electric circuit

The transition from the classical to the quantum description of an electrical circuit is straightforward once the Hamiltonian has been obtained. The classical variables have to be replaced by the corresponding quantum operators in the Hamiltonian, which becomes a function of operators. The node flux and charge operators have the relation:

$$\left[\hat{\Phi}_{n,i}, \hat{\Phi}_{n,j} \right] = 0 \quad \left[\hat{Q}_{n,i}, \hat{Q}_{n,j} \right] = 0 \quad \left[\hat{\Phi}_{n,i}, \hat{Q}_{n,j} \right] = i\hbar \delta_{ij}$$

One can also show that the branch flux and charge operators share the same commutation relations.

2.2.7. Caldeira-Leggett model for dissipative elements

In our description of electrical circuits we have restricted ourselves to non-dissipative components. We would like now to extend our treatment of circuits to dissipative elements like resistors.

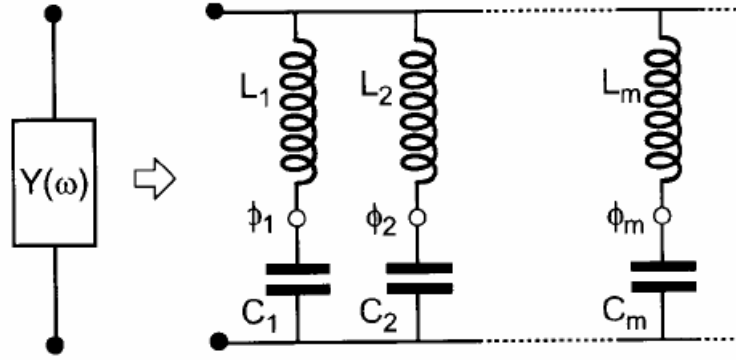


Figure 2.2.3. Caldeira-Leggett model for a dissipative element. The dissipative element, representing the interactions with the surrounding environment, is represented by an admittance. This can then be treated as an infinite set of LC circuits added in parallel to each other [De97].

The essence of the Caldeira-Leggett model [CL83] is to replace, in the context of electrical circuits, a linear dissipative element characterized by a frequency dependant admittance, $Y(\omega)$, by an infinite set of LC oscillators added in parallel to each other, as shown in Fig. 2.2.3. The internal degrees of freedom of the admittance can be thought of as the node flux variables of the LC oscillators. The transition from a finite number of degrees of freedom to an infinite one reconciles the irreversible behavior of a dissipative element with the formal reversibility of the Hamiltonian formalism. In fact, even if the admittance of each individual oscillator is purely imaginary, its generalization to complex frequencies has a real part in an infinitesimally narrow region around its resonant frequency.

The idea of Caldeira and Leggett thus consists in replacing the initial admittance with an infinitely dense set of oscillators reproducing the same total real part on the whole range of frequency of interest. Of course, this model does not reproduce the internal workings of a dissipative element, but it is helpful to evaluate the influence that this component has on the rest of the circuit. This influence can be taken into account by adding to the Hamiltonian of the rest of the electrical circuit the contribution of the infinite set of parallel LC oscillators, that replaces the admittance, coupled to the circuit:

$$h_Y = \sum_m \left[\frac{q_m^2}{2C_m} + \frac{(\Phi_m - \Phi_c)^2}{2L_m} \right]$$

where C_m and L_m represent the components of the m -th oscillator. Choosing one of the terminal of the admittance as ground, Φ_m , is the flux variable of the intermediate node for the m -th oscillator and the charge variable, q_m , is its conjugate momentum. Φ_C is the flux of the capacitor branch in the circuit coupled to the admittance, see Fig. 2.2.1.

2.2.8. Beyond the harmonic oscillator: need for non-linearity

It seems straightforward to realize a macroscopic harmonic oscillator circuit which will exhibit quantum phenomena using easily available fabrication technology. Unfortunately, it would not be easy to demonstrate that it is actually performing quantum mechanically. Indeed, transition frequencies between neighboring quantum states are all degenerate, as a result of the parabolic shape of the potential, and all equal to ω_0 , which is the frequency observed also classically. The harmonic oscillator is in the “correspondence limit” for all quantum numbers. Quantum mechanics would be revealed by measuring higher moments of its basic variables, but these are much more difficult to measure since we are dealing with a single quantum degree of freedom. We could try to observe the zero-point motion of the ground state, a unique quantum property, but this is a very difficult experiment requiring a quantum-limited amplifier. We could also try to measure with low temperature calorimetric experiments the specific heat dependence on temperature to show the difference between classical and quantum behavior, but also this measurement is a very difficult one for the high sensitivity required to reach conclusive results. On the other hand, we can escape the “correspondence limit” using a non-linear component which must obey the additional requirement of being non-dissipative.

3. A non-linear circuit element: the Josephson tunnel junction

There is only one circuit element that is both non-linear and non-dissipative at arbitrarily low temperature: the Josephson tunnel junction [J62]. This component consists of a sandwich of two superconducting thin film electrodes separated by a very thin (typically ~ 1 nm) insulating barrier, see Fig. 3.1, that allows tunneling of Cooper pairs through it, creating a non-linear inductive element [BP92]. The barrier is fabricated by thermal oxidation of one of the superconducting electrode. Aluminum oxide is formed in a self-terminating thermal oxidation process of a thin aluminum layer. If the electrode is fabricated out of some refractory material, then the surface is easily wet by few nanometers of aluminum, whose thermal oxide becomes the junction barrier, before some more metal is deposited to fabricate the top electrode. Aluminum oxide also has a high relative dielectric constant, $\epsilon_r=10$, and a work function of about 1 eV. These favorable material properties have made it the most used barrier material for Josephson tunnel junctions. Unfortunately, the granularity of the film, shown also in Fig. 3.1, on which the extremely thin oxide is grown and the limits of the present fabrication techniques result in actual barriers whose amorphous and non-stoichiometric structure is far from ideal and needs further improvements [TMP05].

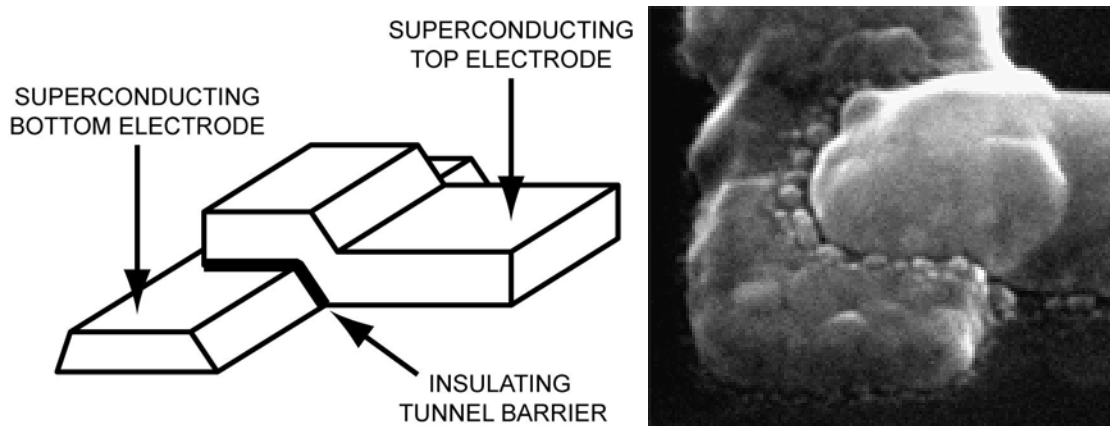


Figure 3.1. Josephson tunnel junction. Left: Sketch of a Josephson tunnel junction: a sandwich of two superconducting thin film electrodes separated by a very thin (~ 1 nm) insulating barrier. Right: SEM image of an actual junction realized at Yale by the commonly used Dolan bridge technique. In this technique, also known as double angle deposition, the two overlapping films are evaporated through a resist stencil. The width of the Al bottom electrode is 150 nm and its thickness is 40 nm. The barrier was realized by thermal oxidation of the bottom electrode. The thickness of the Al top electrode is 70 nm.

However, this barrier material still seems to be better than the natural oxides of other superconducting metals. In this work, we consider the junction area small such that the superconducting order parameter is homogeneous inside the electrodes [BP92].

3.1. A model for the Josephson tunnel junction

The Josephson tunnel junction (JTJ) can be modeled as a pure superconducting tunnel component, called the Josephson element, which can be thought of as a non-linear inductor, in parallel with a capacitor, corresponding to the parallel plates formed by the two overlapping electrodes of the junction, see Fig. 3.2.

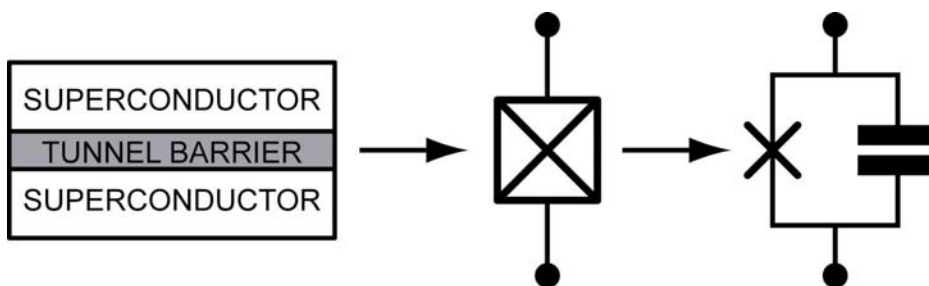


Figure 3.2. Josephson tunnel junction circuit model. Left: Sketch of a Josephson tunnel junction. Center: Branch symbol for the JTJ. Right: Electrical circuit model: the Cooper pair tunneling is represented by a pure tunnel element, which acts as an ideal non-linear inductor, in parallel with a capacitor representing the overlapping electrodes separated by the insulating barrier.

At the temperature of our interest ($T=20$ mK), all the electrons in the two superconducting electrodes are condensed in Cooper pairs. Since all the internal microscopic degrees of freedom are frozen, the Josephson tunnel junction is characterized only by two *a priori* independent collective degrees of freedom: the charge on the capacitor, $Q_c(t)$, and the number, $N(t)$, of Cooper pairs having tunneled through the Josephson element.

The charge flowing through the Josephson element up to a time t , $Q_J(t)=-2eN(t)$, does not in general correspond to $Q_c(t)$ if the junction is connected to an electrical circuit. In fact, $Q_c(t)$ is a continuous variable since it can be any fraction of the charge quantum, e , corresponding to a bodily displacement of the electron fluid with respect to the ion lattice background of the metal. In contrast, $N(t)$ is an integer variable.

The Josephson tunnel junction has a unique many-body ground state. Excited states of the electrode have a minimum energy of 2Δ , where Δ is the superconducting quasiparticle

gap, which we suppose large in comparison with environment energies like those of the temperature fluctuations.

3.2. Josephson equations

The Josephson element is characterized by the following non-linear inductive current-flux constitutive relation, often renamed the second Josephson equation [BP92]:

$$i(t) = I_c \sin(2\pi \Phi_J(t) / \Phi_0) = I_c \sin \delta(t)$$

I_c is a parameter called the critical current of the junction, which scales proportionally to the junction area and decreases exponentially with the barrier thickness. $\Phi_J(t)$ is generalized magnetic flux of the Josephson element, as already defined talking of branch variables. The constant $\Phi_0 = h/2e$ is the superconducting magnetic flux quantum. The variable δ is the dimensionless generalized flux also called the gauge invariant phase difference and appears in the so-called first Josephson equation [BP92], which is a differential form of the generalized flux definition:

$$v(t) = \frac{\Phi_0}{2\pi} \frac{\partial \delta(t)}{\partial t}$$

The phase difference θ between the two superconducting condensates on the two sides of a junction (supposed to be in equilibrium) is related to δ by $\theta = \delta \bmod 2\pi$.

We now introduce two other parameters describing the same Josephson element. The first one is the Josephson inductance $L_{J0} = \Phi_0 / 2\pi I_c$, which can be naturally introduced expanding the sine function in the current-flux constitutive relation in the case $\Phi_J \ll \Phi_0 / 2\pi$. More generally, it is convenient to define the phase-dependent Josephson inductance $L_J = L_{J0} / \cos \delta$. Note that L_J not only depends on δ , it can actually become infinite or even negative. Thus, under the proper conditions, the Josephson element becomes a switch and even an active circuit element, as we will see below.

The other useful parameter is the Josephson energy $E_J = \Phi_0 I_c / 2\pi = R_Q \Delta / 2R_N$, where $R_Q = h/(2e)^2$ is the quantum resistance for Cooper pair and R_N is the resistance of the tunnel junction at voltages higher than 2Δ . If we compute the energy stored in the Josephson element:

$$h_J(t) = \int_{-\infty}^t i(t')v(t')dt' = -E_J \cos(2\pi\Phi_J(t)/\Phi_0)$$

In contrast with the parabolic dependence on flux of the energy of an inductor in a harmonic oscillator, the potential associated with a Josephson element has the shape of a washboard, where the total height of the corrugation is $2E_J$.

3.3. Quantum Hamiltonian of an isolated Josephson tunnel junction

Note that for the special case of the Josephson element, the phase operator, $\hat{\theta}$, and the Cooper pair number operator, \hat{N} , have the property: $[\hat{\theta}, \hat{N}] = i$

In the so-called charge basis, we have:

$$\hat{N} = \sum_{N \in \mathbb{Z}} N |N\rangle \langle N|$$

$$\hat{h}_J = -E_J \cos \hat{\theta} = -\frac{E_J}{2} \sum_{N \in \mathbb{Z}} (|N\rangle \langle N+1| + |N+1\rangle \langle N|)$$

while in the so-called phase basis, we have

$$\hat{N} = |\theta\rangle \frac{\partial}{i\partial} \langle \theta|$$

Note that since \hat{N} has relative integer eigenvalues, its conjugate operator $\hat{\theta}$ has eigenvalues defined only in the interval $[0, 2\pi[$, like angles with support on the goniometric circumference.

Then, the Hamiltonian of an isolated Josephson tunnel junction is the sum of the two contributions from the components of the model:

$$\hat{h}_{JJ} = E_{CJ} (\hat{N} - N_{off})^2 - E_J \cos \hat{\theta}$$

where the Coulomb charging energy for one Cooper pair on the junction capacitor, C_J , is:

$$E_{CJ} = \frac{(2e)^2}{2C_J}$$

and N_{off} is the residual offset number of Cooper pairs on the capacitor. We cannot remove this time independent quantity from the Hamiltonian because the non-linearity does not

allow for a canonical transformation eliminating it to be performed, unlike in the LC oscillator where it was irrelevant to the dynamics of the electrical circuit.

4. Superconducting circuits based on the Cooper Pair Box

4.1. Different competing implementations of quantum computers

In 2001, Shor's factorization algorithm for finding prime numbers has been implemented for the integer 15 using a system of 7 spin-1/2 nuclei in a system of *ad hoc* organic molecules by the IBM-Stanford collaboration [VSB01]. To obtain this impressive result, the system was manipulated and measured using NMR techniques. Unfortunately, this architecture does not allow to address and to measure each qubit independently. Because of the randomness in the initial thermal population of the system states, the NMR signal that comes from entangled states decreases exponentially with the number of qubits involved in it. This clearly sets an upper limit to the size of a register and does not satisfy the requirement of scalability.

There are two classes of systems candidates to implement an actual quantum computer. On one hand, there are the systems coming from quantum optics and atomic physics, like trapped atoms, ions or molecule. They are so far the more advanced for the implementation of qubits and quantum gates. These systems have been manipulated individually in a controlled fashion for about 20 years and techniques have reached a high level of sophistication. They can have very large quality factors, but they are hard to couple and it is not clear yet if these proposals can be extended to the construction of a scalable quantum processor.

Trapped ion systems, such as those developed by Rainer Blatt at the University of Innsbruck in Austria [GRL03] or by David Wineland at NIST in Boulder [LKS05], have remarkable level structures. The ground state is split by the hyperfine interaction, thus yielding basis states for the qubit, while well-resolved excited states hovers well above the ground state at energies corresponding to visible or infra-red photons, thus providing a very good isolation between the degrees of freedom representing the qubits and the ones perturbing the system. At the same time, the ground-to-excited state electronic transitions can be exploited to read-out the value of the qubit by fluorescence photons, which can be easily detected.

On the other hand, there are the systems coming from solid state physics: quantum dots [LDi98], nuclear spin in doped silicon [K98] and superconducting integrated quantum

circuits. It is easier to think that they could be parallel produced using the techniques of micro and nanofabrication already developed in the semiconductor industry, hence benefiting of the same advantages that have made classical processors so powerful today. Most solid-state proposals however are still at a theoretical or very preliminary stage. Only for superconducting integrated quantum circuits, experimental demonstrations of quantum coherence both in frequency and the time domain have been performed on a single controllable qubit. The quality factors of these circuits have only recently been assessed and they seem to show decoherence limiting the number of quantum operations to about 100. The origins of the observed decoherence are not yet fully understood.

4.2. The Cooper Pair box

The simplest superconducting quantum circuit involving a Josephson tunnel junction is the so-called Cooper Pair Box (CPB), for which quantum coherence evidence was measured [BVJ98, Bo97] for the first time by the Qnantronics group at CEA in Saclay, France. The basic CPB consists of a low-capacitance, C_i , superconducting electrode, called “island”, connected to a superconducting reservoir by a Josephson tunnel junction with capacitance C_J and Josephson energy E_J . The residual offset number of Cooper pairs, N_{off} , on the total capacitor $C_\Sigma = C_i + C_J + C_g$ is compensated by biasing the junction with a voltage source U_g through a gate capacitance C_g , see Fig. 4.1. The only degree of freedom of the system is the number of Cooper pairs on the island and \hat{N} is its

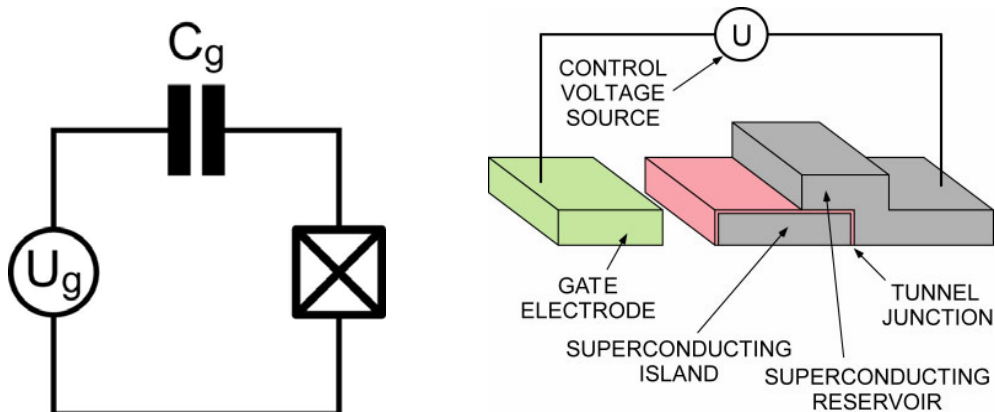


Figure 4.1. The Cooper Pair Box. On the left: the electrical model of the Cooper Pair Box. On the right: sketch of the simplest version of this circuit in which the superconducting island is coupled to a superconducting reservoir through a Josephson tunnel junction and to a gate electrode by a capacitor.

associated operator. Using the techniques introduced before, it is easy to show that the Hamiltonian of the CPB is:

$$\hat{H}_{CPB} = E_C (\hat{N} - N_g)^2 - E_J \cos \hat{\theta}$$

where $E_C = (2e)^2 / 2C_\Sigma$ is the charging energy of the box and $N_g = N_{off} + C_g U_g / 2e$ is the effective gate charge number. It is worth noticing that this Hamiltonian is very similar to that of a isolated Josephson tunnel junction we calculated in the previous chapter, and N_g can be understood as an externally controlled offset charge number.

Moreover, the single junction can be split into two junctions, see Fig. 4.2, with respective capacitance $C_J(1+d)/2$ and $C_J(1-d)/2$, where d is a coefficient of asymmetry. Since they are in parallel the total split junction capacitance is still C_J . The two junctions have respective Josephson energies $E_J(1+d)/2$ and $E_J(1-d)/2$. The total Josephson energy of the split junction CPB is:

$$\hat{h}_{J,split} = -E_J \cos(\hat{\delta}/2) \cos(\hat{\theta}) + dE_J \sin(\hat{\delta}/2) \sin(\hat{\theta})$$

where $\hat{\delta} = \hat{\delta}_1 + \hat{\delta}_2 = \Phi_l / \Phi_0$ and $\hat{\theta} = (\hat{\delta}_1 - \hat{\delta}_2) / 2$ are two linear combination of the operators of the two junctions, where Φ_l is a magnetic flux bias applied to the loop formed by the two tunnel junctions, the island and the superconducting reservoir.

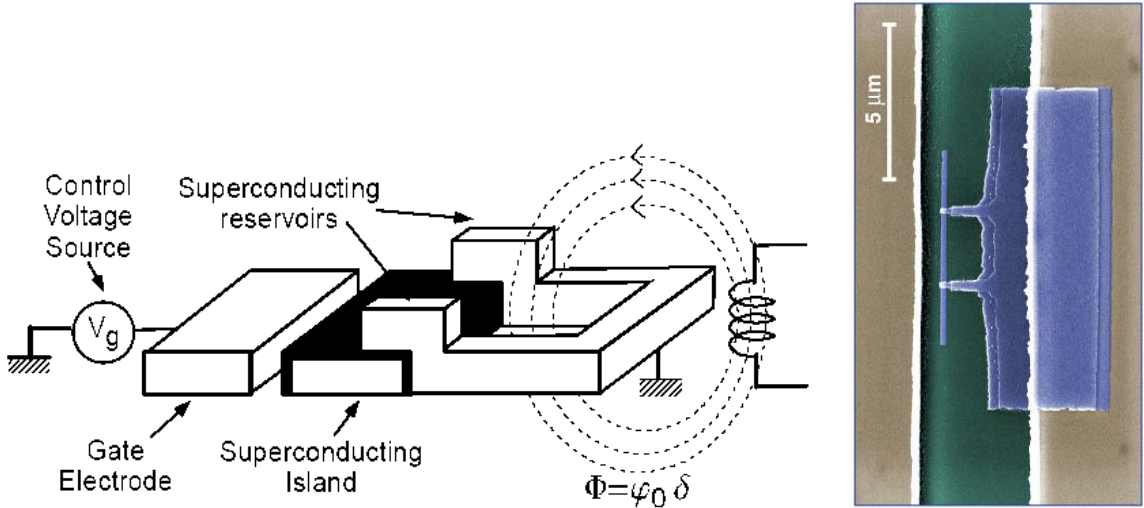


Figure 4.2. The split Cooper Pair Box. Left: sketch of the split version of the CPB. The circuit is voltage biased through its gate and flux biased through its loop [C02]. Right: SEM image of a CPB realized at Yale. The image has been artificially colored.

In the following δ will be considered as a classical parameter since the impedance of the junctions is always lower than the resistance quantum. For $d=0$ the split CPB has an effective Josephson energy, $E_J^* = E_J \cos(\delta/2) = E_J \cos(\pi\Phi_l/\Phi_0)$, proportional to the Josephson energy of the initial single junction, but it can now be tuned by varying Φ_l . In general, it is easy to reduce the asymmetry to $d < 0.1$, with the positive effect of lifting the degeneracies existing for $d=0$ at $N_g=1/2$ and $\Phi_l = \Phi_0/2$. The Hamiltonian of the symmetrically split Cooper pair box is:

$$\hat{H}_{sCPB} = E_C (\hat{N} - N_g)^2 - E_J \cos(\pi\Phi_l/\Phi_0) \cos \hat{\theta}$$

The Schrodinger equations obtained using the Hamiltonians presented above have exact eigenvalues and eigenfunctions which are solutions of the Mathieu equation [C02]. In this way, we design superconducting quantum circuits whose energy spectra can be tuned in situ during the circuit operation by two externally controllable electrodynamic parameters: the voltage applied at the gate and the magnetic flux threaded through the superconducting loop. The other parameters E_C and E_J are engineered during the superconducting quantum circuit fabrication in two different way. As explained in more details in Chapter 8, in the device patterning stage of the fabrication, we modify the island and gate geometries, affecting only E_C , or the barrier area, which varies both E_C and E_J but in opposite directions. In the device deposition stage, we change either the deposition condition or even the material used in the electrode fabrication, in order to obtain different energy gaps for one or both the electrodes, affecting only E_J , or the condition of the barrier formation, in order to obtain different barrier transparency, which varies the two parameters in the same direction but with E_J being much more sensitive to these variations.

The Cooper Pair Box are then considered by quantum engineers what the hydrogen atom is for atomic physicists, and the two external fields compared to the Stark and Zeeman fields. Two comments are in order at this point. In the first place, it is easy to observe that much smaller values of the external fields are required to change entirely the spectrum of the CPB, compared to the situation in atomic physics. Even more important is to notice that, in the case of the quantum circuit, the parameters are fully engineerable and are not constant given once and for all like the Rydberg constant or the Bohr radius in an atom.

We will hopefully be able to generate a wider and even more useful set of atom-like circuits in quantum engineering to match the future demands of many different quantum machines.

4.3. Manipulation of the state of a Cooper Pair box

Because the Hamiltonian is sufficiently non-linear, the ground and the first excited state of the CPB can be considered as a two-level system. Near the degeneracy point $N_g=1/2$, where the electrostatic energy of the two charge states with 0 and 1 excess Cooper pair on the island are equal, and $\Phi=0$ where the Josephson degeneracy splitting is maximized, the tunable qubit is described by the Hamiltonian:

$$\hat{H}_{CPB-qubit} = -\frac{E_z}{2}(\hat{\sigma}_z + X_c \hat{\sigma}_x)$$

where, in the limit $E_J/E_C \ll 1$, $E_z=E_J$ and $X_c = 2E_C/E_J (1/2 - N_g)$. Note that the x direction is chosen along the charge operator, the variable of the box we can naturally couple to. This is why the CPB is considered a “charge” qubit. The Hamiltonian also shows that at the “sweet spot” $X_c=0 \rightarrow N_g=1/2$, the qubit transition frequency is to first order insensitive to the charge noise.

The state of the CPB can be manipulated within the subspace spanned by the two-level system using techniques inspired from Nuclear Magnetic Resonance (NMR). For the CPB qubit Hamiltonian in the eigenframe the representative vector is $\vec{h} = \hbar\omega_{01}\hat{Z}$.

A radiofrequency voltage signal with angular frequency ω_{RF} can be applied to the gate of the CPB. The voltage signal amplitude produces a change in the effective gate charge number, ΔN_g . Thus the free Hamiltonian of the CPB acquires a time dependent term, which in qubit bias is given by:

$$\hat{H}_{RF}(t) = -2E_C \Delta N_g \cos(\omega_{RF} t) \hat{\sigma}_x$$

In a rotating frame precessing with angular frequency ω_{RF} around $\hat{z}_R = \hat{Z}$, the representative vector of the total Hamiltonian, \vec{h}_R , becomes:

$$\vec{h}_{R,TOT} = 2 E_C \Delta N_g \left| \langle 1 | \hat{N} | 0 \rangle \right| \hat{x}_R + \hbar (\omega_{01} - \omega_{RF}) \hat{z}_R$$

The components of this vector generate rotations around their axes, as mentioned in Chapter 2. Indeed, the state vector precesses around \vec{h}_R at the angular frequency:

$$\omega_R = \sqrt{\left(2 E_C \Delta N_g \left| \langle 1 | \hat{N} | 0 \rangle \right| / \hbar \right)^2 + (\omega_{01} - \omega_{RF})^2} .$$

It is easy to observe that when $\omega_{RF} \approx \omega_{01}$ the motion of the state vector becomes a precession around \hat{x}_R at the Rabi angular frequency:

$$\omega_{Rabi} = 2 E_C \Delta N_g \left| \langle 1 | \hat{N} | 0 \rangle \right| / \hbar$$

On the other hand, viewed in the rotating frame the CPB state vector precesses around \hat{z}_R at the Ramsey angular frequency:

$$\omega_{Ramsey} = \omega_{01} - \omega_{RF} .$$

Then, by combining the free evolution and a radiofrequency excitation every possible state on the Bloch sphere, referred to a particular rotating frame imposed by the initial RF pulse, can be prepared.

4.4. Brief summary on other superconducting quantum circuits

Another superconducting quantum circuit based on Josephson tunnel junctions is the so-called RF-SQUID. It can be considered the dual of the CPB, employing a superconducting coil transformer instead of a gate capacitor to tune the Hamiltonian. The two sides of the junction with capacitance C_J are connected by a superconducting loop with inductance L , with an external magnetic flux Φ_{ext} imposed through it. The RF-SQUID Hamiltonian is:

$$\hat{H}_{RF-SQUID} = \frac{\hat{q}^2}{2C_J} + \frac{\hat{\Phi}^2}{2L} - E_J \cos \left(\frac{\hat{\Phi} - \Phi_{ext}}{\Phi_o} \right)$$

The degrees of freedom of this circuit are the flux through the superconducting loop, $\hat{\Phi}$, and the charge, \hat{q} , on the capacitance. Since the latter has continuous eigenvalues the

former one takes its values on a line and not on a circle. We now have three adjustable energy scales: E_J , E_{CJ} and $E_L = \Phi_0^2/2L$.

In the CPB the potential is cosine-shaped and has only one well since θ is defined only on $[0, 2\pi[$, in the RF_SQUID the potential is in general parabolic with a cosine corrugation. We can realize a RF-SQUID with a barrier transparency such that the Josephson inductance L_J is close to L and with an area such that $E_J/E_{CJ} \gg 1$. If we now flux bias it at $\Phi_{ext} = \Phi_0/2$, the potential would have two degenerate wells separated by a shallow barrier with height $E_B = 3E_J (L_J/L - 1)^2 / 2$. This corresponds to the case in which we voltage bias the CPB at the degeneracy value $N_g = 1/2$, replacing the capacitive energy with the inductive energy. At $\Phi_{ext} = \Phi_0/2$, the two lowest energy levels are then the symmetric and anti-symmetric combinations of the two wavefunctions localized in each well, and the energy splitting between the two states can be seen as the tunnel splitting associated with the quantum motion of a fluxon through the potential barrier between the two wells, bearing close resemblance to the dynamics of the ammonia molecule. The first few levels in the RF-SQUID potential have been seen experimentally for the first time by Jim Lukens and his group at University of New York in Stony Brook [FPC00].

Since the Hamiltonian is sufficiently non-linear, the ground and the first excited state of the RF-SQUID can be considered as a two-level system. In the vicinity of the flux degeneracy point the RF-SQUID qubit Hamiltonian is described by [DM04]:

$$\hat{H}_{RF-SQUID-qubit} = -\frac{E_z}{2} (\hat{\sigma}_z + X_c \hat{\sigma}_x)$$

with $E_z = \eta \sqrt{E_B E_{CJ}} \exp\{-\xi \sqrt{E_B/E_{CJ}}\}$ and $X_c = 2\zeta E_L/E_z (1/2 - N_\Phi)$. E_z represents the energy splitting, $N_\Phi = \Phi_{ext}/\Phi_0$ is the so called flux frustration. Because there are no analytical solutions for the RF-SQUID Hamiltonian, the numbers η , ξ and ζ have to be determined numerically in each individual case. Since the x direction is chosen along the flux operator, the variable of the RF-SQUID we can naturally couple to, the qubits derived from this basic quantum circuit are considered “flux” qubits. The Hamiltonian also shows that at the “sweet spot” $X_c = 0 \rightarrow N_\Phi = 1/2$, the qubit transition frequency is to first order insensitive to the flux noise.

Another basic superconducting quantum circuit is the Josephson tunnel junction biased with a DC-current source. This circuit can be thought as arising from a RF-SQUID with a loop inductance $L \rightarrow \infty$ biased by a flux $\Phi \rightarrow \infty$ such that the bias current $I = \Phi/L$ stays finite. The Hamiltonian of the Current Biased Junction (CBJ) is given by [MNA03]:

$$\hat{H}_{CBJ} = E_{CJ} \hat{p}^2 - E_J (\chi \hat{\delta} + \cos \hat{\delta})$$

where $\hat{\delta}$ is the gauge invariant phase difference operator, its conjugate variable \hat{p} is the number of charges on the capacitor and $\chi = I/I_c$. If we realize a CBJ with a barrier transparency such that $E_J/E_{CJ} \gg 1$, we can neglect the effects of charge fluctuation and consider the system as a particle, representing the phase, in a washboard potential, whose tilt is given by α . When I approaches I_c , the potential is very well approximated by the cubic form:

$$U(\chi, \delta) = E_J \left[(1 - \chi)(\delta - \pi/2) - 1/6 (\delta - \pi/2)^3 \right]$$

For $I \leq I_c$, there is a well with a barrier height $\Delta U = 4\sqrt{2}E_J/3 (1 - \chi)^{3/2}$ and the angular frequency at the bottom of the well is $\omega_b = \omega_p [1 - \chi^2]^{1/4}$. Energy levels in the CBJ have been seen experimentally for the first time by John Clarke and his group at University of California at Berkeley in 1985 [MDC85]. The first two levels can be used for qubit states and have an angular transition frequency $\omega_{01} \approx 0.95 \omega_p$. In practice, ω_{01} falls in the 5-20 GHz range and it is determined only by material properties of the junction barrier, since the plasma angular frequency $\omega_p = (L_{J0}C_J)^{-1/2}$ does not depend on junction area. The number of levels in the well is typically of the order of $\Delta U/\omega_p \approx 4-5$.

This qubit circuit has a unique feature: a built-in read-out. For every realization of the qubit in a specified energy level in the cubic potential, there is a probability that it would tunnel through the potential barrier into the continuum outside the barrier. Because the tunneling rate increases by a factor of approximately 500 each time we go from one energy level to the next, the population of the first excited state of the qubit can be reliably measured by sending a probe signal inducing a transition from this state to a higher energy state with larger tunneling probability. This procedure is the base of the qubit read-out. In fact, after tunneling the particle representing the phase accelerates

down the washboard. This is a convenient self-amplification process leading to a voltage $2\Delta/e$ across the junction, which is proportional to the energy gap of the junction electrode material. Therefore after applying the probe signal, if a finite voltage suddenly appears across the junction, it would just imply that the qubit was in the first excited state, whereas no voltage implies that the qubit was in the ground state.

Since the Hamiltonian is sufficiently non-linear, the ground and the first excited state of the CBJ can be considered as a two-level system and the CBJ qubit Hamiltonian is described by [DM04]:

$$\hat{H}_{CBJ-qubit} = \frac{\hbar\omega_{01}}{2}\hat{\sigma}_z - I_c(1-\chi)\sqrt{\frac{\hbar}{2\omega_{01}C_J}}(\hat{\sigma}_x + r\hat{\sigma}_z)$$

where $r = \sqrt{\hbar\omega_{01}/3\Delta U} \approx 0.28$ for typical operating parameters. In contrast with the flux and charge qubit circuits, the CBJ qubit Hamiltonian cannot be cast into the NMR-type form. However, a sinusoidal bias current signal $\chi(t) = 1 + k \sin \omega_{01}t$, where k is a proportionality constant, can still produce $\hat{\sigma}_x$ rotations, whereas a low-frequency signal produces $\hat{\sigma}_z$ operations. Since the x direction is chosen along the phase operator, the variable of the CBJ we can naturally couple to, the qubits derived from this basic quantum circuit are considered “phase” qubits. Note that in this case there is no obvious “sweet” spot where the qubit is first order insensitive to phase noise.

5. Read-out strategy with the Cooper Pair Box

We have introduced in the previous chapter the CPB circuit and the methods to write and manipulate its quantum states. Another task we want to be able to perform with quantum circuits is the read-out of the information contained in the qubit. This can be realized by some system coupled to the qubit for extracting information from it without at the same time submitting it to noise.

The first read-out for CPB qubit, achieving a projective measurement of the two qubit states, was developed in the late 1990's by Yasunobu Nakamura and his group at NEC in Japan [NPT99]. They succeeded in observing the CPB spectroscopy and in preparing coherent superpositions of the qubit states. Their read-out simply measured the current through an auxiliary ultrasmall Josephson tunnel junction directly connected to the CPB island and permanently biased above the gap voltage by a constant voltage source. The spectroscopy was carried out by applying a continuous microwave voltage at the CPB gate, while sweeping the DC gate voltage. The manipulation of the states was performed by square pulses at the CPB gate. The measurement of the current through the auxiliary junction, while repeating these pulses with different time duration, revealed the coherent Rabi oscillations between the two energy states of the qubit. However, the coherence time of this superposition never exceeded few ns because of the decoherence induced by this invasive read-out and because of the charge noise generated by microscopic charges moving at random close to or in the qubit circuit. This charge noise exists in all charging devices and has a $1/f$ power spectrum probed up to 10 MHz with a typical amplitude for metallic devices of $10^{-7} e^2/\text{Hz}$ at 1 Hz.

5.1. Read-out requirements

It is clear that a read-out based on a permanent measurement of the quantum state cannot achieve long coherence times. Thus beyond some sort of state measurement device, an ideal read-out system has to include a switch, which defines an OFF and an ON condition. During the OFF condition, initialization and gate operations can take place, while the measurement device should be completely decoupled from the qubit. During the ON condition, the measurement device should be maximally coupled to a

qubit variable that distinguishes between the two qubit states. Moreover, the back-action of the measurement device, while the switch is ON, should be weak enough to not produce any decoherence of the qubit state.

Decoupling the qubit from the read-out in the OFF phase can be achieved balancing the circuit in the manner of a Wheatstone bridge, with the read-out variable and the qubit control variable corresponding to orthogonal electrical degrees of freedom. Indeed, establishing ways of operation for qubits which would have fully orthogonal modes is a major advancement in realizing easily operable qubit registers.

In addition we should consider the possibility of protecting the system from noise by introducing circuit symmetries that allow neglecting noise contributions arising from one or more of the modes.

The read-out system can be characterized by four parameters:

- 1) the measurement time, t_m , is the time taken by the measuring device to reach a signal-to-noise ratio of one in the determination of the qubit state;
- 2) the depolarization rate, Γ_1^{ON} , of the qubit caused by the measurement in the ON state;
- 3) the decoherence rate, Γ_2^{OFF} , of the qubit information caused by the read-out even if it is in the OFF state;
- 4) the dead time, t_d , needed to reset measuring device and qubit after a measurement.

Minimizing all these parameters at the same time to improve read-out performance cannot be done without running into conflicts. An important quantity to optimize is the fidelity or discriminating power, F , of the read-out system. If F is of order unity the measurement is called “single-shot”. The condition for this to happen is:

$$\Gamma_1^{ON} t_m < 1$$

The speed of the read-out, determined both by t_m and t_d , should be sufficiently fast to allow a complete characterization of all the properties of the qubit before any drift in parameters occurs and to automatically correct for them when they do. Rapidly pulsing the read-out ON and OFF with a large decoupling amplitude such that

$$\Gamma_2^{OFF} T_2 \ll 1$$

requires a fast, strongly non-linear element, which is provided by one or more auxiliary Josephson junctions.

5.2. Weakly coupled read-out of a Cooper Pair Box: charge strategy

The first idea that comes to mind to read-out the state of a charge qubit is obviously to measure the charge on the CPB island. This was the strategy used in 1997-2002 by the Quantronics group at CEA in Saclay [BVJ98, CVJ02], using a single Cooper pair transistor and in 2000-2003 by the Chalmers-Yale collaboration [AJW01, LSB03] using a radiofrequency superconducting single electron transistor (RF-SET). Both electrometers were capacitively coupled to the CPB and they were weakly coupled to the CPB in order to minimize the back-action. Because of the weakness of the coupling, we can describe the effect of the measuring system in simple terms as dephasing and depolarization, as introduced in the last chapter. This means that during the measurement the read-out device projects the CPB state on its charge eigenstates. Then, the measured value is the mean island charge of the two qubit states. In fact, the signal measured by a weakly coupled electrometer is proportional to the difference in charge between the ground and excited states:

$$\Delta N_{01}(N_g, \Phi_l) = \left[\langle 1 | \hat{N} | 1 \rangle - \langle 0 | \hat{N} | 0 \rangle \right]_{N_g, \Phi_l}$$

To evaluate this quantity, we need to step back and calculate the island potential, \hat{V} , from the generalized Josephson equation and make use of the rules that link the conjugated operators describing a system and its Hamiltonian:

$$\hat{V} = \frac{\hbar}{2e} \frac{d\hat{\theta}}{dt} = \frac{i}{2e} \left[\hat{\theta}, \hat{H}_{CPB} \right] = -\frac{1}{2e} \frac{\partial \hat{H}_{CPB}}{\partial \hat{N}} = \frac{1}{2e} \frac{\partial \hat{H}_{CPB}}{\partial N_g} = \frac{2e}{C_\Sigma} (N_g - \hat{N})$$

from the last equality we obtain:

$$\hat{N} = N_g - \frac{1}{2E_C} \frac{\partial \hat{H}_{CPB}}{\partial N_g}$$

We now recast ΔN_{01} as:

$$\Delta N_{01}(N_g) = \left[-\frac{\hbar}{2E_C} \frac{\partial \omega_{01}}{\partial N_g} \right]_{N_g, \Phi_l}$$

The two different electrometers used in this approach induce a back-action on the qubit with very different power spectra. In the RF-SET case, the back-action has a shot noise

spectrum coming from the charges tunneling in and out of the island through the junctions. In the single Cooper pair transistor, the supercurrent induces a back-action in the qubit which follows the phase fluctuations across the transistor. The noise in the phase arises from the thermal fluctuations in the dissipative elements of the read-out circuit.

For both electrometers, it is clearly more favorable to manipulate the qubit state at $N_g=1/2$, where, since ΔN_{01} is zero, charge fluctuations have no effect on the transition angular frequency at the first order. But the severe drawback of the charge measurement strategy is that to measure a charge difference between the two qubit states, the CPB voltage bias has to be moved away from the “sweet” spot just before the electrometer performs any measurement. In addition to the back-action from the electrometer, this exposes the qubit to noise in the control variable, which induces decoherence in the CPB, through a coupling Hamiltonian between the CPB and the gate charge fluctuations, ΔN_g :

$$\hat{H}_c = \frac{\partial \hat{H}_{CPB}}{\partial N_g} \Delta N_g$$

Furthermore, a better immunity to charge noise requires large ratio E_J/E_C which reduces the charge difference between the two states making high resolution charge measurements more difficult.

Using this strategy, the Yale-Chalmers collaboration was able to measure [LBS03] $T_1=1.3 \mu\text{s}$ and $T_2=325 \text{ ps}$ for a transition frequency $\nu_{01}=76 \text{ GHz}$, which implies $Q_1=6.2 \times 10^5$ and $Q_2=155$.

5.3. Weakly coupled read-out of a Cooper Pair Box: loop current strategy

Because of the weaknesses of the charge read-out strategy, a different strategy was proposed by the Quantronics group in 2002 [VAC02]. It consists in reading-out the state of the qubit by measuring the loop current in a split CPB. As we mentioned in the last chapter, the qubit energy spectrum is now controlled also by the phase difference, δ , across the two junctions, which is proportional to the magnetic flux threaded through the superconducting loop. Here, different persistent currents, whose sign depends on the

qubit state for a fixed value of δ , are present providing a new read-out port inductively coupled to the CPB and different, possibly orthogonal to the charge port used for state manipulation. It is possible in this circuit to decouple control and read-out operations. It is also possible to use CPB with higher E_J/E_C ratio to reduce the sensitivity to charge noise. To measure the loop current and discriminate the qubit state, an extra Josephson tunnel junction with $E_J^d \gg E_J$, called the detector junction, has been included in the superconducting loop of a split CPB. This large junction is shunted by a large capacitor, whose main effect is to reduce its plasma frequency. This new quantum circuit has been named *Quantronium*.

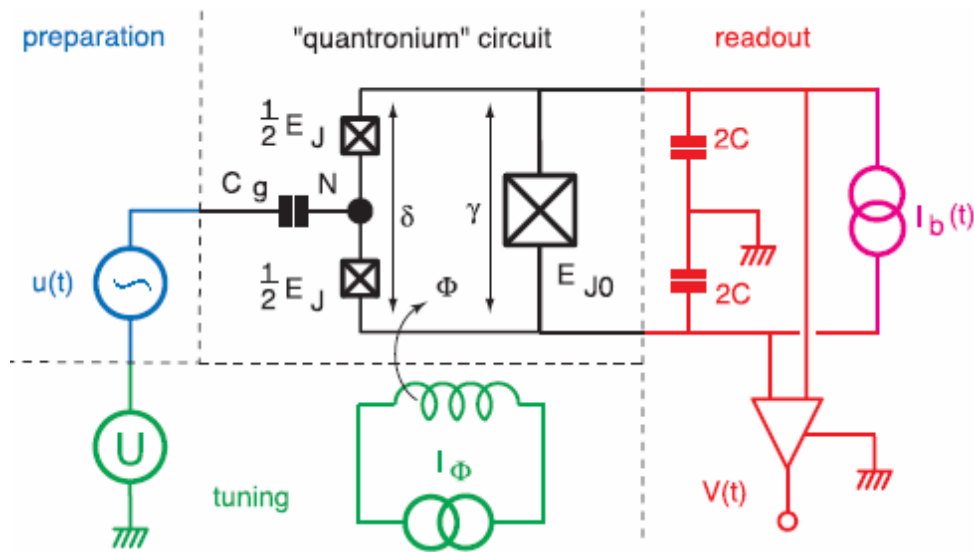


Figure 5.1. The “Quantronium” architecture. Idealized circuit diagram of the Quantronium. The control system for the two tunable parameters of the circuit is represented in green. The preparation circuit is in blue. The split Cooper Pair Box qubit with non-linear inductive Josephson tunnel junction for the phase read-out are in black, while the read-out circuit is in red. This figure has been reproduced from [VAC02].

When a read-out operation is required, a suitable amplitude bias current is applied to the circuit and a loop current develops, which adds or subtracts to the bias current in the detector junction. The detector junction can then be made to switch to a finite voltage with a large probability for one state of the qubit and a smaller one for the other. The outcome of each individual measurement is finite or zero voltage with a probability that represents the weight of that qubit basis state in the measured quantum superposition.

Of course, the current meter is weakly coupled to the CPB in order to minimize the back-action. Because of the weak coupling, during the measurement the read-out device projects the CPB state on its loop current eigenstates measuring the mean loop current of the two qubit states. In fact the signal measured by a weakly coupled current meter is proportional to:

$$\Delta I_{01}(N_g, \Phi_l) = \left[\langle 1 | \hat{I} | 1 \rangle - \langle 0 | \hat{I} | 0 \rangle \right]_{N_g, \Phi_l}$$

To evaluate this quantity, we need to calculate the current in the loop of the CPB, \hat{I} , which depends on the number of Cooper pairs having tunneled through the junctions, \hat{K} . Since this operator is conjugated to $\hat{\delta}$, we use the rules that link the conjugated operators describing a system and its Hamiltonian:

$$\hat{I} = -2e \frac{d\hat{K}}{dt} = -\frac{2e}{i\hbar} [\hat{K}, \hat{H}_{CPB}] = \frac{2e}{\hbar} \frac{\partial \hat{H}_{CPB}}{\partial \hat{\delta}}$$

We now recast ΔI_{01} as:

$$\Delta I_{01}(N_g, \delta) = \left[2e \frac{\partial \omega_{01}}{\partial \delta} \right]_{N_g, \delta}$$

Similarly to what happened in the charge strategy, it is clearly more favorable to manipulate the qubit state at $\delta=0$, where, since ΔI_{01} is zero, current fluctuations have no effect on the transition angular frequency at the first order. However, to measure a current difference between the two qubit states, the flux bias has to be moved away from the “sweet” spot just before the current meter performs any measurement. In addition to the back-action from the current meter, this exposes the qubit to noise in the flux, which may induce decoherence in the CPB, through a coupling Hamiltonian between the CPB and the flux fluctuations, $\Delta \hat{\delta}$:

$$\hat{H}_c = \frac{\partial \hat{H}_{CPB}}{\partial \delta} \Delta \hat{\delta}$$

Spectroscopy has been successfully performed on a Quantonium circuit both as a function of δ at $N_g=1/2$, and as a function of N_g at $\delta=0$, applying a weak continuous microwave irradiation at the gate suppressed just before the read-out pulse. At the double

“sweet” spot, quality factor of 2×10^4 has been observed for the resonance linewidth at a center transition frequency $\nu_{01} = 16.5$ GHz [VAC02]. The peak height decay for different delays between the end of the irradiation and the read-out gave a measurement of the depolarization time $T_I = 1.8$ μ s, which implies $Q_I = 1.8 \times 10^5$. Coherent manipulation of the qubit state has been performed by applying microwave pulses at the gate electrode with frequency ν_{RF} close to the transition frequency, ν_{01} , and with variable time duration. Rabi oscillations [R37] of the switching probability were observed for different pulse durations, whose frequency depended linearly on the pulse amplitude, as expected.

To measure the decoherence time of the qubit state Ramsey experiments [Ra50] have been performed. The qubit has been prepared in the ground state and then driven in a linear superposition of both states with equal weight by a single microwave $\pi/2$ pulse. The qubit has been let free of evolve for different time intervals in the different realization of the experiment. Then a new $\pi/2$ pulse has been applied driving the qubit either in the ground or in the excited state depending only on the phase accumulated during the free evolution.

Ramsey oscillations of the switching probability are observed at the detuning frequency $\nu_{RF} - \nu_{01}$, and their decay allows to measure $T_2 = 0.5$ μ s, which implies $Q_2 = 5.2 \times 10^4$, which is still one of the best results obtained until now.

There are two drawbacks for this strategy. Although a theoretical fidelity of 95% could be attained, which would allow “single-shot” measurement, only a maximum of about 50% has been observed for reason that are still under investigation. Quasiparticles are generated in the split CPB loop every time the read-out procedure produces a switch to finite voltage of the detector junction, requiring dead time before resuming qubit operation.

5.4. Dispersive read-out of a Cooper Pair Box: the non-linear inductive read-out in the RF-Quantronium architecture

All the read-out circuits described until now include an on-chip amplification scheme producing high level signals, which can be read directly by high-temperature low-noise electronics but which also lead to non-equilibrium quasiparticles being

produced in the near vicinity of the qubit junctions. In general, large energy dissipation on the chip may lead to an increase in the noise. To remove non-equilibrium quasiparticles from the qubit circuit we introduced a new strategy based on a purely dispersive measurement of the qubit susceptibility (capacitive or inductive).

In this dispersive strategy, the measurements are realized sending a microwave probe signal to the qubit. The signal is coupled to a qubit variable whose average value is identical in the qubit states. Rather than measuring this variable we measure the susceptibility. In fact, the susceptibility, which is the derivative of the qubit variable with respect to the probe, differs maximally from one qubit state to the other at the “sweet spot”. Thus, for instance, in the capacitive susceptibility measurement, the qubit variable is the island charge in the charge qubit at the degeneracy point. The resulting state-dependent phase shift of the transmitted or reflected photon signal is thus amplified by a low-temperature amplifier and finally discriminated at high temperature against an adequately chosen threshold. In addition to being very thrifty in terms of energy being dissipated on chip, these new schemes also provide a further natural decoupling action: when the probe signal is OFF, the back-action of the amplifier is also completely shut off. Finally, the interrogation of the qubit in a frequency band excluding zero and relatively narrow compared to the center frequency reduces the noise to a negligible level. In addition, the presence of read-out filters, like cavities, suppresses noise at the input and output ports.

One way in which we have realized this dispersive read-out strategy is to couple inductively our CPB qubit to a large Josephson tunnel junction shunted by a capacitor, which, when properly driven, is a nonlinear electrodynamic resonator with two metastable oscillation states. This nonlinear resonator can be seen as a new kind of amplifier very sensitive to the qubit state: the Josephson Bifurcation Amplifier (JBA), which will be presented in more details in section 5.6. The CPB and the JBA are fabricated on the same single chip using a mix of large and small scale electron beam writing techniques that we describe in Chapter 8. This architecture can be called “RF-Quantrium” since it represents the natural extension of the loop current strategy we presented in section 5.3.

The high degree of symmetry of this circuit, which resembles that of a Wheatstone bridge, can achieve a large noise decoupling from the environment, when biased at special operating points.

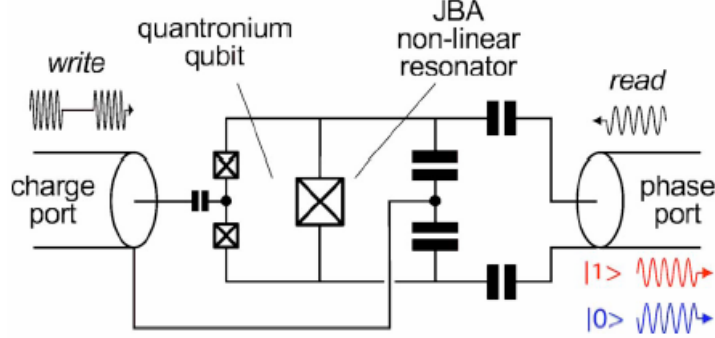


Figure 5.2. Dispersive read-out in the RF-Quantronium architecture. Idealized electrical diagram of a Josephson Bifurcation Amplifier reading-out a split CPB qubit.

We control the CPB qubit by voltage biasing it through the gate capacitance and by flux biasing with an externally applied magnetic field. We can still make use of the NMR-like pulse technique to prepare and manipulate the qubit states through a capacitive (charge) port, while reading-out through an inductive (phase) port.

Close to the optimal bias point where this combined system is, to first order, insensitive to fluctuations in the two bias parameters: the charge of the box island and the phase of the large junction, the Hamiltonian of the RF-Quantronium is given by [SVM06]:

$$\hat{H}_{RF-Q} = E_c \left(\hat{N} - \frac{1}{2} + \frac{C_g U(t)}{2e} \right)^2 - E_J \cos \frac{\hat{\delta}}{2} \cos \hat{\theta} + E_C^d \hat{p}^2 - E_J^d \cos \hat{\gamma} - E_J^d \chi(t) \hat{\gamma}$$

where $U(t) = U_{rf}(t) \cos \omega_{01} t$ and $\chi(t) = I_{rf}(t) / I_0 \cos \omega_d t$ are the control parameters respectively at the charge and phase port and E_C^d and E_J^d are respectively the charging energy and the Josephson energy of the large detector junction. $\hat{\gamma}$ is the gauge invariant phase difference operator for the detector junction and its relation to $\hat{\delta}$ constitutes the coupling between the two parts of the system:

$$\hat{\gamma} = \hat{\delta} + \frac{2\pi \Phi_l}{\Phi_0}$$

The restriction of this Hamiltonian to the two lowest states of the CPB, which represent the qubit states, leads to an effective Hamiltonian:

$$\hat{H}_{RF-Q}^* = \frac{C_g U(t)}{2e} E_c \hat{\sigma}_x - \frac{E_J}{2} \hat{\sigma}_z + \hbar \omega_p (1 + \lambda_{RF-Q} \hat{\sigma}_z) a^\dagger a - \mu \left(1 + \frac{\lambda_{RF-Q}}{4} \hat{\sigma}_z \right) (a + a^\dagger)^4 - f_\chi (a + a^\dagger) \chi(t)$$

where:

$$\lambda_{RF-Q} = \frac{E_J}{4E_C^d} \quad \mu = \frac{E_C^d}{48} \quad f_\chi = E_J \left(\frac{E_C^d}{2E_J^d} \right)^{1/4}$$

The photon creation and annihilation operators a^\dagger , a represent the decomposition of $\hat{\delta}$ into operators of a plasma mode of the large detector junction, whose bare angular frequency is ω_p , according to the relation:

$$\hat{\delta} = \frac{f_\chi}{E_J^d} (a + a^\dagger)$$

The first and last terms can be interpreted respectively as the excitation of the qubit by the charge port drive voltage and that of the resonator by the phase port drive current. The second term is the usual Larmor term $\omega_{01} = E_J/\hbar$ where E_J has been properly renormalized to include the equivalent of the Lamb shift. The third term describes the dominant coupling between qubit and resonator:

$$\hat{H}_{RF-Q}^{\text{int}} = \hbar \omega_p \lambda_{RF-Q} \hat{\sigma}_z a^\dagger a$$

The effect of this interaction term is that the resonator frequency is dispersively shifted by a term $\pm \omega_p \lambda_{RF-Q}$ conditioned by the qubit state being such that $\hat{\sigma}_z = \pm 1$.

The fourth term describes a reduction in the resonator frequency when its photon population increases. It is a peculiarity of the RF-Quantronium and can be neglected if the resonator is populated by a small number of photons. When the current drive is increased while its frequency is sufficiently below ω_p the system becomes metastable with two possible dynamical states and this gives rise to bistability and amplification, as we describe in the section 5.6.

Since the probe Hamiltonian operator commutes with the total Hamiltonian if the photon number in the resonator is small and if $U(t)=0$ (which means if you are not writing at the same time), it is a constant of motion and then repeated observations will yield the same

results. This type of dispersive read-out is often called a quantum non-demolition (QND) measurement [BK92].

The results obtained in the last three years by our group using this dispersive read-out approach in the RF-Quantronium architecture are presented in detail in the next Chapter.

5.5. Dispersive read-out of a Cooper Pair Box: the non-linear capacitive read-out in the Circuit QED architecture

Another way in which we have realized the dispersive read-out strategy is to couple capacitively our CPB qubit to a one dimensional (1D) transmission line resonator consisting of a full-wave section of a superconducting coplanar waveguide, see Fig. 5.3.

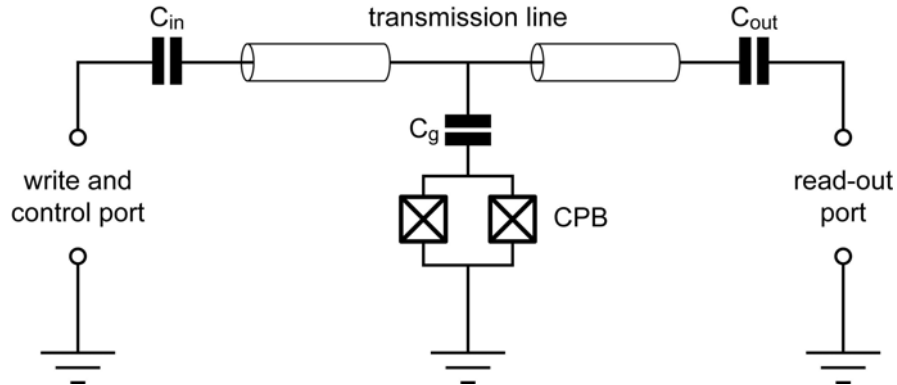


Figure 5.3. The Circuit Quantum Electrodynamics architecture. A Cooper Pair Box qubit capacitively coupled to a one dimensional transmission line resonator implements another dispersive read-out strategy.

As it was in the RF-Quantronium, the CPB and the resonator are fabricated on the same single chip. This time the fabrication requires a mix of photolithographic and electron beam writing techniques that we will describe in Chapter 8. This architecture is now known as circuit quantum electrodynamics (QED) [BHW04]. It has indeed been presented as the electrical circuit version of the cavity QED architecture [RBH01, MD02] in which the basic properties of the interaction of an atom with light are studied. The role of the atom is played here by our artificial atom, the CPB, while that of the cavity is played here by the high intrinsic Q distributed element resonator. The latter is accessed by the microwave measurement apparatus by two coupling capacitors. We control the CPB qubit by voltage biasing it through the gate capacitance and by flux biasing with an

externally applied magnetic field. The Hamiltonian of this combined system close to the optimal bias point, where the system is, to first order, insensitive to fluctuations in the bias parameters, is given by:

$$\hat{H}_{cQED} = E_c \left(\hat{N} - \frac{1}{2} + \frac{C_g U(t)}{2e} \right)^2 - E_J \cos \frac{\delta}{2} \cos \hat{\theta} + \hbar \omega_r \left(a^\dagger a + \frac{1}{2} \right) + \hbar g \hat{N} (a + a^\dagger) + f_U U'(t) (a + a^\dagger)$$

where $U(t) = U_{rf}(t) \cos \omega_{01} t$ and $U'(t) = U'_{rf}(t) \cos \omega_r t$ are the control parameters at the charge port, ω_r is the 1D transmission line resonator frequency, a^\dagger , a are the usual photon creation and annihilation operators and f_U is a voltage-resonator coupling constant.

The restriction of this Hamiltonian to the two lowest states, which represent the qubit states, leads to an effective Hamiltonian [BHW04]:

$$\hat{H}_{cQED}^* = \frac{C_g U(t)}{2e} E_c \hat{\sigma}_x - \frac{E_J}{2} \hat{\sigma}_z + \hbar \omega_r \left(a^\dagger a + \frac{1}{2} \right) + \hbar g (a^\dagger \sigma^- + a \sigma^+) + f_U U'(t) (a + a^\dagger)$$

where σ^+ , σ^- are the spin creation and annihilation operators, and g is a coupling constant given by:

$$g = \frac{eC_g}{\hbar C_\Sigma} \sqrt{\frac{\hbar \omega_r}{C_{TL}}}$$

with C_{TL} the product of the capacitance per unit length and the length of the transmission line resonator. The first and last terms can be interpreted as the excitation of the qubit by the charge port drive voltages. The three central terms are the Jaynes-Cummings Hamiltonian common in atomic physics cavity QED. For large detuning $\Delta = \omega_{01} - \omega_r \gg g$, diagonalization of these three terms leads to:

$$\hat{H}_{JC}^* = \frac{\hbar \omega_{01}}{2} \left(1 + \lambda_{cQED} \frac{\omega_r}{\omega_{01}} \right) \hat{\sigma}_z + \hbar \omega_r \left(1 + \lambda_{cQED} \hat{\sigma}_z \right) a^\dagger a$$

where

$$\lambda_{cQED} = \frac{g^2}{\Delta \omega_r}$$

The Larmor term is renormalized by the so-called Lamb shift that shifts the CPB transition angular frequency by $\omega_r \lambda_{cQED}$. In the second term, there is another contribution that shifts even more the CPB transition angular frequency and that is caused, as well as the previous one, by the resonator backaction. This contribution is called the a.c. Stark effect and induces a shift in ω_{01} of $2n\omega_r \lambda_{cQED}$, where n is the number of photons in the resonator.

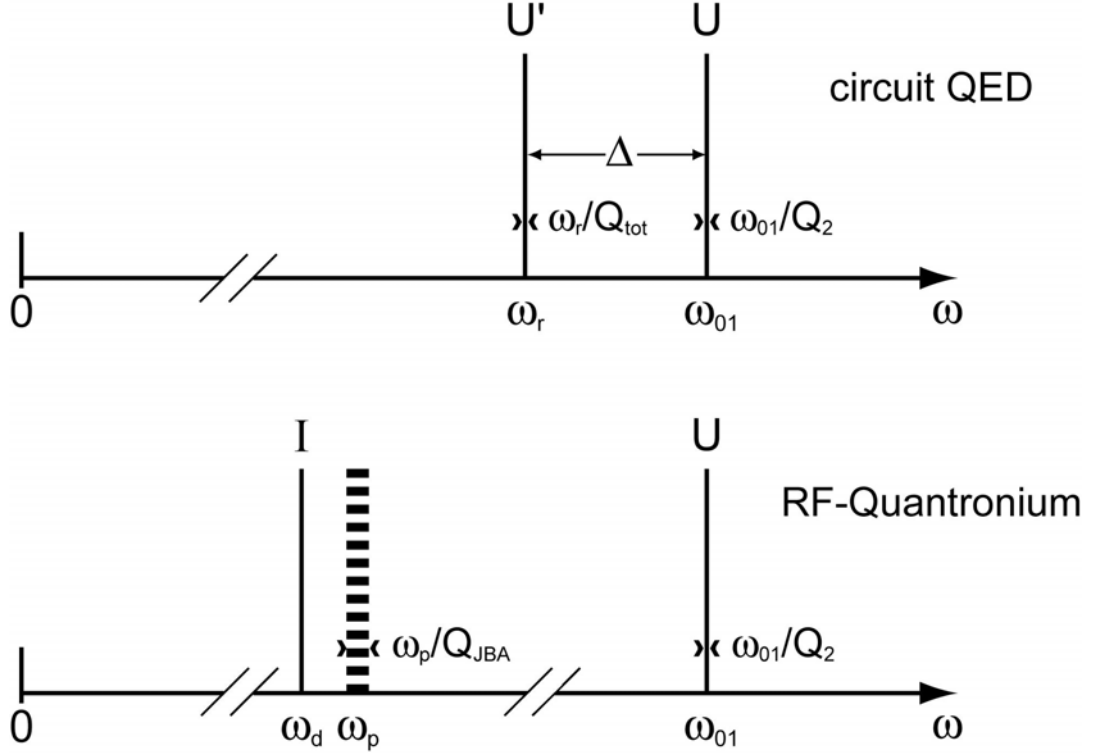


Figure 5.4. Dispersive read-out. Comparative schematics of the irradiation protocol in the circuit QED architecture (top) and in the RF-Quantronium (bottom).

As we did in the RF-Quantronium case, we can write explicitly the coupling between qubit and resonator:

$$\hat{H}_{cQED}^{int} = \hbar \omega_r \lambda_{cQED} \hat{\sigma}_z a^\dagger a$$

that generates a dispersive shift of the resonator frequency by an amount $\pm \omega_r \lambda_{cQED}$ conditioned by the qubit state being such that $\hat{\sigma}_z = \pm 1$. Since this probe Hamiltonian operator is a constant of motion also this type of dispersive read-out is a QND measurement.

The results obtained in the last three years by our group using this dispersive read-out approach in the circuit QED architecture are presented in detail in Chapter 7.

There is a close relation between the two versions of the dispersive read-out we have presented, as shown in Fig. 5.4. The main resemblance is the similar form of the interaction Hamiltonian operator:

$$\hat{H}^{\text{int}} = \hbar\omega\lambda\hat{\sigma}_z a^\dagger a$$

The main differences are: i) the resonators, which are lumped elements in one versus distributed elements in the other version, and ii) the modes for writing and reading. In the RF-Quantronium, they are orthogonal electrical modes which also differ in frequency. In circuit QED, the two modes are only separated in frequency and use the same transmission line.

5.6. Non-linear amplification of quantum signals: the Josephson Bifurcation Amplifier

The central element of the Josephson Bifurcation Amplifier is a Josephson junction, shunted with a lithographic capacitor fabricated on the same chip with electron beam lithography technique, see Fig. 5.5.

The JJ critical current I_0 is modulated by an input signal at an effective input port, which in the case of the RF-Quantronium is the qubit as explained in section 5.4.

Coupling between the junction and the input signal can be achieved through different schemes. The junction is driven with a pure AC signal $i_{RF} \sin\omega t$ in the microwave frequency range fed via a transmission line through a circulator at the drive port. In the underdamped regime, for certain values of ω and i_{RF} , two possible oscillation states which differ in amplitude and phase coexist. The reflected component of the drive signal, measured through another transmission line connected to the circulator at the output port, is a convenient signature of the junction oscillation state.

At the bifurcation point where switching between oscillation states occurs, the system becomes infinitely sensitive, in the absence of thermal and quantum fluctuations, to variations in I_0 .

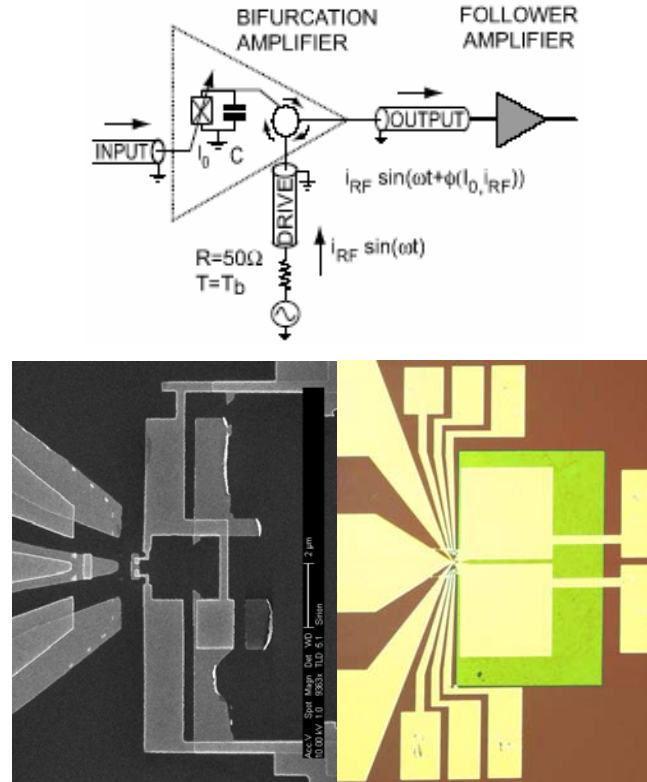


Figure 5.5. The Josephson Bifurcation Amplifier. Top: Idealized electrical diagram of a Josephson Bifurcation Amplifier. Bottom left: SEM image of a Quantonium circuit realized at Yale using the double angle deposition technique described in the Chapter 8. This image has been realized with a 10 keV electron beam. Bottom right: optical microscope picture of the same circuit to evidence the two capacitors used to tune the plasma frequency of the detector Josephson tunnel junction in the JBA amplifier.

At finite temperature, the energy stored in the oscillation can always be made larger than thermal fluctuations by increasing the scale of I_0 , thus preserving sensitivity. Small variations in I_0 are transformed into readily discernible changes in the escape rate from one oscillation state to the other. Back-action is minimized in this arrangement since the only fluctuations felt at the input port arise from the fluctuations of the 50Ω drive port whose dissipative elements are physically separated from the junction via a transmission line of arbitrary length and can therefore be thermalized efficiently to base temperature. Additionally, the frequency band over which the back-action contributes is narrow, and well controlled.

Part of the published works reprinted in the next Chapter focus on presenting the characteristic and properties as understood at the present stage of the development of this new amplifier.

6. Reprints of experimental and theoretical results on the Quantronium architecture with the JBA

This Chapter contains reprints of published works. Be aware that in these articles the definition of $E_C = e^2/2C_\Sigma$ is different from that used in the body of this work.

[SVM06] presents the results obtained using the RF-Quantronium architecture, introduced in section 5.5.

We have used the quantronium phase degree of freedom to perform a nonlinear, dispersive measurement of its inductive response by measuring the phase of a microwave probe beam reflected in the Josephson bifurcation amplifier. This dispersive read-out projects the state of the qubit in a few nanoseconds, and its latching property allows us to record the resulting information in a few hundred nanoseconds.

We have measured, using this technique, the probability of switching between the two states of the JBA, P_{sw} , versus its driving current, I_{rf} , for different qubit states. In different samples, a discrimination power in the range 48-61% was observed, defined as:

$$\eta = \max_{I_{rf}^{\max}} [P_{sw}(|1\rangle) - P_{sw}(|0\rangle)]$$

We have observed Rabi oscillations of P_{sw} with about 45% contrast. Decay experiments on the qubit excited state were performed on different samples. The best result was obtained with a qubit, whose $\nu_{01}=9.5$ GHz, where $T_1=5$ μ s was measured, which implies $Q_1=3.0 \times 10^5$. Ramsey fringe experiments on the same sample were performed measuring $T_2=320$ ns limited by dephasing and improved up to $T_2=500$ ns with echo techniques, implying Q_2 in the range $1.9-3.0 \times 10^4$ and on a second sample, whose $\nu_{01}=19$ GHz, where $T_2=320$ ns was measured, implying $Q_2=3.8 \times 10^4$.

[SVP04] presents the idea and the realization of the Josephson Bifurcation Amplifier introduced in section 5.6. The bifurcation as well as the latching of the amplifier states were observed and understood based on the theory on non-linear oscillators developed in [DK80].

In [SVP05b], we performed a phase-sensitive microwave reflection experiment which directly probed the dynamics of the Josephson plasma resonance in both the linear and the nonlinear regime of the JBA. When the junction was driven below the plasma

frequency into the nonlinear regime, we observed the transition between two different dynamical states of the amplifier predicted for nonlinear systems. This transition appeared as an abrupt change in the reflected signal phase at a critical excitation power. The reflected phase was measured versus power and frequency of the incoming signal and its behavior was found in very good agreement with the expected one from [DS90]. In [SVP05b], we measured P_{sw} versus junction critical current, drive current and temperature finding good agreement with the predictions. We also measured the drive current dependence of the escape rate in the range 280-500 mK which allowed us to estimate the effective potential barrier height.

Dispersive measurements of superconducting qubit coherence with a fast latching readout

I. Siddiqi, R. Vijay, M. Metcalfe, E. Boaknin, L. Frunzio, R. J. Schoelkopf, and M. H. Devoret
Department of Applied Physics and Department of Physics, Yale University, New Haven, Connecticut 06520-8284, USA
 (Received 7 September 2005; published 23 February 2006)

The “quantronium” is a superconducting qubit consisting of a split Cooper pair box in which a large tunnel junction is inserted. This circuit has a special bias point where the Larmor frequency is, to first order, insensitive to fluctuations in the bias parameters—the charge of the box island and the phase of the large junction. At this optimal working point, the state of the qubit can be determined by dispersive measurements that probe the second derivative of the state energy with respect to these bias parameters. We use the quantronium phase degree of freedom to perform a nonlinear, dispersive measurement of its inductive response using bifurcation amplification. This dispersive readout projects the state of the qubit in a few nanoseconds, and its latching property allows us to record the resulting information in a few hundred nanoseconds. We have measured, using this technique, Rabi oscillations and Ramsey fringes with an improved signal-to-noise ratio and contrast. The speed of this readout scheme also opens the door for a class of experiments that would characterize the relaxation processes associated with the measurement protocol.

DOI: [10.1103/PhysRevB.73.054510](https://doi.org/10.1103/PhysRevB.73.054510)

PACS number(s): 85.25.Cp

I. INTRODUCTION

Superconducting tunnel junction circuits were first proposed for quantum information processing several years ago, and at present, are the most advanced solid state qubits with the longest measured coherence times.^{1–7} Yet the physical origin of the noise sources limiting coherence are still debated, even though the theoretical formalism for treating the effects of noise in general is well developed.^{8–10} It has been conjectured that impurities or defects found on chip could act as such noise sources.¹¹ These parasitic elements may exist in the junction tunnel barriers, the metallic electrodes, the circuit substrate, or in some combination thereof. In addition, the shadow-mask evaporation technique used to fabricate many superconducting qubits typically generates extra electrodynamic resonators in close proximity to the qubit junctions.¹² These resonators can have a characteristic frequency comparable to the qubit Larmor frequency, and are thus suspected to decohere the qubit. The precise manner in which a qubit interacts with uncontrolled degrees of freedom in its environment depends on the topology of the tunnel junction circuit and how information is written to and read from the qubit. Circuits which have a high degree of symmetry can be significantly decoupled from a noisy environment^{1,13} when biased at special operating points. The choice of readout scheme is also highly significant. Dispersive measurements of the qubit state^{14–17} probe the reactive part of the response of the circuit, and are thus attractive since they minimally excite the spurious degrees of freedom described above.

We report coherence measurements of a superconducting qubit with a nonlinear dispersive readout. Our approach involves coupling the “quantronium” qubit¹ to the Josephson bifurcation amplifier (JBA).¹⁸ The JBA is based on a nonlinear electrodynamic resonator with two metastable oscillation states.¹⁹ In order to perform a readout, the resonator is rf energized to a level where its oscillation state now acts as a sensitive pointer of the qubit state. This technique does not generate any dissipation on chip since the resonator is only

damped by circuitry outside the chip, i.e., a 50 Ω transmission line with a matched circulator and amplifier, and enables a high-fidelity qubit readout with a megahertz repetition rate. We have measured Rabi oscillations and Ramsey fringes with sufficient speed that real-time filtering to correct for drifts in the charge and flux bias becomes possible. Also, several successive readouts may be performed within the energy relaxation time of the qubit (T_1). This gives valuable information on the readout-induced interaction between the qubit and its environment, and accounts for the observed contrast.

II. THE HAMILTONIAN OF THE QUANTRONIUM QUBIT WITH JBA READOUT

The principle of our experiment is schematically depicted in Fig. 1 and is based, as discussed above, on the quantronium qubit, a three-junction circuit which is analogous to a

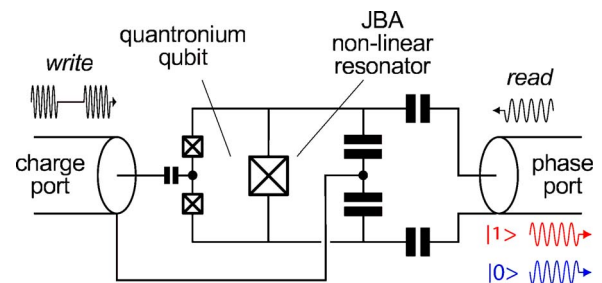


FIG. 1. (Color online) Schematic of the measurement setup. The quantronium qubit is a split Cooper pair box with two small Josephson junctions in which a large junction is inserted for readout. This last junction is shunted by two capacitors in series and forms the nonlinear resonator of the JBA readout. The qubit state is manipulated by sending pulses to the charge port, while readout operation is performed by sending a pulse to the phase port and analyzing the phase of the reflected signal, which carries information on the qubit state.

one-dimensional atom. The set of three junctions consists of two small junctions, which we assume to be identical and which have a Josephson energy comparable to the charging energy of the island between them, and a large junction, whose Josephson energy is approximately 100 times larger than that of each small junction. The gauge-invariant phase difference $\hat{\theta}$ of the island with respect to the midpoint of the capacitance shunting the large junction is analogous to the position of the electron relative to the nucleus of the atom, while the gauge-invariant phase difference $\hat{\delta}$ across the large junction is the absolute position of the nucleus. Neglecting the dissipation induced in the transmission lines, the total Hamiltonian of the split Cooper pair box with a JBA resonator is $\hat{H}(t) = \hat{H}_{\text{box}}(t) + \hat{H}_{\text{res}}(t)$ with

$$\hat{H}_{\text{box}}(t) = 4E_C \left(\hat{N} - \frac{1}{2} + \frac{C_g U(t)}{2e} \right)^2 - \left(E_J \cos \frac{\hat{\delta}}{2} \right) \cos \hat{\theta},$$

$$\hat{H}_{\text{res}}(t) = \frac{\hat{Q}^2}{2C} - E_J^R \cos \hat{\delta} - \varphi_0 I(t) \hat{\delta}.$$

Here, \hat{N} and $\hat{Q}/2e$ are the momenta conjugate to the generalized positions $\hat{\theta}$ and $\hat{\delta}$, respectively. The constants E_C , E_J , E_J^R , C , and C_g are the single-electron charging energy of the island between the small junctions, the sum of the Josephson energy of the two small junctions, the large-junction Josephson energy, the total capacitance shunting the large junction, and the gate capacitance, respectively. Here $\varphi_0 = \hbar/2e$ is the reduced flux quantum. The control parameters $U(t) = U_{rf}(t) \cos \Omega t$ and $I(t) = I_{rf}(t) \cos \omega t$ are analogous to electromagnetic probe fields in an atomic system and induce a charge excitation of the write port and a phase excitation of the read port, respectively. This Hamiltonian has been written supposing that the offset gate charge and loop flux have been compensated to operate at the optimal bias point where the charge $\partial \hat{H} / \partial U$ and the flux $\partial \hat{H} / \partial I$ have zero mean value in both the ground $|0\rangle$ and first excited $|1\rangle$ states of \hat{H}_{box} . Under these conditions, the qubit is minimally sensitive to charge and flux noise.¹

If we keep these two lowest states in the Hilbert space of \hat{H}_{box} ,¹⁰ and express \hat{H}_{res} in terms of creation and annihilation operators, we obtain an effective Hamiltonian

$$\hat{H}_{\text{eff}} = \frac{2C_g U(t)}{e} E_C \sigma_x - \frac{E_J}{2} \sigma_z + \hbar \omega_p (1 + \lambda \sigma_z) a^\dagger a$$

$$- \mu \left(1 + \frac{\lambda}{4} \sigma_z \right) (a + a^\dagger)^4 - f (a + a^\dagger) I(t), \quad (1)$$

where

$$\omega_p = \sqrt{\frac{E_J^R}{\varphi_0^2 C}}, \quad \lambda = \frac{E_J}{4E_J^R},$$

$$\mu = \frac{E_C^R}{12} = \frac{1}{12} \frac{(e)^2}{2C}, \quad f = \varphi_0 \left(\frac{2E_C^R}{E_J^R} \right)^{1/4}.$$

The photon annihilation operator a is related to $\hat{\delta}$ by

$$\hat{\delta} = \frac{a + a^\dagger}{(E_J^R/2E_C)^{1/4}}$$

which represents the decomposition of the gauge-invariant phase difference into annihilation and creation operators of the large junction “plasma” mode whose bare frequency is ω_p . The operators σ_x and σ_z are the Pauli spin operators and E_C^R is the single-electron charging energy of the readout junction. In this effective Hamiltonian, the expansion of $\cos \hat{\delta}$ is carried out only to the first anharmonic term, which describes the nonlinear resonator dynamics with sufficient accuracy for a bifurcation readout.

Let us describe the role of each term in (1). The first term describes the influence on the qubit of the charge port drive which is used to manipulate its state. The second term is the Larmor term $\omega_{01} = E_J/\hbar$. We have supposed here that the ratio E_J/E_C is sufficiently small that corrections to the Larmor frequency involving E_C are small. To model the behavior of qubit samples with an appreciable E_J/E_C ratio, we would keep higher-order terms, yielding renormalized values of the coefficients in (1). The third term describes the dominant coupling between the qubit and the resonator. Note that this term commutes with the Hamiltonian of the qubit when $U = 0$, offering the possibility of quantum nondemolition measurements. The fourth term describes a decrease in the frequency of the resonator when its photon population increases.²⁰ Finally, the fifth term describes the excitation of the resonator by the drive current applied through the phase port. When the drive current is increased while its frequency is sufficiently below ω_p the system becomes metastable with two possible dynamical states with different oscillation amplitudes, i.e., two possible photon populations.¹⁸ We exploit this bistability for our readout, which we describe in the next section.

III. QUBIT READOUT

It is clear from the Hamiltonian (1) above that the dynamics of the nonlinear resonator depend on the value $\sigma_z = \pm 1$ corresponding to the state of the qubit. In particular, the small oscillation “plasma” frequency $\omega_p^{\text{eff}} = \omega_p (1 \pm \lambda)$ varies with the qubit state. We probe the nonlinear resonator by sending down the phase port transmission line a microwave pulse with carrier frequency $\omega = \omega_p - \Delta\omega$, such that the detuning $\Delta\omega > (\sqrt{3}/2Q)\omega_p$ where Q is the quality factor of the plasma resonance.¹⁹ In our circuit, the damping of the plasma resonance arises from the characteristic transmission line impedance $Z_c = 50 \Omega$ and thus $Q = Z_c C \omega_p \approx 10-20$. For this value of detuning, when ramping up the drive current I_{rf} the resonator switches from one dynamical state to another when

$$I_{rf} > I_B(\omega, \omega_p^{\text{eff}}),$$

where I_B is the bifurcation current with expressions given in Ref. 21. Therefore, by choosing the maximum pulse amplitude

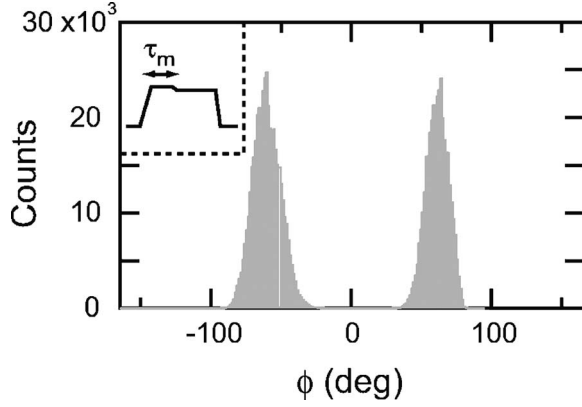


FIG. 2. Typical histogram of the phase of the reflected signal in the JBA readout when the maximum rf drive current is chosen so that the resonator switches approximately half of the time. The switching probability P_{switch} is defined as the fraction of the histogram lying above $\phi=0$. The inset shows schematically the envelope of the readout pulse sent to the phase port. The qubit influences the switching probability during the time interval τ_m which here was 40 ns.

$$I_B[\omega, \omega_p(1-\lambda)] < I_{rf}^{max} < I_B[\omega, \omega_p(1+\lambda)]$$

we can determine, by measuring if the resonator has switched or not, whether the qubit was in state $|0\rangle$ or $|1\rangle$.

The dynamical states of the resonator differ in both the amplitude and phase of the forced oscillations at frequency ω . In this work, we have chosen to use a reflectometry setup in which all the information about the resonator state is carried by the reflected drive signal phase ϕ . This last property occurs because the probed circuit is not intrinsically dissipative (in absence of quasiparticles, which is very well realized in our measurements) and the power reflected from the chip is equal to the incident power in steady state. A further advantage of our nonlinear resonator is that the switching is strongly hysteretic. Once a switching event has occurred we can decrease the drive current I_{rf} to a value which, while much smaller than $I_B[\omega, \omega_p(1-\lambda)]$, is still higher than the reverse bifurcation “retrapping” current I_B^- . This latching property conserves the information about the qubit state acquired during a small time interval τ_m in the resonator and allows us to probe the reflected phase ϕ during a time typically longer than τ_m .

In Fig. 2, we present a typical histogram of the reflected drive signal phase ϕ corresponding to a drive current I_{rf} which causes the resonator to switch, on average, half of the time. The histogram has 800 000 counts acquired in 200 ms.

For qubit measurements shown later, histograms with only 10 000 are used. The shape of the readout pulse used is schematically shown in the inset of Fig. 2. The rise time of the pulse is set by the quality factor of the resonator and is typically 20–40 ns. The maximum current I_{rf}^{max} is applied for 40–120 ns and is optimized for maximizing readout fidelity. The latched section lasts 120 ns, during which the recorded reflected signal phase ϕ is bimodal, with values differing by 124° . The latching time is set by the system noise temperature and is the time required to resolve this phase shift with sufficient accuracy. We have chosen the phase reference so that the value $\phi = \phi_{low} = -62^\circ$ corresponds to the resonator in its initial state, while $\phi = \phi_{high} = 62^\circ$ corresponds to the resonator having switched. We define the switching probability $P_{switch}(I_{rf}^{max}, \Delta\omega, \langle \Psi | \sigma_Z | \Psi \rangle)$, where $|\Psi\rangle$ is the state of the qubit, as the weight of the histogram that lies above $\phi = (\phi_{low} + \phi_{high})/2 = 0$.

IV. COHERENCE RESULTS

We now present experimental results on two different qubit samples whose characteristic parameters are listed in Table I, along with a summary of our results. In the figures that follow, we only show data for sample A. All measurements were performed in a dilution refrigerator at a temperature of 10 mK. Shadow-mask-evaporated Al/AlOx/Al junctions were used for both the qubit and the JBA. Fabrication details can be found in Refs. 18 and 20.

We first characterized our readout by measuring P_{switch} as a function I_{rf}^{max} and $|\Psi\rangle$, as shown in Fig. 3. The blue circles correspond to the qubit in its ground state, obtained by letting the qubit relax spontaneously, while the red circles correspond to the qubit in its first excited state obtained by applying a π pulse, which will be discussed below. An important remark is that only a slight change in shape of $P_{switch}(I_{rf}^{max})$ between the two qubit states is observed, which indicates that the switching process itself does not contribute strongly to the relaxation of the qubit. In cases where the readout is suspected to induce significant relaxation, the switching probability curve for the qubit excited state displays a pronounced kink and can be obtained by a weighted average of the observed curve for the ground state and the prediction for the excited state.^{7,22} The discrimination power of the qubit readout is defined as

$$\eta = \max_{I_{rf}^{max}} [P_{switch}(\langle \sigma_Z \rangle_{\Psi} = 1) - P_{switch}(\langle \sigma_Z \rangle_{\Psi} = -1)]$$

and its observed (η_{expt}) and predicted (η_{calc}) values are given in Table I. Numerical simulations²³ of the full circuit have

TABLE I. Parameters for two measured qubit samples. The readout frequency was 1.55 and 1.70 GHz for samples A and B, respectively. The detuning was 6% of ω_p . The parameter η is the discrimination power of the readout.

Sample	$\omega_{01}/2\pi$ (GHz)	E_J/E_C	$T_{1,typical}$ (μ s)	T_2 (ns)	T_{echo} (ns)	η_{expt}	η_{calc}	η_{expt}/η_{calc}
A	9.513	2.7	4.0	320	400–500	0.48	0.70 ± 0.05	0.69
B	18.989	6.0	1.0	300	300	0.61	0.70 ± 0.05	0.87

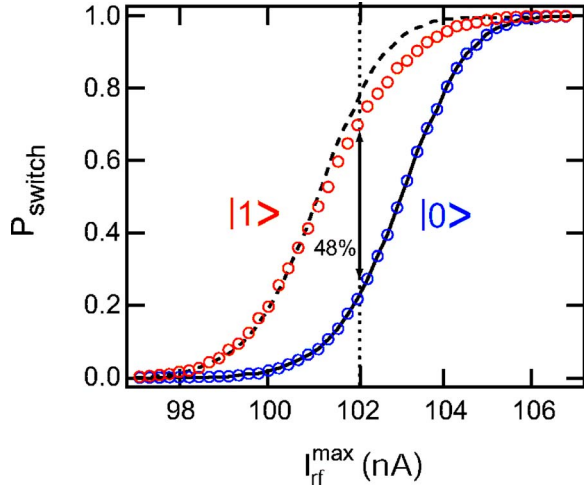


FIG. 3. (Color online) Switching probability as a function of maximum drive current and qubit state for sample A. The vertical dotted line represents the value of drive current at which maximal discrimination power is observed. The width in current of the curves is in reasonable agreement with numerical simulations (data not shown). The solid line connects the observed data points in the $|0\rangle$ state and the dashed line is a copy of the solid line horizontally shifted to overlap the $|1\rangle$ state data at low values of P_{switch} .

been used to compute the predicted values of η . Note that several competing factors enter this calculation, yielding similar values for samples A and B. The error bars reflect uncertainties in the values of stray reactances on chip and the precise resonator temperature.

The observed discrimination power is about 15–30 % smaller than expected, and we attribute this loss to spurious on-chip defects. In a set of experiments to be described in a later publication, we used two readout pulses in succession to determine that a 15–30 % loss of qubit population occurs even before the resonator is energized to its operating point. As photons are injected into the resonator, the effective qubit frequency is lowered due to a Stark shift via the phase port.²⁴ When the Stark-shifted frequency coincides with the frequency of an on-chip defect, a relaxation of the qubit occurs. Typically, the qubit frequency spans 200–300 MHz before the state of the qubit is registered by the readout, and 3–4 spurious resonances are encountered in this range.

For future measurements, we have developed a method to counter this effect. When applying a readout pulse via the phase port, we apply a compensating pulse via the charge port which Stark-shifts the qubit to higher frequencies. When balancing these pulses, we have successfully reduced the net frequency shift to below 20 MHz and have minimized population loss to defects before the resonator switches. To increase the expected discrimination power to unity, we must use samples with either a larger qubit E_J or a stronger phase coupling between the qubit and readout resonator. The latter can be accomplished by using a resonator with two Josephson junctions in series.

Having characterized our readout discrimination power, we performed a series of experiments to assess the coherence of our qubit, namely, the measurements of T_1 , T_2 , T_{echo} , and \tilde{T}_2 . These times characterize the decay of the excited-state

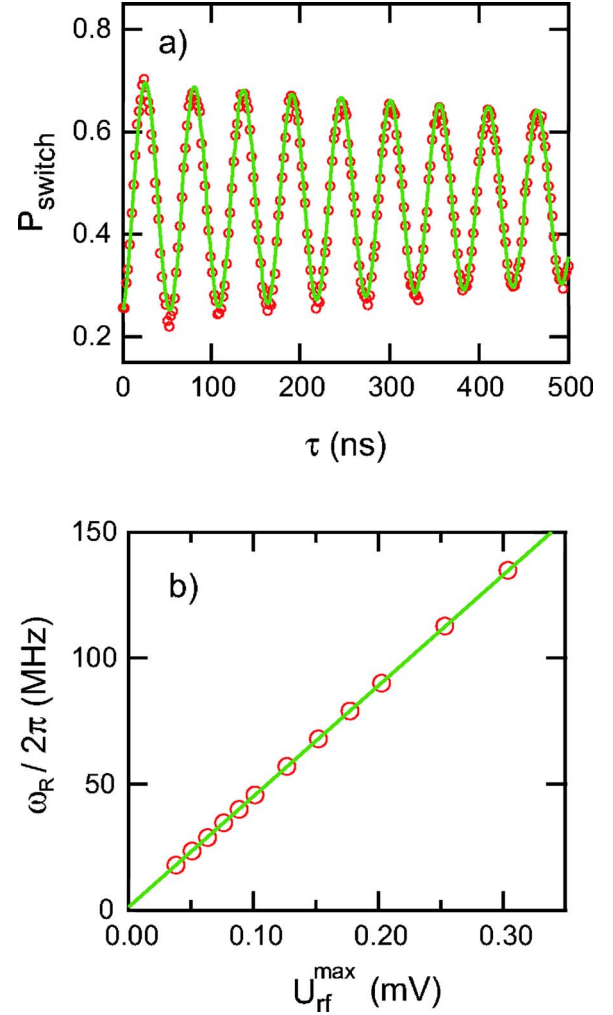


FIG. 4. (Color online) (a) Rabi oscillations of the switching probability of qubit sample A as a function of the duration τ of a square pulse applied on the gate with maximum amplitude $U_{rf}^{max} = 0.12$ mV. Solid (green) curve is an exponentially decaying sinusoidal fit with $\tilde{T}_2 = 1.6$ μ s. Total acquisition time is 3 min and the repetition rate is 16 μ s, set by T_1 (see below). (b) Rabi oscillation frequency measured in (a) as a function of U_{rf}^{max} . Solid (green) line is the expected linear dependence.

population after a π pulse, the decay of Ramsey fringes, the decay of the echo signal after a $(\pi/2, \pi, \pi/2)$ pulse sequence, and the decay of the Rabi oscillations, respectively.

We first applied to the charge port a pulse at the Larmor frequency ω_{01} of varying duration τ and amplitude U_{rf}^{max} , which performs a σ_x rotation of the qubit, followed by a readout pulse on the phase port. The resulting Rabi oscillations in the switching probability signal are plotted in Fig. 4(a) for varying τ and fixed U_{rf}^{max} . Near $\tau=0$ we observe the P_{switch} corresponding to the qubit being in the $|0\rangle$ state. As the pulse length increases, P_{switch} increases, goes through a maximum where the qubit is purely in the $|1\rangle$ state, defining at this point the length of a π pulse. The switching probability then decreases back to the $|0\rangle$ state value, indicating a full 2π rotation of the Bloch vector. This pattern repeats itself but with diminishing contrast. The decay time \tilde{T}_2 is in the range

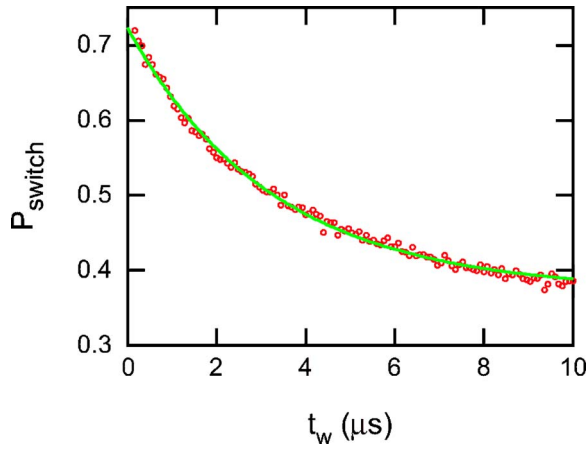


FIG. 5. (Color online) Decay of the excited-state switching probability after preparing the qubit in the excited-state by a π pulse, as a function of the waiting time t_w between the preparation pulse and the readout pulse. Data for sample A. Solid (green) curve is an exponential fit with a $3.2 \mu\text{s}$ decay constant.

$0.8\text{--}1.7 \mu\text{s}$ depending on the sample and precise biasing condition. The Rabi oscillation frequency ω_R is plotted as a function of U_{rf}^{max} in Fig. 4(b). A linear dependence of ω_R with U_{rf}^{max} is observed, in agreement with theory. The shortest π pulse we generated was 2 ns long, and was used in the echo experiments described below.

Having calibrated the π pulse, we then performed a qubit energy relaxation measurement by introducing a waiting time t_w between the π pulse and the readout pulse. The decay of P_{switch} with t_w , shown in Fig. 5, is well fitted by a single exponential, defining T_1 . For sample A, T_1 was in the range $2.5\text{--}5 \mu\text{s}$, and for sample B, T_1 was between 1.0 and $1.3 \mu\text{s}$. The values of T_1 obtained with our dispersive readout are comparable with the results of Vion *et al.*,¹ and are significantly shorter than the values expected from coupling to a well-thermalized 50Ω microwave environment shunting the qubit. The loss mechanisms giving rise to the observed energy relaxation are not understood at this time.

Following measurements of the qubit energy relaxation, we performed a Ramsey fringe experiment to determine the phase coherence of the qubit. In this experiment, two $\pi/2$ pulses were applied to the charge port of the qubit at a frequency $10\text{--}20$ MHz detuned from ω_{01} followed by a readout pulse on the phase port. A free evolution time Δt was introduced between the two $\pi/2$ pulses. In Fig. 6, P_{switch} is plotted as a function of Δt . In the Ramsey sequence, the first $\pi/2$ pulse tips the Bloch vector from the north pole to the equatorial plane. During the time Δt , the Bloch vector precesses around the equatorial plane and is then rotated again by the second $\pi/2$ pulse. For $\Delta t=0$, the two $\pi/2$ pulses back to back act as a single π pulse and the observed value of P_{switch} corresponds to the qubit being in the $|1\rangle$ state. As Δt increases, P_{switch} decreases until it reaches the value corresponding to the qubit being in the $|0\rangle$ state, corresponding to a free evolution time Δt in which the Bloch vector makes a π rotation in the equatorial plane. The switching probability then continues to increase for larger values of Δt until it reaches a maximum value, corresponding to a time Δt where

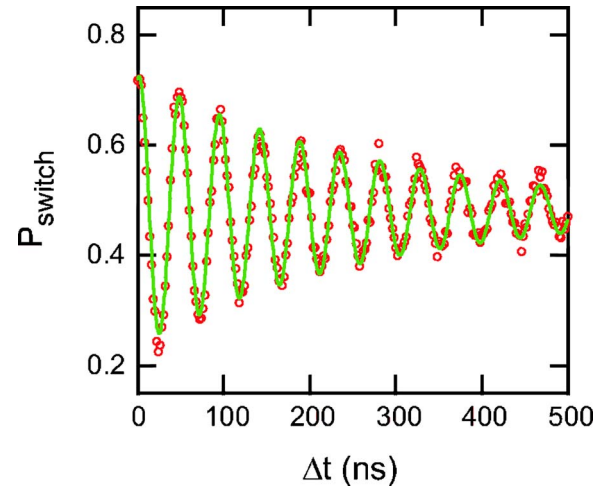


FIG. 6. (Color online) Ramsey fringes obtained with two $\pi/2$ pulses separated by the time interval Δt . The pulse frequency was detuned from the Larmor frequency by 20 MHz. The (green) curve is an exponentially decaying sinusoid fit. The decay time T_2 is 320 ns. Same acquisition conditions as in Fig. 4.

the Bloch vector makes a full 2π rotation in the equatorial plane. This oscillatory pattern then repeats but with decreasing contrast corresponding to the loss of phase coherence with time. The Ramsey fringes decay in a time T_2 which has a component due to energy relaxation and one due to pure dephasing: $1/T_2 = 1/(2T_1) + 1/T_\phi$, where T_ϕ represents pure dephasing. In our measurements, T_2 is dominated by pure dephasing. For sample A, $T_2 = 320$ ns, and for sample B, $T_2 = 300$ ns.

In order to correct dephasing of the qubit due to low-frequency noise,^{2,25} we performed an echo experiment in which we inserted a π pulse in the middle of the two $\pi/2$ pulses of the Ramsey sequence. A set of Ramsey fringes and its corresponding echo decay are shown in Fig. 7 for sample A. For this sample, the decay constant was increased to $400\text{--}500$ ns using the echo technique. For sample B, the echo technique did not increase the phase coherence time.

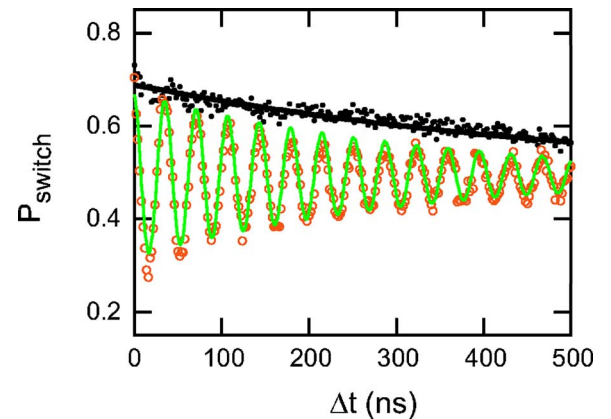


FIG. 7. (Color online) Result of an echo experiment where a π pulse was kept in the middle of the two $\pi/2$ pulses separated by interval Δt (black dots). The Ramsey fringe data, obtained without the π pulse, is shown with (red) circles. The thick black curve is an exponentially decaying fit.

We believe that for sample B, which has a large ratio of E_J/E_C and is protected from $1/f$ offset charge noise, the dominant source of dephasing is due to broadband noise emanating from residual photons in our readout resonator,²⁶ thus explaining the inefficacy of the echo sequence. It is possible that the $50\ \Omega$ environment shunting the qubit on the phase port side was not fully thermalized to the refrigerator temperature of 10 mK. For sample A, where an improvement was observed with the echo sequence, there are likely two contributing factors. First, the ratio E_J/E_C is much smaller and offset charge noise played a stronger role. The low-frequency component of this noise can be corrected using an echo sequence. Second, we added more cryogenic attenuation in the transmission lines directly coupling to the phase port to reduce the resonator temperature, thereby potentially reducing the number of excess photons in the readout resonator and their associated dephasing.

V. CONCLUSION

In conclusion, we have successfully implemented a nonlinear dispersive readout of the qantronium qubit using the

Josephson bifurcation amplifier. The readout speed and discrimination power show a significant improvement when compared with the dc switching readout used in the original qantronium measurements.¹ Perhaps even more important, in the present readout scheme, the total measurement time is much smaller than T_1 , and it is possible to carry out experiments with multiple readout pulses to determine the information flow during a qubit readout and to account for any losses in qubit population. This important aspect can be used to determine the degree to which the measurement is quantum nondemolishing, and we hope to describe it in later publications.

ACKNOWLEDGMENTS

The authors are grateful to Patrice Bertet, Daniel Esteve, Steve Girvin, Daniel Prober, and Denis Vion for helpful discussions. This work was supported by ARDA (ARO Grant No. DAAD19-02-1-0044), the Keck Foundation, and the NSF (Grant No. DMR-0325580).

-
- ¹D. Vion, A. Aassime, A. Cottet, P. Joyez, H. Pothier, C. Urbina, D. Esteve, and M. H. Devoret, *Science* **296**, 886 (2002); E. Collin, G. Ithier, A. Aassime, P. Joyez, D. Vion, and D. Esteve, *Phys. Rev. Lett.* **93**, 157005 (2004).
- ²I. Chiorescu, P. Bertet, K. Semba, Y. Nakamura, C. J. P. M. Harmans, and J. E. Mooij, *Nature (London)* **431**, 159 (2004); P. Bertet, I. Chiorescu, G. Burkard, K. Semba, C. J. P. M. Harmans, D. P. DiVincenzo, and J. E. Mooij, *Phys. Rev. Lett.* **95**, 257002 (2005).
- ³T. Kutsuzawa, H. Tanaka, S. Saito, H. Nakano, K. Semba, and H. Takayanagi, *Appl. Phys. Lett.* **87**, 073501 (2005).
- ⁴B. L. T. Plourde, T. L. Robertson, P. A. Reichardt, T. Hime, S. Linzen, C.-E. Wu, and John Clarke, *Phys. Rev. B* **72**, 060506 (2005).
- ⁵A. Wallraff, D. I. Schuster, A. Blais, L. Frunzio, J. Majer, M. H. Devoret, S. M. Girvin, and R. J. Schoelkopf, *Phys. Rev. Lett.* **95**, 060501 (2005).
- ⁶R. McDermott, R. W. Simmonds, Matthias Steffen, K. B. Cooper, K. Cicak, K. D. Osborn, Seongshik Oh, D. P. Pappas, and John M. Martinis, *Science* **307**, 1299 (2005); John M. Martinis, K. B. Cooper, R. McDermott, Matthias Steffen, Markus Ansmann, K. D. Osborn, K. Cicak, Seongshik Oh, D. P. Pappas, R. W. Simmonds, and Clare C. Yu, *Phys. Rev. Lett.* **95**, 210503 (2005).
- ⁷Y. Nakamura (private communication).
- ⁸D. J. Van Harlingen, T. L. Robertson, B. L. T. Plourde, P. A. Reichardt, T. A. Crane, and John Clarke, *Phys. Rev. B* **70**, 064517 (2004).
- ⁹Alexander Shnirman, Gerd Schön, Ivar Martin, and Yuriy Makhlin, *Phys. Rev. Lett.* **94**, 127002 (2005).
- ¹⁰G. Ithier, E. Collin, P. Joyez, P. J. Meeson, D. Vion, D. Esteve, F. Chiarello, A. Shnirman, Y. Makhlin, J. Schrieffer, and G. Schon, *Phys. Rev. B* **72**, 134519 (2005).
- ¹¹R. W. Simmonds, K. M. Lang, D. A. Hite, S. Nam, D. P. Pappas, and John M. Martinis, *Phys. Rev. Lett.* **93**, 077003 (2004).
- ¹²D. Esteve (private communication).
- ¹³L. B. Ioffe, M. V. Feigel'man, A. Ioselevich, D. Ivanov, M. Troyer, and G. Blatter, *Nature (London)* **415**, 503 (2002).
- ¹⁴E. Il'ichev, N. Oukhanski, A. Izmailkov, Th. Wagner, M. Grajcar, H.-G. Meyer, A. Yu. Smirnov, Alec Maassen van den Brink, M. H. S. Amin, and A. M. Zagoskin, *Phys. Rev. Lett.* **91**, 097906 (2003).
- ¹⁵M. Grajcar, A. Izmailkov, E. Il'ichev, Th. Wagner, N. Oukhanski, U. Hübner, T. May, I. Zhilyaev, H. E. Hoenig, Ya. S. Greenberg, V. I. Shnyrkov, D. Born, W. Krech, H.-G. Meyer, Alec Maassen van den Brink, and M. H. S. Amin, *Phys. Rev. B* **69**, 060501(R) (2004).
- ¹⁶A. Lupascu, C. J. M. Verwijs, R. N. Schouten, C. J. P. M. Harmans, and J. E. Mooij, *Phys. Rev. Lett.* **93**, 177006 (2004).
- ¹⁷A. Wallraff, D. I. Schuster, A. Blais, L. Frunzio, R.-S. Huang, J. Majer, S. Kumar, S. M. Girvin, and R. J. Schoelkopf, *Nature (London)* **431**, 162 (2004).
- ¹⁸I. Siddiqi, R. Vijay, F. Pierre, C. M. Wilson, M. Metcalfe, C. Rigetti, L. Frunzio, and M. H. Devoret, *Phys. Rev. Lett.* **93**, 207002 (2004).
- ¹⁹M. I. Dykman and M. A. Krivogla, *Physica A* **104**, 480 (1980).
- ²⁰I. Siddiqi, R. Vijay, F. Pierre, C. M. Wilson, L. Frunzio, M. Metcalfe, C. Rigetti, R. J. Schoelkopf, M. H. Devoret, D. Vion, and D. Esteve, *Phys. Rev. Lett.* **94**, 027005 (2005).
- ²¹I. Siddiqi, R. Vijay, F. Pierre, C. M. Wilson, L. Frunzio, M. Metcalfe, C. Rigetti, and M. H. Devoret, cond-mat/0507248 (unpublished).
- ²²P. Bertet, I. Chiorescu, C. J. P. M. Harmans, and J. E. Mooij, *Phys. Rev. B* **70**, 100501(R) (2004).
- ²³R. Vijay, I. Siddiqi, and M. H. Devoret (unpublished).
- ²⁴D. I. Schuster, A. Wallraff, A. Blais, L. Frunzio, R.-S. Huang, J. Majer, S. M. Girvin, and R. J. Schoelkopf, *Phys. Rev. Lett.* **94**, 123602 (2005).
- ²⁵D. Vion, A. Aassime, A. Cottet, P. Joyez, H. Pothier, C. Urbina, D. Esteve, and M. H. Devoret, *Fortschr. Phys.* **51**, 462 (2003).
- ²⁶P. Bertet, I. Chiorescu, C. J. P. M. Harmans, and J. E. Mooij, cond-mat/0507290 (unpublished).

RF-Driven Josephson Bifurcation Amplifier for Quantum Measurement

I. Siddiqi, R. Vijay, F. Pierre, C. M. Wilson, M. Metcalfe, C. Rigetti, L. Frunzio, and M. H. Devoret

Departments of Applied Physics and Physics, Yale University, New Haven, Connecticut 06520-8284, USA

(Received 11 February 2004; published 10 November 2004)

We have constructed a new type of amplifier whose primary purpose is the readout of superconducting quantum bits. It is based on the transition of a rf-driven Josephson junction between two distinct oscillation states near a dynamical bifurcation point. The main advantages of this new amplifier are speed, high sensitivity, low backaction, and the absence of on-chip dissipation. Pulsed microwave reflection measurements on nanofabricated Al junctions show that actual devices attain the performance predicted by theory.

DOI: 10.1103/PhysRevLett.93.207002

PACS numbers: 85.25.Cp, 05.45.-a

Quantum measurements of solid-state systems, such as the readout of superconducting quantum bits [1–7], challenge conventional low-noise amplification techniques. Ideally, the amplifier for a quantum measurement should minimally perturb the measured system while maintaining sufficient sensitivity to overcome the noise of subsequent elements in the amplification chain. Additionally, the drift of materials properties in solid-state systems mandates a fast acquisition rate to permit measurements in rapid succession. To meet these inherently conflicting requirements, we propose to harness the sensitivity of a dynamical system—a single rf-driven Josephson tunnel junction—tuned near a bifurcation point. In this new scheme, all available degrees of freedom in the dynamical system participate in information transfer and none contribute to unnecessary dissipation resulting in excess noise. The superconducting tunnel junction is the only electronic circuit element that remains nonlinear and nondissipative at arbitrary low temperatures. As the key component of present superconducting amplifiers [8–10], it is known to exhibit a high degree of stability.

The operation of our Josephson bifurcation amplifier (JBA) is represented schematically in Fig. 1. The central element is a Josephson junction whose critical current I_0 is modulated by the input signal using an application-specific coupling scheme, such as a SQUID loop (see inset of Fig. 1) or a superconducting single-electron transistor (SSET) like in superconducting charge qubits (input port). The junction is driven with a sinusoidal signal $i_{\text{rf}} \sin(\omega t)$ fed from a transmission line through a circulator (drive port). In the underdamped regime, when the drive frequency ω is detuned from the natural oscillation frequency ω_p , the system can have two possible oscillation states that differ in amplitude and phase [11,12]. Starting in the lower amplitude state, at the bifurcation point $i_{\text{rf}} = I_B \ll I_0$, the system becomes infinitely sensitive, in absence of thermal and quantum fluctuations, to variations in I_0 . At finite temperature, sensitivity scales as $k_B T / \varphi_0$, where $\varphi_0 = \hbar/2e$ is the reduced flux quantum and T the temperature. The reflected component of the drive signal, measured through another transmission line

connected to the circulator (output port), is a convenient signature of the junction oscillation state that carries with it information about the input signal. This arrangement minimizes the backaction of the amplifier since the only fluctuations felt at its input port arise from the load impedance of the circulator, which is physically separated from the junction via a transmission line of arbitrary length and can therefore be thermalized efficiently to base temperature. In this Letter, we present an experiment that demonstrates the principle of bifurcation amplification.

The dynamics of the junction are described by the time evolution of the junction gauge-invariant phase difference $\delta(t) = \int_{-\infty}^t dt' 2eV(t')/\hbar$, where V is the voltage across the junction. In presence of the microwave drive $i_{\text{rf}} \sin(\omega t)$, the oscillations of the junction phase can be parameterized using in-phase and quadrature-phase components $\delta(t) = \delta_{\parallel} \sin(\omega t) + \delta_{\perp} \cos(\omega t)$ (higher harmonics of oscillation are negligible). When the detuning $\alpha = (1 - \omega/\omega_p)$ and the quality factor $Q = \omega_p RC$ satisfy $\alpha Q > \sqrt{3}/2$, then two steady-state solutions can exist for $\delta(t)$ (see Fig. 2). Here $\omega_p = (2eI_0/\hbar C)^{1/2}$ is the junc-

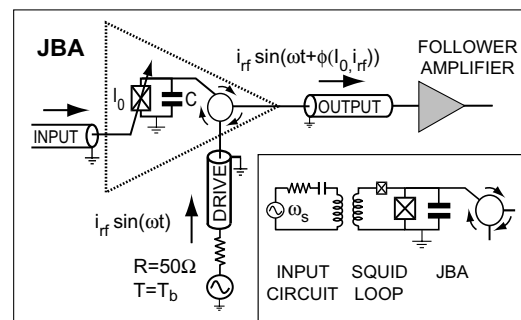


FIG. 1. Schematic diagram of the Josephson bifurcation amplifier. A junction with critical current I_0 , parametrically coupled to the input port, is driven by a rf signal which provides the power for amplification. In the vicinity of the dynamical bifurcation point $i_{\text{rf}} = I_B$, the phase of the reflected signal ϕ depends critically on the input signal. Inset: example of a parametric input coupling circuit.

tion plasma frequency, C is the capacitance shunting the Josephson element, and $R = 50 \Omega$ is the characteristic impedance of the transmission line at the output and drive ports. Figure 2 has been calculated for $\alpha = 0.122$, $Q = 20$, and $i_{\text{rf}}/I_B = 0.87$, where $I_B = 16/(3\sqrt{3}) \times \alpha^{3/2}(1 - \alpha)^{3/2}I_0 + O[1/(\alpha Q)^2]$. These values correspond to operating conditions for measurements described below. The dynamical switching from state 0 to 1 is characterized by a phase shift given here by $\tan^{-1}[(\delta_{\parallel}^1 - \delta_{\parallel}^0)/(\delta_{\perp}^1 - \delta_{\perp}^0)] = -139$ deg. Using the junction phase-voltage relationship and the transmission line equations, we can calculate the steady-state magnitude and phase of the reflected microwave drive signal. The change in the oscillation of δ results in a shift of the reflected signal phase $\Delta\phi_{01} = 89$ deg. (In very recent experiments, we have been able to optimize parameters and achieve $\Delta\phi_{01} = 180$ deg.) Since there is no source of dissipation in the junction chip, there should be no change in the magnitude of the reflected signal power, even though $\sqrt{(\delta_{\parallel}^1 - \delta_{\parallel}^0)^2 + (\delta_{\perp}^1 - \delta_{\perp}^0)^2} \neq 0$.

Our sample consisted of a single shadow-mask evaporated Al/Al₂O₃/Al tunnel junction with $I_0 = 1.17 \mu\text{A}$, shunted with an on-chip lithographic capacitance $C =$

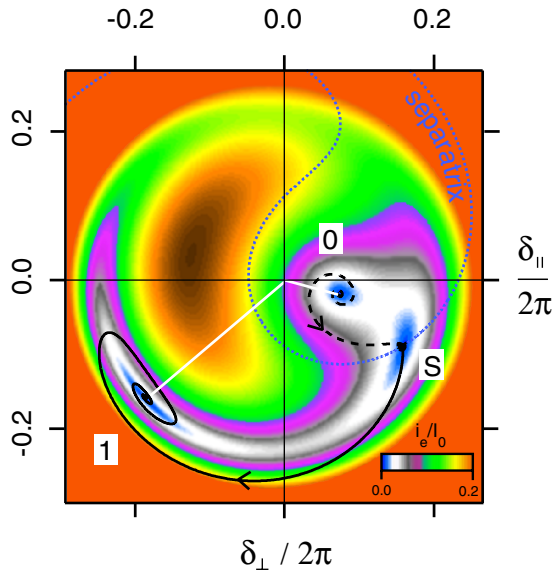


FIG. 2 (color online). Poincaré section of a rf-driven Josephson junction in the bistable regime [$\alpha = (1 - \omega/\omega_p) = 0.122$, $i_{\text{rf}}/I_B = 0.87$]. The coordinates δ_{\parallel} and δ_{\perp} are the in-phase and quadrature-phase components of the junction gauge-invariant phase difference δ . The color code gives the magnitude of the error current i_e [18], which describes the “force” on δ . The two stable oscillation states, labeled by 0 and 1, are indicated by white line segments. The basins of attraction corresponding to the two states are separated by the blue dotted line (separatrix). Point S , which lies on the separatrix, is the saddle point at which the escape trajectory from state 0 (dashed line) meets the retrapping trajectory into state 1 (solid line).

27.3 pF [12] to obtain a reduced plasma frequency $\omega_p/2\pi = 1.80$ GHz. The dynamics of the transition between the two oscillation states were probed using microwave pulses, generated by the amplitude modulation of a cw source with a phase-locked arbitrary waveform generator with 1 ns resolution. The reflected signal was passed through a circulator at base temperature $T = 0.25$ K to a matched high electron mobility transistor (HEMT) amplifier at $T = 4.2$ K. At room temperature, the reflected signal was further amplified, mixed down to 100 MHz and finally digitally demodulated using a 2 GS/s digitizer to extract the signal phase ϕ .

We first probed the drive current dependence of the reflected signal phase $\phi(i_{\text{rf}})$ by applying a 4 μs long symmetric triangular shaped pulse with a peak value $0.185I_0$. The demodulated reflected signal was divided into 20 ns sections, each yielding one measurement of ϕ for a corresponding value of i_{rf} . The measurement was repeated 6×10^5 times to obtain a distribution of $\phi(i_{\text{rf}})$. In Fig. 3, the mode of the distribution is plotted as a function of i_{rf}/I_0 . For $i_{\text{rf}}/I_0 < 0.125$, the bifurcation amplifier is always in state 0 and ϕ is constant and assigned a value of 0 deg. As the drive current is increased above $i_{\text{rf}}/I_0 = 0.125$, thermal fluctuations are sufficiently large to cause transitions to the 1 state. In the region between the two dashed lines at $i_{\text{rf}}/I_0 = 0.125$ and $i_{\text{rf}}/I_0 = 0.160$, ϕ displays a bimodal distribution with peaks centered at 0 and 74 deg with the latter corresponding to the amplifier in the 1 state, as we have demonstrated previously [12]. The dotted line in Fig. 3 is the average reflected signal phase $\langle\phi\rangle$. When i_{rf}/I_0 is increased above 0.160, the system is only found in state 1. In the decreasing part of the i_{rf} ramp, the system does not start to switch back to state 0 until $i_{\text{rf}}/I_0 = 0.065$. The critical switching cur-

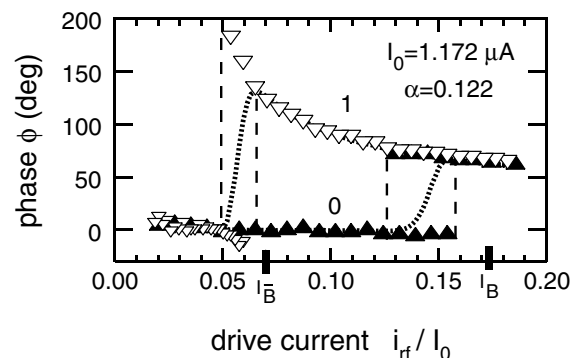


FIG. 3. Hysteretic variation of the reflected signal phase ϕ with drive current i_{rf}/I_0 . Symbols denote the mode of ϕ , with up and down triangles corresponding to increasing and decreasing i_{rf} , respectively. The dotted line is $\langle\phi\rangle$. The calculated bifurcation points, $I_{\bar{B}}$ and I_B , are marked on the horizontal axis. The 0 and 1 phase states are reminiscent of the superconducting and dissipative states of the dc current-biased junction.

rents I_B for the $0 \rightarrow 1$ transition and $I_{\bar{B}}$ for the $1 \rightarrow 0$ transition, calculated from numerical simulations to treat the inductance of wire bonds, are denoted with ticks in Fig. 3, and are in good agreement with experiment. The $0 \rightarrow 1$ transition at $i_{\text{rf}} = I_B$ is nearly irreversible, allowing the bifurcation amplifier to latch and store its output during the integration time set by the sensitivity of the follower amplifier.

We have then characterized the switching phenomenon in the vicinity of the $0 \rightarrow 1$ transition. The drive current was ramped from 0 to its maximum value in 40 ns and was then held constant at a plateau for 40 ns before returning to 0. Only the final 20 ns of the signal in the plateau were analyzed to determine the oscillation phase, the first 20 ns being allotted for settling of the phase. Histograms taken at an acquisition rate of 10 MHz are shown in Fig. 4. The 0 and 1 peaks can easily be resolved with a small relative overlap of 10^{-2} . We have also “latched” the state of the amplifier by reducing the drive amplitude of the analysis plateau by 20% relative to the settling plateau. Now, by increasing the analysis time to 300 ns, the overlap was reduced to 6×10^{-5} .

The switching probability $P_{0 \rightarrow 1}(i_{\text{rf}})$, i.e., the weight of the 1 peak in Fig. 4, was measured for different values of the temperature T and I_0 , the latter being varied with a magnetic field applied parallel to the junction plane (see Fig. 5). Defining the discrimination power d as the maximum difference between two switching probability curves that differ in I_0 , we find that at $T = 340$ mK, $d = 57\%$ for $\Delta I_0/I_0 = 1\%$ —the typical variation between qubit states in a “quantrium” circuit [2], which is in essence a SSET coupled to a readout junction operated in dc switching mode. The switching probability curves should shift according to $(\Delta I_B/I_B)/(\Delta I_0/I_0) = 3/(4\alpha) - 1/2 + O[1/(\alpha Q)^2]$, which for our case takes the value 5.6. In Fig. 5, the curves are shifted by 6%, which agrees well with this prediction. For the case of the dc current-biased junction, similar curves would shift only by 1% since the switching current is I_0 itself. Comparable discrimination

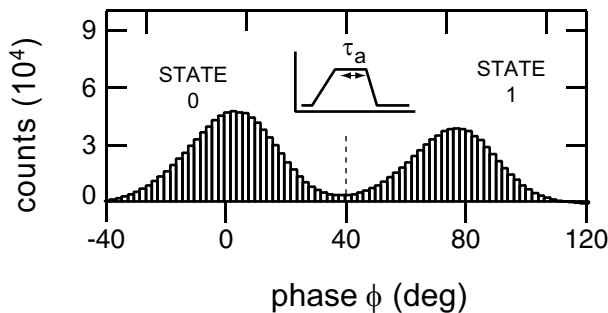


FIG. 4. Histograms of the reflected signal phase ϕ at $i_{\text{rf}}/I_0 = 0.145$. The histogram contains 1.6×10^6 counts with an analysis time $\tau_a = 20$ ns. Data here have been taken under the same operating conditions as in Fig. 3. The dashed line represents the discrimination threshold between the 0 and 1 state.

power using dc switching has only been achieved in these devices at $T \lesssim 60$ mK. As the temperature is increased, the switching probability curves broaden due to increased thermal fluctuations and the discrimination power decreases: at $T = 540$ mK, $d = 49\%$. With improved rf filtering and a more optimized sample, we reached $T = 250$ mK and obtained $d = 80\%$. This temperature dependence of the discrimination power is in agreement with both analytical predictions and independent measurement of the rate of escape out of the dynamical well (data not shown). The temperatures quoted above are inferred from the measured escape rate and calculated barrier heights using the method of Ref. [13].

With the Josephson bifurcation amplifier operating at $T = 340$ mK, it is possible to resolve with a signal/noise ratio of 1 a 10 nA variation in I_0 in a total time $\tau \lesssim 80$ ns, corresponding to a critical current sensitivity of $S_{I_0}^{1/2} = 3.3 \times 10^{-12}$ A/Hz $^{1/2}$. This value is in agreement with the analytical theory prediction $S_{I_0}^{1/2} = \eta(i_{\text{rf}}/I_0, \alpha) \times (k_B T / \varphi_0) \cdot \tau^{1/2}$, where $\eta \approx 1.4$ near the bifurcation point. Dispersive readout in the linear regime has been proposed [14] on account of its minimal effect on qubit coherence and relaxation. Increasing the drive amplitude near the dynamical bifurcation has the further benefit, for a given Q , of maximizing the phase shift between the two qubit states and thus eliminating any loss of fidelity due to noise of the follower amplifier.

The JBA can also be operated in the nonhysteretic regime when $\alpha Q \lesssim \sqrt{3}/2$. In this mode, it is straightforward to define conventional amplifier quantities such as power gain and noise temperature, thus allowing direct comparison with other ultra-low-noise amplifiers such as the SQUID [15]. With the model shown in the inset of Fig. 1, and assuming that the modulation of drive signal has symmetric sidebands, we calculate the power gain and the noise temperature to be $2\omega_p/\omega_s$ and $\hbar\omega_s/k_B$, respectively, where ω_s is the input signal frequency. We

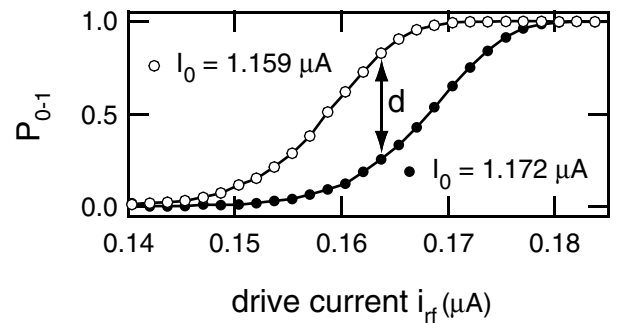


FIG. 5. Switching probability curves at $T = 340$ mK as a function of the drive current i_{rf} . The discrimination power $d = 0.57$ is the maximum difference between the two curves. The measurement protocol is the same as shown in the upper panel of Fig. 4. Though the two curves differ by approximately 1% in I_0 , they are shifted by 6% in drive current.

believe that a more precise calculation, taking into account the single sideband modulation character found at the bifurcation, would yield a quantum-limited temperature $\hbar\omega_s/2k_B$. These calculations, which follow step-by-step the analysis of the SQUID [10], assume ideal matching to the noise impedance of the device, with components similar to those in conventional SQUID circuits. Although these results do not differ from those of the SQUID, the real advantage of our device lies in the spectral content of the total backaction noise, which is not contained in the usual definition of the noise temperature at ω_s . Since there is no on-chip dissipation, the only fluctuations contributing to the total backaction originate from our matched circulator load, within a band ω_p/Q centered at ω_p . In the SQUID, the total backaction consists of a wide spectrum extending from dc to several harmonics of the Josephson frequency. Efficient filtering over this wide band, leaving only the signal frequency unattenuated, is difficult. Moreover, it is easier in the JBA to fully thermalize [16] the requisite dissipation needed for amplification since it is completely in the off-chip circulator. Finally, the bifurcation amplifier does not suffer from quasiparticle generation associated with hysteretic SQUIDS [4] and dc current-biased junctions [2] that switch into the voltage state. Long quasiparticle recombination times at low temperatures limit the acquisition rate of these devices while the recombination process itself produces excess noise for adjacent circuitry [17].

In conclusion, we have developed a new amplification principle harnessing the nonlinear, nondissipative inductance of the Josephson junction to improve the performance of Josephson effect based amplifiers. The Josephson bifurcation amplifier is competitive with the SQUID for applications where low backaction is required. Its speed, suppression of on-chip dissipation, and latching make it ideal for the readout of superconducting qubits. At temperatures such that $T \leq 85$ mK, the discrimination power for qubits would be greater than 95%, hence permitting stringent tests of quantum mechanics, like the violation of Bell's inequalities.

We would like to thank E. Boaknin, J. Clarke, M. Dykman, D. Esteve, S. Girvin, L. Grober, D. Prober,

R. Schoelkopf, and D. Vion for discussions and assistance. This work was supported by the ARDA (ARO Grant No. DAAD19-02-1-0044), the NSF (ITR Grants No. DMR-0325580 and No. DMR-0072022), and the Keck Foundation.

-
- [1] A. Aassime, G. Johansson, G. Wendin, R. J. Schoelkopf, and P. Delsing, *Phys. Rev. Lett.* **86**, 3376 (2001).
 - [2] D. Vion, A. Aassime, A. Cottet, P. Joyez, H. Pothier, C. Urbina, D. Esteve, and M. Devoret, *Science* **296**, 886 (2002).
 - [3] J. M. Martinis, S. Nam, J. Aumentado, and C. Urbina, *Phys. Rev. Lett.* **89**, 117901 (2002).
 - [4] I. Chiorescu, Y. Nakamura, C. J. P. M. Harmans, and J. E. Mooij, *Science* **299**, 1869 (2003).
 - [5] O. Buisson, F. Balestro, J. P. Pekola, and F. W. J. Hekking, *Phys. Rev. Lett.* **90**, 238304 (2003).
 - [6] T. V. Filippov, S. K. Tolpygo, J. Mannik, and J. E. Lukens, *IEEE Trans. Appl. Supercond.* **13**, 1005 (2003).
 - [7] A. B. Zorin, *J. Exp. Theor. Phys.* **98**, 1250 (2004).
 - [8] R. Tucker and M. J. Feldman, *Rev. Mod. Phys.* **57**, 1055 (1985).
 - [9] B. Yurke, L. R. Corruccini, P. G. Kaminsky, L. W. Rupp, A. D. Smith, A. H. Silver, R. W. Simon, and E. A. Whittaker, *Phys. Rev. A* **39**, 2519 (1989).
 - [10] J. Clarke, *Proc. IEEE* **77**, 1208 (1989).
 - [11] M. I. Dykman and M. A. Krivoglaz, *Physica A (Amsterdam)* **104**, 480 (1980).
 - [12] I. Siddiqi, R. Vijay, F. Pierre, C. M. Wilson, L. Frunzio, M. Metcalfe, C. Rigetti, R. J. Schoelkopf, M. H. Devoret, D. Vion, and D. E. Esteve, *cond-mat/0312553*.
 - [13] C. Urbina, D. Esteve, J. M. Martinis, E. Turlot, M. H. Devoret, H. Grabert, and S. Linkwitz, *Physica B (Amsterdam)* **169**, 26 (1991).
 - [14] A. Lupascu, C. J. M. Verwijs, R. N. Schouten, C. J. P. M. Harmans, and J. E. Mooij, *Phys. Rev. Lett.* **93**, 177006 (2004).
 - [15] M. Mück, J. B. Kycia, and J. Clarke, *Appl. Phys. Lett.* **78**, 967 (2001).
 - [16] F. C. Wellstood, C. Urbina, and J. Clarke, *Appl. Phys. Lett.* **54**, 2599 (1989).
 - [17] J. Mannik and J. E. Lukens, *Phys. Rev. Lett.* **92**, 057004 (2004).
 - [18] R. L. Kautz, *Phys. Rev. A* **38**, 2066 (1988).

Direct Observation of Dynamical Bifurcation between Two Driven Oscillation States of a Josephson Junction

I. Siddiqi, R. Vijay, F. Pierre, C. M. Wilson, L. Frunzio, M. Metcalfe, C. Rigetti, R. J. Schoelkopf, and M. H. Devoret
Departments of Applied Physics and Physics, Yale University, New Haven, Connecticut 06520-8284, USA

D. Vion and D. Esteve

Service de Physique de l'Etat Condensé, CEA-Saclay, F-91191 Gif-sur-Yvette, France
(Received 1 October 2003; published 20 January 2005)

We performed a novel phase-sensitive microwave reflection experiment which directly probes the dynamics of the Josephson plasma resonance in both the linear and the nonlinear regime. When the junction was driven below the plasma frequency into the nonlinear regime, we observed for the first time the transition between two different dynamical states predicted for nonlinear systems. In our experiment, this transition appears as an abrupt change in the reflected signal phase at a critical excitation power. This controlled dynamical switching can form the basis of a sensitive amplifier, in particular, for the readout of superconducting qubits.

DOI: 10.1103/PhysRevLett.94.027005

PACS numbers: 85.25.Cp, 05.45.-a

As first understood by Josephson, a superconducting tunnel junction can be viewed as a nonlinear, nondissipative, electrodynamic oscillator [1]. The question we address in this Letter is whether the nonlinearity of the Josephson junction can be harnessed controllably and robustly to provide an amplification mechanism that will remain efficient in the quantum limit [2].

The tunneling of Cooper pairs manifests itself as a nonlinear inductance that shunts the linear junction self-capacitance C_J , formed by the junction electrodes and the tunnel oxide layer. The constitutive relation of the nonlinear inductor can be written as $I(t) = I_0 \sin \delta(t)$, where $I(t)$, $\delta(t) = \int_{-\infty}^t dt' V(t')/\varphi_0$ and $V(t)$ are the current, gauge-invariant phase difference and voltage corresponding to the inductor, respectively, while the parameter I_0 is the junction critical current. Here $\varphi_0 = \hbar/2e$ is the reduced flux quantum. For small oscillation amplitude, the frequency of oscillation is given for zero bias current by the so-called plasma frequency $\omega_p = 1/\sqrt{L_J C_J}$, where $L_J = \varphi_0/I_0$ is the effective junction inductance. As the oscillation amplitude increases, the oscillation frequency decreases, an effect which has been measured in both the classical and the quantum regime [2–6]. However, a more dramatic nonlinear effect should manifest itself if the junction is driven with an ac current $i_{rf} \sin \omega t$ at a frequency ω slightly below ω_p . If the quality factor $Q = C_J \omega_p / \text{Re}[Z^{-1}(\omega_p)]$ is greater than $\sqrt{3}/2\alpha$, where $Z(\omega_p)$ is the impedance of the junction electrodynamic environment and $\alpha = 1 - \omega/\omega_p$ is the detuning parameter, then the junction should transit from one dynamical oscillation state to another when i_{rf} is ramped above a critical value i_B [7]. For $i_{rf} < i_B$, the oscillation state would be low amplitude and phase lagging, while for $i_{rf} > i_B$, the oscillation state would be high amplitude and phase leading. This generic nonlinear phenomenon, which we refer to as “dynamical bifurcation,” is reminiscent of the usual switching

of a hysteretic junction from the zero-voltage state to the voltage state when the current bias exceeds the critical current I_0 [8]. However, an important distinction between dynamical bifurcation and switching is that in the former, the phase particle remains confined to only one well of the junction cosine potential $U(\delta) = -\varphi_0 I_0 \cos(\delta)$, and the time-average value of δ and $\dot{\delta}$ is always zero in each state. Note also that, unlike the critical current in switching, i_B depends both on Q and on the detuning α . In this Letter we report the first observation of a controlled dynamical bifurcation effect in a Josephson junction. As with switching, controlled dynamical bifurcation can be used for amplification [9], but with the added advantage that no energy dissipation occurs in the junction chip, a desirable feature for the readout of superconducting qubits [10].

Typical junction fabrication parameters limit the plasma frequency to the 20–100 GHz range where techniques for addressing junction dynamics are inconvenient. We have chosen to shunt the junction by a capacitive admittance to lower the plasma frequency by more than an order of magnitude and attain a frequency in the 1–2 GHz range (microwave L band). In this frequency range, a simple on-chip electrodynamic environment with minimum parasitic elements can be implemented, and the hardware for precise signal generation and processing is readily available. In our experiment, we directly measure the plasma resonance in a coherent microwave reflection measurement. Unlike previous experiments which measured only the microwave power absorption at the plasma resonance [3,4,6], we also measure the phase ϕ of the reflected microwave signal. Thus, we can detect the characteristic signature of the transition between different oscillating states of the junction—a change of oscillation phase relative to the drive. Note that the phase ϕ of the reflected signal which probes the phase of the oscillation state should not be

TABLE I. Sample parameters. $L_J = \varphi_0/I_0$ and ω_p are measured values. C and L_S are fit values to the data. Samples 1, 2, and 2a have a 100 nm thick Au underlayer, sample 3 has a 50 nm thick Nb underlayer, sample 4 has a 1 μm thick Cu underlayer, and sample 5 has a 200 nm thick Nb underlayer.

Sample	L_J (nH)	$\omega_p/2\pi$ (GHz)	C (pF)	L_S (nH)
1	0.28	1.18	39 ± 1	0.20 ± 0.02
2	0.18	1.25	30 ± 4	0.34 ± 0.04
2a	0.17	1.66	18 ± 1	0.32 ± 0.02
3	0.32	1.64	16 ± 1	0.27 ± 0.02
4	0.38	1.81	19 ± 1	0.026 ± 0.02
5	0.40	1.54	19 ± 1	0.15 ± 0.02

confused with the junction gauge-invariant phase difference δ .

In the first step of sample fabrication, a metallic underlayer—either a normal metal (Au, Cu) or a superconductor (Nb)—was deposited on a silicon substrate to form one plate of the shunting capacitor, followed by the deposition of an insulating Si_3N_4 layer. Using e -beam lithography and double-angle shadow mask evaporation, we subsequently fabricated the top capacitor plates along with a micron sized Al/ Al_2O_3 /Al tunnel junction. The critical current of the junction was in the range $I_0 = 1\text{--}2 \mu\text{A}$. By varying both the dielectric layer thickness and the pad area, the capacitance C was varied between 16 and 40 pF. Sample parameters are listed in Table I.

The junction + capacitor chip is placed on a microwave circuit board and is wire bonded to the end of a coplanar strip line which is soldered to a coaxial launcher affixed to the sidewall of the copper sample box. We anchor the rf leak-tight sample box to the cold stage of a ^3He refrigerator with a base temperature $T = 280 \text{ mK}$. The measurement setup is schematically shown in Fig. 1. Microwave excitation signals are generated by a HP 8722D vector network analyzer and coupled to the sample via the -13 dB side port of a directional coupler. The reflected microwave signal passes through the direct port of the coupler and is amplified first using a cryogenic $1.20\text{--}1.85 \text{ GHz}$ high electron mobility transistor amplifier with noise temperature $T_N = 4 \text{ K}$ before returning to the network analyzer. A bias current can be applied to the junction by way of a bias tee and a passive filter network.

We locate the linear plasma resonance by sweeping the excitation frequency from 1 to 2 GHz and measuring the complex reflection coefficient $\Gamma(\omega) = (1 - \epsilon)e^{j\phi} = [Z(\omega) - Z_0]/[Z(\omega) + Z_0]$, where $Z_0 = 50 \Omega$ is the characteristic impedance of our transmission lines and $Z(\omega)$ is the impedance presented to the analyzer by the chip and the measurement lines. For an ideal LC resonator without intrinsic dissipation, we expect a phase shift $\phi_{\omega \gg \omega_p} - \phi_{\omega \ll \omega_p} = 2\pi$, which we verified by placing a chip capacitor and an inductive wire bond in place of the junction chip. An important aspect of our experiment is that Q is now

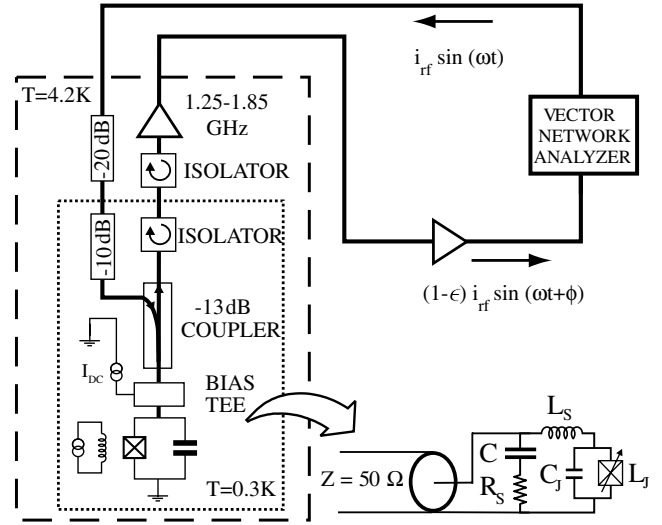


FIG. 1. Schematic of the measurement setup. Thick lines correspond to 50Ω coaxial transmission lines. A lumped element model for the junction chip and measurement line is shown in the lower right corner.

determined by the ratio $Z_0/Z_J \sim 10$, where $Z_J = \sqrt{L_J/(C_J + C)}$ and not by the intrinsic junction losses which are negligible. An excitation power $P = i_{\text{rf}}^2 Z_0/4 \approx -120 \text{ dBm}$ (1 fW) corresponding to a current $i_{\text{rf}} = 9 \text{ nA} \ll I_0$ keeps the junction in the linear regime.

In Fig. 2, we present the reflected signal phase ϕ as a function of excitation frequency for sample 5. In order to remove the linear phase evolution associated with the finite length of the measurement lines, we have subtracted from

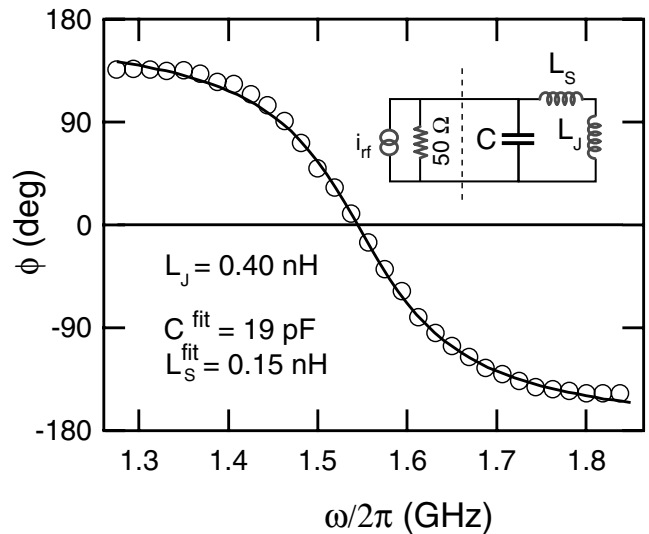


FIG. 2. Normalized reflected signal phase ϕ as a function of the excitation frequency for sample 5. The open circles are measured data for $L_J = 0.40 \text{ nH}$. The solid line is calculated from the equivalent circuit model shown in the inset. Here $\epsilon = 0$ for this sample.

our measurement in the superconducting state the reflection coefficient measured with the junction in the normal state. The frequency where $\phi = 0$ thus yields the linear-regime plasma frequency. For sample 5, $\omega_p/2\pi = 1.54$ GHz.

The precise frequency and critical current dependence of the reflected signal phase of our samples can be accounted for by a three-element model for the electrodynamic environment seen by the junction. This lumped element model is shown in the lower right corner of Fig. 1. The parasitic inductance L_S and resistance R_S model the nonideality of the shunting capacitor C . They arise from the imperfect screening of currents flowing in the capacitor plates and the finite conductivity of these plates. The plasma frequency in the linear regime is determined by the total inductance $L_J + L_S$ and capacitance $C_{\text{eff}} = C_J + C \simeq C$ and is given by the following relation:

$$\left(\frac{1}{\omega_p}\right)^2 = C(L_J + L_S) = \frac{\varphi_0 C}{I_0} + CL_S.$$

We thus plot $1/\omega_p^2$ versus $1/I_0 = L_J/\varphi_0$ in Fig. 3 for samples 1, 2, 4, and 5. As the critical current is decreased by applying a magnetic field, the junction inductance increases, and the plasma frequency is reduced. For each sample, a linear fit to the data of Fig. 3 yields the values of C and L_S (see Table I). The fit values for C agree well with simple estimates made from the sample geometry. Samples 1 and 2 have nominally the same capacitance but a different critical current and hence lie approximately on the same line in Fig. 3. A total of four capacitive pads were used to make the shunting capacitor in samples 1 and 2, and after initial measurements, we scratched off two of

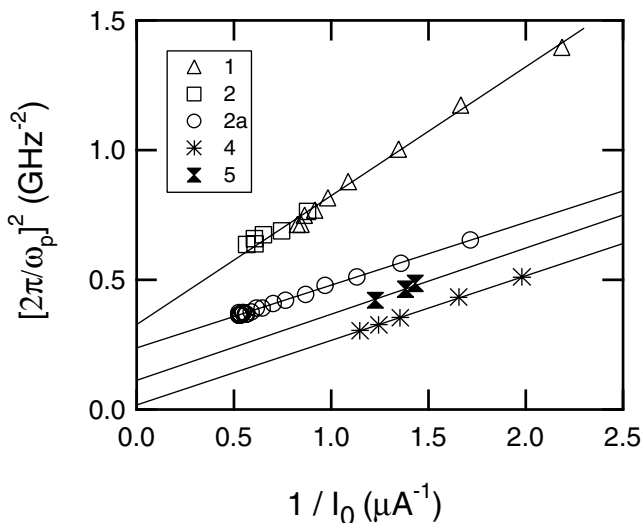


FIG. 3. Inverse square of the plasma frequency $1/\omega_p^2$ as a function of the inverse critical current $1/I_0 = L_J/\varphi_0$ for samples 1, 2, 4, and 5. Solid lines are linear fits to the data corresponding to the model of Fig. 1, with a single best fit line drawn for samples 1 and 2 which nominally differ only in I_0 .

the pads from sample 2 to obtain sample 2a, and the resulting capacitance is indeed halved. For samples with a thin underlayer (1, 2, and 3), a stray inductance in the range $L_S = 0.20$ – 0.34 nH is observed. For samples 4 and 5 with a significantly thicker underlayer, L_S was reduced to 0.026 and 0.15 nH, respectively. This behavior is consistent with the calculated screening properties of our thin films. To verify that the values of C and L_S were not affected by the magnetic field used to vary I_0 , we varied L_J by applying a bias current [6] at zero magnetic field. The resonance data obtained by this method agree with the magnetic field data. Using L_S and C we can accurately predict the observed resonant line shape of Fig. 2, in which $R_S = 0$. For samples with a normal underlayer, we find the data are accurately fit by $R_S = 0.8\Omega$ for samples 1 and 2 and $R_S = 0.02\Omega$ for sample 4. Finally, we have independently verified the effect of the shunting capacitor on the plasma resonance by performing resonant activation experiments [5].

We now address our main interest: the nonlinear regime of the plasma resonance. The reflection coefficient as a function of frequency for increasing power for sample 5 is presented in the lower panel of Fig. 4 as a two dimensional color plot, in which each row is a single frequency sweep, similar to Fig. 2. For small excitation power, we recover the linear plasma resonance at 1.54 GHz, shown as a yellow line corresponding to $\phi = 0$. As the power is increased above -115 dBm, the plasma frequency decreases as is expected for a junction driven with large amplitude [5]. The boundary between the leading-phase region (green) and the lagging-phase region (red) therefore curves for high powers. This curvature has an interesting consequence: When we increase the drive power at a constant frequency slightly below the plasma frequency, the phase as a function of power undergoes an abrupt step, as predicted. For yet greater powers (> -90 dBm), we encounter a new dynamical regime (black region in Fig. 4) where δ appears to diffuse between the wells of the cosine potential. This was confirmed by the presence of an unambiguous audiofrequency ac resistance in the black region. In the lower panel of Fig. 4, we illustrate the sequence of dynamical transitions by plotting ϕ as a function of incident power at $\omega/2\pi = 1.375$ GHz. For $P < -102$ dBm, the phase is independent of power (δ oscillates in a single well in the harmonic-like, phase-leading state (A)]. For $-102 < P < -90$ dBm, the phase evolves with power and δ still remains within the same well but oscillates in the anharmonic phase-lagging state (B). Finally, for $P > -90$ dBm, the average phase of the reflected signal saturates to -180° , corresponding to a capacitive short circuit (C). This last value is expected if δ hops randomly between wells, the effect of which is to neutralize the Josephson inductive admittance.

The value of the current i_B for the A-B transition, which is a function of both the detuning α and power P , is in good

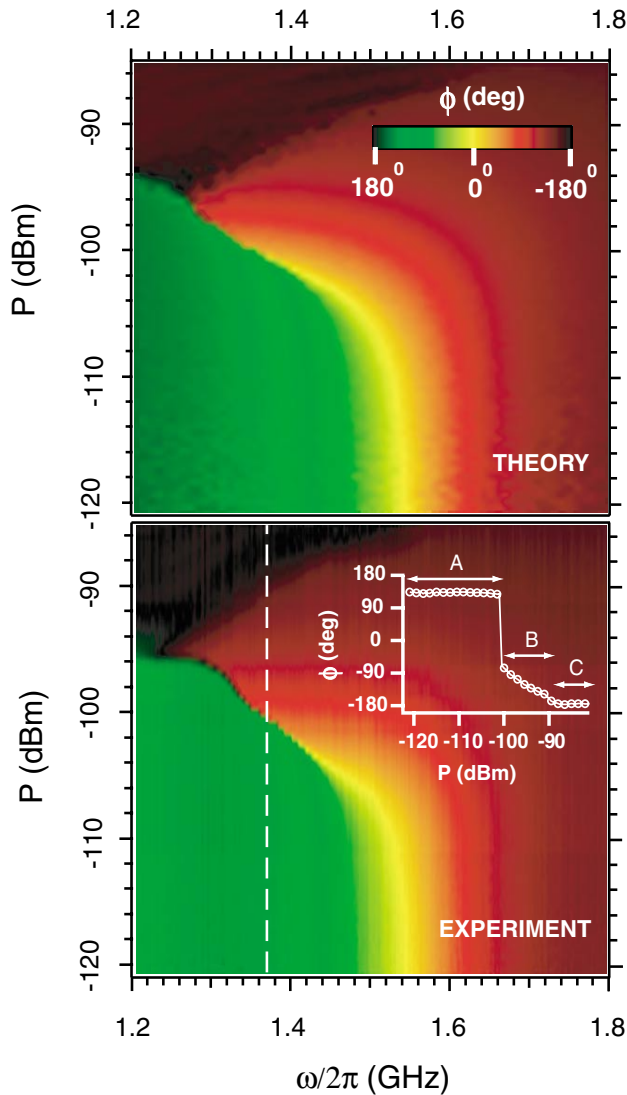


FIG. 4 (color). Normalized reflected signal phase ϕ (wrap-around color scheme) as a function of excitation frequency $\omega/2\pi$ and excitation power P . In the lower panel, a vertical slice taken at $\omega/2\pi = 1.375$ GHz (dashed line) shows the abrupt transition between two oscillation states of the system. The upper panel is the result of numerical simulations.

qualitative agreement with the analytical theory which retains only the first anharmonic term in the cosine potential [11]. For instance, the slope of the A-B transition line at the linecut in Fig. 4, dP (dBm)/ $d\alpha$ (%) = 0.8 for the experiment while we calculate its value to be 0.7. Furthermore, in measurements in which the power is ramped in less than 100 ns, we verified that the transition between dynamical states is hysteretic, another prediction of the theory. To explain the complete frequency and power dependence of the transitions shown in the lower panel of Fig. 4, we have performed numerical simulations by solving the full circuit model of the lower corner of Fig. 1, including the exact junction nonlinear constitutive relation.

The result of this calculation is shown in the upper panel of Fig. 4. It correctly predicts the variation of the plasma frequency with excitation power, and the boundaries of the phase diffusion region. The agreement between theory and experiment is remarkable in view of the simplicity of the model which uses only measured parameters, and only small differences in the exact shape of region boundaries are observed. It is important to mention that the overall topology of Fig. 4 is unaffected by changes in the parameter values within the bounds of Table I.

In conclusion, we have performed a novel, phase-sensitive, microwave experiment demonstrating that the Josephson plasma oscillation can transition between the two dynamical states predicted for a driven nonlinear system. Using different samples, we have shown that this dynamical phenomenon is stable, reproducible, and can be precisely controlled, thus opening the possibility for practical applications such as amplification. Following the methodology invented for trapped electron systems [12], we can use this dynamical effect as the basis for a single-shot and latching qubit readout.

We thank D. Prober for the use of his laboratory equipment and useful discussions, Abdel Aassime for help in the initial sample fabrication, and L. Grober for assistance with the electron microscope. This work was supported by the ARDA (ARO Grant No. DAAD19-02-1-0044) and by the NSF (Grant No. DMR-0072022).

-
- [1] B. Josephson, *Rev. Mod. Phys.* **36**, 216 (1964).
 - [2] B. Yurke, L. R. Corruccini, P. G. Kaminsky, L. W. Rupp, A. D. Smith, A. H. Silver, R. W. Simon, and E. A. Whittaker, *Phys. Rev. A* **39**, 2519 (1989).
 - [3] A. J. Dahm, A. Denenstien, T. F. Finnegan, D. N. Langenberg, and D. J. Scalapino, *Phys. Rev. Lett.* **20**, 859 (1968).
 - [4] J. Mygind, N. F. Pedersen, and O. H. Soerensen, *Appl. Phys. Lett.* **29**, 317 (1976).
 - [5] M. H. Devoret, D. Esteve, J. M. Martinis, A. Cleland, and J. Clarke, *Phys. Rev. B* **36**, 58 (1987).
 - [6] T. Holst and J. Bindslev Hansen, *Physica (Amsterdam)* **165B-166B**, 1649 (1990).
 - [7] L. D. Landau and E. M. Lifshitz, *Mechanics* (Reed, Oxford, 1981).
 - [8] T. A. Fulton and L. N. Dunkleberger, *Phys. Rev. B* **9**, 4760 (1974).
 - [9] I. Siddiqi, R. Vijay, F. Pierre, C. M. Wilson, M. Metcalfe, C. Rigetti, L. Frunzio, and M. H. Devoret, *Phys. Rev. Lett.* **93**, 207002 (2004). This work was carried out after the submission of the present Letter.
 - [10] D. Vion, A. Aassime, A. Cottet, P. Joyez, H. Pothier, C. Urbina, D. Esteve, and M. Devoret, *Science* **296**, 886 (2002).
 - [11] M. I. Dykman and V. N. Smelyanski, *Phys. Rev. A* **41**, 3090 (1990).
 - [12] C. H. Tseng, D. Enzer, G. Gabrielse, and F. L. Walls, *Phys. Rev. A* **59**, 2094 (1999).

THE JOSEPHSON BIFURCATION AMPLIFIER FOR QUANTUM MEASUREMENTS

I. Siddiqi, R. Vijay, F. Pierre, C.M. Wilson, L. Frunzio, M. Metcalfe, C. Rigetti, and M.H. Devoret

Departments of Applied Physics and Physics

Yale University, USA

irfan.siddiqi@yale.edu

Abstract We have constructed a new type of amplifier whose primary purpose is the read-out of superconducting quantum bits. It is based on the transition of an RF-driven Josephson junction between two distinct oscillation states near a dynamical bifurcation point. The main advantages of this new amplifier are speed, high-sensitivity, low back-action, and the absence of on-chip dissipation. Using pulsed microwave techniques, we demonstrate bifurcation amplification in nanofabricated Al junctions and verify that the performance predicted by theory is attained.

1. Introduction

Josephson first noted that the superconducting tunnel junction can be viewed as a non-linear, non-dissipative, electrodynamic oscillator [1]. We exploit this non-linearity to produce a new type of high-sensitivity amplifier, the Josephson Bifurcation Amplifier (JBA). No shunt resistors are required in our amplification scheme, and it is thus possible to take advantage of the elastic character of the junction and eliminate on-chip dissipation, thereby minimizing the back-action of the amplifier. The combination of high-sensitivity and minimal back-action makes the JBA well-suited for measurements on quantum systems such as superconducting qubits, and make it a strong candidate for reaching the quantum noise limit.

The operation of the JBA is represented schematically in Fig. 1. The central element is a Josephson junction, shunted with a lithographic capacitor, whose critical current I_0 is modulated by an input signal (input port). Coupling between the junction and the input signal can be achieved through different schemes, examples of which involve placing the JBA in a SQUID loop [2] or in parallel with a SSET [3]. The junction is driven with a pure AC signal $i_{RF} \sin(\omega t)$ in the microwave frequency range fed via a transmission

line through a circulator (drive port). In the underdamped regime, for certain values of ω and i_{RF} , two possible oscillation states which differ in amplitude and phase (denoted "0" and "1") can coexist. The reflected component of the drive signal, measured through another transmission line connected to the circulator (output port), is a convenient signature of the junction oscillation state. At the bifurcation point where switching between oscillation states occurs, the system becomes infinitely sensitive, in the absence of thermal and quantum fluctuations, to variations in I_0 . At finite temperature, the energy stored in the oscillation can always be made larger than thermal fluctuations by increasing the scale of I_0 , thus preserving sensitivity. Small variations in I_0 are transformed into readily discernible changes in the escape rate Γ_{01} from state 0 to 1. Back-action is minimized in this arrangement since the only fluctuations felt at the input port arise from the fluctuations of the $50\ \Omega$ drive port whose dissipative elements are physically separated from the junction via a transmission line of arbitrary length and can therefore be thermalized efficiently to base temperature. Additionally, the frequency band over which the back-action contributes is narrow, and well controlled.

In section 2, simplified expressions adapted from the theory of activated escape in a driven non-linear oscillator [4] are presented. Details of the devices and the measurement setup are presented in Section 3. Experimental results are given in Section 3, and concluding remarks are in Section 4.

2. Theory

The tunnelling of Cooper pairs manifests itself as a non-linear inductance that shunts the linear junction self-capacitance C_J , formed by the junction electrodes and the tunnel oxide layer. The constitutive relation of the non-linear inductor can be written as $I(t) = I_0 \sin \delta(t)$, where $I(t)$, $\delta(t) = \int_{-\infty}^t dt' V(t')/\varphi_0$ and $V(t)$ are the current, gauge-invariant phase-difference and voltage corresponding to the inductor, respectively, while the parameter I_0 is the junction critical current. Here $\varphi_0 = \hbar/2e$ is the reduced flux quantum. The dynamics of the junction are given by the time evolution of δ , which exhibits the motion of a phase particle in a cosine potential $U(\delta) = -\varphi_0 I_0 \cos(\delta)$. For small oscillation amplitude about the potential minima, the frequency of oscillation is given for zero DC bias current by the plasma frequency $\omega_{P0} = 1/\sqrt{L_J C_J}$ where $L_J = \varphi_0/I_0$ is the effective junction inductance. As the oscillation amplitude increases, the potential "softens" and ω_P decreases, an effect which has been measured in both the classical and quantum regime [5–8]. A more dramatic non-linear effect manifests itself if the junction is driven with an AC current $i_{RF} \sin \omega t$ at a frequency ω slightly below ω_{P0} . If the quality factor $Q = C_J \omega_{P0} / \text{Re}[Z^{-1}(\omega_{P0})]$ is greater than $\sqrt{3}/2\alpha$, where $Z(\omega_{P0})$ is the impedance of the junction electrodynamic envi-

rument and $\alpha = 1 - \omega/\omega_{p0}$ the detuning parameter, then the junction switches from one dynamical oscillation state to another when i_{RF} is ramped above a critical value I_B [9]. For $i_{RF} < I_B$, the oscillation state is low-amplitude and phase-lagging while for $i_{RF} > I_B$, the oscillation state is high-amplitude and phase-leading. This generic non-linear phenomenon, which we refer to as "dynamical switching", is reminiscent of the usual "static switching" of the junction from the zero-voltage state to the voltage state when the DC current bias exceeds the critical current I_0 [10]. However, an important distinction between dynamical and static switching is that in dynamical switching, the phase particle remains confined to only one well of the junction cosine potential, and the time-average value of δ is always zero. The junction never switches to the voltage state, and thus no DC voltage is generated. Also, for dynamical switching, the current I_B depends both on Q and on the detuning α .

In presence of the microwave drive $i_{RF} \sin(\omega t)$, the oscillations in the junction phase can be parameterized using in-phase and quadrature phase components $\delta(t) = \delta_{\parallel} \sin(\omega t) + \delta_{\perp} \cos(\omega t)$ (higher harmonics of oscillation are negligible). The two oscillation states appear as two points in the $(\delta_{\parallel}, \delta_{\perp})$ plane and are denoted by vectors labelled 0 and 1 (see Fig. 2). The error-current [11]

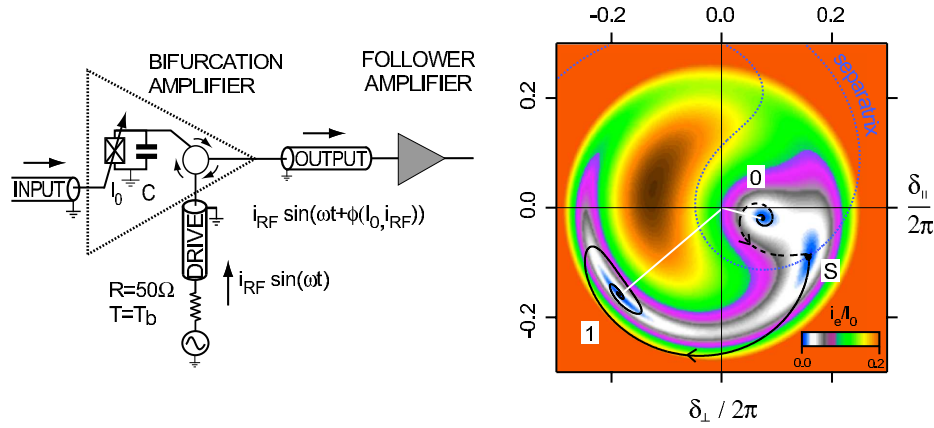


Figure 1. Schematic diagram of the Josephson bifurcation amplifier. A junction with critical current I_0 , parametrically coupled to the input port, is driven by an RF signal which provides the power for amplification. In the vicinity of the dynamical bifurcation point $i_{RF} = I_B$, the reflected signal phase ϕ depends critically on the input signal.

Figure 2. Poincare section of an RF-driven Josephson junction in the bistable regime ($\alpha = (1 - \omega/\omega_p) = 0.122$, $i_{RF}/I_B = 0.87$). The two stable oscillation states, labelled by 0 and 1, are indicated by white line segments. Point S which lies on the separatrix is the saddle point at which the escape trajectory from state 0 (dashed line) meets the retrapping trajectory into state 1 (solid line).

which describes the generalized force felt by the system is also plotted in the $(\delta_{\parallel}, \delta_{\perp})$ plane. Its value goes to zero at the attractors corresponding to states 0 and 1 and also at a third extremum which is the dynamical saddle point. Also shown in Fig. 2 is the calculated escape trajectory [12] from state 0 (dashed) and the corresponding retrapping trajectory [13] into state 1 (solid line). Fig. 2 has been computed for $\alpha = 0.122$, $Q = 20$ and $i_{RF}/I_B = 0.87$. These values correspond to typical operating conditions in our experiment. The dynamical switching from state 0 to 1 is characterized by a phase shift given here by $\tan^{-1} \left[(\delta_{\parallel}^1 - \delta_{\parallel}^0) / (\delta_{\perp}^1 - \delta_{\perp}^0) \right] = -139$ deg. Using the junction phase-voltage relationship and the transmission line equations, we can calculate the steady-state magnitude and phase of the reflected microwave drive signal. The change in the oscillation of δ results in a shift of the reflected signal phase $\Delta\phi_{01} = 89$ deg. Since there is no source of dissipation in the junction chip, there should be no change in the magnitude of the reflected signal power, even though $\sqrt{(\delta_{\parallel}^1 - \delta_{\parallel}^0)^2 + (\delta_{\perp}^1 - \delta_{\perp}^0)^2} \neq 0$.

Both static and dynamical switching can be described by an Arrhenius law in which the escape rate $\Gamma_{01} = (\omega_{att}/2\pi) \exp(-\Delta U/k_b T)$ is written as the product of an attempt frequency $\omega_{att}/2\pi$ and a Boltzman factor which contains the potential barrier height ΔU and the system temperature T . For the case of a DC current bias, the cosine potential, near the switching point, is approximated as a cubic potential with height $\Delta U_{st} = (4\sqrt{2}/3) \varphi_0 I_0 (1 - i_{DC}/I_0)^{3/2}$ where i_{DC} is the bias current. The attempt frequency is the plasma frequency ω_P . In the absence of fluctuations, the characteristic current at which switching occurs is I_0 . For the AC driven junction, the dynamical switching from oscillation state 0 to 1 can be cast in a similar form using the model of a particle in a cubic metapotential [4]. In this case, the effective barrier height is, to lowest order in $1/(\alpha Q)$, $\Delta U_{dyn} = u_{dyn} (1 - (i_{RF}/I_B)^2)^{3/2}$ with $u_{dyn} = 64\hbar/(18e\sqrt{3}) I_0 \alpha (1 - \alpha)^3$. The attempt frequency in the metapotential is given by $\omega_a = \omega_{a0} (1 - (i_{RF}/I_B)^2)^{1/2}$ with $\omega_{a0} = 4/(3\sqrt{3} RC) (\omega_p - \omega)^2$. The bifurcation current I_B where the 0 state ceases to exist is given by $I_B = 16/(3\sqrt{3}) \alpha^{3/2} (1 - \alpha)^{3/2} I_0$.

3. Devices and Setup

Typical junction fabrication parameters limit the plasma frequency to the 20 - 100 GHz range where techniques for addressing junction dynamics are inconvenient. We have chosen to shunt the junction by a capacitive admittance to lower the plasma frequency by more than an order of magnitude and attain a frequency in 1-2 GHz range (microwave L-band). In this frequency range, a simple on-chip electrodynamic environment with minimum parasitic elements can be implemented, and the hardware for precise signal generation and pro-

cessing is readily available. In the first step of sample fabrication, a metallic underlayer – either a normal metal (Au, Cu) or a superconductor (Nb) – was deposited on a silicon substrate to form one plate of the shunting capacitor, followed by the deposition of an insulating Si_3N_4 layer. Using e-beam lithography and double-angle shadow mask evaporation, we subsequently fabricated the top capacitor plates along with a micron sized $\text{Al}/\text{Al}_2\text{O}_3/\text{Al}$ tunnel junction. The critical current of the junction was in the range $I_0 = 1 - 2 \mu\text{A}$. By varying both the dielectric layer thickness and the pad area, the capacitance C was varied between 16 and 40 pF.

The junction + capacitor chip is placed on a microwave circuit-board and is wire-bonded to the end of a coplanar stripline which is soldered to a coaxial launcher affixed to the side wall of the copper sample box. We anchor the RF leak-tight sample box to the cold stage of a ^3He refrigerator with base temperature $T = 280 \text{ mK}$. The measurement setup is schematically shown in Fig. 3. Microwave excitation signals are coupled to the sample via the -13 dB side port of a directional coupler. The reflected microwave signal passes through the direct port of the coupler, and is amplified first using a cryogenic 1.20–1.85 GHz HEMT amplifier with noise temperature $T_N = 4 \text{ K}$. A DC bias current can be applied to the junction by way of a bias tee. We use cryogenic attenuators, isolators, and specially developed dissipative microstrip filters on the microwave lines in addition to copper-powder and other passive filters [6] on the DC lines to shield the junction from spurious electromagnetic noise. In the first set of experiments which probe the plasma resonance, a vector network analyzer was used to both source a CW microwave signal and to analyze the reflected power [14]. The dynamics of the transition between the two oscillation states was then probed using microwave pulses [15], generated by the amplitude modulation of a CW source with a phase-locked arbitrary waveform generator with 1 ns resolution. For the pulsed experiments, the reflected signal was mixed down to 100 MHz and digitally demodulated using a 2 GS/s digitizer to extract the signal phase ϕ .

4. Results

We first probed the drive current dependence of the reflected signal phase $\phi(i_{RF})$ by applying a $4 \mu\text{s}$ long symmetric triangular shaped pulse with a peak value $0.185 I_0$. The demodulated reflected signal was divided into 20 ns sections, each yielding one measurement of ϕ for a corresponding value of i_{RF} . The measurement was repeated 6×10^5 times to obtain a distribution of $\phi(i_{RF})$. In Fig. 4, the mode of the distribution is plotted as a function of i_{RF}/I_0 . For $i_{RF}/I_0 < 0.125$, the bifurcation amplifier is always in state 0, ϕ is constant and assigned a value of 0 deg. As the drive current is increased above $i_{RF}/I_0 = 0.125$, thermal fluctuations are sufficiently large to cause transitions

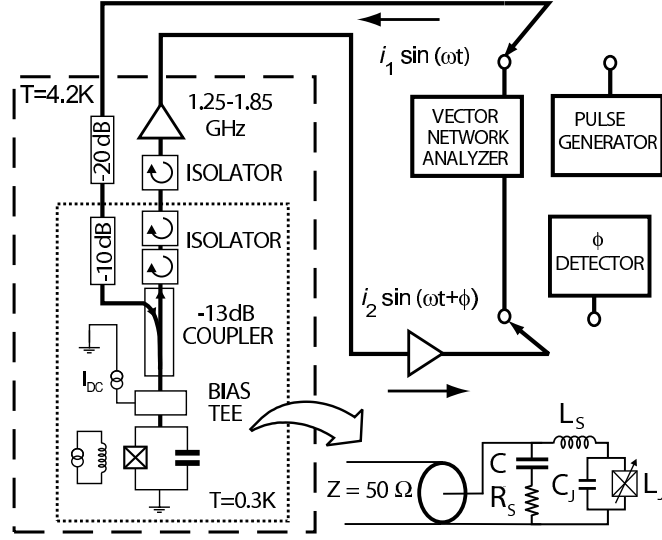


Figure 3. Schematic of the measurement setup. Thick lines correspond to $50\ \Omega$ coaxial transmission lines. The network analyzer is used for CW measurements. For probing the dynamics, the sample is switched to the pulse generator and phase detector. A lumped element model for the junction chip and measurement line is shown in the lower right. The two ideal current sources actually represent external sources.

to the 1 state. In the region between the two dashed lines at $i_{RF}/I_0 = 0.125$ and $i_{RF}/I_0 = 0.160$, ϕ displays a bimodal distribution with peaks centered at 0 and 74 deg with the latter corresponding to the amplifier in the 1 state. The dotted line in Fig. 4 is the average reflected signal phase $\langle\phi\rangle$. When i_{RF}/I_0 is increased above 0.160, the system is only found in state 1. In the decreasing part of the i_{RF} ramp, the system does not start to switch back to state 0 until $i_{RF}/I_0 = 0.065$. The critical switching currents I_B for the $0 \rightarrow 1$ transition and $I_{\bar{B}}$ for the $1 \rightarrow 0$ transition, calculated from numerical simulations to treat the inductance of wire bonds, are denoted with ticks in Fig. 4, and are in good agreement with experiment. The hysteresis $I_{\bar{B}} < I_B$ is a consequence of the asymmetry in the escape barrier height for the two states. Thus, the $0 \rightarrow 1$ transition at $i_{RF} = I_B$ is nearly irreversible, allowing the bifurcation amplifier to latch and store its output during the integration time set by the sensitivity of the follower amplifier.

To determine the sensitivity of the bifurcation amplifier, we have characterized in detail the switching in the vicinity of the $0 \rightarrow 1$ transition. We excited the system with two different readout pulse protocols. In the first protocol, the drive current was ramped from 0 to its maximum value in 40 ns and was then held constant for 40 ns before returning to 0. Only the final 20 ns of the constant drive period were used to determine the oscillation phase with the first

20 ns allotted for settling of the phase. Histograms taken with a 10 MHz acquisition rate are shown in Fig. 5. In the upper panel, the two peaks corresponding to states 0 and 1 can easily be resolved with a small relative overlap of 10^{-2} . The width of each peak is consistent with the noise temperature of our HEMT amplifier. In this first method, the latching property of the system has not been exploited. In our second protocol for the readout pulse, we again ramp for 40 ns and allow a settling time of 20 ns, but we then reduce the drive current by 20% and measure the reflected signal for 300 ns. In that latter period, whatever state was reached at the end of the initial 60 ns period is "latched" and time is spent just increasing the signal/noise ratio of the reflected phase measurement. As shown in the lower panel of Fig. 5, the two peaks are now fully separated, with a relative overlap of 6×10^{-5} allowing a determination of the state 1 probability with an accuracy better than 10^{-3} . This second protocol would be preferred only for very precise time-resolved measurements of I_0 or for applications where a low-noise follower amplifier is impractical.

A third experiment was performed to study the state 1 switching probability $P_{01}(i_{RF})$ for different values of the temperature T and I_0 , the latter being varied with a magnetic field applied parallel to the junction plane. Using the

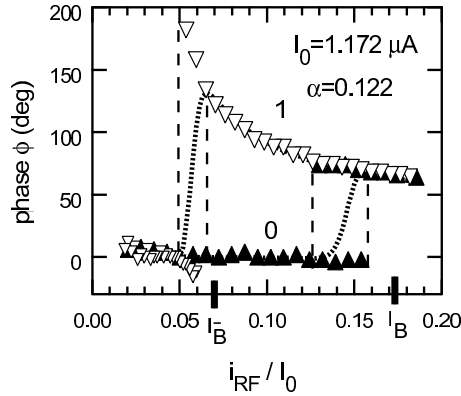


Figure 4. Hysteretic variation of the reflected signal phase ϕ with drive current i_{RF}/I_0 . Symbols denote the mode of ϕ , with up and down triangles corresponding to increasing and decreasing $i_{RF} = I_B$, respectively. The dotted line is $\langle \phi \rangle$. The calculated bifurcation points, $I_{\bar{B}}$ and I_B , are marked on the horizontal axis. The 0 and 1 phase states are reminiscent of the superconducting and dissipative states of the DC current biased junction.

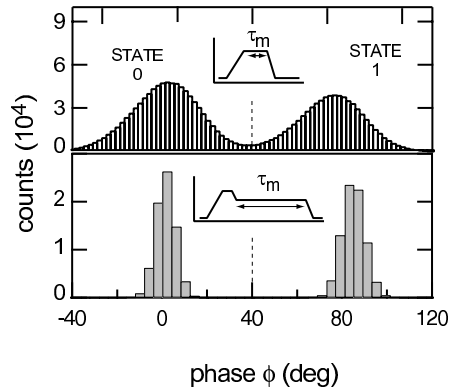


Figure 5. Histograms of the reflected signal phase ϕ at $i_{RF}/I_0 = 0.145$. The upper histogram contains 1.6×10^6 counts with a measurement time $\tau_m = 20$ ns. The lower panel, taken with the latching technique, has 1.5×10^5 counts with a measurement time $\tau_m = 300$ ns. Data here has been taken under the same operating conditions as in Fig 4. The dashed line represents the discrimination threshold between the 0 and 1 state.

first readout protocol and the discrimination threshold shown in Fig. 5, we obtain the switching probability curves shown in Fig. 6. Defining the discrimination power d as the maximum difference between two switching probability curves which differ in I_0 we find that at $T = 280$ mK, $d = 57\%$ for $\Delta I_0/I_0 = 1\%$ – the typical variation observed in a superconducting charge-phase qubit [16]. The switching probability curves should shift according to $(\Delta I_B/I_B)/(\Delta I_0/I_0) = 3/(4\alpha) - 1/2 + O(1/(\alpha Q)^2)$, which for our case takes the value 5.6. In Fig. 6, the curves are shifted by 6%, which agrees well with this prediction. For the case of the DC current biased junction, similar curves would shift only by 1% since the switching current is I_0 itself. Comparable discrimination power using DC switching has only been achieved in these devices at $T \leq 60$ mK. As the temperature is increased, the switching probability curves broaden due to increased thermal fluctuations and the discriminating power decreases: at $T = 480$ mK, $d = 49\%$.

Finally, we determined the escape rate $\Gamma_{01}(i_{RF}, I_0, T)$ as a function of i_{RF} by measuring the time dependence of the switching probability, using a method previously applied to the determination of the static switching rates to the voltage state [17]. After the initial ramp (40 ns) and settling period (20 ns), the reflected signal phase was extracted every 20 ns for a duration of 1 μ s. By repeating this measurement, we generated switching probability histograms which we analyzed as $P_{01}(t) = 1 - \exp(-\Gamma_{01} \cdot t)$. To obtain the escape rate at different temperatures, two different techniques were used. In the first method, we varied the temperature of the cryostat and used a magnetic field to keep the critical current constant at $I_0 = 1.12 \mu$ A. In the second method, I_0 was kept fixed at 1.17 μ A, and a 1 – 2 GHz white noise source irradiating the junction was used to increase the effective temperature. In Fig. 7 we show the drive current dependence of the escape rate as $(\ln(2\pi\omega_a/\Gamma_{01}))^{2/3}$ plotted versus i_{RF}^2 for two different sample temperatures. Data in this format should fall on a straight line with a slope $s(T)$ proportional to $(u_{dyn}/k_B T)^{2/3}$. A trace taken at $T = 500$ mK is also shown in Fig 7.

In parallel with these dynamical switching measurements, we ran static switching measurements to obtain an escape temperature T_{st}^{esc} . Due to insufficient filtering in our RF amplifier line outside the measurement band, T_{st}^{esc} exceeded T by 60 mK. Using u_{dyn}^{calc} and $s(T)$ we can cast the results of the dynamical switching measurements into a dynamical escape temperature $T_{dyn}^{esc} = u_{dyn}^{calc}/k_B s(T)^{3/2}$. We plot T_{dyn}^{esc} versus T_{st}^{esc} in the inset of Fig. 7. The agreement is very good, and only deviations at the highest temperatures are observed. Analyzing the dynamical switching data with T_{st}^{esc} in place of T , we extract a value of $u_{dyn} = 10.7$ K from the $T = 280$ mK data with $I_0 = 1.17 \mu$ A while the calculated value keeping higher order terms in $1/\alpha Q$ is $u_{dyn}^{calc} = 11.0$ K.

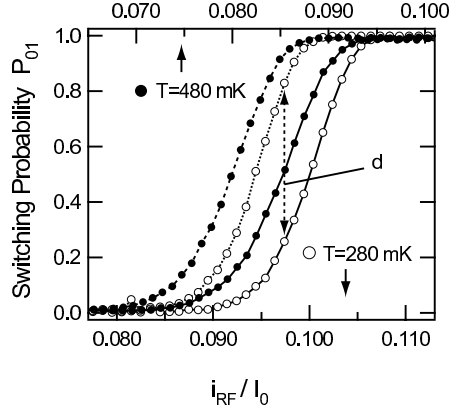


Figure 6. Switching probability curves at $T = 280$ mK and $T = 480$ mK as a function of the drive current i_{RF} . The discrimination power d is the maximum difference between two curves at the same temperature which differ by approximately 1% in I_0 .

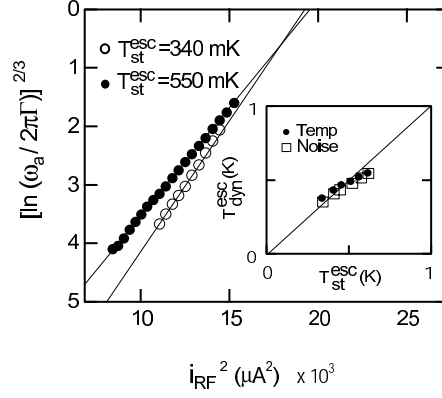


Figure 7. Escape rate as a function of drive power for two different operating temperatures with $I_0 = 1.12 \mu\text{A}$. The inset shows the relationship between dynamic and static escape temperatures when varying either the sample temperature or the injected noise power.

5. Conclusion

With the JBA operating at $T_{st}^{esc} = 340$ mK, it is possible to resolve with a signal/noise ratio of 1 a 10 nA variation in I_0 in a total time ≤ 80 ns, corresponding to a critical current sensitivity of $S_{I_0}^{1/2} = 3.3 \times 10^{-6} \text{ A} \cdot \text{Hz}^{-1/2}$. This value is in agreement with the prediction from the analytical theory $S_{I_0}^{1/2} = \eta(i_{RF}/I_0, \alpha) (k_B T / \varphi_0) \cdot \tau_m^{1/2}$, where $\eta \approx 1.4$ near the bifurcation point and $\varphi_0 = \hbar/2e$. The advantage of the bifurcation amplifier over SQUIDs [18] resides in its extremely low back-action. Since there is no on-chip dissipation, the only source of back-action is the matched isolator load, which is efficiently thermalized at $T = 280$ mK. An important point is that in the JBA, only fluctuations from the load that occur in a narrow band centered about the plasma frequency contribute to the back-action, whereas in the SQUID noise from many high frequency bands is also significant. Finally, the bifurcation amplifier does not suffer from quasiparticle generation associated with hysteretic SQUIDs [2] and DC current-biased junctions [3] which switch into the voltage state. Long quasiparticle recombination times at low temperatures limit the acquisition rate of these devices while the recombination process itself produces excess noise for adjacent circuitry [19].

In conclusion, the JBA is competitive with the SQUID for applications where low back-action is required. Its speed, suppression of on-chip dissi-

pation, and latching make it ideal for the readout of superconducting qubits. At temperatures such that $T_{dyn}^{esc} \leq 60$ mK, the discrimination power would be greater than 95%, hence permitting stringent tests of Quantum Mechanics, like the violation of Bell's inequalities.

Acknowledgments

We would like to thank D. Prober, E. Boaknin, M. Dykman, L. Grober, D. Esteve, D. Vion, S. Girvin and R. Schoelkopf for discussions and assistance. This work was supported by the ARDA (ARO Grant DAAD19-02-1-0044), the NSF (Grant ITR DMR-0325580, DMR-0072022), and the Keck foundation.

References

- [1] B. Josephson, Rev. Mod. Phys. 36, 216 (1964).
- [2] I. Chiorescu, Y. Nakamura, C.J.P.M. Harmans, and J.E. Mooij, Science 299, 5614 (2003).
- [3] A. Cottet, D. Vion, A. Aassime, P. Joyez, D. Esteve, and M.H. Devoret, Physica C 367, 197 (2002).
- [4] M.I. Dykman and M.A. Krivoglaz, Physica A 104, 480 (1980).
- [5] M.H. Devoret, D. Esteve, J.M. Martinis, A. Cleland, and J. Clarke, Phys. Rev. B 36, 58 (1987).
- [6] J.M. Martinis, M.H. Devoret, and J. Clarke, Phys. Rev. B 35, 4682 (1987).
- [7] B. Yurke, L.R. Corruccini, P.G. Kaminsky, L.W. Rupp, A.D. Smith, A.H. Silver, R.W. Simon, and E.A. Whittaker, Phys. Rev. A 39, 2519 (1989).
- [8] T. Holst and J. Bindslev Hansen, Physica B 165-166, 1649 (1990).
- [9] L.D. Landau and E.M. Lifshitz, Mechanics (Reed, Oxford, 1981).
- [10] T.A. Fulton and L.N. Dunkleberger, Phys. Rev. B 9, 4760 (1974).
- [11] R.L. Kautz, Phys. Rev. A 38, 2066 (1988).
- [12] M.I. Dykman and M.A. Krivoglaz, JETP 50, 30 (1980).
- [13] A.P. Dmitriev, M.I. D'yakonov, and A.F. Ioffe, JETP 63, 838 (1986).
- [14] I. Siddiqi, R. Vijay, F. Pierre, C.M. Wilson, L. Frunzio, M. Metcalfe, C. Rigetti, R.J. Schoelkopf, M.H. Devoret, D. Vion, and D.E. Esteve, arXiv:cond-mat/0312553 v1 21 Dec 2003.
- [15] I. Siddiqi, R. Vijay, F. Pierre, C.M. Wilson, M. Metcalfe, C. Rigetti, L. Frunzio, and M.H. Devoret, arXiv:cond-mat/0312623 v1 23 Dec 2003.
- [16] D. Vion, A. Aassime, A. Cottet, P. Joyez, H. Pothier, C. Urbina, D. Esteve, and M. Devoret, Science 296, 886 (2002).
- [17] C. Urbina, D. Esteve, J.M. Martinis, E. Turlot, M.H. Devoret, H. Grabert, and S. Linkwitz, Physica B 169, 26 (1991).
- [18] M. Muck, J.B. Kycia, and J. Clarke, Appl. Phys. Lett. 78, 967 (2001).
- [19] J. Mannik and J.E. Lukens, arXiv:cond-mat/0305190 v2 6 Nov 2003.

7. Reprints of experimental and theoretical results on the Circuit QED architecture

This Chapter contains reprints of published works. Be aware that in these articles the definition of $E_C = e^2/2C_\Sigma$ and $N_g = C_g U_g/e$ are different from those used in the body of this work.

[WSB04] presents experimental results obtained using the circuit QED architecture, introduced in section 5.4. We have achieved with this circuit a regime, called the strong coupling regime, in which the coupling between the CPB qubit and the quantized electromagnetic field in the resonator happens with an energy exchange rate much larger than the decoherence rate generated by coupling to external degrees of freedom. This regime is not easily accessible in atomic physics.

The properties of this coupled system are determined by measuring the transmission amplitude and phase of a microwave probe beam transmitted through the resonator versus probe frequency.

Measurements of the phase of the transmitted probe signal versus the bias voltage and bias flux show the response periodicity, respectively $2e$ and Φ_0 , and allow to estimate for our circuit $E_J=8.0$ GHz and $E_c=20.8$ GHz.

After preparing both the resonator and the qubit in their ground states, the resonator transmission is measured with a large detuning Δ . The probe beam populates the high intrinsic Q resonator with about one photon and the resonance at $\nu_r=6.045$ GHz has a broadening $Q_{\text{tot}}=7.3 \times 10^3$, which shows that the total quality factor of the resonator is limited by the coupling load.

When the probe beam is in resonance with the qubit transition frequency, $\Delta=0$, two clearly well resolved spectral lines have been observed separated by $\nu_{Rabi}=11.6$ MHz. This means that the coupling constant between qubit and resonator is $2g/2\pi=5.8$ MHz, while the photon decay rate is $\kappa/2\pi=0.8$ MHz and the qubit depolarization rate is $\gamma/2\pi=0.7$ MHz. Indeed, the system is in the strong coupling regime.

The resonator transmission has been measured changing probe frequency, but keeping the beam in resonance with the qubit via flux bias changes, and voltage bias around the

“sweet” spot. The system spectroscopy obtained shows avoided crossings between the single photon resonator state and the qubit excited state.

Detailed measurements of the a.c. Stark effect have been presented in [SWB05]. In this work, the application of a second spectroscopy tone to the resonator allows to map the transition angular frequency between the energy levels of the qubit, ω_{01} , in function of the spectroscopy tone frequency, ν_s , and the gate bias voltage. The experiment was carried on a CPB with $E_J=6.2$ GHz and $E_c=19.2$ GHz immersed in a resonator with $\nu_r=6.045$ GHz.

Photon shot noise in the spectroscopy field induces qubit level fluctuations leading to dephasing, which represents the backaction of the measurement on the qubit. From the broadening of the phase response at resonance a $T_2 \approx 200$ ns has been measured for a qubit transition frequency $\nu_{01}=6.15$ GHz, which implies $Q_2=7.7 \times 10^3$.

In [WSB05] time-domain control of the qubit state has been demonstrated. A series of experiments is performed in which the qubit state is manipulated by a spectroscopy tone in resonance with the qubit transition frequency, $\nu_{01}=4.3$ GHz, while the phase and the amplitude of the transmission through the cavity of a coherent microwave beam at the resonator resonant frequency is continuously monitored.

In performing Rabi-like experiments, the phase of the transmitted beam is measured versus time for a fixed time length of the Rabi pulse with a contrast, ratio of measured value to maximum value, of about 85%. The extracted level population oscillations have shown a visibility, defined as the maximum observed qubit population difference of about 95%, approaching unity. have been observed with a depolarization time $T_1=7.3$ μ s, which implies $Q_1=2.0 \times 10^5$.

For that set-up the fidelity of a single shot measurement of the qubit state integrated over the depolarization time is about 30% and is limited by the noise temperature of the low-temperature amplifier and by the small signal power.

In Ramsey fringe experiments at charge degeneracy, population oscillations have been observed at the detuning frequency $\nu_{01}-\nu_s=6$ MHz, which decay with $T_2=0.5$ μ s, which implies $Q_2=1.4 \times 10^4$, which is similar to the best values obtained in the Quantronium architecture.

[FWS05] presents design considerations for devices for circuit QED and details of the fabrication procedure for both the resonators and the CPB, together with a preliminary RF-characterization of the superconducting transmission line resonators versus temperature and magnetic field. A more complete treatment of the fabrication of this circuit is in Chapter 8.

coupled system by applying pulses of varying length. In Fig. 3b, Rabi oscillations are shown for the $|00\rangle$ to $|11\rangle$ transition. When the microwave frequency is detuned from resonance, the Rabi oscillations are accelerated (bottom four curves, to be compared with the fifth curve). After a π pulse which prepares the system in the $|10\rangle$ state, these oscillations are suppressed (second curve in Fig. 3b). After a 2π pulse they are revived (first curve in Fig. 3b). In the case of Fig. 3c, the qubit is first excited onto the $|10\rangle$ state by a π pulse, and a second pulse in resonance with the red sideband transition drives the system between the $|10\rangle$ and $|01\rangle$ states. The Rabi frequency depends linearly on the microwave amplitude, with a smaller slope compared to the bare qubit driving. During the time evolution of the coupled Rabi oscillations shown in Fig. 3b and c, the qubit and the oscillator experience a time-dependent entanglement, although the present data do not permit us to quantify it to a sufficient degree of confidence.

The sideband Rabi oscillations of Fig. 3 show a short coherence time (~ 3 ns), which we attribute mostly to the oscillator relaxation. To determine its relaxation time, we performed the following experiment. First, we excite the oscillator with a resonant low power microwave pulse. After a variable delay Δt , during which the oscillator relaxes towards $n = 0$, we start recording Rabi oscillations on the red sideband transition (see Fig. 4a for $\Delta t = 1$ ns). The decay of the oscillation amplitude as a function of Δt corresponds to an oscillator relaxation time of ~ 6 ns (Fig. 4b), consistent with a quality factor of 100–150 estimated from the width of the ν_p resonance. The exponential fit (continuous line in Fig. 4b) shows an offset of $\sim 4\%$ due to thermal effects. To estimate the higher bound of the sample temperature, we consider that the visibility of the oscillations presented here (Figs 2–4) is set by the detection efficiency and not by the state preparation. When related to the maximum signal of the qubit Rabi oscillations of $\sim 40\%$, the 4%-offset corresponds to $\sim 10\%$ thermal occupation of oscillator excited states (an effective temperature of ~ 60 mK). Consistently, we also observe low-amplitude red sideband oscillations without preliminary microwave excitation of the oscillator.

We have demonstrated coherent dynamics of a coupled superconducting two-level plus harmonic oscillator system, implying that the two subsystems are entangled. Increasing the coupling strength and the oscillator relaxation time should allow us to quantify the entanglement, as well as to study non-classical states of the oscillator. Our results provide strong indications that solid-state quantum devices could in future be used as elements for the manipulation of quantum information. \square

Received 25 May; accepted 5 July 2004; doi:10.1038/nature02831.

1. Nielsen, M. A. & Chuang, I. L. *Quantum Computation and Quantum Information* (Cambridge Univ. Press, Cambridge, 2000).
2. Nakamura, Y. *et al.* Coherent control of macroscopic quantum states in a single-Cooper-pair box. *Nature* **398**, 786–788 (1999).
3. Vion, D. *et al.* Manipulating the quantum state of an electrical circuit. *Science* **296**, 886–889 (2002).
4. Yu, Y., Han, S., Chu, X., Chu, S. & Wang, Z. Coherent temporal oscillations of macroscopic quantum states in a Josephson junction. *Science* **296**, 889–892 (2002).
5. Martinis, J. M., Nam, S., Aumentado, J. & Urbina, C. Rabi oscillations in a large Josephson-junction qubit. *Phys. Rev. Lett.* **89**, 117901 (2002).
6. Chiorescu, I., Nakamura, Y., Harmans, C. J. P. M. & Mooij, J. E. Coherent quantum dynamics of a superconducting flux qubit. *Science* **299**, 1869–1871 (2003).
7. Pashkin, Yu. A. *et al.* Quantum oscillations in two coupled charge qubits. *Nature* **421**, 823–826 (2003).
8. Berkley, A. J. *et al.* Entangled macroscopic quantum states in two superconducting qubits. *Science* **300**, 1548–1550 (2003).
9. Majer, J. B., Pavauw, F. G., ter Haar, A. C. J., Harmans, C. J. P. M. & Mooij, J. E. Spectroscopy on two coupled flux qubits. Preprint at (<http://arxiv.org/abs/cond-mat/0308192>) (2003).
10. Izmalkov, A. *et al.* Experimental evidence for entangled states formation in a system of two coupled flux qubits. Preprint at (<http://arxiv.org/abs/cond-mat/0312332>) (2003).
11. Yamamoto, T., Pashkin, Yu. A., Astafiev, O., Nakamura, Y. & Tsai, J. S. Demonstration of conditional gate operation using superconducting charge qubits. *Nature* **425**, 941–944 (2003).
12. Leibfried, D., Blatt, R., Monroe, C. & Wineland, D. Quantum dynamics of single trapped ions. *Rev. Mod. Phys.* **75**, 281–324 (2003).
13. Mandel, O. *et al.* Controlled collisions for multi-particle entanglement of optically trapped atoms. *Nature* **425**, 937–940 (2003).
14. Raimond, J. M., Brune, M. & Haroche, S. Manipulating quantum entanglement with atoms and photons in a cavity. *Rev. Mod. Phys.* **73**, 565–582 (2001).

15. Mooij, J. E. *et al.* Josephson persistent-current qubit. *Science* **285**, 1036–1039 (1999).
16. van der Wal, C. H. *et al.* Quantum superposition of macroscopic persistent-current states. *Science* **290**, 773–777 (2000).
17. Burkard, G. *et al.* Asymmetry and decoherence in double-layer persistent-current qubit. Preprint at (<http://arxiv.org/abs/cond-mat/0405273>) (2004).
18. Goorden, M. C., Thorwart, M. & Grifoni, M. Entanglement spectroscopy of a driven solid-state qubit and its detector. Preprint at (<http://arxiv.org/abs/cond-mat/0405220>) (2004).
19. Tinkham, M. *Introduction to Superconductivity* 2nd edn (McGraw-Hill, New York, 1996).
20. Cohen-Tannoudji, C., Dupont-Roc, J. & Grynberg, G. *Atom-photon Interactions: Basic Processes and Applications* Ch. II E (Wiley & Sons, New York, 1992).

Acknowledgements We thank A. Blais, G. Burkard, D. DiVincenzo, G. Falci, M. Grifoni, S. Lloyd, S. Miyashita, T. Orlando, R. N. Schouten, L. Vandersypen and F. K. Wilhelm for discussions. This work was supported by the Dutch Foundation for Fundamental Research on Matter (FOM), the EU Marie Curie and SQUBIT grants, and the US Army Research Office.

Competing interests statement The authors declare that they have no competing financial interests.

Correspondence and requests for materials should be addressed to I.C. (chiorescu@pa.msu.edu) and J.E.M. (mooij@qt.tn.tudelft.nl).

Strong coupling of a single photon to a superconducting qubit using circuit quantum electrodynamics

A. Wallraff¹, D. I. Schuster¹, A. Blais¹, L. Frunzio¹, R.-S. Huang^{1,2}, J. Majer¹, S. Kumar¹, S. M. Girvin¹ & R. J. Schoelkopf¹

¹Departments of Applied Physics and Physics, Yale University, New Haven, Connecticut 06520, USA

²Department of Physics, Indiana University, Bloomington, Indiana 47405, USA

The interaction of matter and light is one of the fundamental processes occurring in nature, and its most elementary form is realized when a single atom interacts with a single photon. Reaching this regime has been a major focus of research in atomic physics and quantum optics¹ for several decades and has generated the field of cavity quantum electrodynamics^{2,3}. Here we perform an experiment in which a superconducting two-level system, playing the role of an artificial atom, is coupled to an on-chip cavity consisting of a superconducting transmission line resonator. We show that the strong coupling regime can be attained in a solid-state system, and we experimentally observe the coherent interaction of a superconducting two-level system with a single microwave photon. The concept of circuit quantum electrodynamics opens many new possibilities for studying the strong interaction of light and matter. This system can also be exploited for quantum information processing and quantum communication and may lead to new approaches for single photon generation and detection.

In atomic cavity quantum electrodynamics (QED), an isolated atom with electric dipole moment d interacts with the vacuum state electric field E_0 of a cavity. The quantum nature of the field gives rise to coherent oscillations of a single excitation between the atom and the cavity at the vacuum Rabi frequency $\nu_{\text{Rabi}} = 2dE_0/\hbar$, which can be observed when ν_{Rabi} exceeds the rates of relaxation and decoherence of both the atom and the field. This effect has been observed in the time domain using Rydberg atoms in three-dimensional microwave cavities³ and spectroscopically using alkali atoms in very small optical cavities with large vacuum fields⁴.

Coherent quantum effects have been recently observed in several superconducting circuits^{5–10}, making these systems well suited for use as quantum bits (qubits) for quantum information processing.

Of the various superconducting qubits, the Cooper pair box¹¹ is especially well suited for cavity QED because of its large effective electric dipole moment d , which can be 10^4 times larger than in an alkali atom and ten times larger than a typical Rydberg atom¹². As suggested in our earlier theoretical study¹², the simultaneous combination of this large dipole moment and the large vacuum field strength—due to the small size of the quasi one-dimensional transmission line cavity—in our implementation is ideal for reaching the strong coupling limit of cavity QED in a circuit. Other solid-state analogues of strong coupling cavity QED have been envisaged in superconducting^{13–20}, semiconducting^{21,22}, and even micro-mechanical systems²³. First steps towards realizing such a regime have been made for semiconductors^{21,24,25}. To our knowledge, our experiments constitute the first experimental observation of strong coupling cavity QED with a single artificial atom and a single photon in a solid-state system.

The on-chip cavity is made by patterning a thin superconducting film deposited on a silicon chip. The quasi-one-dimensional coplanar waveguide resonator²⁶ consists of a narrow centre conductor of length l and two nearby lateral ground planes, see Fig. 1a. Close to its full-wave ($l = \lambda$) resonance frequency, $\omega_r = 2\pi\nu_r = 1/\sqrt{LC} = 2\pi \cdot 6.044$ GHz, where ν_r is the bare resonance frequency, the resonator can be modelled as a parallel combination of a capacitor C and an inductor L (the internal losses are negligible). This simple resonant circuit behaves as a harmonic oscillator described by the hamiltonian $H_r = \hbar\omega_r(a^\dagger a + 1/2)$, where $\langle a^\dagger a \rangle = \langle \hat{n} \rangle = n$ is the average photon number. At our operating temperature of $T < 100$ mK, much less than $\hbar\omega_r/k_B \approx 300$ mK, the resonator is nearly in its ground state, with a thermal occupancy $n < 0.06$. The vacuum fluctuations of the resonator give rise to a root mean square (r.m.s.) voltage $V_{\text{rms}} = \sqrt{\hbar\omega_r/2C} \approx 1 \mu\text{V}$ on its centre conductor,

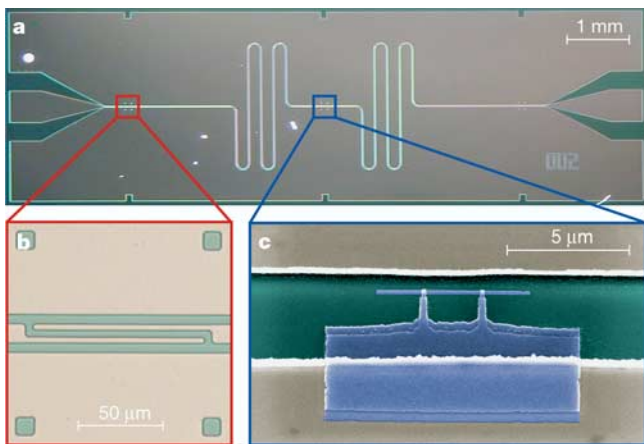


Figure 1 Integrated circuit for cavity QED. **a**, The superconducting niobium coplanar waveguide resonator is fabricated on an oxidized $10 \times 3 \text{ mm}^2$ silicon chip using optical lithography. The width of the centre conductor is $10 \mu\text{m}$ separated from the lateral ground planes extending to the edges of the chip by a gap of width $5 \mu\text{m}$ resulting in a wave impedance of the structure of $Z = 50 \Omega$ being optimally matched to conventional microwave components. The length of the meandering resonator is $l = 24 \text{ mm}$. It is coupled by a capacitor at each end of the resonator (see **b**) to an input and output feed line, fanning out to the edge of the chip and keeping the impedance constant. **b**, The capacitive coupling to the input and output lines and hence the coupled quality factor Q is controlled by adjusting the length and separation of the finger capacitors formed in the centre conductor. **c**, False colour electron micrograph of a Cooper pair box (blue) fabricated onto the silicon substrate (green) into the gap between the centre conductor (top) and the ground plane (bottom) of a resonator (beige) using electron beam lithography and double angle evaporation of aluminium. The Josephson tunnel junctions are formed at the overlap between the long thin island parallel to the centre conductor and the fingers extending from the much larger reservoir coupled to the ground plane.

and an electric field between the centre conductor and the ground plane that is a remarkable $E_{\text{rms}} \approx 0.2 \text{ V m}^{-1}$, some hundred times larger than in the three-dimensional cavities used in atomic microwave cavity QED³. The large vacuum field strength results from the extremely small effective mode volume ($\sim 10^{-6}$ cubic wavelengths) of the resonator¹².

The resonator is coupled via two coupling capacitors $C_{\text{in/out}}$, one at each end (see Fig. 1b), to the input and output transmission lines that allow its microwave transmission to be probed (see Fig. 2a–c). The predominant source of dissipation is the loss of photons from the resonator through these ports at a rate $\kappa = \omega_r/Q$, where Q is the (loaded) quality factor of the resonator. The internal (uncoupled) loss of the resonator is negligible ($Q_{\text{int}} \approx 10^6$). Thus, the average photon lifetime in the resonator $T_r = 1/\kappa$ exceeds 100 ns, even for our initial choice of a moderate quality factor $Q \approx 10^4$.

The Cooper pair box (CPB) consists of a several micrometre long and submicrometre wide superconducting island which is coupled via two submicrometre size Josephson tunnel junctions to a much larger superconducting reservoir, and is fabricated in the gap between the centre conductor and the ground plane of the resonator, at an antinode of the field (see Fig. 1c). The CPB is a two-state system described by the hamiltonian¹³ $H_a = -(E_{\text{el}}\sigma_x + E_J\sigma_z)/2$, where $E_{\text{el}} = 4E_C(1 - n_g)$ is the electrostatic energy and $E_J = E_{J,\text{max}}\cos(\pi\Phi_b)$ is the Josephson energy. The overall energy scales of these terms, the charging energy E_C and the Josephson energy $E_{J,\text{max}}$, can be readily engineered during the fabrication by the choice of the total box capacitance and resistance respectively, and then further tuned in situ by electrical means. A gate voltage V_g applied to the input port (see Fig. 2a), induces a gate charge $n_g = V_g C_g^*/e$ that controls E_{el} , where C_g^* is the effective capacitance between the input port of the resonator and the island of the CPB. A flux bias $\Phi_b = \Phi/\Phi_0$, applied with an external coil to the loop of the box, controls E_J . Denoting the ground state of the box as $|\downarrow\rangle$ and the first excited state as $|\uparrow\rangle$ (see Fig. 2d), we have a two-level system whose energy separation $E_a = \hbar\omega_a$ can be widely varied as shown in Fig. 3c. Coherence of the CPB is limited by relaxation from the excited state at a rate γ_1 , and by fluctuations of the level separation giving rise to dephasing at a rate γ_φ , for a total decoherence rate $\gamma = \gamma_1/2 + \gamma_\varphi$ (ref. 13).

The Cooper pair box couples to photons stored in the resonator by an electric dipole interaction, via the coupling capacitance C_g . The vacuum voltage fluctuations V_{rms} on the centre conductor of the resonator change the energy of a Cooper pair on the box island by an amount $\hbar g = dE_0 = eV_{\text{rms}}C_g/C_S$. We have shown¹² that this coupled system is described by the Jaynes–Cummings hamiltonian $H_{\text{JC}} = H_r + H_a + \hbar g(a^\dagger\sigma^- + a\sigma^+)$, where σ^+ (σ^-) creates (annihilates) an excitation in the CPB. It describes the coherent exchange of energy between a quantized electromagnetic field and a quantum two-level system at a rate $g/2\pi$, which is observable if g is much larger than the decoherence rates γ and κ . This strong coupling limit³ $g > [\gamma, \kappa]$ is achieved in our experiments. When the detuning $\Delta = \omega_a - \omega_r$ is equal to zero, the eigenstates of the coupled system are symmetric and antisymmetric superpositions of a single photon and an excitation in the CPB $|\pm\rangle = (|0, \uparrow\rangle \pm |1, \downarrow\rangle)/\sqrt{2}$ with energies $E_\pm = \hbar(\omega_r \pm g)$. Although the cavity and the CPB are entangled in the eigenstates $|\pm\rangle$, their entangled character is not addressed in our current cavity QED experiment which spectroscopically probes the energies E_\pm of the coherently coupled system.

The strong coupling between the field in the resonator and the CPB can be used to perform a quantum nondemolition (QND) measurement of the state of the CPB in the non-resonant (dispersive) limit $|\Delta| \gg g$. Diagonalization of the coupled quantum system leads to the effective hamiltonian¹²:

$$H \approx \hbar \left(\omega_r + \frac{g^2}{\Delta} \sigma_z \right) a^\dagger a + \frac{1}{2} \hbar \left(\omega_a + \frac{g^2}{\Delta} \right) \sigma_z$$

The transition frequency $\omega_r \pm g^2/\Delta$ is now conditioned by the qubit state $\sigma_z = \pm 1$. Thus, by measuring the transition frequency of the resonator, the qubit state can be determined. Similarly, the level separation in the qubit $\hbar(\omega_a + 2a^\dagger a g^2/\Delta + g^2/\Delta)$ depends on the number of photons in the resonator. The term $2a^\dagger a g^2/\Delta$, linear in \hat{n} , is the alternating current (a.c.) Stark shift and g^2/Δ is the Lamb shift. All terms in this hamiltonian, with the exception of the Lamb shift, are clearly identified in the results of our circuit QED experiments.

The properties of this coupled system are determined by probing the resonator spectroscopically¹². The amplitude T and phase ϕ of a microwave probe beam of power P_{RF} transmitted through the resonator are measured versus probe frequency ω_{RF} . A simplified schematic of the microwave circuit is shown in Fig. 2a. In this setup, the CPB acts as an effective capacitance that is dependent on its σ_z eigenstate, the coupling strength g , and detuning Δ . This variable capacitance changes the resonator frequency and its transmission spectrum. The transmission T^2 and phase ϕ of the resonator for a far-detuned qubit ($g^2/\kappa\Delta \ll 1$), that is, when the qubit is effectively decoupled from the resonator, are shown in Fig. 2b and c. In this case, the transmission is a lorentzian of width $\delta\nu_r = \nu_r/Q = \kappa/2\pi$ at ν_r , and the phase ϕ displays a corresponding step of π . The expected transmission at smaller detuning corresponding to a frequency shift $\pm g^2/\Delta = \kappa$ are shown by dashed lines in Fig. 2b and c. Such small shifts in the resonator frequency are sensitively measured as a phase shift $\phi = \pm \tan^{-1}(2g^2/\kappa\Delta)$ of the transmitted microwave at a fixed

probe frequency ω_{RF} using beam powers P_{RF} which controllably populate the resonator with average photon numbers from $n \approx 10^3$ down to the sub-photon level $n \ll 1$. We note that both the resonator and qubit can be controlled and measured using capacitive and inductive coupling only, that is, without attaching any d.c. connections to either system.

Measurements of the phase ϕ versus n_g are shown in Fig. 3b, and two different cases can be identified for a Cooper pair box with Josephson energy $E_{J,max}/\hbar > \nu_r$. In the first case, for bias fluxes such that $E_J(\Phi_b)/\hbar > \nu_r$, the qubit does not come into resonance with the resonator for any value of gate charge n_g (see Fig. 3a). As a result, the measured phase shift ϕ is maximum for the smallest detuning Δ at $n_g = 1$ and gets smaller as Δ increases (see Fig. 3b). Moreover, ϕ is periodic in n_g with a period of $2e$, as expected. In the second case, for values of Φ_b resulting in $E_J(\Phi_b)/\hbar < \nu_r$, the qubit goes through resonance with the resonator at two values of n_g . Thus, the phase shift ϕ is largest as the qubit approaches resonance ($\Delta \rightarrow 0$) at the points indicated by red arrows (see Fig. 3a, b). As the qubit goes through resonance, the phase shift ϕ changes sign when Δ changes sign. This behaviour is in perfect agreement with predictions based on the analysis of the circuit QED hamiltonian in the dispersive regime.

In Fig. 3c the qubit level separation $\nu_a = E_a/\hbar$ is plotted versus the bias parameters n_g and Φ_b . The qubit is in resonance with the resonator at the points $[n_g, \Phi_b]$, indicated by the red curve in one quadrant of the plot. The measured phase shift ϕ is plotted versus

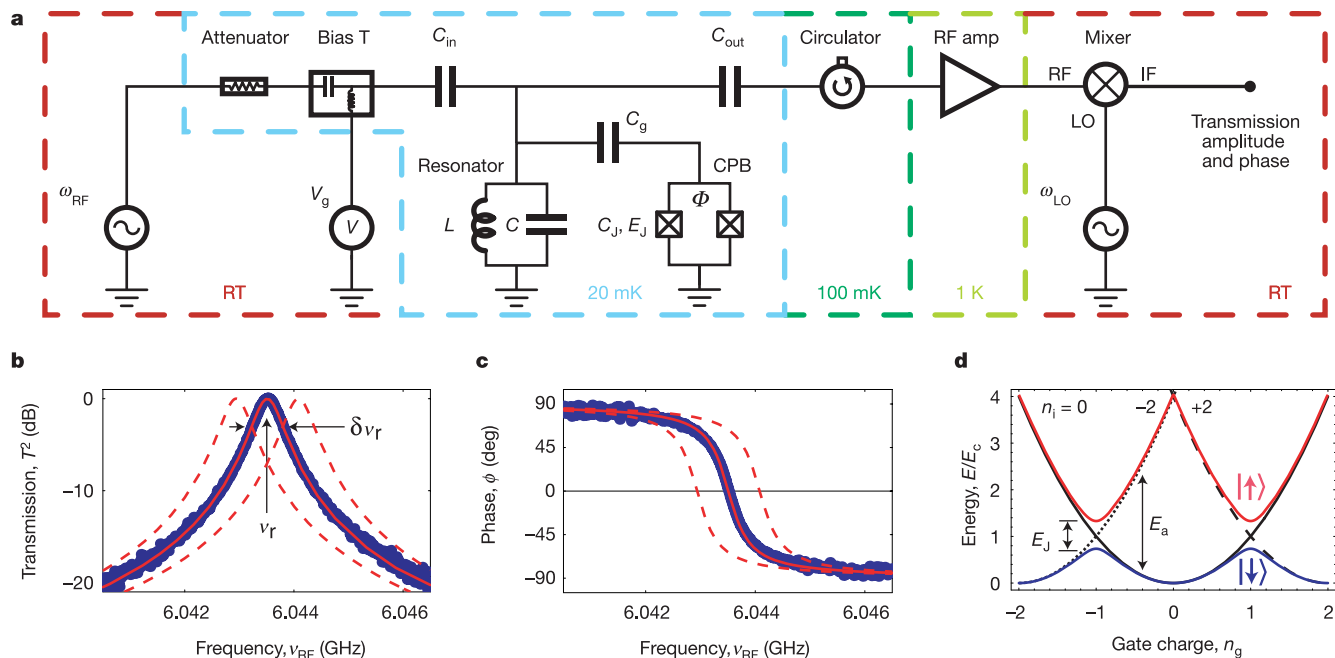


Figure 2 Measurement scheme, resonator and Cooper pair box. **a**, The resonator with effective inductance L and capacitance C coupled through the capacitor C_0 to the Cooper pair box with junction capacitance C_J and Josephson energy E_J forms the circuit QED system which is coupled through $C_{in/out}$ to the input/output ports. The value of E_J is controllable by the magnetic flux Φ . The input microwave at frequency ω_{RF} is added to the gate voltage V_g using a bias-tee. After the transmitted signal at ω_{RF} is amplified using a cryogenic high electron mobility (HEMT) amplifier and mixed with the local oscillator at ω_{LO} , its amplitude and phase are determined. The circulator and the attenuator prevent leakage of thermal radiation into the resonator. The temperature of individual components is indicated. **b**, Measured transmission power spectrum of the resonator (blue dots), the full linewidth $\delta\nu_r$ at half-maximum and the centre frequency ν_r are indicated. The solid red line is a fit to a lorentzian with $Q = \nu_r/\delta\nu_r \approx 10^4$. **c**, Measured transmission phase ϕ (blue dots) with fit (red line). In panels **b** and **c** the dashed lines are theory curves shifted by

$\pm \delta\nu_r$ with respect to the data. **d**, Energy level diagram of a Cooper pair box. The electrostatic energy $E_c(n_i - n_0)^2$, with charging energy $E_c = e^2/2C_\Sigma$, is indicated for $n_i = 0$ (solid black line), -2 (dotted line) and $+2$ (dashed line) excess electrons forming Cooper pairs on the island. C_Σ is the total capacitance of the island given by the sum of the capacitances C_J of the two tunnel junctions, the coupling capacitance C_0 to the centre conductor of the resonator and any stray capacitances. In the absence of Josephson tunnelling the states with n_i and $n_i + 2$ electrons on the island are degenerate at $n_g = 1$. The Josephson coupling mediated by the weak link formed by the tunnel junctions between the superconducting island and the reservoir lifts this degeneracy and opens up a gap proportional to the Josephson energy $E_J = E_{J,max} \cos(\pi\Phi_b)$, where $E_{J,max} = \hbar\Delta_{Al}/8e^2R_J$, with the superconducting gap of aluminium Δ_{Al} and the tunnel junction resistance R_J . A ground-state band $|\downarrow\downarrow\rangle$ and an excited-state band $|\uparrow\uparrow\rangle$ are formed with a gate charge and flux-bias-dependent energy level separation of E_a .

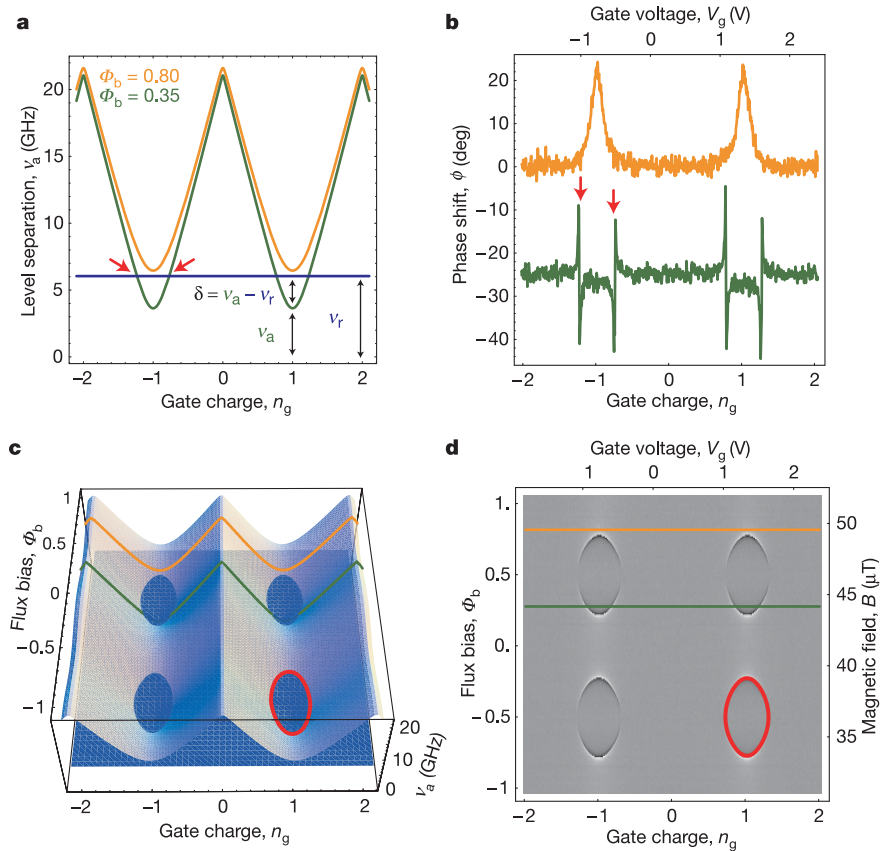


Figure 3 Strong coupling circuit QED in the dispersive regime. **a**, Calculated level separation $\nu_a = \omega_a/2\pi = E_a/h$ between ground $|\downarrow\rangle$ and excited state $|\uparrow\rangle$ of qubit for two values of flux bias $\Phi_b = 0.8$ (orange line) and $\Phi_b = 0.35$ (green line). The resonator frequency $\nu_r = \omega_r/2\pi$ is shown by a blue line. Resonance occurs at $\nu_a = \nu_r$ symmetrically around degeneracy $n_g = \pm 1$; also see red arrows. The detuning $\Delta/2\pi = \delta = \nu_a - \nu_r$ is indicated. **b**, Measured phase shift ϕ of the transmitted microwave for values of Φ_b in **a**. Green curve is offset by -25 deg for visibility. **c**, Calculated qubit level separation ν_a versus bias parameters n_g and Φ_b . The resonator frequency ν_r is indicated by the blue plane. At the intersection, also indicated by the red

curve in the lower right-hand quadrant, resonance between the qubit and the resonator occurs ($\delta = 0$). For qubit states below the resonator plane the detuning is $\delta < 0$, above $\delta > 0$. **d**, Density plot of measured phase shift ϕ versus n_g and Φ_b . Light colours indicate positive ϕ ($\delta > 0$), dark colours negative ϕ ($\delta < 0$). The red line is a fit of the data to the resonance condition $\nu_a = \nu_r$. In **c** and **d**, the line cuts presented in **a** and **b** are indicated by the orange and the green line, respectively. The microwave probe power P_{RF} used to acquire the data is adjusted such that the maximum intra-resonator photon number n at ν_r is about ten for $g^2/\kappa\Delta \ll 1$. The calibration of the photon number has been performed in situ by measuring the a.c.-Stark shift of the qubit levels.

both n_g and Φ_b in Fig. 3d. We observe the expected periodicity in flux bias Φ_b with one flux quantum Φ_0 . The set of parameters $[n_g, \Phi_b]$ for which the resonance condition is met is marked by a sudden sign change in ϕ , which allows a determination of the Josephson energy $E_{J,max} = 8.0 (\pm 0.1)$ GHz and the charging energy $E_C = 5.2 (\pm 0.1)$ GHz.

These data clearly demonstrate that the properties of the qubit can be determined in a transmission measurement of the resonator and that full in situ control over the qubit parameters is achieved. We note that in the dispersive regime this new read-out scheme for the Cooper pair box is most sensitive at charge degeneracy ($n_g = 1$), where the qubit is to first order decoupled from $1/f$ fluctuations in its charge environment, which minimizes dephasing⁶. This property is advantageous for quantum control of the qubit at $n_g = 1$, a point where traditional electrometry, using a single electron transistor (SET) for example²⁷, is unable to distinguish the qubit states. We note that this dispersive QND measurement of the qubit state¹² is the complement of the atomic microwave cavity QED measurement in which the state of the cavity is inferred non-destructively from the phase shift in the state of a beam of atoms sent through the cavity^{3,28}.

Making use of the full control over the qubit hamiltonian, we then tune the flux bias Φ_b so that the qubit is at $n_g = 1$ and in resonance with the resonator. Initially, the resonator and the qubit are cooled into their combined ground state $|0, \downarrow\rangle$; see inset in

Fig. 4b. Owing to the coupling, the first excited states become a doublet $|\pm\rangle$. Similarly to ref. 4, we probe the energy splitting of this doublet spectroscopically using a weak probe beam so that $n \ll 1$. The intra-resonator photon number, n , is calibrated by measuring the a.c.-Stark shift of the qubit in the dispersive case. The resonator transmission T^2 is first measured for large detuning Δ with a probe beam populating the resonator with a maximum of $n \approx 1$ at resonance; see Fig. 4a. From the lorentzian line the photon decay rate of the resonator is determined as $\kappa/2\pi = 0.8$ MHz. The probe beam power is subsequently reduced by 5 dB and the transmission spectrum T^2 is measured in resonance ($\Delta = 0$); see Fig. 4b. We clearly observe two well-resolved spectral lines separated by the vacuum Rabi frequency $\nu_{Rabi} \approx 11.6$ MHz. The individual lines have a width determined by the average of the photon decay rate κ and the qubit decoherence rate γ . The data are in excellent agreement with the transmission spectrum numerically calculated using the given value $\kappa/2\pi = 0.8$ MHz and the single adjustable parameter $\gamma/2\pi = 0.7$ MHz.

The transmission spectrum shown in Fig. 4b is highly sensitive to the photon number in the cavity. The measured transmission spectrum is consistent with the expected thermal photon number of $n \leq 0.06$ ($T < 100$ mK); see red curve in Fig. 4b. Owing to the anharmonicity of the coupled atom-cavity system in the resonant case, an increased thermal photon number would reduce trans-

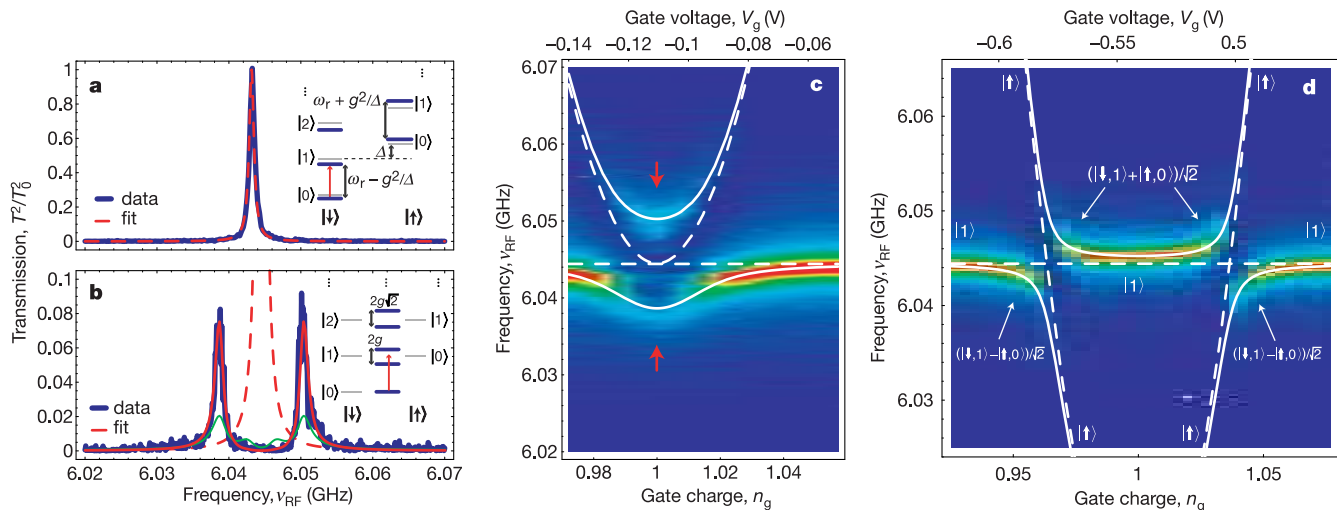


Figure 4 Vacuum Rabi mode splitting. **a**, Measured transmission T^2 (blue line) versus microwave probe frequency ν_{RF} for large detuning ($g^2/\Delta\kappa \ll 1$) and fit to Lorentzian (dashed red line). The peak transmission amplitude is normalized to unity. The inset shows the dispersive dressed states level diagram. **b**, Measured transmission spectrum for the resonant case $\Delta = 0$ at $n_g = 1$ (blue line) showing the vacuum Rabi mode splitting compared to numerically calculated transmission spectra (red and green lines) for thermal photon numbers of $n = 0.06$ and 0.5 , respectively. The dashed red line is the calculated transmission for $g = 0$ and $\kappa/2\pi = 0.8$ MHz. The inset shows the resonant dressed

states level diagram. **c**, Resonator transmission amplitude T plotted versus probe frequency ν_{RF} and gate charge n_g for $\Delta = 0$ at $n_g = 1$. Blue colour corresponds to small T , red colour to large T . Dashed lines are uncoupled qubit level separation ν_a and resonator resonance frequency ν_r . Solid lines are level separations found from exact diagonalization of H_{JC} . Spectrum shown in **b** corresponds to line cut along red arrows. **d**, As in **c**, but for $E_J/h < \nu_r$. The dominant character of the corresponding eigenstates is indicated.

mission and give rise to additional peaks in the spectrum owing to transitions between higher excited doublets³⁰. The transmission spectrum calculated for a thermal photon number of $n = 0.5$ (see green curve in Fig. 4b) is clearly incompatible with our experimental data, indicating that the coupled system has in fact cooled to near its ground state, and that we measure the coupling of a single qubit to a single photon. The nonlinearity of the cavity QED system is also observed at higher probe beam powers, as transitions are driven between states higher up the dressed state ladders (not shown).

We also observe the anti-crossing between the single photon resonator state and the first excited qubit state by tuning the qubit into and out of resonance with a gate charge near $n_g = 1$ and measuring the transmission spectrum (see Fig. 4c). The vacuum Rabi peaks evolve from a state with equal weight in the photon and qubit at $n_g = 1$ (as shown in Fig. 4b) to predominantly photon states for $n_g \gg 1$ or $n_g \ll 1$. The observed peak positions agree well with calculations considering the qubit with level separation ν_a , a single photon in the resonator with frequency ν_r and a coupling strength of $g/2\pi$; see solid lines in Fig. 4c. For a different value of flux bias Φ_b such that $E_a/h < \nu_r$ at $n_g = 1$, two anti-crossings are observed (see Fig. 4d) again in agreement with theory.

The observation of the vacuum Rabi mode splitting and the corresponding avoided crossings demonstrates that the strong coupling limit of cavity QED has been achieved, and that coherent superpositions of a single qubit and a single photon can be generated on a superconducting chip. This opens up many new possibilities for quantum optical experiments with circuits. Possible applications include using the cavity as a quantum bus to couple widely separated qubits in a quantum computer, or as a quantum memory to store quantum information, or even as a generator and detector of single microwave photons for quantum communication. □

Received 11 June; accepted 12 July 2004; doi:10.1038/nature02851.

1. Walls, D. & Milburn, G. *Quantum Optics* (Springer, Berlin, 1994).
2. Mabuchi, H. & Doherty, A. Cavity quantum electrodynamics: Coherence in context. *Science* **298**, 1372–1377 (2002).
3. Raimond, J., Brune, M. & Haroche, S. Manipulating quantum entanglement with atoms and photons in a cavity. *Rev. Mod. Phys.* **73**, 565–582 (2001).

4. Thompson, R. J., Rempe, G. & Kimble, H. J. Observation of normal-mode splitting for an atom in an optical cavity. *Phys. Rev. Lett.* **68**, 1132–1135 (1992).
5. Nakamura, Y., Pashkin, Y. A. & Tsai, J. S. Coherent control of macroscopic quantum states in a single-Cooper-pair box. *Nature* **398**, 786–788 (1999).
6. Vion, D. *et al.* Manipulating the quantum state of an electrical circuit. *Science* **296**, 886–889 (2002).
7. Martinis, J. M., Nam, S., Aumentado, J. & Urbina, C. Rabi oscillations in a large Josephson-junction qubit. *Phys. Rev. Lett.* **89**, 117901 (2002).
8. Chiorescu, I., Nakamura, Y., Harmans, C. J. P. M. & Mooij, J. E. Coherent quantum dynamics of a superconducting flux qubit. *Science* **299**, 1869–1871 (2003).
9. Yamamoto, T., Pashkin, Y. A., Astafiev, O., Nakamura, Y. & Tsai, J. S. Demonstration of conditional gate operation using superconducting charge qubits. *Nature* **425**, 941–944 (2003).
10. Berkley, A. J. *et al.* Entangled macroscopic quantum states in two superconducting qubits. *Science* **300**, 1548–1550 (2003).
11. Bouchiat, V., Vion, D., Joyez, P., Esteve, D. & Devoret, M. H. Quantum coherence with a single Cooper pair. *Phys. Scr.* **T76**, 165–170 (1998).
12. Blais, A., Huang, R.-S., Wallraff, A., Girvin, S. & Schoelkopf, R. Cavity quantum electrodynamics for superconducting electrical circuits: an architecture for quantum computation. *Phys. Rev. A* **69**, 062320 (2004).
13. Makhlin, Y., Schön, G. & Shnirman, A. Quantum-state engineering with Josephson-junction devices. *Rev. Mod. Phys.* **73**, 357–400 (2001).
14. Buisson, O. & Hekking, F. in *Macroscopic Quantum Coherence and Quantum Computing* (eds Averin, D. V., Ruggiero, B. & Silvestrini, P.) (Kluwer, New York, 2001).
15. Marquardt, F. & Bruder, C. Superposition of two mesoscopically distinct quantum states: Coupling a Cooper-pair box to a large superconducting island. *Phys. Rev. B* **63**, 054514 (2001).
16. Al-Saidi, W. A. & Stroud, D. Eigenstates of a small Josephson junction coupled to a resonant cavity. *Phys. Rev. B* **65**, 014512 (2001).
17. Plastina, F. & Falcì, G. Communicating Josephson qubits. *Phys. Rev. B* **67**, 224514 (2003).
18. Blais, A., Maassen van den Brink, A. & Zagoskin, A. Tunable coupling of superconducting qubits. *Phys. Rev. Lett.* **90**, 127901 (2003).
19. Yang, C.-P., Chu, S.-I. & Han, S. Possible realization of entanglement, logical gates, and quantum-information transfer with superconducting-quantum-interference-device qubits in cavity QED. *Phys. Rev. A* **67**, 042311 (2003).
20. You, J. Q. & Nori, F. Quantum information processing with superconducting qubits in a microwave field. *Phys. Rev. B* **68**, 064509 (2003).
21. Kiraz, A. *et al.* Cavity-quantum electrodynamics using a single InAs quantum dot in a microdisk structure. *Appl. Phys. Lett.* **78**, 3932–3934 (2001).
22. Childress, L., Sørensen, A. S. & Lukin, M. D. Mesoscopic cavity quantum electrodynamics with quantum dots. *Phys. Rev. A* **69**, 042302 (2004).
23. Irish, E. K. & Schwab, K. Quantum measurement of a coupled nanomechanical resonator–Cooper-pair box system. *Phys. Rev. B* **68**, 155311 (2003).
24. Weisbuch, C., Nishioka, M., Ishikawa, A. & Arakawa, Y. Observation of the coupled exciton-photon mode splitting in a semiconductor quantum microcavity. *Phys. Rev. Lett.* **69**, 3314–3317 (1992).
25. Vucokovic, J., Fattal, D., Santori, C., Solomon, G. S. & Yamamoto, Y. Enhanced single-photon emission from a quantum dot in a micropost microcavity. *Appl. Phys. Lett.* **82**, 3596 (2003).
26. Day, P. K., LeDuc, H. G., Mazin, B. A., Vayonakis, A. & Zmuidzinas, J. A broadband superconducting detector suitable for use in large arrays. *Nature* **425**, 817–821 (2003).
27. Lehnert, K. *et al.* Measurement of the excited-state lifetime of a microelectronic circuit. *Phys. Rev. Lett.* **90**, 027002 (2003).

28. Nogues, G. *et al.* Seeing a single photon without destroying it. *Nature* **400**, 239–242 (1999).
 29. Schuster, D. I. *et al.* AC-Stark shift and dephasing of a superconducting qubit strongly coupled to a cavity field. Preprint at <http://www.arXiv.org/cond-mat/0408367> (2004).
 30. Rau, I., Johansson, G. & Shnirman, A. Cavity QED in superconducting circuits: susceptibility at elevated temperatures. Preprint at <http://www.arXiv.org/cond-mat/0403257> (2004).

Acknowledgements We thank J. Teufel, B. Turek and J. Wyatt for their contributions to the project and are grateful to P. Day, D. DeMille, M. Devoret, S. Weinreb and J. Zmuidzinas for numerous conversations. This work was supported in part by the National Security Agency and Advanced Research and Development Activity under the Army Research Office, the NSF, the David and Lucile Packard Foundation, the W. M. Keck Foundation, and the Natural Science and Engineering Research Council of Canada.

Competing interests statement The authors declare that they have no competing financial interests.

Correspondence and requests for materials should be addressed to A. W. (andreas.wallraff@yale.edu).

Generation of ultraviolet entangled photons in a semiconductor

Keiichi Edamatsu^{1,2}, Goro Oohata^{1,3}, Ryosuke Shimizu² & Tadashi Itoh^{4,2}

¹Research Institute of Electrical Communication, Tohoku University, Sendai 980-8577, Japan

²CREST, Japan Science and Technology Agency (JST), Japan

³ERATO Semiconductor Spintronics Project, JST, Japan

⁴Graduate School of Engineering Science, Osaka University, Toyonaka 560-8531, Japan

Entanglement is one of the key features of quantum information and communications technology. The method that has been used most frequently to generate highly entangled pairs of photons^{1,2} is parametric down-conversion. Short-wavelength entangled photons are desirable for generating further entanglement between three or four photons, but it is difficult to use parametric down-conversion to generate suitably energetic entangled photon pairs. One method that is expected to be applicable for the generation of such photons³ is resonant hyper-parametric scattering (RHPS): a pair of entangled photons is generated in a semiconductor via an electronically resonant third-order nonlinear optical process. Semiconductor-based sources of entangled photons would also be advantageous for practical quantum technologies, but attempts to generate entangled photons in semiconductors have not yet been successful^{4,5}. Here we report experimental evidence for the generation of ultraviolet entangled photon pairs by means of biexciton resonant RHPS in a single crystal of the semiconductor CuCl. We anticipate that our results will open the way to the generation of entangled photons by current injection, analogous to current-driven single photon sources^{6,7}.

The material we used in this study was copper chloride (CuCl) single crystal. Because CuCl has a large bandgap (~3.4 eV), it is suitable for generating photon pairs in the short wavelength region near ultraviolet. Furthermore, the material has large binding energies for the exciton (~200 meV) and biexciton (~30 meV). These characteristics have made CuCl one of the most thoroughly investigated materials on the physics of excitons and biexcitons (ref. 8 and references therein). In particular, the ‘giant oscillator strength’ in the two-photon excitation of the biexciton results in a large increase in RHPS efficiency, which is advantageous for our experiment. In fact the RHPS in CuCl has been observed since the 1970s (refs 8, 9 and ref. 10 and references therein). Figure 1a schematically shows the RHPS process in resonance to the biexciton state. The two pump (parent) photons (frequency ω_i) resonantly create the

biexciton, and are converted into the two scattered (daughter) photons (ω_s, ω_s'). The biexciton state (Γ_1) created in this process has zero angular momentum ($J = 0$), so we expected the polarizations of the daughter photons to be entangled so that their total angular momentum is also zero. With this expectation in mind, we note that polarization correlation between two classical pump beams has been known since the early 1980s (ref. 11). In practice, instead of the oversimplified picture in Fig. 1a, we must consider the exciton-polariton picture; the RHPS obeys the phase-matching condition that takes into account the polariton dispersion relation⁸. The RHPS in this case is also called two-photon resonant polariton scattering or spontaneous hyper-Raman scattering. In this process, shown in Fig. 1b, the biexciton is created from a pair of parent photons (polaritons, more accurately). The sum of the parent photons’ energies matches the biexciton energy. The biexciton progressively coherently decays into two polaritons, the sum of whose photon energies, as well as the sum of momenta, is conserved as that of the biexciton. Although the RHPS in CuCl has been known for decades, the possibility of generating entangled photons by this process was theoretically pointed out only lately¹². In addition, a large parametric gain via the biexcitonic resonance in CuCl was reported recently¹³. Similar stimulated parametric scattering of polaritons has also been observed in semiconductor microcavities, even at high temperatures¹⁴.

In the present experiment, we used a vapour-phase-grown thin single crystal of CuCl. Figure 2 presents the schematic drawing of our experimental set-up and Fig. 3 shows the spectrum of light emitted from the sample. The large peak at the downward arrow in Fig. 3 is the Rayleigh scattered light of the pump beam that was tuned to the two-photon excitation resonance of the biexciton. The two peaks indicated by LEP and HEP (lower and higher energy polaritons) on either side of the pump beam originate from the RHPS. The RHPS is very efficient (a few orders of magnitude higher than that of typical parametric down-conversion): We got of the order of 10^{10} photons $s^{-1} sr^{-1}$ by using pump light of ~2 mW. A pair of photons, one from LEP and the other from HEP, is emitted into different directions according to the phase-matching condition, so we placed two optical fibres at appropriate positions and led each photon within the pair into two independent monochromators followed by two photomultipliers (PMTs). A time-interval analyser recorded the time interval (τ) between the detected

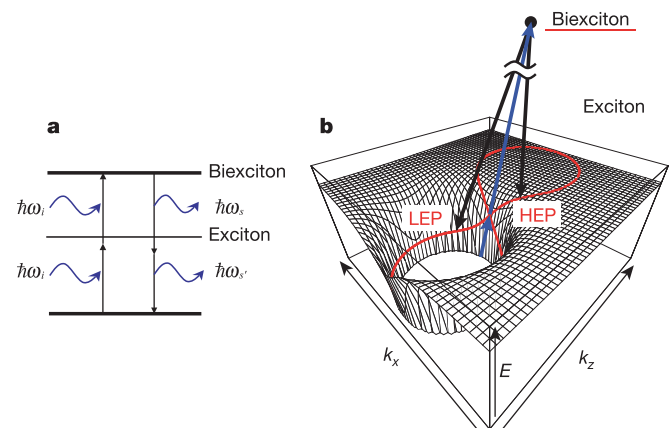


Figure 1 Schematic diagram of the resonant hyper-parametric scattering (RHPS) via biexciton. **a**, Two pump (parent) photons of frequency ω_i are converted to the two scattered (daughter) photons (ω_s, ω_s'). **b**, The polariton dispersion drawn in two dimensions of momentum space. The biexciton decays into two polaritons that satisfy the phase-matching condition so that both energy and momentum are conserved. The red curve on the polariton-dispersion surface indicates the states on which the phase-matching condition can be satisfied.

ac Stark Shift and Dephasing of a Superconducting Qubit Strongly Coupled to a Cavity Field

D. I. Schuster, A. Wallraff, A. Blais, L. Frunzio, R.-S. Huang,* J. Majer, S. M. Girvin, and R. J. Schoelkopf

Departments of Applied Physics and Physics, Yale University, New Haven, Connecticut 06520, USA

(Received 16 August 2004; published 30 March 2005)

We have performed spectroscopy of a superconducting charge qubit coupled nonresonantly to a single mode of an on-chip resonator. The strong coupling induces a large ac Stark shift in the energy levels of both the qubit and the resonator. The dispersive shift of the resonator frequency is used to nondestructively determine the qubit state. Photon shot noise in the measurement field induces qubit level fluctuations leading to dephasing which is characteristic for the measurement backaction. A crossover in line shape with measurement power is observed and theoretically explained. For weak measurement a long intrinsic dephasing time of $T_2 > 200$ ns of the qubit is found.

DOI: 10.1103/PhysRevLett.94.123602

PACS numbers: 42.50.Pq, 32.60.+i, 42.50.Lc, 85.35.Gv

The investigation of strong coupling between a single quantum two-level system and a single photon, as first realized in atomic cavity quantum electrodynamics (CQED) [1], is not only at the forefront of research in quantum optics and atomic physics [2] but also has great prospects in the realm of quantum information processing [3] where realizing entanglement between qubits and photons is essential for quantum communication. Recently, it has been proposed [4] and demonstrated for the first time in a solid state system that strong coupling CQED [5,6] can be realized in superconducting quantum circuits [7]. Following these results, strong coupling has also been achieved in a second solid state system, namely, semiconducting quantum dots embedded in microcavities [8,9]. In this Letter we demonstrate the use of *nonresonant (dispersive)* strong coupling between a Cooper pair box (CPB) [10] and a coherent microwave field in a high quality transmission line resonator to measure the quantum mechanical state of the Cooper pair box in a quantum nondemolition (QND) scheme [4,11,12]. The interaction between the Cooper pair box and the measurement field containing n photons on average gives rise to a large ac Stark shift of the qubit energy levels, analogous to the one observed in CQED [13], demonstrated here for the first time in superconducting qubits. As a consequence of the strong coupling, quantum fluctuations in n induce a broadening of the transition linewidth, which represents the backaction of the measurement on the qubit.

In our circuit QED architecture [4] [see Fig. 1(a)] a split Cooper pair box [10], modeled by the two-level Hamiltonian $H_a = -1/2(E_{el}\sigma_x + E_J\sigma_z)$ [14], is coupled capacitively to the electromagnetic field of a full wave ($l = \lambda$) transmission line resonator, described by a harmonic oscillator Hamiltonian $H_r = \hbar\omega_r(a^\dagger a + 1/2)$. In the Cooper pair box, the energy difference $E_a = \hbar\omega_a = (E_{el}^2 + E_J^2)^{1/2}$ between the ground state $|\downarrow\rangle$ and the first excited state $|\uparrow\rangle$ [see Fig. 1(b)], is determined by its electrostatic energy $E_{el} = 4E_C(1 - n_g)$ and its Josephson coupling energy $E_J = E_{J,max} \cos(\pi\Phi_b)$. Here, $E_C = e^2/2C_\Sigma \approx 5$ GHz is the charging energy given by the total

box capacitance C_Σ , $n_g = C_g^*V_g/e$ is the gate charge controlled by the gate voltage V_g applied through a gate with effective capacitance C_g^* , and $E_{J,max} \approx 8$ GHz is the maximum Josephson coupling energy of the two junctions which is modulated by applying a flux bias $\Phi_b = \Phi/\Phi_0$ to the loop of the split box [see Fig. 1(a)]. $\Phi_0 = 2e/h$ is the magnetic flux quantum. Near its resonance frequency $\omega_r = 1/\sqrt{LC} \approx 2\pi \cdot 6$ GHz, the resonator is accurately modeled as a harmonic oscillator with lumped inductance L and capacitance C .

In the presence of strong mutual coupling between the qubit and the resonator [5], their *dressed* excitation ener-

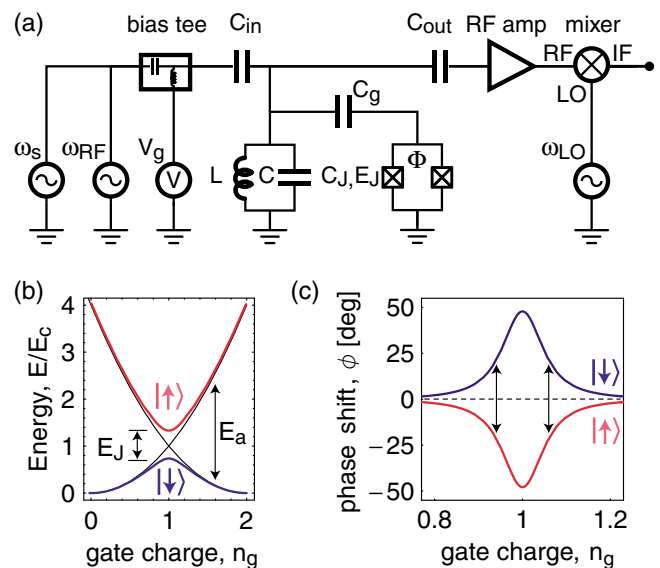


FIG. 1 (color online). (a) Simplified circuit diagram of measurement setup. The phase ϕ and amplitude T of a microwave at ω_{rf} transmitted through the resonator, amplified, and mixed down to an intermediate frequency $\omega_{IF} = \omega_{rf} - \omega_{LO}$ using a local oscillator at ω_{LO} is measured. An additional spectroscopy microwave at ω_s is applied to the input port of the resonator. (b) Ground $|\downarrow\rangle$ and excited $|\uparrow\rangle$ state energy levels of CPB vs gate charge n_g . (c) Calculated phase shift ϕ in ground and excited states vs n_g for $\Delta_{a,r}/2\pi = 100$ MHz.

gies $\tilde{\omega}_a$ and $\tilde{\omega}_r$, are modified from their bare values ω_a and ω_r . For large detuning $\Delta_{a,r} = \omega_a - \omega_r$ the dressed energy levels are determined by the Hamiltonian [4]

$$H \approx \hbar \left(\omega_r + \frac{g^2}{\Delta_{a,r}} \sigma_z \right) a^\dagger a + \frac{1}{2} \hbar \left(\omega_a + \frac{g^2}{\Delta_{a,r}} \right) \sigma_z, \quad (1)$$

where $g/2\pi \approx 5.8$ MHz is the coupling strength between a single photon and the qubit [5]. In this nonresonant case, the dressed resonator frequency $\tilde{\omega}_r = \omega_r \pm g^2/\Delta_{a,r}$ depends on the qubit state $\sigma_z = \pm 1$ and the detuning $\Delta_{a,r}$. The qubit state can thus be inferred from the phase shift ϕ that a probe microwave transmitted through the resonator at frequency ω_{rf} experiences because of the interaction with the qubit [4,5]. In Fig. 1(c), the expected phase shift $\phi = \pm \tan^{-1}(2g^2/\kappa\Delta_{a,r})$, where $\kappa = \omega_r/Q$ is the decay rate of photons from the resonator with quality factor $Q \approx 10^4$, is plotted versus gate charge n_g . ϕ is maximum at $n_g = 1$ where the detuning $\Delta_{a,r}$ is smallest and falls off as the detuning is increased with increasing n_g . Moreover, ϕ has opposite signs in the ground $|\downarrow\rangle$ and excited $|\uparrow\rangle$ states of the CPB.

Qubit state transitions can be driven by applying an additional microwave of frequency ω_s , detuning $\Delta_{s,a} = \omega_s - \tilde{\omega}_a$, and power P_s to the input port of the resonator [see Fig. 1(a)]. On resonance ($\Delta_{s,a} = 0$) and for a continuous (cw) large amplitude spectroscopy drive, the qubit transition saturates and the populations in the excited and the ground states approach 1/2. In this case, the measured phase shift of the probe beam at ω_{rf} is expected to saturate at $\phi = 0$ [see Fig. 1(c)]. By sweeping the spectroscopy frequency ω_s and the gate charge n_g and *continuously* measuring ϕ , we have mapped out the energy level separation

$\tilde{\omega}_a$ of the qubit (see Fig. 2). In the lower panel of Fig. 2(a), the measured phase shift ϕ is shown for the nonresonant case, where $\omega_s < \tilde{\omega}_a$ for all values of gate charge n_g . The measured phase shift is, as expected, a continuous curve similar to the one shown in Fig. 1(c). In the middle panel of Fig. 2(a), the spectroscopy microwave at $\nu_s = \omega_s/2\pi = 6.15$ GHz is in resonance with the qubit at $n_g = 1$, populating the excited state and thus inducing a dip in the measured phase shift ϕ around $n_g = 1$, as expected. Note that, as predicted [4], our measurement scheme has the advantage of being most sensitive at charge degeneracy, a bias point where traditional electrometry, using a radio frequency single electron transistor [15], for example, is unable to distinguish the qubit states.

When ν_s is increased to higher values, resonance with the qubit occurs for two values of n_g situated symmetrically around $n_g = 1$, leading to two symmetric dips in ϕ [see upper panel of Fig. 2(a)]. From the $[n_g, \nu_s]$ positions of the spectroscopic lines in the measured phase ϕ , the Josephson energy $E_J = 6.2$ GHz and the charging energy $E_C = 4.8$ GHz are determined in a fit using the full qubit Hamiltonian beyond the two-level approximation [14] [see density plot of ϕ vs n_g and ν_s in Fig. 2(b)]. In this experiment the flux bias Φ_b has been chosen to result in a minimum detuning of about $\Delta_{a,r}/2\pi \approx 100$ MHz at $n_g = 1$. The tunability of E_J (i.e., the detuning at charge degeneracy) has been demonstrated previously [5]. It is also worth noting that the spectroscopy frequency ω_s typically remains strongly detuned ($\Delta_{s,r} = \omega_s - \omega_r > 2\pi 100$ MHz) from the resonator, such that a large fraction of the spectroscopy photons are reflected at the input port and only a small number n_s , determined by the Lorentzian line shape of the resonator, populates the resonator.

Various other radio or microwave frequency qubit readout schemes have been developed recently [15–17]. In a related experiment, the level separation of a split Cooper pair box coupled *inductively* to a *low frequency, moderate Q* tank circuit has been determined spectroscopically [18].

The width and the saturation level of the spectroscopic lines discussed above depend sensitively on the power P_s of the spectroscopic drive. Both quantities are related to the excited state population

$$P_\uparrow = 1 - P_\downarrow = \frac{1}{2} \frac{n_s \omega_{\text{vac}}^2 T_1 T_2}{1 + (T_2 \Delta_{s,a})^2 + n_s \omega_{\text{vac}}^2 T_1 T_2}, \quad (2)$$

found from the Bloch equations in steady state [19], where $\omega_{\text{vac}} = 2g$ is the vacuum Rabi frequency, n_s the average number of spectroscopy photons in the resonator, T_1 the relaxation time, and T_2 the dephasing time of the qubit. We have extracted the transition linewidth and saturation from spectroscopy frequency scans for different drive powers P_s with the qubit biased at charge degeneracy ($n_g = 1$). We observe that the spectroscopic lines have a Lorentzian line shape with width and depth in accordance with Eq. (2). The

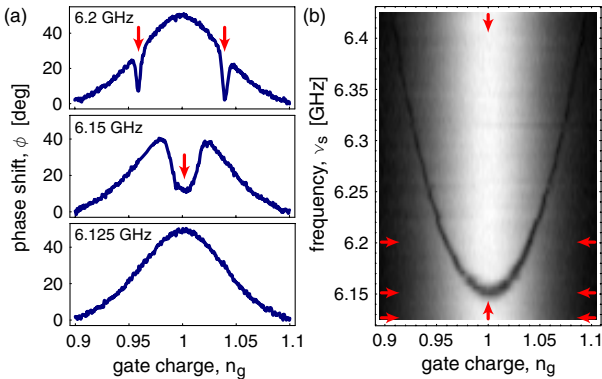


FIG. 2 (color online). (a) Probe microwave phase shift ϕ vs gate charge n_g at spectroscopy frequency $\nu_s = 6.125$ GHz (lower panel), 6.15 GHz (middle panel), and 6.2 GHz (upper panel). (b) Density plot of ϕ vs n_g and ν_s ; white (black) corresponds to large (small) phase shift. Horizontal arrows indicate line cuts shown in (a); vertical arrows indicate line cuts shown in Fig. 4(a). Measurements in (a) and (b) were performed populating the resonator with $n \sim 25$ photons on average.

half width at half maximum (HWHM) of the line is found to follow the expected power dependence $2\pi\delta\nu_{\text{HWHM}} = 1/T_2' = (1/T_2^2 + n_s\omega_{\text{vac}}^2 T_1/T_2)^{1/2}$ [19], where the input microwave power P_s is proportional to $n_s\omega_{\text{vac}}^2$ [see Fig. 3(a)]. In the low power limit ($n_s\omega_{\text{vac}}^2 \rightarrow 0$), the unbroadened linewidth is found to be small, $\delta\nu_{\text{HWHM}} \approx 750$ kHz, corresponding to a long dephasing time of $T_2 > 200$ ns at $n_g = 1$, where the qubit is only second order sensitive to charge fluctuations limiting the dephasing time in this sample. At a larger drive, the width increases proportionally to the drive amplitude. The depth of the spectroscopic dip at resonance ($\Delta_{s,a} = 0$) reflects the probability of the qubit to be in the excited state P_\uparrow and depends on P_s as predicted by Eq. (2) [see Fig. 3(b)]. At low drive the population increases linearly with P_s and then approaches 0.5 for large P_s . From time resolved measurements (data not shown), T_1 is found to be on the order of a few microseconds, a value which is much shorter than that expected for radiative decay of the qubit in the cavity [4], indicating the existence of other, possibly non-radiative decay channels.

In the above we have demonstrated that the strong coupling of the qubit to the radiation field modifies the resonator transition frequency in a way that can be exploited to measure the qubit state. Correspondingly, the resonator acts back onto the qubit through their mutual strong coupling. Regrouping the terms of the Hamiltonian in Eq. (1) one sees that the *dressed* qubit level separation is given by $\tilde{\omega}_a = \omega_a + 2ng^2/\Delta_{a,r} + g^2/\Delta_{a,r}$, where we note that the resonator gives rise to an ac Stark shift of the qubit levels of $\pm ng^2/\Delta_{a,r}$, proportional to the intracavity photon number $n = \langle a^\dagger a \rangle$, as well as a Lamb shift $\pm g^2/2\Delta_{a,r}$, due to the coupling to the vacuum fluctuations. The ac Stark shift is measured spectroscopically at $n_g = 1$ for fixed power P_s by varying the probe beam power P_{rf} which changes the average measurement photon number n in the resonator (see Fig. 4). We observe that the qubit level

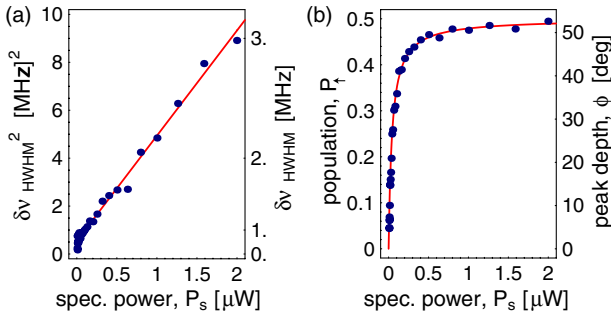


FIG. 3 (color online). (a) Measured qubit linewidth $\delta\nu_{\text{HWHM}}$ vs input spectroscopy power P_s (solid circles) with fit (solid line). Probe beam power P_{rf} is adjusted such that $n < 1$. (b) Measured peak depth ϕ and excited state population probability P_\uparrow on resonance $\Delta_{s,a} = 0$ vs P_s (solid circles) with fit (solid line).

separation $\tilde{\nu}_a = \tilde{\omega}_a/2\pi$ is linear in P_{rf} [see Fig. 5(a)], i.e., that the ac Stark shift $\nu_{\text{ac}} = 2ng^2/2\pi\Delta_{a,r}$ is linear in the photon number n , as expected. In the limit of $P_{\text{rf}} \rightarrow 0$ ($n \rightarrow 0$), the bare qubit level separation $\omega_a + g^2/\Delta_{a,r} = 2\pi \cdot 6.15$ GHz is determined, where $g^2/\Delta_{a,r}$ is the small Lamb shift which cannot be separated from ω_a in our current experiments. Knowing the coupling constant g from an independent measurement of the vacuum Rabi mode splitting [5] and $\Delta_{a,r}$ from spectroscopic measurements in the $n \rightarrow 0$ limit, the dependence of the intracavity photon number n on the input power P_{rf} is determined from the measured ac Stark shift ν_{ac} . We find that an input microwave power of $P_{\text{rf}} = -29$ dBm corresponds to $n = 1$ which is consistent with an intended attenuation of approximately 105 dB in the input coaxial line. The ac Stark shift of the qubit at this particular detuning is a remarkable 0.6 MHz per photon in the cavity and is comparable to the linewidth. Using this method, the intracavity photon number was calibrated to a precision of $\sim \pm 1$ dB for the vacuum Rabi mode splitting measurements presented in Ref. [5].

Quantum fluctuations (photon shot noise) δn around the average photon number n of the coherent field populating the resonator give rise to random fluctuations in the qubit transition frequency due to the ac Stark shift. This leads to measurement-induced dephasing, and thus to a broadening of the qubit linewidth (see Figs. 4 and 5). This is the measurement backaction and can be understood quantitatively by considering the relative phase $\varphi(t) = 2g^2/\Delta_{a,r} \int_0^t dt' \delta n(t')$ accumulated in time between the ground and the excited states of the qubit. Following Ref. [4], the measurement-induced phase decay of the qubit is then characterized by

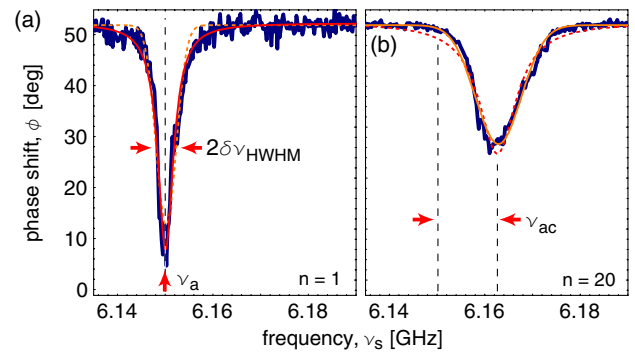


FIG. 4 (color online). Measured spectroscopic lines (wide lines with noise) at (a) intracavity photon number $n \approx 1$ ($P_{\text{rf}} = -30$ dBm) with fit to Lorentzian line shape (solid line) and at (b) $n \approx 20$ ($P_{\text{rf}} = -16$ dBm) with fit to Gaussian line shape (solid line). Dashed lines are best fits to (a) Gaussian or (b) Lorentzian line shapes, respectively. The qubit transition frequency ν_a at low P_{rf} , the half width half maximum $\delta\nu_{\text{HWHM}}$, and the ac Stark shift ν_{ac} of the lines are indicated.

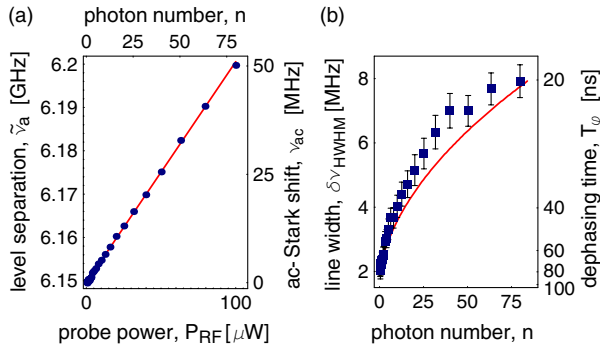


FIG. 5 (color online). (a) Measured qubit level separation $\tilde{\nu}_a$ and fit (solid line) vs input microwave probe power P_{rf} . The ac Stark shift ν_{ac} and the intracavity photon number n extracted from the fit are also indicated. (b) Measurement broadened qubit linewidth $\delta\nu_{\text{HWHM}}$ vs n . Error bars are reflecting estimated systematic uncertainties in the extracted linewidth. The corresponding total dephasing time $T_\varphi = 1/2\pi\delta\nu_{\text{HWHM}}$ is also indicated. The solid line is obtained from Eq. (4) with a spectroscopy power broadened $T_2' \approx 80$ ns.

$$\langle e^{i\varphi(t)} \rangle = \exp\left[-\frac{2g^4}{\Delta_{a,r}^2} \iint_0^t dt_1 dt_2 \langle \delta n(t_1) \delta n(t_2) \rangle\right], \quad (3)$$

where the fluctuations δn are assumed to be Gaussian. In the above expression, the photon correlation function $\langle \delta n(t) \delta n(0) \rangle = n \exp(-\kappa|t|/2)$ of the coherent probe beam in the resonator is governed by the cavity decay rate κ and physically represents the white photon shot noise filtered by the cavity response. The spectroscopic line shape $S(\omega)$ is obtained from the Fourier transform of $\langle \exp[i\varphi(t)] \rangle e^{-t/T_2'}$, where $1/T_2'$ takes into account dephasing mechanisms independent of the measurement

$$S(\omega) = \frac{1}{\pi} \sum_{j=0}^{\infty} \frac{(-4\chi)^j}{j!} \frac{1/T_2' + 2\kappa\chi + j\kappa/2}{(\omega - \tilde{\omega}_a)^2 + (1/T_2' + 2\kappa\chi + j\kappa/2)^2}. \quad (4)$$

The form of the line shape depends on the dimensionless parameter $\chi = n\theta_0^2$, where $\theta_0 = 2g^2/\kappa\Delta_{a,r}$ is the transmission phase shift describing the strength of the measurement. For small χ the measurement rate is slow compared to κ and the phase diffuses in a random walk $\langle \varphi(t)^2 \rangle \sim 4\theta_0^2 n \kappa t$, leading to a homogeneously broadened Lorentzian line of HWHM of $2\theta_0^2 n \kappa + 1/T_2'$. For large χ , i.e., strong measurement, the measurement rate exceeds κ leading to a qubit transition frequency which depends on the instantaneous value of the cavity photon number and hence to an inhomogeneously broadened Gaussian line [see Fig. 4(b)], whose variance is simply \sqrt{n} multiplied by the Stark shift per photon. The full crossover from intrinsic Lorentzian line shape with width $\propto n$ at small n to Gaussian line shape with width $\propto \sqrt{n}$ at large n as described by Eq. (4) with no adjustable parameters is in good agreement with the measured dependence of the linewidth on n [see Fig. 5(b)]. The slightly increased measured linewidth could be attributed

to fluctuations (e.g., charge noise) activated at high photon numbers and to the nonlinearity of the ac Stark shift above the critical photon number [4]. We note that this effect is not seen in Fig. 4(a) because of compensation by the change of the cavity pull at large n from the zero-photon limit g^2/Δ .

In our experiments we have demonstrated that the strong coupling of a Cooper pair box to a nonresonant microwave field in an on-chip cavity gives rise to a large qubit dependent shift in the excitation energy of the resonator. The ac Stark effect shifts the qubit level separation by about one linewidth per photon at 2% detuning, and the backaction of the fluctuations in the field gives rise to a large broadening of the qubit line. Good agreement of the line shape with theory indicates that the dispersive measurement is QND, as expected.

We thank M. Devoret and I. Chiorescu for discussions. This work was supported in part by NSA and ARDA under ARO Contract No. DAAD19-02-1-0045, and the NSF under Grants No. ITR-0325580 and No. DMR-0342157, the David and Lucile Packard Foundation, the W. M. Keck Foundation, and the NSERC of Canada.

*Also at Ames Laboratory, Iowa State University, Ames, IA 50011, USA.

- [1] H. Mabuchi and A. Doherty, *Science* **298**, 1372 (2002).
- [2] D. Walls and G. Milburn, *Quantum Optics* (Springer-Verlag, Berlin, 1994).
- [3] M. A. Nielsen and I. L. Chuang, *Quantum Computation and Quantum Information* (Cambridge University Press, Cambridge, U.K., 2000).
- [4] A. Blais *et al.*, *Phys. Rev. A* **69**, 062320 (2004).
- [5] A. Wallraff *et al.*, *Nature (London)* **431**, 162 (2004).
- [6] I. Chiorescu *et al.*, *Nature (London)* **431**, 159 (2004).
- [7] Y. Nakamura, Y. A. Pashkin, and J. S. Tsai, *Nature (London)* **398**, 786 (1999); D. Vion *et al.*, *Science* **296**, 886 (2002); J. M. Martinis, S. Nam, J. Aumentado, and C. Urbina, *Phys. Rev. Lett.* **89**, 117901 (2002); Y. Yu *et al.*, *Science* **296**, 889 (2002); I. Chiorescu, Y. Nakamura, C. J. P. M. Harmans, and J. E. Mooij, *Science* **299**, 1869 (2003); T. Yamamoto *et al.*, *Nature (London)* **425**, 941 (2003).
- [8] T. Yoshie *et al.*, *Nature (London)* **432**, 200 (2004).
- [9] J. P. Reithmaier *et al.*, *Nature (London)* **432**, 197 (2004).
- [10] V. Bouchiat *et al.*, *Phys. Scr.* **T76**, 165 (1998).
- [11] P. Grangier, J. A. Levenson, and J.-P. Poziat, *Nature (London)* **396**, 537 (1998).
- [12] G. Nogues *et al.*, *Nature (London)* **400**, 239 (1999).
- [13] P. Brune *et al.*, *Phys. Rev. Lett.* **72**, 3339 (1994).
- [14] Y. Makhlin, G. Schön, and A. Shnirman, *Rev. Mod. Phys.* **73**, 357 (2001).
- [15] K. Lehnert *et al.*, *Phys. Rev. Lett.* **90**, 027002 (2003).
- [16] A. Lupascu *et al.*, *Phys. Rev. Lett.* **93**, 177006 (2004).
- [17] I. Siddiqi *et al.*, *Phys. Rev. Lett.* **93**, 207002 (2004).
- [18] D. Born *et al.*, *Phys. Rev. B* **70**, 180501 (2004).
- [19] A. Abragam, *The Principles of Nuclear Magnetism* (Oxford University Press, Oxford, 1961).

Approaching Unit Visibility for Control of a Superconducting Qubit with Dispersive Readout

A. Wallraff, D. I. Schuster, A. Blais, L. Frunzio, J. Majer, M. H. Devoret, S. M. Girvin, and R. J. Schoelkopf

Departments of Applied Physics and Physics, Yale University, New Haven, Connecticut 06520, USA

(Received 27 February 2005; published 1 August 2005)

In a Rabi oscillation experiment with a superconducting qubit we show that a visibility in the qubit excited state population of more than 95% can be attained. We perform a dispersive measurement of the qubit state by coupling the qubit nonresonantly to a transmission line resonator and probing the resonator transmission spectrum. The measurement process is well characterized and quantitatively understood. In a measurement of Ramsey fringes, the qubit coherence time is larger than 500 ns.

DOI: [10.1103/PhysRevLett.95.060501](https://doi.org/10.1103/PhysRevLett.95.060501)

PACS numbers: 03.67.Pp, 42.50.Pq, 85.35.Gv

One of the most promising solid-state architectures for the realization of a quantum information processor [1] is based on superconducting electrical circuits [2]. A variety of such circuits acting as qubits [1], the basic carriers of quantum information in a quantum computer, have been created and their coherent control has been demonstrated [3–8]. Recent experiments have realized controlled coupling between different qubits [9–13] and also first two-qubit quantum logic gates [14].

An outstanding question for superconducting qubits, and in fact for all solid-state implementations of quantum information processors, is whether the qubits are sufficiently well isolated to allow long coherence times and high-fidelity preparation and control of their quantum states. This question is complicated by inevitable imperfections in the measurement. A canonical example is a Rabi oscillation experiment, where the experimenter records the oscillations of a meter's response as a function of pulse length to infer the qubit's excited state population immediately after the pulse. The measurement contrast (e.g., the amplitude of the meter's measured swing relative to its maximum value) is reduced in general by both errors in the qubit preparation and readout, and sets a lower limit on the visibility of oscillations in the qubit population. Most experiments with superconducting qubits to date have reported only the measurement contrast, implying only a lower limit on the visibility in the range of 10%–50% [3–8,14].

A full understanding of the measurement process is required to extract the qubit population from the meter's output. The qubit control is then characterized by the visibility, defined as the maximum qubit population difference observed in a Rabi oscillation or Ramsey fringe experiment. It is essential to demonstrate that a qubit can be controlled without inducing undesired leakage to other qubit states or entanglement with the environment. Some experiments [15] observe a substantial reduction of the visibility due to entanglement with spurious environmental fluctuators [16]. In the few experiments in which the contrast has been characterized, it was close to the expected value [17,18], which implies that high visibility should be achievable with superconducting qubits.

In this Letter, we report results on time-domain control of the quantum state of a superconducting qubit, where the qubit state is determined using a dispersive microwave measurement in a circuit quantum electrodynamics (QED) architecture [19]. This novel technique has shown good agreement with predictions in steady-state experiments [20]. Here, we observe the measurement response, both during and after qubit state manipulation, which is in quantitative agreement with the theoretical model of the system, allowing us to separate the contributions of the qubit and the readout to the observed contrast. The observed contrast of 85% and a visibility of greater than 95% for Rabi oscillations demonstrates that high accuracy control is possible in superconducting qubits.

In our circuit QED architecture [19], a Cooper pair box [21], acting as a two level system with ground $|\downarrow\rangle$ and excited states $|\uparrow\rangle$ and level separation $E_a = \hbar\omega_a = \sqrt{E_{el}^2 + E_J^2}$ is coupled capacitively to a single mode of the electromagnetic field of a transmission line resonator with resonance frequency ω_r ; see Fig. 1(a). As demonstrated for this system, the electrostatic energy E_{el} and the Josephson energy E_J of the split Cooper pair box can be controlled *in situ* by a gate voltage V_g and magnetic flux Φ [20,22]; see Fig. 1(a). In the resonant ($\omega_a = \omega_r$) strong coupling regime a single excitation is exchanged coherently between the Cooper pair box and the resonator at a rate g/π , also called the vacuum Rabi frequency [22]. In the nonresonant regime ($|\Delta| = |\omega_a - \omega_r| > g$) the capacitive interaction gives rise to a dispersive shift $(g^2/\Delta)\sigma_z$ in the resonance frequency of the cavity which depends on the qubit state σ_z , the coupling g , and the detuning Δ [19,20]. We have suggested that this shift in resonance frequency can be used to perform a quantum nondemolition (QND) measurement of the qubit state [19]. With this technique we have recently measured the ground state response and the excitation spectrum of a Cooper pair box [20,22].

In the experiments presented here, we coherently control the quantum state of a Cooper pair box in the resonator by applying microwave pulses of frequency ω_s , which are resonant or nearly resonant with the qubit transition frequency $\omega_a/2\pi \approx 4.3$ GHz, to the input port C_{in} of the resonator; see Fig. 1(a). Even though ω_s is strongly de-

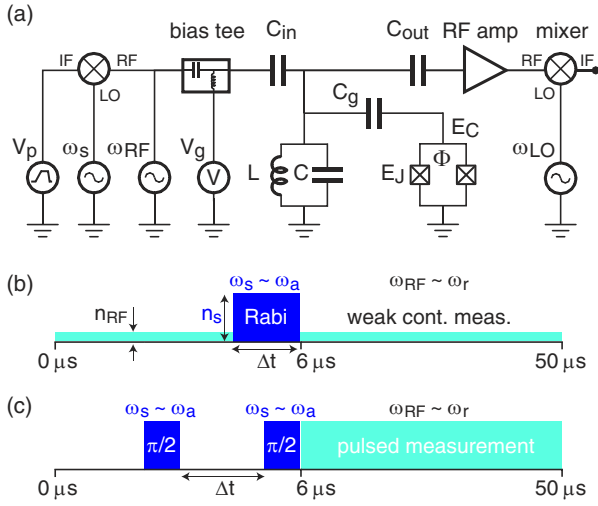


FIG. 1 (color online). (a) Simplified circuit diagram of measurement setup. A Cooper pair box with charging energy E_C and Josephson energy E_J is coupled through capacitor C_g to a transmission line resonator, modeled as parallel combination of an inductor L and a capacitor C . Its state is determined in a phase sensitive heterodyne measurement of a microwave transmitted at frequency ω_{RF} through the circuit, amplified and mixed with a local oscillator at frequency ω_{LO} . The Cooper pair box level separation is controlled by the gate voltage V_g and flux Φ . Its state is coherently manipulated using microwaves at frequency ω_s with pulse shapes determined by V_p [8]. (b) Measurement sequence for Rabi oscillations with Rabi pulse length Δt , pulse frequency ω_s , and amplitude $\propto \sqrt{n_s}$ with continuous measurement at frequency ω_{RF} and amplitude $\propto \sqrt{n_{RF}}$. (c) Sequence for Ramsey fringe experiment with two $\pi/2$ pulses at ω_s separated by a delay Δt and followed by a pulsed measurement.

tuned from the resonator frequency ω_r , the resonator can be populated with n_s drive photons which induce Rabi oscillations in the qubit at a frequency of $\nu_{\text{Rabi}} = \sqrt{n_s}g/\pi$. Simultaneously, we perform a continuous dispersive measurement of the qubit state by determining both the phase and the amplitude of a coherent microwave beam transmitted through the resonator at frequency ω_{RF} which is resonant or nearly resonant with the resonator frequency $\omega_r/2\pi \approx 5.4$ GHz [19,22]. The phase shift $\phi = \tan^{-1}(2g^2/\kappa\Delta)\sigma_z$ is the response of our meter from which we determine the qubit population. For the measurement, we chose a resonator that has a quality factor of $Q \sim 0.7 \times 10^4$ corresponding to a photon decay rate of $\kappa/2\pi = 0.73$ MHz. The resonator is populated with $n \sim 1$ measurement photons on average, where n is calibrated using the ac-Stark shift [20]. All experiments are performed in a dilution refrigerator at a temperature of 20 mK. The charging energy of the box is $E_C = e^2/2C \approx h 5.2$ GHz. Details on the device fabrication can be found in Ref. [23].

We initially determine the maximum swing of the meter in a calibration measurement by first maximizing the detuning Δ to minimize the interaction ($g^2/\Delta \rightarrow 0$) which defines $\phi = 0$. We prepare the Cooper pair box in the

ground state $|\downarrow\rangle$ by relaxation, the thermal population of excited states being negligible. The box is biased at charge degeneracy ($E_{el} = 0$), where its energy is to first-order insensitive to charge noise [4]. Using flux bias, the detuning is adjusted to $\Delta/2\pi \approx -1.1$ GHz corresponding to a maximum in the Josephson coupling energy of $E_J/h \approx 4.3$ GHz $< \omega_r/2\pi$. In this case we measure a minimum meter response of $\phi_{|\downarrow\rangle} = -35.3$ deg corresponding to a coupling strength of $g/2\pi = 17$ MHz. Saturating the qubit transition by applying a long microwave pulse which incoherently mixes the ground and excited states such that the occupation probabilities are $P_{|\downarrow\rangle} = P_{|\uparrow\rangle} = 1/2$, the measured phase shift is found to be $\phi = 0$, as expected [20]. From these measurements, the predicted phase shift induced by a fully polarized qubit ($P_{|\uparrow\rangle} = 1$) would be $\phi_{|\uparrow\rangle} = 35.3$ deg. Thus, the maximum swing of the meter is bounded by $\phi_{|\uparrow\rangle} - \phi_{|\downarrow\rangle}$.

In our measurement of Rabi oscillations, a short microwave pulse of length Δt is applied to the qubit in its ground state with a repetition rate of 20 kHz while the measurement response ϕ is continuously monitored and digitally averaged 5×10^4 times; see Fig. 1(b). The signal to noise ratio (SNR) in the averaged value of ϕ in an integration time of 100 ns is approximately 25, see Fig. 2, corresponding to a SNR of 0.1 in a single shot. For the present setup the single shot readout fidelity for the qubit state integrated over the relaxation time ($T_1 \sim 7 \mu\text{s}$) is approximately 30% [24]. Either a readout amplifier with lower noise temperature or a larger signal power would potentially allow a high-fidelity single shot measurement of the qubit state in this setup.

The time dependence of the averaged value of ϕ in response to a π pulse of duration $\Delta t \sim 16$ ns applied to the qubit is shown in Fig. 2(a). Before the start of the pulse the measured phase shift is $\phi_{|\downarrow\rangle} \approx -35.3$ deg corresponding to the qubit being in the ground state. Because of the state change of the qubit induced by the pulse, the resonator frequency is pulled by $2g^2/\Delta$ and, thus, the measured phase shift is seen to rise exponentially towards $\phi_{|\uparrow\rangle}$ with the resonator amplitude response time $2/\kappa \approx 400$ ns, i.e., twice the photon life time. After the π pulse, the qubit excited state decays exponentially with its energy relaxation time $T_1 \sim 7.3 \mu\text{s}$, as extracted from the decay in the measured phase shift; see Fig. 2(a). As a result, the maximum measured response ϕ_{max} does not reach the full value of $\phi_{|\uparrow\rangle}$. In general, the measurement contrast $C = (\phi_{\text{max}} - \phi_{\text{min}})/(\phi_{|\uparrow\rangle} - \phi_{|\downarrow\rangle})$ will be reduced in any qubit readout for which the qubit lifetime is not infinitely longer than the measurement response time. Additionally, in non-QND measurements the contrast is reduced even further due to mixing of the qubit states induced by the interaction with the measurement apparatus. In our QND measurement presented here, the qubit lifetime is about 15 times the response time of the measurement, allowing us to reach a high maximum contrast of $C \sim 85\%$ in the bare measurement response ϕ .

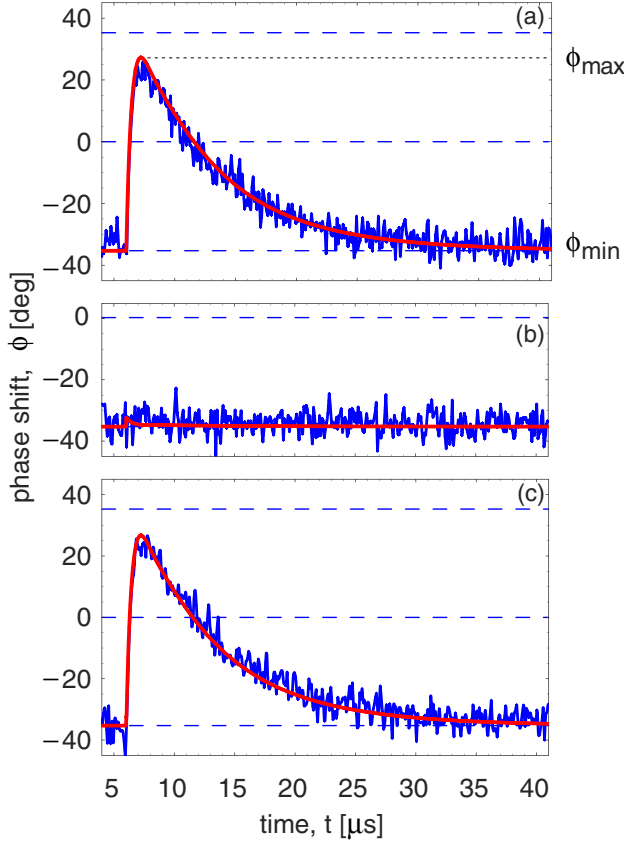


FIG. 2 (color online). Measurement response ϕ (blue lines) and theoretical prediction (red lines) vs time. At $t = 6 \mu$ s (a) a π pulse, (b) a 2π pulse, and (c) a 3π pulse is applied to the qubit. In each panel the dashed lines correspond to the expected measurement response in the ground state $\phi_{||}$, in the saturated state $\phi = 0$, and in the excited state ϕ_{\perp} .

In Figs. 2(b) and 2(c), the measured response ϕ of the meter to a 2π and a 3π pulse acting on the qubit is shown. As expected, no phase shift is observable for the 2π pulse since the response time of the resonator is much longer than the duration $\Delta t = 32$ ns of the pulse. In agreement with the expectations for this QND scheme, the measurement does not excite the qubit, i.e., $\phi_{\min} = \phi_{\max} = \phi_{||}$. The response to the 3π pulse is virtually indistinguishable from the one to the π pulse, as expected for the long coherence and energy relaxation times of the qubit. In the 2D density plot Fig. 3, Rabi oscillations are clearly observed in the phase shift acquired versus measurement time t and Rabi pulse length Δt .

The observed measurement response ϕ is in excellent agreement with theoretical predictions, see red lines in Fig. 2, demonstrating a good understanding of the measurement process. The temporal response $\phi(t) = \arg\{i\langle a(t) \rangle\}$ of the cavity field a is calculated by deriving and solving Bloch-type equations of motion for the cavity and qubit operators [25] using the Jaynes-Cummings Hamiltonian in the dispersive regime [19,20] as the starting

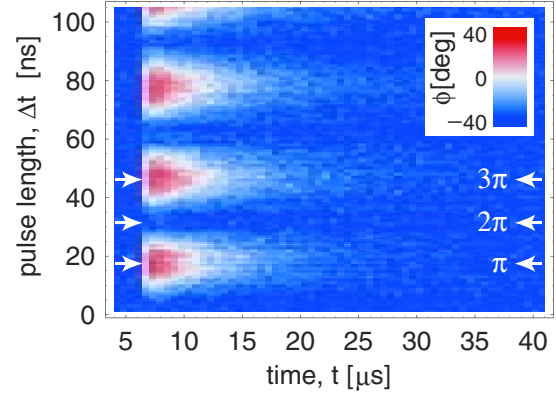


FIG. 3 (color online). Color density plot of phase shift ϕ (see inset for scale) versus measurement time t and Rabi pulse length Δt . Data shown in Fig. 2 are slices through this data set at the indicated pulse lengths.

point. A semiclassical factorization approximation is done to truncate the resulting infinite set of equations to a finite set (e.g., $\langle a^\dagger a \sigma_z \rangle \sim \langle a^\dagger a \rangle \langle \sigma_z \rangle$; all lower order products are kept). This amounts to neglecting higher order correlations between qubit and field which is a valid approximation in the present experiment. The calculations accurately model the exponential rise in the observed phase shift on the time scale of the resonator response time due to a state change of the qubit. They also accurately capture the reduced maximum response ϕ_{\max} due to the exponential decay of the qubit. Overall, excellent agreement in the temporal response of the measurement is found over the full range of qubit and measurement time scales with no adjustable parameters; see Fig. 2.

The visibility of the excited state population $P_{|1\rangle}$ in the Rabi oscillations is extracted from the time dependent measurement response ϕ for each Rabi pulse length Δt . We find $P_{|1\rangle}$ by calculating the normalized dot product between the measured response ϕ and the predicted response taking into account the systematics of the measurement. This amounts to comparing the area under a measured response curve to the theoretically predicted area; see Fig. 2. The averaged response of all measurements taken over a window in time extending from the start of the Rabi pulse out to several qubit decay times T_1 is used to extract $P_{|1\rangle}$. This maximizes the signal to noise ratio in the extracted Rabi oscillations.

The extracted qubit population $P_{|1\rangle}$ is plotted versus Δt in Fig. 4(a). We observe a visibility of $95 \pm 6\%$ in the Rabi oscillations with error margins determined from the residuals of the experimental $P_{|1\rangle}$ with respect to the predicted values. Thus, in a measurement of Rabi oscillations in a superconducting qubit, a visibility in the population of the qubit excited state that approaches unity is observed for the first time. Moreover, the decay in the Rabi oscillation amplitude out to pulse lengths of 100 ns is very small and consistent with the long T_1 and T_2 times of this charge

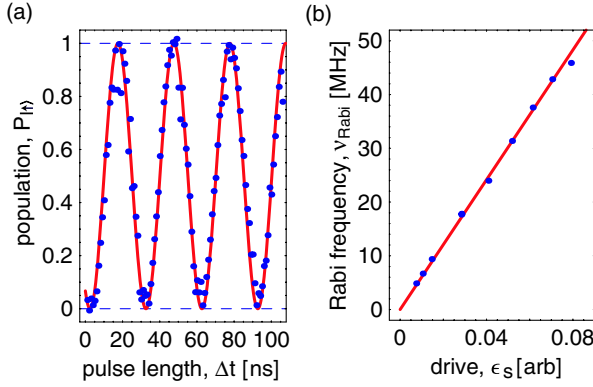


FIG. 4 (color online). (a) Rabi oscillations in the qubit population $P_{|\uparrow\rangle}$ vs Rabi pulse length Δt (blue dots) and fit with unit visibility (red line). (b) Measured Rabi frequency ν_{Rabi} vs pulse amplitude ϵ_s (blue dots) and linear fit.

qubit; see Fig. 4(a) and Ramsey experiment discussed below. We have also verified the expected linear scaling of the Rabi frequency ν_{Rabi} with the pulse amplitude $\epsilon_s \propto \sqrt{n_s}$; see Fig. 4(b).

We have determined the coherence time of the Cooper pair box from a Ramsey fringe experiment at charge degeneracy using $\pi/2$ pulses of 20 ns duration; see Fig. 1(c). To avoid dephasing induced by a weak continuous measurement beam [20] we switch on the measurement beam only after the end of the second $\pi/2$ pulse. The resulting Ramsey fringes oscillating at the detuning frequency $\delta_{a,s} = \omega_a - \omega_s \sim 6$ MHz decay with a long coherence time of $T_2 \sim 500$ ns; see Fig. 5(a). The corresponding qubit phase quality factor of $Q_\phi = T_2 \omega_a / 2 \sim 6500$ is

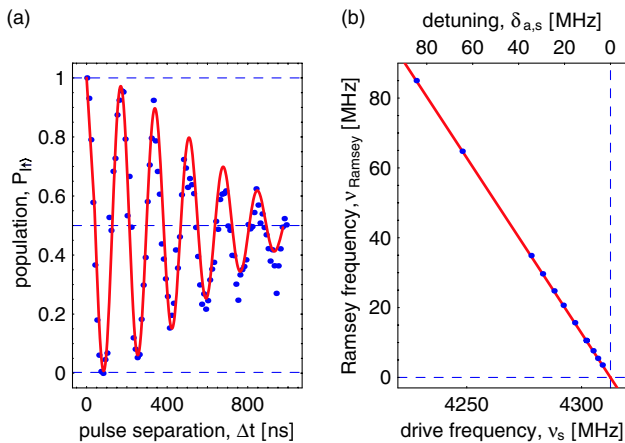


FIG. 5 (color online). (a) Measured Ramsey fringes (blue dots) observed in the qubit population $P_{|\uparrow\rangle}$ vs pulse separation Δt using the pulse sequence shown in Fig. 1(b) and fit of data to sinusoid with Gaussian envelope (red line). (b) Measured dependence of Ramsey frequency ν_{Ramsey} on detuning $\delta_{a,s}$ of drive frequency (blue dots) and linear fit (red line).

similar to the best values measured so far in qubits biased at an optimal point [4]. The Ramsey frequency is shown to depend linearly on the detuning $\delta_{a,s}$, as expected; see Fig. 5(b). We note that a measurement of the Ramsey frequency is an accurate time resolved method to determine the qubit transition frequency $\omega_a = \omega_s + 2\pi\nu_{\text{Ramsey}}$.

In conclusion, performing Rabi and Ramsey experiments we have observed high visibility in the oscillations of state population of a superconducting qubit. The temporal response and the backaction of the readout are quantitatively understood and well characterized. Our charge qubit, which is embedded in a well-controlled electromagnetic environment, has T_1 and T_2 times among the longest realized so far in superconducting systems. The simplicity and level of control possible in this circuit QED architecture makes it an attractive candidate for superconducting quantum computation.

We thank Jay Gambetta for discussions. This work was supported in part by NSA and ARDA under ARO Contract No. DAAD19-02-1-0045, and the NSF under Grants No. ITR-0325580 and No. DMR-0342157, the David and Lucile Packard Foundation, the W.M. Keck Foundation, and the NSERC of Canada.

-
- [1] M. A. Nielsen and I. L. Chuang, *Quantum Computation and Quantum Information* (Cambridge University Press, Cambridge, 2000).
 - [2] M. H. Devoret, A. Wallraff, and J. M. Martinis, cond-mat/0411174.
 - [3] Y. Nakamura, Y. A. Pashkin, and J. S. Tsai, *Nature* (London) **398**, 786 (1999).
 - [4] D. Vion *et al.*, *Science* **296**, 886 (2002).
 - [5] J. M. Martinis *et al.*, *Phys. Rev. Lett.* **89**, 117901 (2002).
 - [6] Y. Yu *et al.*, *Science* **296**, 889 (2002).
 - [7] I. Chiorescu *et al.*, *Science* **299**, 1869 (2003).
 - [8] E. Collin *et al.*, *Phys. Rev. Lett.* **93**, 157005 (2004).
 - [9] A. J. Berkley *et al.*, *Science* **300**, 1548 (2003).
 - [10] Y. A. Pashkin *et al.*, *Nature* (London) **421**, 823 (2003).
 - [11] J. B. Majer *et al.*, *Phys. Rev. Lett.* **94**, 090501 (2005).
 - [12] I. Chiorescu *et al.*, *Nature* (London) **431**, 159 (2004).
 - [13] R. McDermott *et al.*, *Science* **307**, 1299 (2005).
 - [14] T. Yamamoto *et al.*, *Nature* (London) **425**, 941 (2003).
 - [15] R. Simmonds *et al.*, *Phys. Rev. Lett.* **93**, 077003 (2004).
 - [16] F. Meier and D. Loss, *Phys. Rev. B* **71**, 094519 (2005).
 - [17] T. Duty *et al.*, *Phys. Rev. B* **69**, 140503 (2004).
 - [18] O. Astafiev *et al.*, *Phys. Rev. B* **69**, 180507 (2004).
 - [19] A. Blais *et al.*, *Phys. Rev. A* **69**, 062320 (2004).
 - [20] D. I. Schuster *et al.*, *Phys. Rev. Lett.* **94**, 123602 (2005).
 - [21] V. Bouchiat *et al.*, *Phys. Scr.* **176**, 165 (1998).
 - [22] A. Wallraff *et al.*, *Nature* (London) **431**, 162 (2004).
 - [23] L. Frunzio *et al.*, *IEEE Trans. Appl. Supercond.* **15**, 860 (2005).
 - [24] D. I. Schuster *et al.* (unpublished).
 - [25] A. Blais *et al.* (unpublished).

Fabrication and Characterization of Superconducting Circuit QED Devices for Quantum Computation

Luigi Frunzio, Andreas Wallraff, David Schuster, Johannes Majer, and Robert Schoelkopf

Abstract—We present fabrication and characterization procedures of devices for circuit quantum electrodynamics (cQED). We have made 3-GHz cavities with quality factors in the range 10^4 – 10^6 , which allow access to the strong coupling regime of cQED. The cavities are transmission line resonators made by photolithography. They are coupled to the input and output ports via gap capacitors. An Al-based Cooper pair box is made by e-beam lithography and Dolan bridge double-angle evaporation in superconducting resonators with high quality factor. An important issue is to characterize the quality factor of the resonators. We present an RF-characterization of superconducting resonators as a function of temperature and magnetic field. We have realized different versions of the system with different box-cavity couplings by using different dielectrics and by changing the box geometry. Moreover, the cQED approach can be used as a diagnostic tool of qubit internal losses.

Index Terms—Distributed parameter circuits, Q factor, scattering parameters measurement, superconducting cavity resonators.

I. INTRODUCTION

WE have recently demonstrated that a superconducting quantum two-level system can be strongly coupled to a single microwave photon [1], [2]. The strong coupling between a quantum solid state circuit and an individual photon, analogous to atomic cavity quantum electrodynamics (CQED) [3], has previously been envisaged by many authors, see [4] and references therein. Our circuit quantum electrodynamics architecture [4], in which a superconducting charge qubit, the Cooper pair box (CPB) [5], is coupled strongly to a coplanar transmission line resonator, has great prospects both for performing quantum optics experiments [6] in solids and for realizing elements for quantum information processing [7] with superconducting circuits [8]–[14] and also for other architectures [15], [16].

In developing these qubit-resonator systems, one key ingredient is to design and realize transmission line resonators with high internal quality factor, Q_{int} , and with resonant frequency, ν_o , in the 5–15 GHz range to match the other energy scales of our device, and to be in the quantum regime ($h\nu_o \gg k_B T$) at $T = 30$ mK. On the other hand, the resonator is loaded with input and output capacitances and we need a loaded quality

factor $Q_L \approx 10^4$ in order to obtain reasonably fast rate of measurement, $\kappa = \nu_o/Q_L \approx 1$ MHz.

In fabricating the transmission line resonator, we opted for a coplanar waveguide (CPW) for many different reasons. First, a CPW has a simple layer structure with no need for deposited insulators. Second, it has a balanced structure with a relatively easy planar connection to the CPB. Third, a CPW has a ν_o that is relatively insensitive to kinetic inductance and dominated by geometrical distributed inductance. Last but not the least, CPW-based structures, made by Al thin film deposited on sapphire, have been recently shown [17] to allow very high Q 's (order of 10^6).

We decided to fabricate on passivated Si wafers because this is the substrate on which we had previously developed the qubit fabrication. We also decided to try as material for the resonators both Al, for easy compatibility with the qubit process, and Nb, because its higher critical temperature allows testing of resonators at higher temperatures.

In Section II, we present design consideration for devices for circuit quantum electrodynamics (cQED). We will show that we can engineer Q with different coupling of the resonator to the input and output ports and that the internal losses can be made negligible at the designed Q [1], [2]. Section III introduces the fabrication procedures for both the resonator and the CPB. Sections IV–VI present an RF-characterization of the superconducting transmission line resonators versus temperature and magnetic field.

II. CIRCUIT DESIGN

A picture of a 10×3 mm² chip containing a 3-GHz superconducting Nb CPW resonator is shown in Fig. 1(a). The length of the meandering resonator is $2l = 4$ mm. The center conductor is $10 \mu\text{m}$ wide, separated from the lateral ground planes extending to the edges of the chip by a $5 \mu\text{m}$ gap, resulting in a wave impedance of the coplanar waveguide of $Z = 50 \Omega$ to match the impedance of conventional microwave components. The capacitance per unit length is $C_s \approx 0.13$ fF/ μm^2 which gives a total resonator capacitance of $C = C_s l/2 = 1.6$ pF. The resonator is coupled by identical capacitors at each end (see solid line square in Fig. 1(a)) to an input and output feed line, fanning out to the edge of the chip and keeping the impedance constant. In Fig. 1(b) and (1d) are shown micrographs of two of the coupling capacitors with different geometries. The one in Fig. 1(b) consists of two $100\text{-}\mu\text{m}$ long and $4\text{-}\mu\text{m}$ wide fingers separated by a $2\text{-}\mu\text{m}$ gap. It has a capacitance, $C_{\kappa,b} \approx 6$ fF, larger than that in Fig. 1(d), which has a simpler geometry with a $4\text{-}\mu\text{m}$ gap and $C_{\kappa,d} \approx 0.3$ fF.

Manuscript received October 4, 2004. This work was supported in part by the National Security Agency (NSA) and Advanced Research and Development Activity (ARDA) under Army Research Office (ARO) Contract DAAD19-02-1-0045, the NSF ITR Program under Grant DMR-0325580, the NSF under Grant DMR-0342157, the David and Lucile Packard Foundation, and the W. M. Keck Foundation.

The authors are with the Department of Applied Physics, Yale University, New Haven, CT 06520 USA (e-mail: luigi.frunzio@yale.edu).

Digital Object Identifier 10.1109/TASC.2005.850084

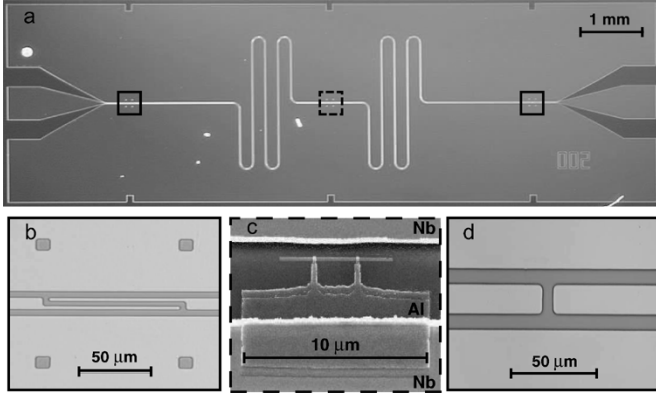


Fig. 1. Picture of a device for circuit QED. (a) The 3 GHz superconducting coplanar waveguide resonator is fabricated using optical lithography. The length of the meandering resonator is $l = 24$ mm. The center conductor is $10 \mu\text{m}$ wide, separated from the lateral ground planes extending to the edges of the chip by a $5 \mu\text{m}$ gap. The resonator is coupled by identical capacitors at each end (solid line squares) to input and output ports. (b) Micrograph of a coupling capacitance with two $100 \mu\text{m}$ long and $4 \mu\text{m}$ wide fingers separated by a $2 \mu\text{m}$ gap. (c) Scanning electron micrograph of a Cooper pair box fabricated onto the silicon substrate into the gap between the center conductor (top) and the ground plane (bottom) in the center of a resonator (dashed line square) using electron beam lithography and double angle evaporation of aluminum. (d) Micrograph of a coupling capacitance with a $4 \mu\text{m}$ gap.

The capacitive coupling to the input and output lines, together with the loading impedance, $R_L = 50 \Omega$, are very important in determining the loaded quality factor Q_L , defined by

$$\frac{1}{Q_L} = \frac{1}{Q_{\text{int}}} + \frac{1}{Q_{\text{ext}}} \quad (1)$$

where the external quality factor is

$$Q_{\text{ext}} = \frac{\omega C}{G_{\text{ext}}} \quad (2)$$

with

$$G_{\text{ext}} = \frac{2R_L C_\kappa^2 \omega^2}{1 + R_L^2 C_\kappa^2 \omega^2}. \quad (3)$$

There are two possible regimes for the resonator. It can be undercoupled when C_κ is small (like $C_{\kappa,d}$) and then $Q_L \approx Q_{\text{int}}$. This is the regime in which it is possible to measure Q_{int} . Otherwise, the resonator can be overcoupled when C_κ is large (like $C_{\kappa,b}$) and then $Q_L \approx Q_{\text{ext}}$. It is then possible to engineer the Q_L to obtain fast measurement with κ much larger than the qubit decay rates [1], [2].

In Fig. 1(c) an electron micrograph of a Cooper pair box is shown. The CPB consists of a $7\text{-}\mu\text{m}$ long and 200-nm wide superconducting island parallel to the center conductor which is coupled via two $200 \times 100 \text{ nm}^2$ size Josephson tunnel junctions to a much larger superconducting reservoir. The CPB is fabricated onto the silicon substrate [see dashed line square in Fig. 1(a)] in the gap between the center conductor (top) and the ground plane (bottom) at an antinode of the electric field in the resonator. The Josephson junctions are formed at the overlap between the island and the fingers extending from the reservoir, which is capacitively coupled to the ground plane. The CPB is a two-state system described by the Hamiltonian $H =$

$-(E_{el}\sigma_x + E_J\sigma_z)/2$ where E_{el} is the electrostatic energy and $E_J = E_{J,max} \cos(\pi\Phi_b)$ is the Josephson energy. The overall energy scales of these terms, the charging energy E_{el} and the Josephson energy $E_{J,max}$, can be readily engineered during the fabrication by the choice of the total box capacitance and resistance respectively, and then further tuned *in situ* by electrical means. A flux bias $\Phi_b = \Phi/\Phi_o$, applied with an external coil to the loop of the box, controls E_J . We have demonstrated that changing the length of the CPB island and its distance to the center conductor and changing the dielectrics (removing the passivation step of the Si substrate), we can obtain stronger couplings of qubit and resonator as predicted by simple electrostatic calculations of the capacitances.

III. DEVICE FABRICATION

The pattern of 36 different Nb resonators is generated exposing a bilayer photoresist (600 nm LOR5A and $1.2 \mu\text{m}$ S1813) through a mask with traditional UV photolithography. Then a 200-nm thick Nb film is dc magnetron sputtered in Ar at 1.5 Pa with a rate of 1 nm/s in an UHV system with a base pressure of $20 \mu\text{Pa}$. The substrate is a $2''$ $300\text{-}\mu\text{m}$ thick p-doped (Boron) (100) oriented Si wafer with resistivity $\rho > 1000 \Omega\text{cm}$ previously passivated by thermal wet oxidation with a 470-nm thick layer of SiO_2 . A lift-off process in NMP followed by ultrasonic agitation completes the resonator fabrication.

Al resonators are fabricated on the same type of substrate depositing a 200-nm thick Al film by thermal evaporation at a rate of 1 nm/s in the same UHV system. Then the same mask is used to expose a single photoresist layer ($1.2 \mu\text{m}$ S1813) and then realized by wet etching ($8 : 4 : 1 : 1 = \text{H}_3\text{PO}_4 : \text{CH}_3\text{COOH} : \text{HNO}_3 : \text{H}_2\text{O}$) the metal.

In both cases, chips containing individual resonators are obtained by dicing the Si wafer. The CPB qubit [Fig. 1(c)] is then fabricated on an individual resonator by a simple Dolan bridge technique [18] exposing a bilayer resist (500 nm MMA-(8.5)MAA EL13 and 100 nm 950 K PMMA A3) by e-beam lithography and then e-beam evaporating Al (35 nm for the base and 70 nm for the top electrode) at a rate of 1 nm/s in a double-angle UHV system with a base pressure of $20 \mu\text{Pa}$. The junction barrier is realized with a 12 min thermal oxidation in a 400 Pa of O_2 . A lift-off process in hot acetone and ultrasonic agitation complete the device. To couple the qubit reservoir to ground with a large capacitance, the base electrode is deposited with a little angle taking advantage of the shadow of the thicker Nb film to define the capacitor.

IV. MEASUREMENT TECHNIQUE

The frequency dependence of the transmission through the resonators¹ was measured using a vector network analyzer. The equivalent circuit of the measurement setup is shown in the inset of Fig. 3. The sample was mounted on a PC board in a closed copper sample box (Fig. 2) equipped with blind mate SMP connectors that launch the microwaves onto the PC board CPW's. The sample was cooled to temperatures ranging from

¹The transmission is measured in $\text{dB} = 10 \log |V_2/V_1|^2$, where V_2 is the voltage measured at the input port of the analyzer and V_1 is the voltage applied at the output port of the analyzer.

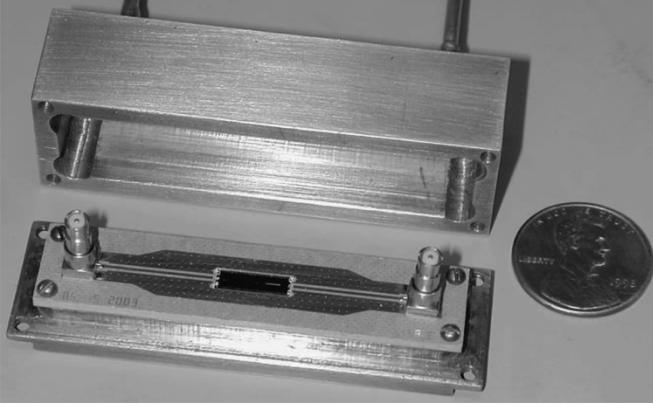


Fig. 2. Picture of the copper sample box containing a resonator mounted on the PC board.

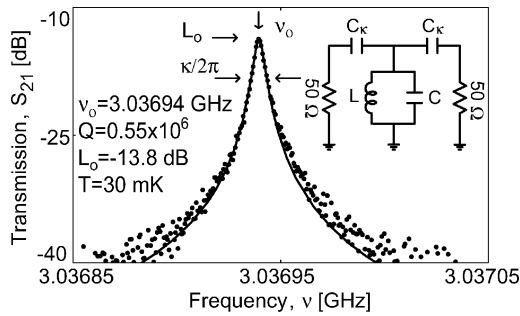


Fig. 3. Measured transmission power spectrum of an undercoupled resonator. The solid line is a fit to a Lorentzian line.

the critical temperature, T_c of the superconducting films down to $T = 30$ mK.

The transmission S_{21} through the resonator around its fundamental resonant frequency ν_o is shown in Fig. 3 at $T = 30$ mK. The curve was acquired using a -60 dBm input power² and a room temperature amplifier. The input power was lowered until no distortion of the resonance curve due to excessive input power could be observed. The network analyzer was response calibrated (S_{21}) up to the input and output ports of the cryostat and the absorption of the cabling in the cryostat was determined to be approximately -7 dB in a calibrated S_{11} and S_{22} reflection measurement. The quality factor of the resonator is determined by fitting a Lorentzian line to the measured power spectrum as shown by the solid line in Fig. 3. This is the power spectrum of an undercoupled resonator and from the fit we have extracted $\nu_o = 3.03694$ GHz. At this frequency the insertion loss is $L_o = -13.8$ dB. The quality factor is determined from the full width at half max of the fitted power spectrum and is found to be $Q_L \approx Q_{\text{int}} = \nu_o/2\delta\nu_o = 2\pi\nu_o/\kappa = 0.55 \times 10^6$.

V. TEMPERATURE DEPENDENCE OF Q AND ν_o

In Fig. 4, we show the measured temperature dependence of the quality factor Q for an undercoupled resonator (solid dots) and an overcoupled one (open dots). The lines in Fig. 4 are generated by summing a Q_{int} that scales exponentially with the reduced temperature, T_c/T , in parallel with a constant Q_{ext} . At

²The input power is in dBm where -60 dBm = $20 \log(1 \mu\text{W}/1 \text{ mW})$.

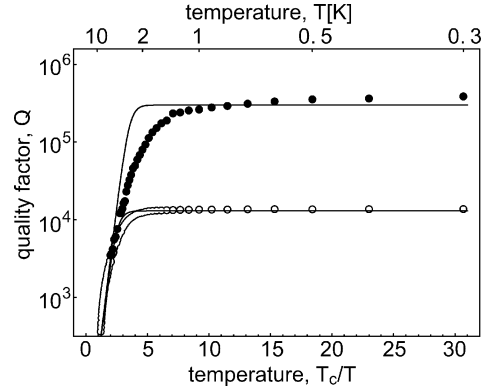


Fig. 4. Temperature dependence of the quality factor Q of two 3 GHz superconducting Nb coplanar waveguide resonators at their first harmonic resonant frequency (6 GHz). Solid dots are data collected on a undercoupled resonator and open dots are from an overcoupled one. The lines are generated by summing a Q_{int} that scales exponentially with the reduced temperature, T_c/T , in parallel with a constant Q_{ext} .

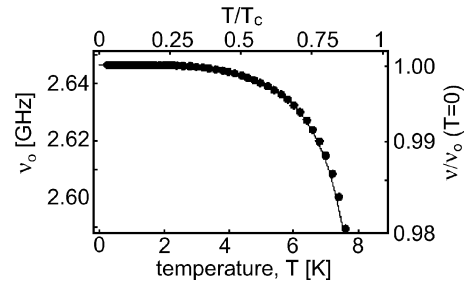


Fig. 5. Temperature dependence of the resonant frequency ν_o of a superconducting Nb coplanar waveguide resonator. Solid line is a fit to a kinetic inductance model.

low temperature, the coupling saturates the Q of the overcoupled resonator, while it seems that Q for the undercoupled one has still some weak temperature dependence whose nature is still unknown. We speculate that either vortices or losses in the dielectrics could limit the Q of this resonator but neither of these interpretations offer an easy understanding of the weak temperature dependence.

We have observed a shift of the resonant frequency ν_o with temperature as shown in Fig. 5, which can be understood in terms of the temperature dependent kinetic inductance of the resonator [17], [19]. ν_o is proportional to $1/\sqrt{L}$, where the total inductance of the resonator L is the sum of the temperature independent geometric inductance L_m and the temperature dependent kinetic inductance L_k . The kinetic inductance scales as $L_k \propto \lambda_L(T)^2$, where $\lambda_L(T)$ is the temperature dependent London penetration depth. The best fit in Fig. 4 was achieved for a ratio $L_k/L_m \approx 4\%$ and a critical temperature of $T_c \approx 8.75$ K, which we have independently measured on a test sample fabricated on the same wafer.

VI. MAGNETIC FIELD DEPENDENCE OF Q

As explained in Section II, we need to apply a magnetic field perpendicular to the qubit loop in order to tune E_J . Then, we measured the quality factor of two resonators as a function of the magnetic field at $T = 300$ mK, as shown in Fig. 6. It is evident that the Nb film (upper part) is less sensitive to the applied

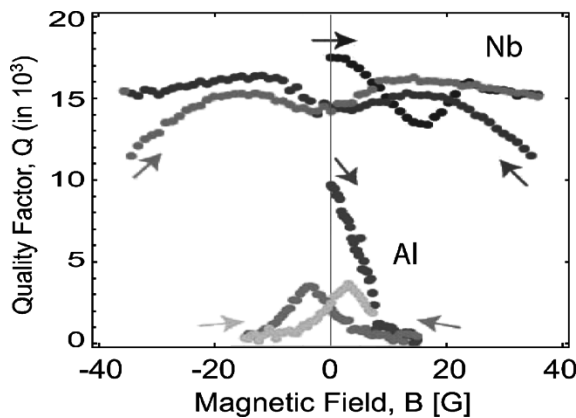


Fig. 6. Magnetic field dependence of the quality factor Q of two different superconducting coplanar waveguide resonators at $T = 300$ mK. In the upper part data refer to a Nb resonator, while in the lower part they refer to an Al resonator. Arrows indicate the direction in which the magnetic field was swept in both case starting from zero.

field than the Al film (lower part). In both cases there seems to be a reproducible and irreversible hysteretic behavior that can be reset by thermal cycling the sample. In our recent works [1], [2] we have observed a focusing effect on the magnetic field such that the effective field in the gap of the resonator was approximately two orders of magnitude larger than the applied magnetic field. We believe that the hysteretic phenomena could be in fact a result of vortices being trapped in the resonator film due to these large effective fields.

VII. CONCLUSION

In summary, we have designed and fabricated devices for realizing a circuit quantum electrodynamics architecture in which a qubit can be strongly coupled to a single microwave photon. We have shown that we can engineer Q with different coupling of the resonator to the input and output ports and that the internal losses can be made negligible at the designed Q . Indeed, we have achieved high $Q = 0.55 \times 10^6$ in the undercoupled CPW resonators and $Q \approx 10^4$ in the overcoupled ones, which allow fast measurement of the qubit.

To help determine the mechanism of the losses, one can fabricate resonators on different substrates [Si with different resistivity, sapphire, Si_3N_4], or in different superconductors (Ta, Al). In fact, quality factor measurements in this type of resonant circuits serve as a sensitive probe of material losses in dielectrics and superconductors in the GHz frequency range at millikelvin temperatures. These presently unknown properties may in fact pose a serious limit for all superconducting qubits, though the large internal Q 's already observed are highly encouraging. Better knowledge of the material losses, and tech-

niques to characterize them, may be crucial not only for future improvements of circuit QED devices, but also for designing and realizing robust, long-lived superconducting qubits.

REFERENCES

- [1] A. Wallraff, D. Schuster, A. Blais, L. Frunzio, R.-S. Huang, J. Majer, S. Kumar, S. Girvin, and R. Schoelkopf, "Strong coupling of a single photon to a superconducting qubit using circuit quantum electrodynamics," *Nature*, vol. 431, pp. 162–167, 2004.
- [2] D. Schuster, A. Wallraff, A. Blais, L. Frunzio, R.-S. Huang, J. Majer, S. M. Girvin, and R. J. Schoelkopf, "AC-Stark shift and dephasing of a superconducting qubit strongly coupled to a cavity field," *Phys. Rev. Lett.*, to be published.
- [3] H. Mabuchi and A. Doherty, "Cavity quantum electrodynamics: Coherence in context," *Science*, vol. 298, pp. 1372–1377, 2002.
- [4] A. Blais, R.-S. Huang, A. Wallraff, S. Girvin, and R. Schoelkopf, "Cavity quantum electrodynamics for superconducting electrical circuits: an architecture for quantum computation," *Phys. Rev. A*, vol. 69, p. 062 320, 2004.
- [5] V. Bouchiat, D. Vion, P. Joyez, D. Esteve, and M. H. Devoret, "Quantum coherence with a single Cooper pair," *Physica Scripta*, vol. T76, pp. 165–170, 1998.
- [6] D. Walls and G. Milburn, *Quantum Optics*. Berlin, Germany: Springer-Verlag, 1994.
- [7] M. A. Nielsen and I. L. Chuang, *Quantum Computation and Quantum Information*. Cambridge, U.K.: Cambridge Univ. Press, 2000.
- [8] Y. Nakamura, Y. A. Pashkin, and J. S. Tsai, "S. Coherent control of macroscopic quantum states in a single-Cooper-pair box," *Nature*, vol. 398, pp. 786–788, 1999.
- [9] D. Vion, A. Aassime, A. Cottet, P. Joyez, H. Pothier, C. Urbina, D. Esteve, and M. H. Devoret, "Manipulating the quantum state of an electrical circuit," *Science*, vol. 296, pp. 886–889, 2002.
- [10] J. M. Martinis, S. Nam, J. Aumentado, and C. Urbina, "Rabi oscillations in a large Josephson-junction qubit," *Phys. Rev. Lett.*, vol. 89, p. 117 901, 2002.
- [11] Y. Yu, S. Han, X. Chu, S.-I. Chu, and Y. Wang, "Coherent temporal oscillations of macroscopic quantum states in a Josephson junction," *Science*, vol. 296, pp. 889–892, 2002.
- [12] I. Chiorescu, Y. Nakamura, C. J. P. M. Harmans, and J. E. Mooij, "Coherent quantum dynamics of a superconducting flux qubit," *Science*, vol. 299, pp. 1869–1871, 2003.
- [13] T. Yamamoto, Y. A. Pashkin, O. Astafiev, Y. Nakamura, and J. S. Tsai, "Demonstration of conditional gate operation using superconducting charge qubits," *Nature*, vol. 425, pp. 941–944, 2003.
- [14] I. Chiorescu, P. Bertet, K. Semba, Y. Nakamura, C. J. P. M. Harmans, and J. E. Mooij, "Coherent dynamics of a flux qubit coupled to a harmonic oscillator," *Nature*, vol. 431, pp. 159–162, 2004.
- [15] A. S. Srensen, C. H. van derWal, L. Childress, and M. D. Lukin, "Capacitive coupling of atomic systems to mesoscopic conductors," *Phys. Rev. Lett.*, vol. 92, p. 063 601, 2004.
- [16] L. Tian, P. Rabl, R. Blatt, and P. Zoller, *Interfacing Quant. Opt. Solid State Qubits*, to be published.
- [17] P. K. Day, H. G. LeDuc, B. A. Mazin, A. Vayonakis, and J. Zmuidzinas, "A broad-band superconducting detector suitable for use in large arrays," *Nature*, vol. 425, pp. 817–821, 2003.
- [18] G. J. Dolan, "Offset masks for lift-off processing," *Appl. Phys. Lett.*, vol. 31, pp. 337–339, 1977.
- [19] K. Yoshida, K. Watanabe, T. Kisu, and K. Enpuku, "Evaluation of magnetic penetration depth and surface resistance of superconducting thin films using coplanar waveguides," *IEEE Trans. Appl. Supercond.*, vol. 5, no. 2, pp. 1979–1982, Jun. 1995.

8. Fabrication techniques used for this work

Superconducting circuits including Josephson tunnel junctions and connecting wires are fabricated using techniques developed for conventional semiconducting integrated circuits. Using these methods circuits containing up to several thousands junctions have been successfully fabricated for applications like the Josephson processor and the voltage standard. In our case, the challenge comes from junction areas that need two to four orders of magnitude smaller than in those applications. In fact, the fabrication of reliable devices, whose typical junction size ($0.1 \times 0.1 \mu\text{m}$) is comparable to the grain size of the superconducting materials used for realizing the electrodes, implies dealing with grain and perimeter effects, barrier properties changing in time and so on. We indicate in this chapter the main features of the fabrication protocols of our devices.

8.1. Substrates

Typically superconducting circuits have been fabricated on silicon substrates, which allow for conducting layer at room temperature to reduce effects of statical discharge, while becoming insulators at low temperature.

To start, we use as substrates single side polished 2" silicon wafer doped with boron (acceptor type p) with medium resistivity ($>1 \text{ k}\Omega\text{cm}$) cut out of a single crystal, realized by Floating Zone process, with orientation (100) and thickness of $300 \mu\text{m}$. The wafers have been bought from Siltronix SAS, a French-Swiss company. They are used as they come out of the package with just a very thin natural oxide on their surface, which does not withstand the following metal depositions. Whenever, instead, we want to perform room temperature resistance measurements on our samples, we need electrical insulation between the different parts of the circuit. We achieve this result either by oxidation of the substrate surface or by using insulating substrates.

In the first case, the surface of the wafers is thoroughly cleaned immersing it in two solvents, first acetone and then methanol, while ultrasounding it at each step. It is then immersed in a hydrofluoric acid based buffer oxide etching solution to remove the natural oxide and washed with de-ionized water. Immediately after, a wet oxidation process in an oven at 1000 C follows to grow a good silicon dioxide insulating layer. In some circuit

QED experiments, we wanted to modify the coupling between resonator and CPB and we did that also varying the oxide thickness. We realized silicon dioxide thickness of 230, 360 and 470 nm keeping the substrate in the hot oven for respectively 60, 80 and 100 minutes.

In the second case, we use single side epipolished 2" sapphire wafers with a (1102) R-plane orientation and a thickness of 430 μm , obtained from CrysTec, a German substrate provider. Sapphire may also improve the quality of the metal deposition because of the better lattice match with aluminum, niobium and tantalum we can achieve.

We wanted also to test if the resistivity of the substrate affects our circuit QED experiments. The idea is that higher resistivity substrates, as we could obtain from less doped silicon, could modify the charge noise experienced by the qubit. For these experiments, we use single side polished 2" silicon wafer doped with boron but this time with high resistivity ($>20 \text{ k}\Omega\text{cm}$), without changing single crystal process, orientation and thickness.

In circuit QED experiments, to eliminate some of the possible modes in the sample set-up which may be affecting the quality of the resonators, we decided to modify the RF-tight box in which the sample is allocated. The new set-up requires thicker substrate and in it we use single side polished 2" silicon wafer doped with boron with high resistivity ($>20 \text{ k}\Omega\text{cm}$) and thickness of 500 μm , all the other properties unchanged.

Also in the case of high resistivity silicon wafers, we fabricated circuits on the bare substrate but also on substrates that had been oxidized with the process described before.

8.2. Optical photolithography for resonator patterning

At the beginning of any lithographic process, the first thing to do is to make sure that the substrate surface is clean. This is essential to achieve a good resist adhesion and to remove specks of dust, which obstruct the proper spinning and patterning of the resist. To clean the substrate surface, we immerse the substrate in two solvents, first acetone and then methanol, and we ultrasound it in each step. Then in the case of optical photolithography, we wash the substrate with de-ionized water and we blow nitrogen on it to quickly dry the sample.

The resonators, used in this work, have been realized using a lift-off technique. In this technique, a resist is spun and patterned on the substrate. After that, a thin film is deposited and it will stick to the substrate only on the portion of it where the resist has been removed. On the contrary, the parts of the film deposited on the resist are lifted-off together with the resist when the latter is removed by an immersion in the proper solvent. The lift-off works well if the resist profile has the right “mushroom” shape, shown in Fig. 8.1, so that the thin metal film cannot be deposited on the side wall of the patterned resist. We realize this profile by using a double layer resist process.

The first layer is made by a pre-exposed resist, Microchem-LOR 5A, composed by propylene glycol methyl ether solved in cyclopentanone. We spin this resist at 4000 rpm for 60 s to obtain a thickness of about 500 nm. This resist is removed during the development stage at a rate which is inversely proportional to the baking temperature. Because we want to obtain low development speed we bake it at 195 C for about 15 minutes. The prolonged high temperature baking also helps to harden the resist layer to reduce intermixing with the next layer, since the two resist have a very similar chemistry. After that, we spin a second layer with a common photo-sensitive resist Rohm and Haas-S1808, containing propylene glycol monomethyl ether acetate, at 4000 rpm for 60 s to obtain a thickness of about 750 nm. We bake the double layer again at 115 C for 1 minute. This resist will be developed and removed only in the region where the polymer bonds are weakened by the exposure to energy delivered by photons in the 350-450 nm wavelength region. The pre-exposed resist is instead insensitive to exposure giving some level of “orthogonality” between the two resist layer behaviors that allows for properly shaping them.

The UV exposure of the resist covered sample is done in an EVG620 maskaligner through a chromium-on-soda lime glass mask with a mercury lamp light whose energy density is about 31 mJ/cm^2 , as measured at a wavelength of 365 nm.

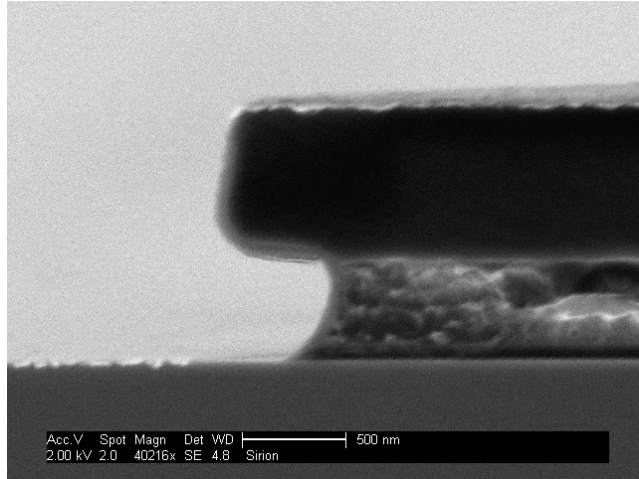


Figure 8.1. The double layer resist “mushroom”. SEM image of a resist bilayer realized at Yale. The two resists used are 500 nm thick Microchem-LOR5A and 720 nm thick Rohm and Haas-S1808. In order to realize a good lift-off, the lower part of the resist complex has been developed more than the upper part. Indeed, this profile obstructs the thin metal film directional deposition on the resist side wall, improving the separation with the film deposited on the substrate. This image has been realized after depositing few nm of copper on the resist bilayer and using a 2 keV electron beam for the shortest time possible to avoid overcharging of the insulating surface and the consequent melting of the resist.

Then, we develop the double layer resist by immersion in a developer called MF-319, which is a 0.237 N solution of tetra methyl ammonium hydroxide (TMAH, $(\text{CH}_3)_4\text{NOH}$) in water, for 140 s. This developer dissolves the resist where the mask was not protecting it from the UV photon exposure. After 25 to 40 s the top resist is fully developed and the remaining time allows us to obtain the desired undercut size in the lower resist layer. Optical microscope inspection of the sample verifies the quality of the process each time. At this point, we proceed to the metal deposition. We have fabricated some of the resonators by depositing 180 nm of aluminum by e-beam evaporation, a very directional deposition procedure.

The e-beam evaporation is performed in a UHV Plassys system with a liquid nitrogen trap. The base pressure is about 4.4×10^{-6} Pa, immediately after a short titanium getter deposition. The aluminum deposition rate is 0.5 nm/s, while the sample is rotating at a speed of 10 rpm and was oriented 3.5 degree off the normal from the crucible to obtain a side wall profile of the resonator with a nice 35 degree slope out of the vertical, shown in

Fig. 8.2. This slope will be used to facilitate the step coverage during the deposition of subsequent metal or insulating layers.

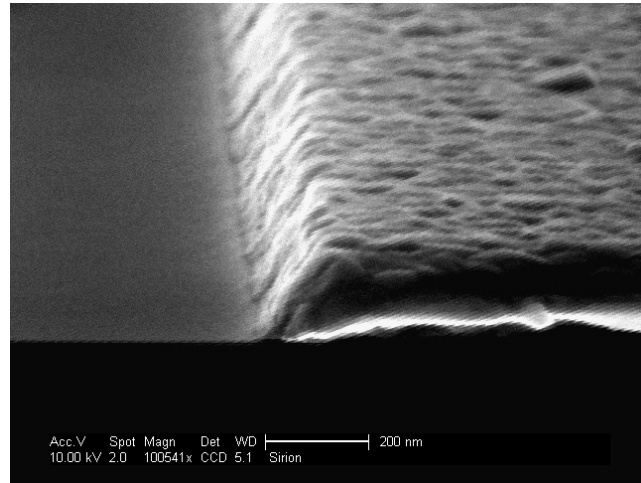


Figure 8.2. Aluminum profile after lift-off. SEM image of the profile of an aluminum resonator realized at Yale. The film thickness is 180 nm. The slope size is 130 nm, which gives for the side wall an angle of 35 deg out of the vertical. This image has been realized with a 10 keV electron beam.

The lift-off process is completed by one hour immersion in 50 C Microchem-PG Remover, based on 1-methyl 2-pyrrolidinone, followed by 60 s in ultrasound bath. This step completely remove the metal film deposited on the resist surface.

Other resonators have been fabricated depositing 200 nm thick niobium by dc magnetron sputtering, which on the contrary is an isotropic deposition procedure. The dc sputtering is performed in a UHV K.J. Lesker system with a base pressure of 1.3×10^{-6} Pa. The deposition rate is 1.25 nm/s in an argon plasma with a pressure of 0.17 Pa and a power density of 17.5 W/cm^2 .

Because of the non-directionality of the sputtering deposition we have observed an “apron” at the film edge, due to the deposition of niobium in the undercut region, see Fig. 8.3. Sometimes we also observe also the presence at the edge of the sample of the so-called “flags”, which are the residues of the niobium film deposited on the resist wall and has not been completely removed during the lift-off step.

We believe these defects could be eliminated patterning niobium by reactive ion etching and we are equipping our fabrication facility for this purpose.

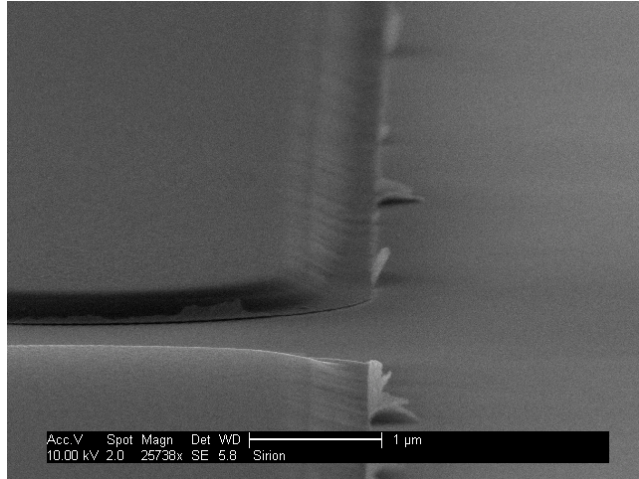


Figure 8.3. Edges of a Niobium resonator. SEM image of the edges of a niobium resonator realized at Yale. The film thickness is 200 nm. A very thin “apron” is visible almost everywhere around the thicker film. In few places also residue from the niobium deposited on the resist wall are visible. This image has been realized with a 10 keV electron beam.

8.3. Capacitor fabrication

In order to reduce the plasma frequency of the detector junction in the Quantronium architecture, we have fabricated capacitors using an e-beam version of the lift-off technique. The bottom plate of the capacitor is essentially copper, which plays also the role of a groundplane for the superconducting connections between the capacitors and the junction. The capacitor insulator is silicon nitride, deposited by Plasma Enhanced Chemical Vapor Deposition (PECVD) in a GIS system, and the top plate of the capacitors is the same aluminum deposited in the junction fabrication.

We clean the 2” silicon wafer with the same procedure explained in the previous section, but we do not use de-ionized water, which is believed incompatible with e-beam resist.

Since we will use a beam of electrons instead of UV photons to expose the resist double layer, we need to adopt electron beam sensitive resists. The first resist layer is made by Microchem-MMA (8.5) MAA EL15, Poly-(Methylmethacrilate /Methacrylic Acid) solved in ethyl lactate. This copolymer is very sensitive to electron beam exposure. So for the same electron dose we will obtain a higher dissolution rate during the development stage and that will give us the desired undercut profile. We spin the copolymer at 3000 rpm for 60 s to obtain a thickness of about 1100 nm and we bake it at 170 C for 60 s to

harden it. We use a shorter baking time in this case because the two resist layer use different solvents making the intermixing less relevant.

After that, we use a second layer with a common e-beam sensitive resist Microchem-950 PMMA A4, containing 950 kDa Poly-Methylmethacrilate solved in anisole. We spin it at 4000 rpm for 60 s to obtain a thickness of about 190 nm. We bake the double layer again at 170 C for 30 minutes to remove most of the solvents and harden the resists. This long baking time also improves the resolution we achieve in the exposure/development process.

Then, using the 30 keV electron beam of a converted XL40 SFEG FEI scanning electron microscope, we write the desired geometry on the sample located at 10 mm from the final microscope aperture, exposing with a dose of about $400 \mu\text{C}/\text{cm}^2$ the area where we want the resist to be removed.

Then, we develop the double layer resist by immersion in a solution of 1:3 methyl isobutyl ketone and isopropanol for 50 s and we stop the development by immersion in pure isopropanol for 10 s. We blow nitrogen on the sample to quickly dry it. Optical microscope inspection of the sample verifies the dimension of the desired undercut and the quality of the process each time.

At this point we are ready to deposit the bottom plate of the capacitor. We noticed that if this plate was fabricated using only copper, it was subsequently deformed and damaged in the deposition of the silicon nitride insulator. This happens because of the 400 C temperature at which the PECVD is realized. In fact at that temperature, copper is too soft and cannot stop either gases or water vapors, trapped during its deposition on the silicon surface underneath it, from bubbling through it. In order to avoid this problem, we decided to add two containment layers for copper and to fabricate them using a metal with high melting point, like chromium. In order to help the adhesion of the next silicon nitride layer to the top chromium film, we covered it with a titanium film.

We deposit the multilayer chromium-copper-chromium-titanium by e-beam evaporation in a UHV Plassys system with a base pressure of about 2×10^{-5} Pa. The deposition rate is 1 nm/s for copper and 0.2 nm/s for the other two metals. The four layers have a thickness respectively of 20, 800, 20 and 15 nm from bottom to top.

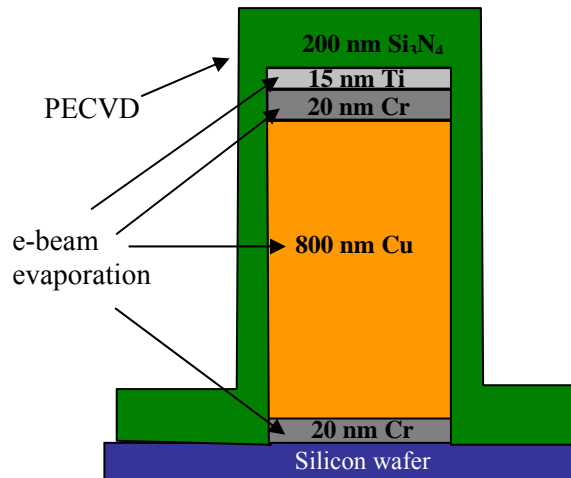


Figure 8.4. Josephson Bifurcation Amplifier capacitor fabrication. Sketch not to scale of the multilayer structure of the bottom electrode and insulator of the capacitor used to reduce the plasma frequency of the Josephson tunnel junction in the JBA.

The lift-off process is completed by one hour immersion in 50 C acetone followed by 60 seconds in ultrasound bath to completely remove the metal films deposited on the resist surface.

Then, the silicon nitride (Si_3N_4) insulator is deposited all over the capacitor bottom plate and the silicon substrate by PECVD at 400 C with a rate of 0.65 nm/s using a gas mix of silane (SiH_4), ammonia (NH_3) and nitrogen (N_2) with a total pressure of 160 Pa.

By Atomic Force Microscopy (AFM) measurements, we observed that the silicon nitride layer in few micrometers from the edge of the capacitor bottom plate is almost completely flat. We have now to fabricate the junction using a variation of the lift-off technique, which we will introduce in the next section. At that stage, the insulator flatness helps to obtain uniformity of the next thick resist double layer both on the surface of the bottom plate and a few micrometers from it, where the JTJ-based circuit will be realized.

Thus, the following lift-off process defines at the same time the aluminum top plate, the junction-based circuit and a short wiring connecting them.

Two capacitors in series are fabricated each time with a total capacitance between 16 and 40 pF. Fine tuning of the capacitance value is provided by properly sizing the capacitor area during the resist exposure.

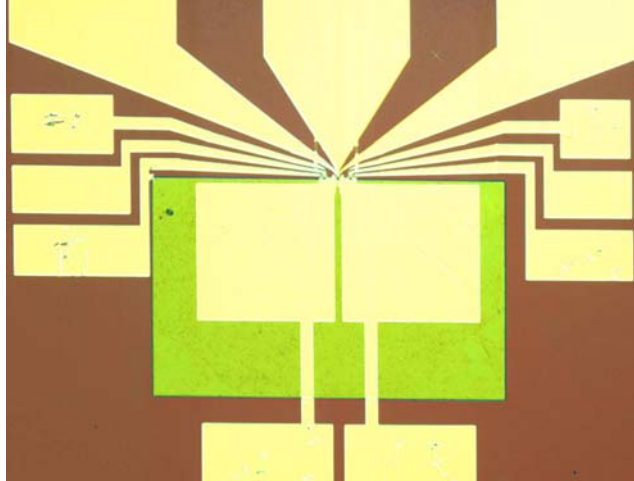


Figure 8.5. Capacitors for a Quantronium circuit. Optical microscope picture of a Quantronium circuit. In the center in green is the bottom plate of the two capacitors used to reduce the plasma frequency of the Josephson tunnel junction detector of the JBA. The top plate is realized in aluminum at the same time of the rest of the circuit by lift-off.

8.4. Dolan bridge technique to fabricate JTJ-based circuits

In this work, we fabricated different circuits in which the Josephson tunnel junctions are the basic ingredients like CPB, Quantronium, JBA. Let us now describe in general how we fabricate the junctions using the famous Dolan bridge technique [Do77], which is a special type of lift-off technique, and the double angle deposition procedure.

In all cases, we clean the substrate in the same way we did for our capacitor fabrication. This step is extremely important if something has already been fabricated on the substrate, like capacitors or resonators, because residues from previous step of the fabrication process can really impair the results.

In general, we first spin the desired resist double layer for the lift-off on a whole wafer and then we cleave a piece of the desired size from the wafer on which the JTJ-based circuit will be fabricated. This order in the two operations optimizes quality and uniformity of the resist on the substrate and improves reliability and repeatability of the fabrication process on each individual chip.

For circuit QED experiments, we fabricate the resonator first and then we fabricate the CPB inside the resonator gap. In this case, we have to spin the resist double layer on the individual resonator chip, whose size is either $3 \times 10 \text{ mm}^2$ or $2 \times 7 \text{ mm}^2$. This operation

requires extra care and precision to obtain a good degree of reliability and repeatability, because the resist tends to be strongly non-uniform toward the edges of the sample.

At this point, we spin Microchem-MMA (8.5) MAA EL13, a thinner version of the copolymer used in the capacitor fabrication, at 5000 rpm for 60 s to obtain a thickness of about 500 nm and we bake it at 170 C for 60 s to harden it.

After that, we spin a second layer with Microchem-950 PMMA A3, a thinner version of the e-beam sensitive polymer used in the capacitor fabrication, at 4000 rpm for 60 s to obtain a thickness of about 100 nm. We bake the double layer again at 170 C for 30 minutes. This long baking time of a thin resist layer gives the high resolution we need in the exposure/development process to fabricate 40 nm wide trenches. With an even thinner polymer film, about 70 nm, we achieved the best resolution with 20 nm lines written in the resist double layer.

In the Quantronium experiments, we fabricate the JJ-based circuit close to the thick bottom plate and insulator multilayer of the capacitor. Then, we have to use a thicker resist double layer, as mentioned in the previous section, to overcome that thickness and realize a good step coverage with the resist double layer. We obtain that by spinning the copolymer at 3000 rpm for 60 s to achieve a thickness of about 900 nm.

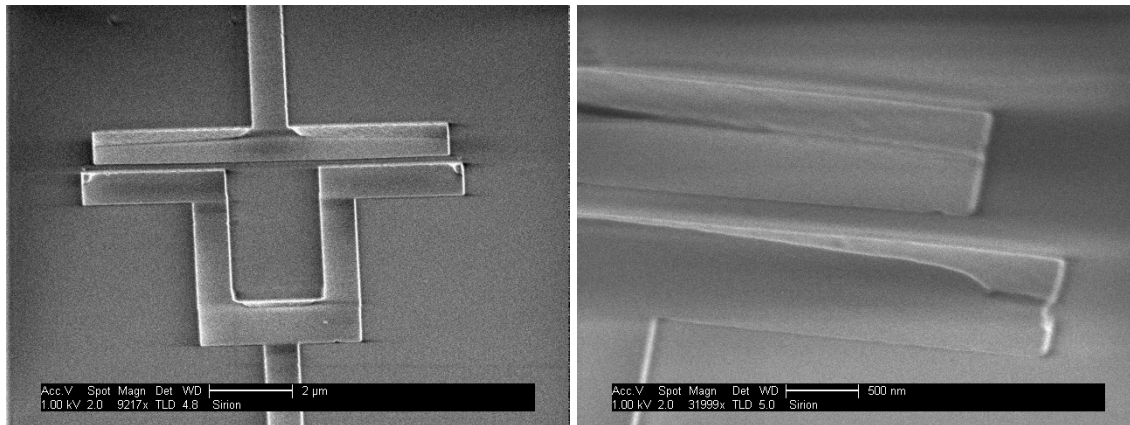


Figure 8.6. Resist bilayer patterned for a double angle deposition. SEM image of a e-beam sensitive resist bilayer realized at Yale. The two resists used are 500 nm thick Microchem-MMA (8.5) MAA EL13 and 720 nm thick Microchem-950 PMMA A3. Left: trenches and suspended bridges have been dug in the resist to fabricate a SQUID. The two suspended bridge are 5 mm long and 500 nm wide and no sagging is visible. Right: detail of the side of a bridge underneath which is visible some non completely removed copolymer. These images have been realized after depositing few nm of copper on the resist bilayer and using a 1 keV electron beam for the shortest time possible to avoid overcharging of the insulating surface and the consequent melting of the resist.

In general, the two thin metal films that constitute the two overlapping electrodes of the superconducting junction are fabricated using the double angle deposition technique [Do77]. The resist needs to be patterned with a geometry that includes trenches, in which the metal will be deposited, and suspended bridges. In order to fabricate a suspended bridge into a double layer resist, we have to develop and remove, in some location, the lower resist layer without damaging the upper resist layer, see Fig. 8.6. The presence of a suspended bridge obstructs the two step metal deposition obtained by orienting, for each deposition step, the substrate at a different angle respect to the normal to the metal evaporation source. This procedure realizes the overlap between two thin films that constitutes the junction.

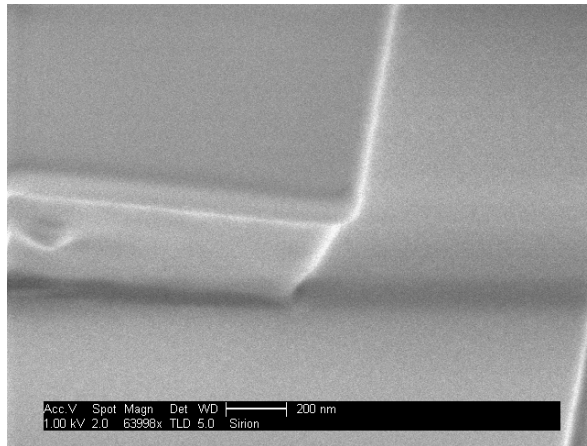


Figure 8.7. Undercut double layer resist. SEM image of a e-beam sensitive resist bilayer realized at Yale. The two resists used are 500 nm thick Microchem-MMA (8.5) MAA EL13 and 720 nm thick Microchem-950 PMMA A3. The undercut in this image is about 200 nm. This image has been realized after depositing few nm of copper on the resist bilayer and using a 1 keV electron beam for the shortest time possible to avoid overcharging of the insulating surface and the consequent melting of the resist.

Using the 30 keV electron beam of our converted SEM, we write the desired geometry on the sample located at 10 mm from the last microscope aperture. We expose the locations where we want the resist to be removed. We are able to write features with different width using different electron doses in the range $150\text{-}600 \mu\text{C}/\text{cm}^2$. To find the exact dose to be used, we fabricate test samples looking for the best result in terms of feature size, especially if they are close to the minimum size we can fabricate with our equipment ($\approx 20\text{-}30 \text{ nm}$). In these calibration tests we have to take into proper account the proximity effect and the different exposure sensitivity of the two layers. Of course, the desired

undercut profile, see Fig. 8.7, will be obtained due to the different sensitivity of the two resist layers and to local additional exposure we may perform.

We need also to carefully design the exposure mask in order to obtain only the desired geometries. In fact, the double angle deposition generates double layers of all the features which are parallel to the evaporation direction and reduced double images of those orthogonal to it. We remove some of those undesired double images using little or no undercut in the double layer resist, which becomes as a wall on which one image is going to be deposited and then removed during the lift-off. We can also use the undercut profile and some easy trigonometry to exactly evaluate the shift of the different parts of the design and to counter the size reduction.

In some circuit QED experiment, we have also intentionally used the thickness of the resonator film to produce a shadow effect in the junction fabrication. In this way, it is possible to fabricate gate capacitors for the CPB with plate distance of less than 20 nm.

In general, to fabricate suspended resist bridges, we collect an additional dose in the region where the bridge has to be realized either using the proximity effect from close by feature or exposing with low doses, usually in the range 40-100 $\mu\text{C}/\text{cm}^2$. In this way we are able to completely remove the copolymer without poking a hole through the upper resist layer.

In the next step, we develop the double layer resist by immersion in a solution of 1:3 methyl isobutyl ketone and isopropanol for 50 s and we stop the development by immersion in pure isopropanol for 10 s. We blow nitrogen on the sample to quickly dry it. Optical microscope inspection are required to verify the quality of the results and in test run also SEM imaging of the resist profile may be useful to identify problems.

Once the resist is patterned, we e-beam evaporate, frequently at zero degree, which means with the substrate and the evaporation plane parallel, 30-50 nm thick aluminum film to fabricate the junction bottom electrode. The e-beam evaporation is performed in a UHV Plassys system. In order to reduce water vapor and oxygen content we use a liquid nitrogen trap to cryopump into the chamber and a short titanium getter deposition. The aluminum is evaporated at a rate of 1 nm/s starting from a base pressure of about 4.4×10^{-6} Pa.

In order to realize the insulating barrier, a thermal oxidation of the bottom electrode surface takes place in a mixture of 15% oxygen in argon gas with total pressure ranging between 130 and 2600 Pa for a time between 5 and 20 minutes depending on the desired critical current density. The presence of the argon, increasing the total pressure, helps to contain degassing from the resist and then barrier contamination during the oxidation time. We have obtained critical current densities ranging between 30 A/cm² with oxygen exposure of 1.9x10⁶ Pa s and 175 A/cm² with 5.6x10⁴ Pa s, with a scaling similar to a root square behavior.

Without breaking vacuum and as soon as the system pressure drops under 1.5x10⁻⁴ Pa, a 50-90 nm thick aluminum top electrode is evaporated at a different angle with the same rate used for the bottom one. The lift-off process is completed by one hour immersion in 50 C acetone followed by 10 s in ultrasound bath.

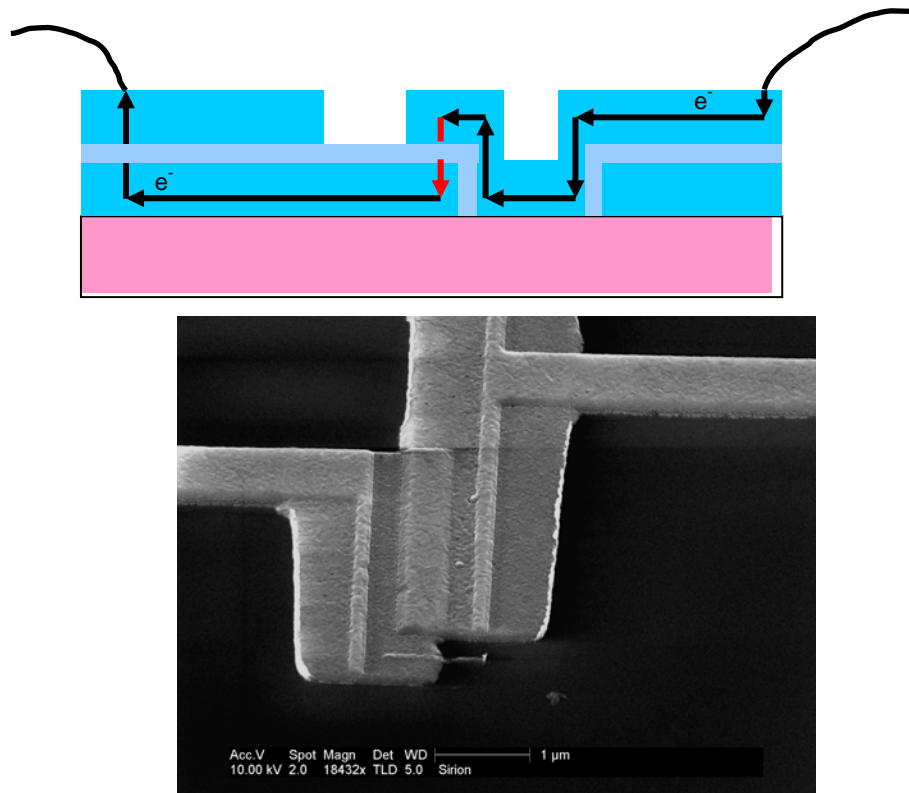


Figure 8.8. Josephson tunnel junction fabricated by double angle evaporation. Top: Sketch of the complete device with the charge carrier path. Bottom: SEM image of a device realized at Yale. The two aluminum electrodes are 40 and 70 nm thick. The intended junction is clearly visible in the center as well as the two others on the two sides. This image has been realized with a 10 keV electron beam.

An unavoidable effect of this double angle deposition technique is the presence of undesired large junctions in the final circuit, which come out of the topology of the two layers, see Fig. 8.8.

Of course, if the area of the intended junction is much smaller than that of the undesired one, this larger device is always biased on the supercurrent branch and will not generate quasiparticles in the device. However, the undesired junction, even if unbiased, can still be a source of noise. If we accept the idea of breaking vacuum we could fabricate the junction-based circuit without generating any unintentional junction. Of course, this comes with an additional cost in terms of barrier quality and reproducibility.

A different way to go would be taking advantage of the trilayer fabrication technology, which has already been developed for micron sized niobium-based superconducting electronics. The two electrodes and barrier are all deposited without breaking vacuum on the bare substrate. This reduces the possible sources of contamination and non uniformity in the electrode as well as in the barrier. It requires the use of reactive ion etching, which for niobium is performed using a fluorine-based chemistry. The equivalent for aluminum can only be done with chlorine-based chemistry which is more dangerous and corrosive and requires an expensive treatment of the reaction gas products. We are planning to expand our fabrication facility with two reactive ion etching systems to perform both fluorine and a chlorine based processes.

9. Conclusion and perspectives

In this work, we have presented a new type of dispersive qubit read-out in two different, but also closely related versions (RF-Quantronium and circuit QED). The principle of this type of read-out is to couple the photon number operator of a microwave resonator to the energy operator of the qubit. In the circuit QED version, the resonator is linear and is read-out by a very low noise out-of-chip HEMT amplifier. In the RF-Quantronium version, the microwave resonator incorporates a non-linear element in the form of a large Josephson tunnel junction and provides some in-situ amplification. This last scheme can achieve a larger read-out speed and gain at the expense of a more complex operation.

These two dispersive read-out schemes offer:

- 1) the ability of realizing quantum non-demolition measurements: since the probe operator commutes with the qubit Hamiltonian, the read-out does not change the state. The measurement can be done in principle with very high fidelity. Although in the present single-shot experiments fidelity has reached a maximum of about 60%, improved experiments could yield fidelity deviating from unity by only few percent.
- 2) access to the strong coupling regime of cavity QED, which is not easily achievable in present atomic physics experiments. The advantage of the superconducting circuits is that the mode volume can be much smaller than in the cavities used in atomic and molecular optics. In fact, the difficulty of working with superconducting qubits is to provide them with enough isolation from unwanted degrees of freedom, rather than the opposite as in atomic physics.

However, although the Q_1 measured with these read-out schemes are among the best ones obtained up to now in solid state qubits, their numerical values are lower than predicted by theory. The same can be said about Q_2 [VAC02, CIA04, CBS04, BCB05]. Nevertheless, several interesting gate experiments can be performed with the qubits in their present state. In particular, we would like to demonstrate the entanglement between two superconducting qubits and the violation of Bell's inequalities [B87, A02] in this case. In this latter project, the read-out fidelity is a crucial ingredient to close all loopholes.

To reach these goals, we propose to orient our research activity in two directions, which we believe deserve great attention. On one side, we will explore material science suggestions for the control of the many parameters influencing tunnel junction fabrication. For instance, as recently suggested by [TMP05], we would like to apply energy to the oxygen molecules during the barrier growth using either UV photons or high energy electrons to move the aluminum oxide stoichiometry toward the ideal one and in this way improve, hopefully, the quality of the tunnel barrier. We are also fabricating resonators on sapphire to improve their quality factor and we have measurements of losses in insulating layers in process aiming at improving the resonator and qubit performances.

On the other side, we will develop new circuit design. For instance, we can integrate several CPB qubits in different superconducting transmission line resonators, as already done for a single qubit in the circuit QED. These resonators, with proper coupling elements, will act as quantum bus to couple distant frequency multiplexed qubits which will be read-out using JBAs. They will be manipulated by frequency-selective RF pulses to perform one and two-qubit gates. This design will fully exploits the advantages of our QND probe operators and will orient a search toward a fully scalable architecture for superconducting qubits.

The results of these future experiments may give answers to the key question of quantum engineering: *do fully entangled quantum superpositions still exist for complex systems like computers with many hundreds of qubits?*

Appendix: text and slides from the defense presentation

(Slide 1 - Title)

Good afternoon, I would like to thank the jury members for accepting to participate in my thesis defense about design and fabrication of superconducting circuits for amplification and processing of quantum signals.

I will begin by introducing the motivation of this work: to realize quantum machines we need to develop a new branch of physics: quantum engineering. I will then talk about quantum measurement, a little bit more in detail, to clarify what we mean by Quantum Non-Demolition (QND) measurement. The concept of QND measurement is in fact central in understanding our experiments.

I will then present the actual design and fabrication of the two versions of superconducting circuit architecture for dispersive read-out, we have realized. I will present actual experimental data measuring their quality factors in order to evaluate these circuits. I will then conclude indicating some perspectives for future work.

(Slide 2 – Do quantum machines exist?)

In the last eighty years quantum mechanics has generated a large number of new devices: lasers, transistors, photo-detectors and so on. They have changed the way in which we do physics as well as the way in which we conduct our everyday life. Quantum mechanics has been instrumental in understanding and predicting the values of the basic parameters of these machines: material dependent work functions, transition frequencies, semiconductor energy gap, which involve the Planck constant and the electron mass and charge. These quantities are consequences of fundamental aspect ratios of the Universe and are in no way tunable by an engineer. On the other side, the dynamics of these devices at the macroscopic level is completely described by classical equations of motion for collective degrees of freedom, like current, voltage, electric and magnetic fields.

(Slide 3 – An example of quantum machine: superconducting integrated quantum circuit)

On this slide I am showing a superconducting integrated quantum circuit which has been designed and fabricated as an elementary component of a quantum computer at CEA in

Saclay. In fact in this talk, I will use the idea of a quantum computer as an archetype of a quantum machine. A quantum machine is a machine whose working is entirely described by quantum mechanics and for which quantum parameters are fully tunable. We would like to convince you that such machines are feasible and that it will be the quantum engineer job to realize them practically.

These quantum circuits will have to be operated at very low temperatures to reduce thermal fluctuations and with very low dissipation, which means very little interactions with the environment, since interactions can scramble the state of our quantum circuit. It is then a quite natural choice to fabricate quantum circuits using superconducting electrical circuits, whose quantum behavior is well known.

(Slide 4 - Information units)

In a classical computer the basic information unit is the bit, which can be realized by any implementation of a bistable switch. It has two energy states, “0” and “1”, separated by a tall barrier with lot of dissipation to make the bit insensitive to small perturbations. It can be thought as a capacitor with or without charges, as a MOSFET in one of our CCD cameras.

The quantum information unit, “qubit”, is a two-level quantum system. It may be thought as a complex system, like an atom, with quantized energy levels, two of which are very well separated by all the others and can then be treated as a two-level system, usually called a pseudo-spin, in an effective magnetic field. Once we restrict the description of this system to the subspace of the total Hilbert space defined by the two energy levels of interest, the “qubit” Hamiltonian is the product of a quantum of energy at the Larmor frequency times the Pauli operator σ_z .

The great difference with the classical bit is that the qubit can be prepared in any possible quantum superposition of the two basic states. We are then losing the mutual exclusion character of the classical bit states.

(Slide 5 – Surprising properties of quantum information)

In general, the quantum superposition or qubit state can be written as shown in the slide and represented by a point on a Bloch sphere with a latitude and a longitude. If let free,

the qubit state will precess at the Larmor frequency around the z axis. We can now “write” or “prepare” a qubit in a particular state by exciting the system with a force oscillating at the qubit transition frequency and adjusting amplitude and duration of the excitation properly, generating in such a way a rotation of the qubit state or a one-qubit gate by using an interaction which do not commute with σ_z , that is any combination of σ_x and σ_y .

The surprising properties of quantum information derive from the deep asymmetry between the “write” protocol and the read-out of a state. In fact, when we measure the energy of the qubit, we always find only one of the two eigenvalues associated to the two eigenstates, $|0\rangle$ and $|1\rangle$. And if we prepare the same superposition over and over again we will randomly find one eigenvalue or the other with the probability shown. Only the eigenstates will be read-out with certainty. As you see, the read-out operation destroys any information about the longitude and out of the infinite set of values of the latitude, it only produces a single bit of information, either up or down. The collapse of the superposition prevents the read-out to be in general faithful and the qubit to be copiable. But the information contained in the superposition exists, in fact we can prepare a superposition and instead of reading it out right away, we can rotate the state until it coincides with an eigenstate and read it out faithfully. We need then to think to a smart way of reading-out whatever information is encoded in the qubit state

(Slide 6 – The power of quantum information)

Let me describe the power of quantum information. If we consider a classical register with N bits, and let’s say that $N=10$, we know we can use it to store a single N digit binary number between 0 and 2^N-1 , which means between 0 and 1023. If we consider the state of a quantum register with N qubits, it will be represented by $2^{N+1}-2$ independent real numbers each of which can assume an infinite number of values. For 1 qubit that means two real numbers, as we have seen in the latitude and longitude of the Bloch sphere representation. For two qubits, it becomes 6 real numbers, for three 14 and so on. So, the quantity of information grows exponentially with the number of qubits, where classically it grows only linearly in the number of bits. If we want to double the amount of quantum information carried by a quantum register we just need to add one more

qubit. But as I told you before this massive amount of information would be lost and wasted if not properly read-out.

It is then clear that algorithms which are able to exploit the properties of quantum information are not easy to produce, still there are some examples of them, but it is not my intention to talk about them. I will instead concentrate on the read-out strategy.

(Slide 7 – Elementary quantum processor)

Let us now look at an elementary quantum processor. It needs logic qubits, the two level systems we introduced in the beginning, to realize a quantum register. Each of them needs a port to prepare the qubit state or implement one-qubit gates. This port has to be realized in such a way to avoid interactions with the environment, while not in use. The effect of these unwanted interactions is to induce decoherence in the qubit state, like depolarization or state flip and dephasing or state fuzzyness. We can define quality factors that tell us the average number of qubit state precession before depolarization or in general decoherence occur.

In order to be able to perform error corrections on our register of N logic qubits, we will need at least five qubits to encode for each single logic qubit, but this is only a small price to pay. The real problem is that performing these corrections will also require about 10^4 gate operations and since each gate operation requires about 10-20 precessions to be realized, we will need at least 10^5 decoherence free precessions, implying Q_2 of the order of 10^6 .

A quantum processor will also need qubit-qubit interactions, at least between neighbor qubits, to realize two-qubit gates, which are required to obtain a universal gate set.

But now, let us concentrate on the focus of this talk. For each qubit, we also need another port connected “on demand”, with some sort of switch, to a meter that has to read-out the information contained in the qubits, introducing the less possible noise and not altering the qubit state so that computation can go on.

(Slide 8 – The meter system: an oscillator)

Let us now talk about the concept of QND measurement. In the first place, to measure we need a meter. We use the most elementary meter: a quantum harmonic oscillator, for

instance a single mode of an oscillating electric field or an electrical LC circuit, or a Josephson tunnel junction, which we can model as a pendulum oscillating with small angles around its equilibrium position. The Hamiltonian of this system is well known and its dynamics is represented by a phasor, or Fresnel vector, in the plane of its conjugated observables. We can set the oscillator in a frame rotating at its frequency so that the vector would be fixed in a certain position. Now when we close the switch to perform a measurement, the meter interacts with the two-level system changing its oscillation frequency in such a way that the final frequency depends on the state of the qubit, phasor lagging for qubit in ground state, or leading for qubit in the excited state. This way we have obtained the meter we wanted with a needle pointing in different directions depending on the qubit state.

(Slide 9 – The meter system: an oscillator with anharmonicity)

We can wonder if we can make the two objects, qubit and meter, interchangeable, so that one acts as a meter or as a qubit depending on our needs. Well, this is possible as soon as we add a little anharmonicity to our meter, enough to separate two energy levels from the others and then we can treat it as a qubit or as a meter. It will become clear by the end of the talk, that in this framework we can think of qubit as computational element as well as carrier able to transport and exchange information among different computational sites.

(Slide 10 – We want a QND read-out)

We now have a good meter, to be able to read-out the qubit without altering the qubit state we have to define the right interaction. A sufficient condition for a measurement to be QND is that the operator we want to measure commutes with the total Hamiltonian including the meter and the interaction operators.

(Slide 11 – We want a QND read-out)

In our case this means that the qubit and the interaction operators commute. It also implies that the energy of the qubit is conserved in the measurement process. It means we have to implement a measurement without dissipation, a dispersive measurement.

(Slide 12 – How to measure without dissipation?)

This is not in general a new kind of measurement in physics. For instance in optics, the dielectric constant of a material is measured by evaluating the ratio of the difference and sum of the two orthogonal components read-out by photo-detectors at the outputs of a Mach-Zender interferometer, with or without the material inserted along one of the arms.

(Slide 13 – How to measure without dissipation?)

This ratio is a sinusoidal curve whose shift in presence of the dielectric material is proportional to the value of the dielectric constant. This is a measurement of the susceptibility, either electric or magnetic, of the material which does not require any energy to be left behind in the interferometer and does not change the state of the material.

(Slide 14 – Correspondence between oscillator and spin $S \gg 1$)

We now have all the ingredients for a measurement: qubit, meter, the type of interaction. But, do we really need to consider the qubit as a spin and the meter as an oscillator? Are they really that different?

Here the energy levels of an oscillator are represented in the energy-position-momentum space by slices in a paraboloid surface where all of the oscillator dynamics takes place. On the other side energy levels of a spin system with a large S are represented in the same way.

Well, it is true that the Hilbert space of a spin is bounded while that one of an oscillator is not. But we can approximate the first N energy levels of an oscillator with the $2S+1$ energy levels of the spin system. And we can make our approximation better, if we need it, either taking a larger spin number or considering other terms in the expansion of the oscillator Hamiltonian beyond the Pauli matrices, like quadrupole or hexapole and so on. So our meter can be treated as a pseudo-spin as well as our qubit. We will see that this correspondence has some relevance in the rest of the talk.

(Slide 15 – Possible “natural” qubit-meter interactions)

Let us now look into which interaction satisfies the QND requirement. Here I wrote the most natural interaction I could think of between a qubit (spin) and a meter (oscillator) and then I reformulated it for the different cases in which either the qubit is itself an oscillator (with a little anharmonicity) or the meter is represented as a second spin. These are some of the most common interactions in mechanics and atomic physics, but unfortunately none of them is satisfying our requirement to commute with the qubit Hamiltonian and to not change the qubit state.

(Slide 16 – A new QND read-out interaction)

Here is a simple form that the interaction operator may take in order to commute with the qubit operator defining a QND measurement but also commuting with the meter operator so that the total system is completely symmetrical.

(Slide 17 – Magnetomechanical analog)

To drive you a little closer to my intention of making the two objects, qubit and meter, interchangeable, let me start showing you an ideal experiment in which the QND read-out is in fact realized. It is the magnetomechanical classical analog of the situation I would like to achieve. Here two rigid magnetic pendula oscillate around their equilibrium position, one of them is on top of a magnetic slab mounted with the attracting polarity up. The slab sits on springs that bring the slab back in its own equilibrium position. The pendulum and the slab attract each other depending on their distance and on the pendulum oscillation amplitude. Let us assume for simplicity that the line is inextensible and that there is no friction in the system.

Let us see what happens if we modify the state of the left pendulum increasing the amplitude of its oscillations. The magnetic slab will be less attracted and will move down due to the spring action. Its movement through line and pulleys is transferred to a small weight sliding down along the axis of the other rigid pendulum. The latter will then have its frequency decreased. The right pendulum frequency would instead increase if the left pendulum oscillation amplitude was initially reduced. So, the pendulum on the right measures the oscillation amplitude change of the left one, without changing its energy.

(Slide 18 – Magnetomechanical analog)

Moreover, the experiment can easily be made symmetric, as shown in this slide. The two pendula may exchange role between them, the left can become the meter of the right.

(Slide 19 – A new symmetric QND read-out interaction)

So if we want to explicit this symmetry between qubit and meter we can write the interaction Hamiltonian in a QND way which is also fully symmetric.

Well, staring at this formula, it looks very easy to read and understand, but as I have shown you with the magnetomechanical analog example, this does not mean in any sense that it is easy to implement.

(Slide 20 –Fabrication)

I am now going to switch gear and explain to you briefly how we have realized the things I have been talking about until now.

As I told at the beginning, I will describe quantum mechanical circuits realized using superconducting thin films, whose preview is shown in the slide, and operated at very low temperature, lower than 0.5 K, to reduce dissipation and thermal fluctuations. We also need, as I mentioned before, some non-linearity in our circuit to define two energy levels well separated from all the others.

I will only tell you few words about the techniques we have developed to be able to fabricate the superconducting integrated quantum circuits, which I will properly introduce briefly. I will not present any fabrication recipe because, as you may know, fabrication is an opportunistic activity which adapts to the available equipment following their drifts.

I grew up in Naples, in southern Italy, just along the Mediterranean seashore. There I learnt that in order to sail you cannot perform a predetermined sequence of operation, since there are never two identical waves, or gusts of wind or undersea streams. To be a good sailor, you need to know where to go and you need to feel the elements around you to use them at your best toward the goal of reaching the harbor. You need to hold the helm of your boat and adjust to the sea. This practice makes you humble in

acknowledging the power of the sea, while teaches you to enjoy and harness the change around you.

(Slide 21 –Fabrication)

I will then present what we have done and I want you to really to understand that to fabricate these circuits it is necessary the best possible control over all the ingredients used, substrates, metal films, resists, equipments, like keeping the helm for a good sailor, and that this control must be effective over dimensions that go from the nanometers of the barrier thickness of the junctions to the millimeters of the connections of the chip to the rest of the experimental set-up. Six orders of magnitude, like wanting to be able to landscape your own backyard and the entire country where you live and all it may be in between, at the same time. Quite a task, but we managed to sail through it !!!

(Slide 22 – Josephson junction: the only non-linear and non-dissipative component)

Let us go back to our superconducting quantum circuits. There is only one circuit component that can satisfy the quantum engineer's need for non-linearity and for no dissipation and it is the Josephson tunnel junction, a masterpiece in most superconducting electronics circuits. The SEM image here is that of an actual Al-based junction fabricated at Yale by lift-off using the Dolan bridge patterning and double angle deposition technique. Ideally, a Josephson junction is made by overlapping two thin films made out of superconductors, separated by a nanometer thick insulating barrier, which allows for the tunneling of Cooper pairs without any potential difference. This is the well-known dc Josephson Effect. The current-flux constitutive relation shows the non-linearity of its inductance, which we will use to build up our qubit. We model the Josephson junction as an ideal non-linear inductor in parallel with a capacitor that represents the electrodes separated by the tunnel barrier.

I think that it is interesting to notice how something, that looks quite different from the idealized version of it, actually works in a way which is very well described by that idealization. There is maybe here something deep about the fundamental nature of condensed matter physics, but this is the subject of another talk.

(Slide 23 – Split Cooper Pair Box Qubit)

A quantum engineer, using Josephson junctions, a thin film superconducting reservoir and capacitors, realizes what it is considered one of the basic elements in superconducting quantum circuits: the split Cooper Pair Box. I am showing on the left a SEM artificially colored image of an actual realization fabricated at Yale of this ideal circuit component and its idealized electrical diagram. The 40 nanometers thick and six microns long line deposited, in this case on a silicon substrate, is called the “superconducting island” and it is in fact a piece of superconductor (Al in this case) connected to the Al circuit through two Josephson tunnel junctions in parallel and separated from the Nb around it by capacitors. Using the quantum theory of electrical circuits, presented in my thesis, it is possible to write down a Hamiltonian that describes the circuit dynamics of the split Cooper Pair Box in the case of symmetric junctions. It contains two terms: the first one represents the electrostatic energy of the Cooper pairs on the total circuit capacitance and is tuned by the bias voltage applied to the gate capacitor and the second one is the contribution of the Josephson elements and is tuned by the magnetic flux threaded through the circuit loop. The two quantities in red are the charging energy and the Josephson energy and are tunable during fabrication by patterning and positioning the circuit elements, adjusting the barrier thickness or changing the electrode material.

(Slide 24 – Split Cooper Pair Box Qubit)

This is the artificial atom I introduced at the very beginning of my talk, and its energy levels are fully tunable by a quantum engineer either during fabrication or in situ. If properly realized, the two lowest energy levels are well separated by the others and can be treated as a two-level system and his Hamiltonian becomes the one written on the slide. We eventually meet the practical realization of a pseudo-spin $\frac{1}{2}$.

(Slide 25 – Meter using electrical microwave resonators (1))

As I told you before, we need meters for being able to read-out our qubits. I am, indeed, showing to you an optical microscope image of a distributed resonator we have fabricated at Yale. It hosts the photons, the single mode oscillating electric field whose phase and

amplitude after transmission through it provide the meter we need. The fabrication of this resonator has been realized by lift-off techniques using optical lithography and by deposition of a thin film Nb layer using dc magnetron sputtering. The niobium transmission line resonator is shown together with some detail of the coupling capacitor, whose role will become clear in few slides. The location of the qubit in the resonator is also shown.

(Slide 26 – Meter using electrical microwave resonators (2))

In this slide I am showing an optical microscope image of a lumped resonator together with a SEM image showing the detail of the split Cooper Pair Box in the quantum superconducting electrical circuit. In this case, reflection measurements of the phase and amplitude of a single mode oscillating electric field provide the meter. The fabrication of the resonator has been realized at Yale by lift-off techniques using either e-beam lithography and by deposition of thin film metal layers using e-beam evaporation for the metals and Plasma Enhanced Chemical Vapor Deposition for silicon nitride used as insulator. On the right an out of scale sketch of a cross-section of the bottom electrode and insulator of one of the lumped element capacitor we have fabricated is shown.

Let me now spend few words on why we have developed this multilayer structure as a small example of the control required in quantum engineering. Silicon nitride, the capacitor insulator, is known to have high dielectric constant and good insulating properties if deposited by PECVD and it also demonstrated good step coverage. These are important properties for us since we wanted a leak-less thin capacitor and we wanted to deposit the capacitor Al top electrode at the same time of the junctions without risking any interruption in the connecting wires. Our silicon nitride is deposited by PECVD at 400 C, this required the base electrode to be resistant to heat induced stress, but at the same time it needed a low resistivity to suppress stray inductances in the circuit on top of it. We obtained all of that by developing a multilayer. The first Cr layer plays the role of stopping degassing from the substrate from moving through the softer copper layer, which carries the image currents. The upper Cr/Ti layer reduces the stress transferred from Cu to the nitride layer while increasing at the same time the nitride adhesion to the metal underneath. By patterning the area, the capacitance is adjusted to obtain the

intended value to reduce the plasma frequency of a Josephson junction down in a range compatible with the rest of the experimental set-up.

(Slide 27 – Two versions of the dispersive read-out strategy)

As we already established, we want to perform a dispersive read-out of our split CPB qubit. Actually, we have realized two versions of this dispersive read-out strategy. In both cases, the measurements are realized sending a microwave signal to the qubit, while the qubit is biased at the optimal point where it is insensitive to first order to noise in the probe variable. The signal is coupled to a qubit variable whose average value at the optimal point is identical in the two qubit states. We measure the derivative of that qubit variable with respect to the probe, the susceptibility, which differs maximally between qubit states at the optimal point.

The resulting state-dependent phase shift of the transmitted or reflected photon signal is thus amplified by a low-temperature amplifier and finally discriminated at high temperature against an adequately chosen threshold.

In addition to being very thrifty in terms of energy being dissipated on chip, these new schemes also provide a further natural decoupling action: when the read-out signal is OFF, the back-action of the amplifier is also completely shut off.

Finally, the interrogation of the qubit in a frequency band excluding zero and relatively narrow compared to the center frequency reduces the noise to a negligible level. In addition, the presence of read-out filters, like cavities, suppresses noise at the input and output ports.

(Slide 28 – Inductively coupling qubit and meter: “RF-Quantronium” architecture)

Let me now introduce the first of the two versions of the dispersive read-out in which the qubit and the meter have been inductively coupled. Here there are a SEM image and an idealized electrical diagram of this “RF-Quantronium” architecture. It is composed by a split Cooper Pair Box, our qubit of choice, read-out by a meter represented by a non-linear lumped element resonator, made by a larger Josephson junction in parallel to a capacitance series.

This circuit has been invented in Saclay, few kilometers from where we are. In the original work they read-out the direction of the current, which depends on the qubit state, circulating in the loop biased close to the optimal point by observing the switching probability to a finite voltage state of the current biased large junction. They manipulate the state of the qubit by NMR-style pulses through the gate capacitor, which acts as the input port.

The main modification we made was to introduce a dispersive read-out for it. Using different oscillation states at zero voltage of the non-linear resonator, large junction plus capacitors, driven by a pure RF signal, we measure the inverse inductance of the circuit, which depends on the qubit state, by observing the acquired phase shift of the reflected signal. The non-linear resonator acts also as our amplifier and has been named Josephson Bifurcation Amplifier.

(Slide 29 – The RF-Quantronium reduced Hamiltonian)

The Hamiltonian of this circuit restricted to the first two levels of the CPB, which are the states of our qubit, shows the terms we have been talking about in the first part of the talk: in green we have the qubit term, in magenta the meter term and in red the interaction term. The only new terms are those in brown which represent the input (charge) and output (phase) control of the circuit and the black term which represents the amplification.

The interaction term in red clearly commutes with the qubit term, and as we pointed before this means the measurement is a Quantum Non-Demolition one.

(Slide 30 – The RF-Quantronium reduced Hamiltonian)

It also commutes with the meter term which indicates a further symmetry. We can better represent this symmetry by writing the interaction operator in a more symmetrical way using the equivalence between meter and spin, I introduced before.

(Slide 31 – Capacitively coupling qubit and meter: “circuit QED” architecture)

Let me now introduce the other architecture in which we have realized the dispersive read-out strategy by capacitively coupling the CPB qubit to the meter, which here is

represented by a 1-D transmission line resonator, with the qubit fabricated in the resonator gap. The resonator consists of a full-wave section of a Nb superconducting coplanar waveguide and it is connected to the rest of the experimental set up through coupling capacitors.

The qubit and the resonator are fabricated on the same chip, which requires mastering optical (for the resonator) and e-beam (for the qubit) lithography techniques.

The dispersive read-out is realized by measuring at the optimal point the capacitance of the circuit, which depends on the qubit state, by observing the acquired phase shift of an RF signal transmitted through the cavity at its resonant frequency.

We have named this architecture “circuit Quantum ElectroDynamics” since it could be seen as the electrical circuit version of the well-known cavity QED. In the case of the cavity QED, an atom passing through a Fabry-Perot cavity interacts with the photon in the cavity with a coupling g , the vacuum Rabi frequency, absorbing or emitting a photon at the transition frequency, where γ and κ are respectively the decay rate of the excited state of the atom and the rate at which photons leak out of the cavity. In the electrical circuit version, the split Cooper Pair Box plays the role of the atom and the cavity role is taken by the transmission line resonator terminated on the two sides by coupling capacitors playing the role of mirrors.

In the electrical version, the strong coupling regime where g is much bigger than γ and κ has been realized, a regime that is not easily accessible in atomic physics.

From the point of view of a quantum engineer the electrical circuit version is clearly more interesting because the “artificial atom” does not have the God-given parameters of real atoms but can indeed be tuned almost at will both at the fabrication level (E_c and E_J) and at the measurement level by the voltage bias at the gate capacitance and the flux bias with an externally applied magnetic field.

(Slide 32 – The circuit QED reduced Hamiltonian)

I am not going in any more detail of this architecture, except showing the Hamiltonian for the full circuit at the optimal point restricted to the first two states of the CPB, which are the states of our qubit.

This Hamiltonian contains the brown terms which, as before, represent the input and output control, the green term of the qubit, the magenta of the meter but the term in red, the interaction term, is actually one of those we discarded in our initial discussion.

However, if we limit our measurement at large detuning between the qubit and the resonator frequency, larger than g , we can expand the Hamiltonian at the second order in g and arrive at the more friendly form on the slide, where the brown term have been omitted for simplicity.

Here the red interaction term clearly commutes with the qubit term indicating a Quantum Non-Demolition measurement, at least up to the second order in g .

(Slide 33 – The circuit QED reduced Hamiltonian)

Here too the interaction term commutes with the meter term and can be presented in a form which underlines this further symmetry, using again the concepts I introduced before.

(Slide 34 – Rabi oscillations: latitude control)

I would like to show only some of the results of experiments that have been run using the two dispersive architectures I just presented.

The first set of results deals with latitude control of the qubit state, generating what are called Rabi oscillations. The experiment consists in applying at the input (charge) port a voltage pulse at the qubit transition frequency and varying its amplitude and time duration. This pulse performs a σ_x rotation of the qubit starting from the ground state, where the qubit was prepared just by waiting and letting it relax. Then in the RF-Quantonium case, each time a read-out pulse follows. The figure on the left shows all the data accumulated by performing this experiment 32 million times in about 10 minutes. It reports the results as switching probability between the two oscillation states at zero voltage of the JBA versus pulse duration. On the right hand side, results of a similar group of experiments in the case of circuit QED are shown. Here, simultaneously with the detuned input pulse, a continuous dispersive measurement of the qubit state is performed by determining phase and amplitude of a very weak coherent microwave beam (about one photon populating the resonator on average) transmitted through the resonator

at its resonant frequency. The data accumulated over more than 5 millions repetitions of this experiment are presented as occupation probability of the excited state versus pulse length.

In the RF-Quantronium case a discrimination power of about 61%, which is 87% of the calculated value, was observed. In the circuit QED case, the measurement showed a transmitted beam phase contrast of about 85%, and gave a level population oscillation with a visibility approaching unity.

(Slide 35 – Excited state relaxation: measuring Q_1)

The second set of results deals with measuring the time it takes for the qubit excited state to decay. This is a measurement of Q_1 , the depolarization quality factor, we defined early. The experiment consists in applying at the input (charge) port a calibrated σ_x rotation, a π pulse, to flip the qubit state from ground to the excited state. On the left side, in the “RF-Quantronium” case the data have been plotted versus a waiting time between the π pulse and the read-out pulse. The figure reports the data as switching probability between the two oscillation states of the JBA over about 50,000 realizations of the experiment for each point. The exponential decay defines T_1 .

On the right hand side, results of a similar group of experiments in the case of circuit QED are shown. Here, the same weak continuous measurement is performed and the data are presented as the time dependence of the transmitted beam phase shift averaged over about 50,000 realizations of the experiment. Here too, the exponential decay defines T_1 .

(Slide 36 – Ramsey fringes: longitude control measuring Q_2)

The third and last set of results deals with longitude control of the qubit state, observing what are called Ramsey fringes in order to measure Q_2 , the decoherence quality factor, which is crucial to evaluate the possibility of using the qubit in an actual computation. In this experiment, two $\pi/2$ pulses are applied at the input port of the qubit at a frequency slightly detuned from the qubit transition frequency (20 MHz on the left side, 6 MHz on the right) followed in both cases by a read-out pulse. A free evolution was introduced between the two pulses and the data are plotted versus pulse separation. In the RF-Quantronium case, the oscillation of the switching probability gave a $T_2=300$ ns, which

implies $Q_2=38,000$. In the circuit QED case, $T_2=500$ ns has been measured with $Q_2=14,000$.

(Slide 37 – Comparison with published results)

How these results compare with the ones published in literature regarding superconducting qubits? This is the question I tried to answer with the table presented in this slide. In the first place I think that the best way to compare results obtained using qubits with different transition frequencies is to compare quality factors. So, in green are the experiments I have been talking about and the Q_1 and Q_2 columns are the one to compare.

It is evident that if we look at Q_1 only few set of experiments (six to be precise, the two we did, and the ones done at Saclay, Delft, NTT and by the Yale/Chalmers collaboration) present similar results, and if we then look at the more relevant Q_2 only three of them are in the same range (the two we did and the one done in Saclay). By the way, none of them obtains results for either Q_1 or Q_2 that match the theoretical predictions and even if there have been a lot of fingerprinting to some of the possible reasons, I am not sure we know so much about them.

(Slide 38 – Perspectives: improving the parts)

Of course, there is always room for improvements both in the qubit and in the meter. Material science may help in dealing with better control of the barrier properties or with different choice of substrates for our circuits as well as going beyond lift-off technique can help in eliminating “inactive” junctions and optimizing electrode patterning and resonator quality.

(Slide 39 – Perspectives: good enough for new experiments)

But at the same time I think that what we have achieved can be considered good enough for some new gate experiments and to demonstrate entanglement between qubits and eventually Bell’s inequalities violation. I also think we are ready to develop some new circuit design toward fully scalable architectures for superconducting qubits. For instance, integrating several qubits in different transmission line resonators, properly

coupled to act as quantum bus to couple distant frequency multiplexed qubits, read-out using JBAs and manipulated by RF pulses to perform universal gate protocols.

I believe that these future experiments may help quantum engineers to get closer to their Holy Grail:

(Slide 40 – Acknowledgement)

Design and fabrication of superconducting circuits for amplification and processing of quantum signals

Luigi Frunzio

Outline

Motivation: quantum engineering for quantum machines

Quantum non demolition (QND) measurement

Design and fabrication of practical architectures

Experimental results

Perspectives

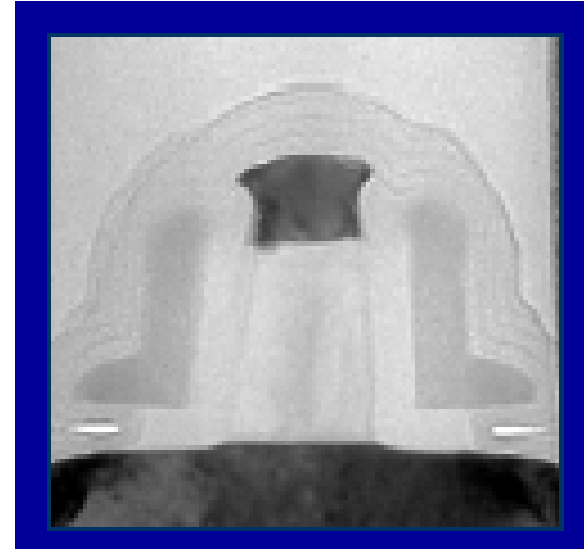
Do quantum machines exist ?

Laser



Discrete energy levels

CMOS transistor



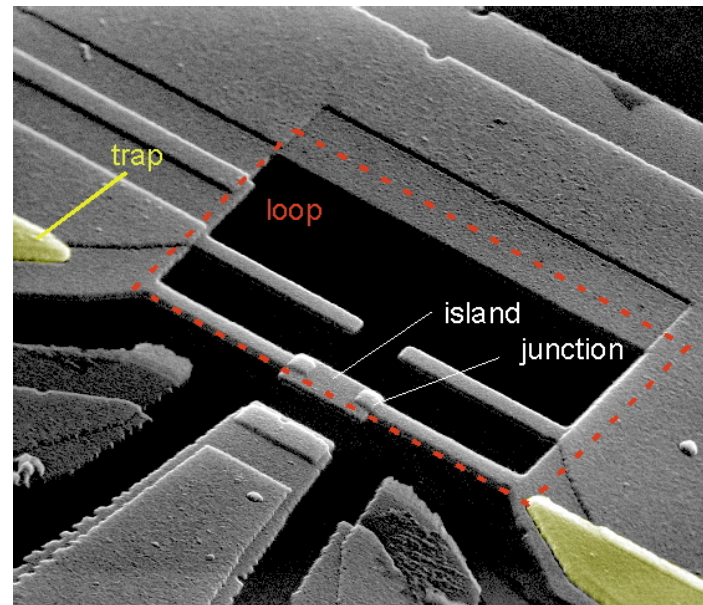
Bandstructure of Si

Quantum mechanics determines *material parameters*

but

collective degrees of freedom remain classical ...

An example of quantum machine: superconducting integrated quantum circuit



Courtesy of Quantronics Group

Elementary part of quantum information processor

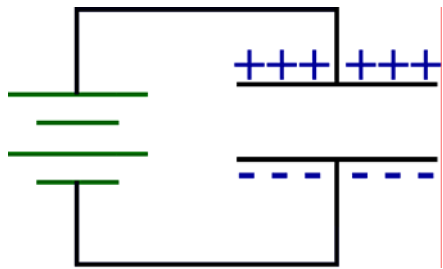
operates quantum-mechanically

and

quantum parameters are engineerable

Information units

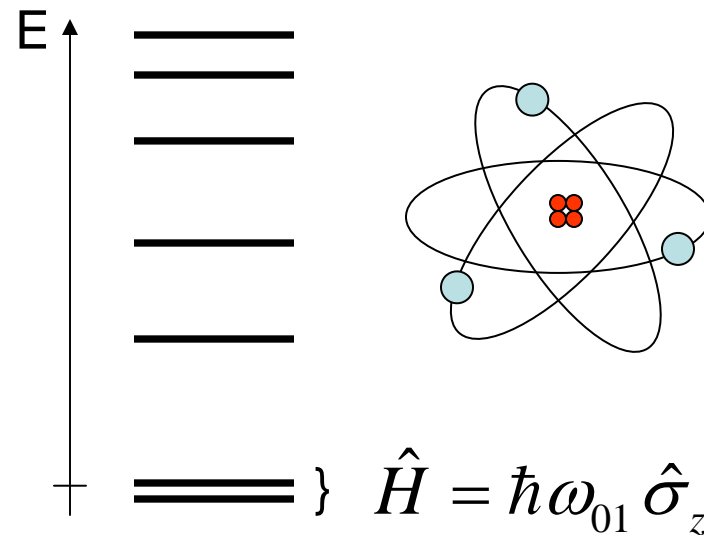
Classical bit



Bistable switch

“0” or “1”

Quantum bit (or “qubit”)

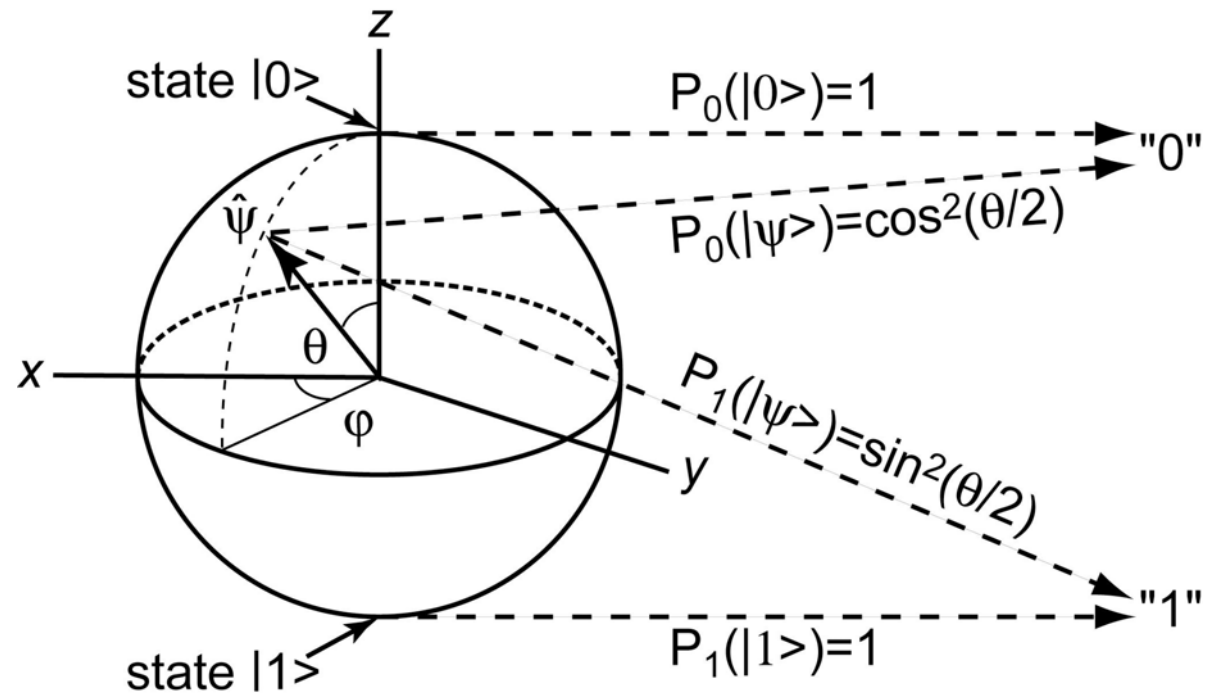
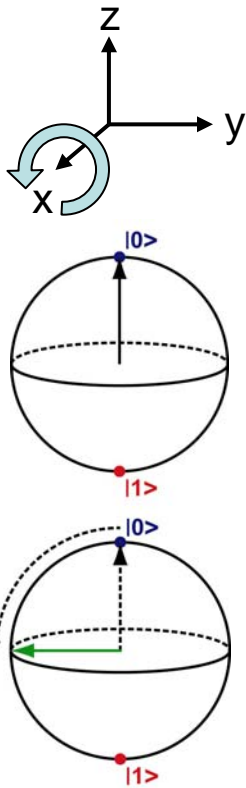


Two-level quantum system

$$|\psi\rangle = \alpha|0\rangle + \beta|1\rangle$$

Surprising properties of quantum information

Write



Read-out

$$|\psi\rangle = \cos(\theta/2) e^{-i\phi/2} |0\rangle + \sin(\theta/2) e^{i\phi/2} |1\rangle$$

latitude
longitude

The power of quantum information

REGISTER WITH N=10 BITS:

0000000000

0000000001

0000000010

• • •
• • •
• • •
• • •

1111111110

1111111111

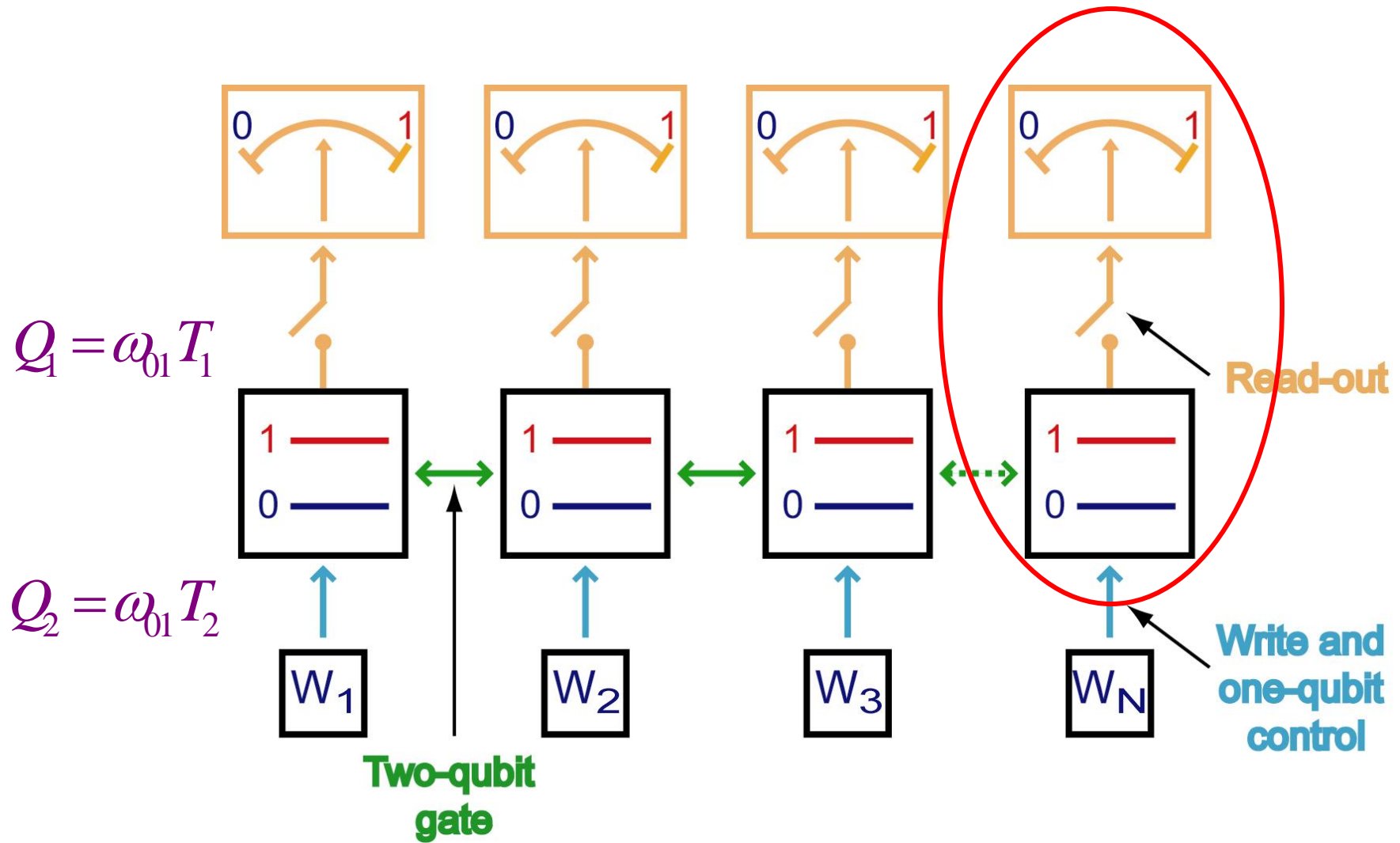
REGISTER WITH N QUBITS:

$$|\psi^{(N)}\rangle = \sum_{n=0}^{2^N-1} a_n |\psi_n^{(N)}\rangle$$

There are $2^{N+1}-2$ independent **real numbers** specifying the wave function

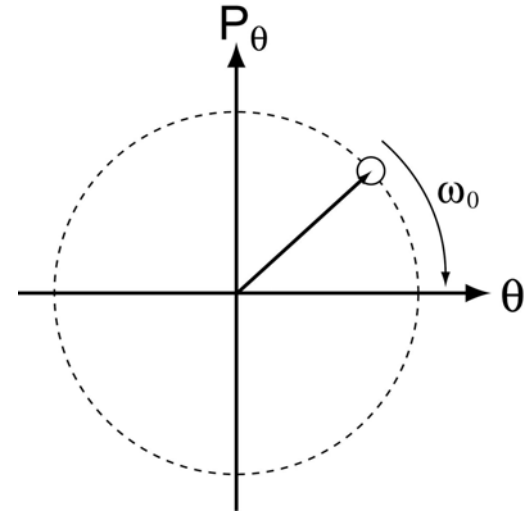
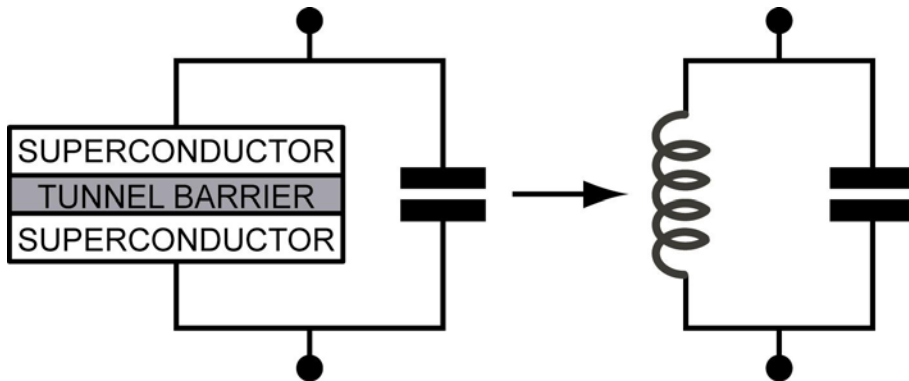
One number between 0 and $2^N-1=1023$

Elementary quantum processor

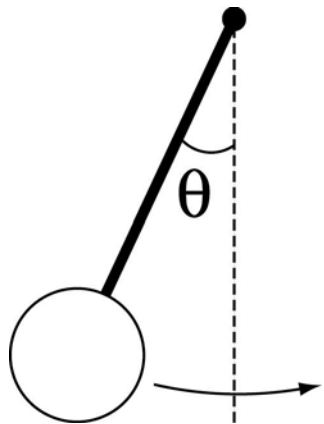


The meter system: an oscillator

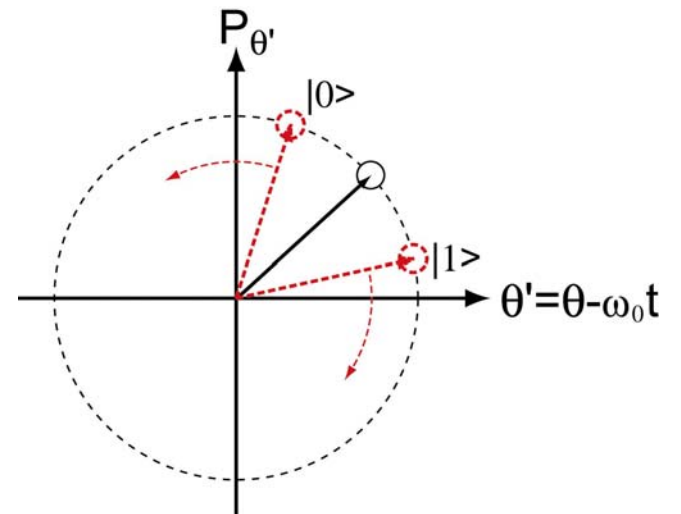
$$\hat{H} = \hbar\omega_0(a^\dagger a + 1/2)$$



In the rotating frame



$$\hat{H}_{tot} = \hat{H}_{qubit} + \hat{H}_{meter} + \hat{H}_{int}$$



The meter system: an oscillator with anharmonicity

$$\hat{H} = \hbar\omega_0(a^\dagger a + \frac{1}{2}) + \textit{higher order terms}$$

We want a QND read-out

$$\hat{H}_{tot} = \hat{H}_{qubit} + \hat{H}_{meter} + \hat{H}_{int}$$

Quantum Non-Demolition measurement:

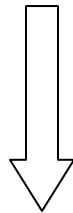
$$\left[\hat{H}_{qubit}, \hat{H}_{tot} \right] = 0$$

We want a QND read-out

$$\hat{H}_{tot} = \hbar\omega_L \hat{\sigma}_z + \hbar\omega_0 a^\dagger a + \hat{H}_{int}$$

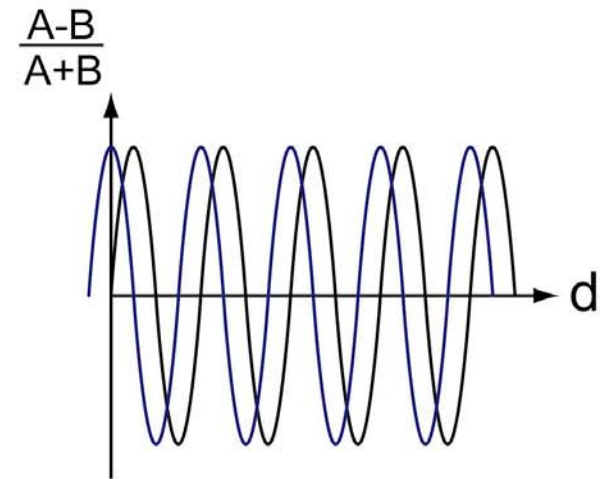
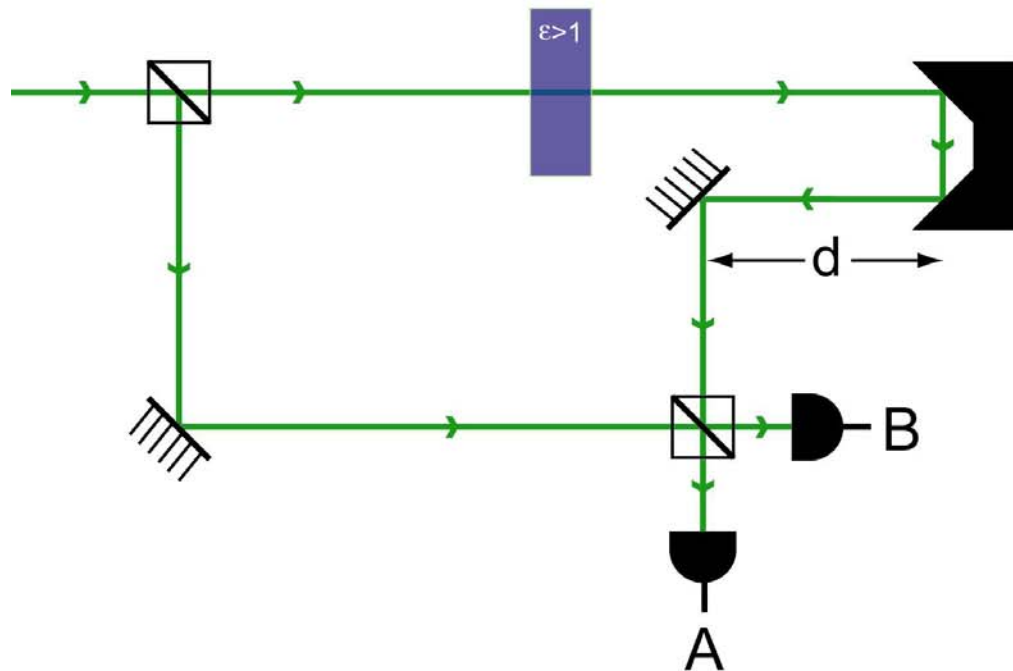
Quantum Non-Demolition measurement:

$$\left[\hat{H}_{qubit}, \hat{H}_{tot} \right] = 0$$



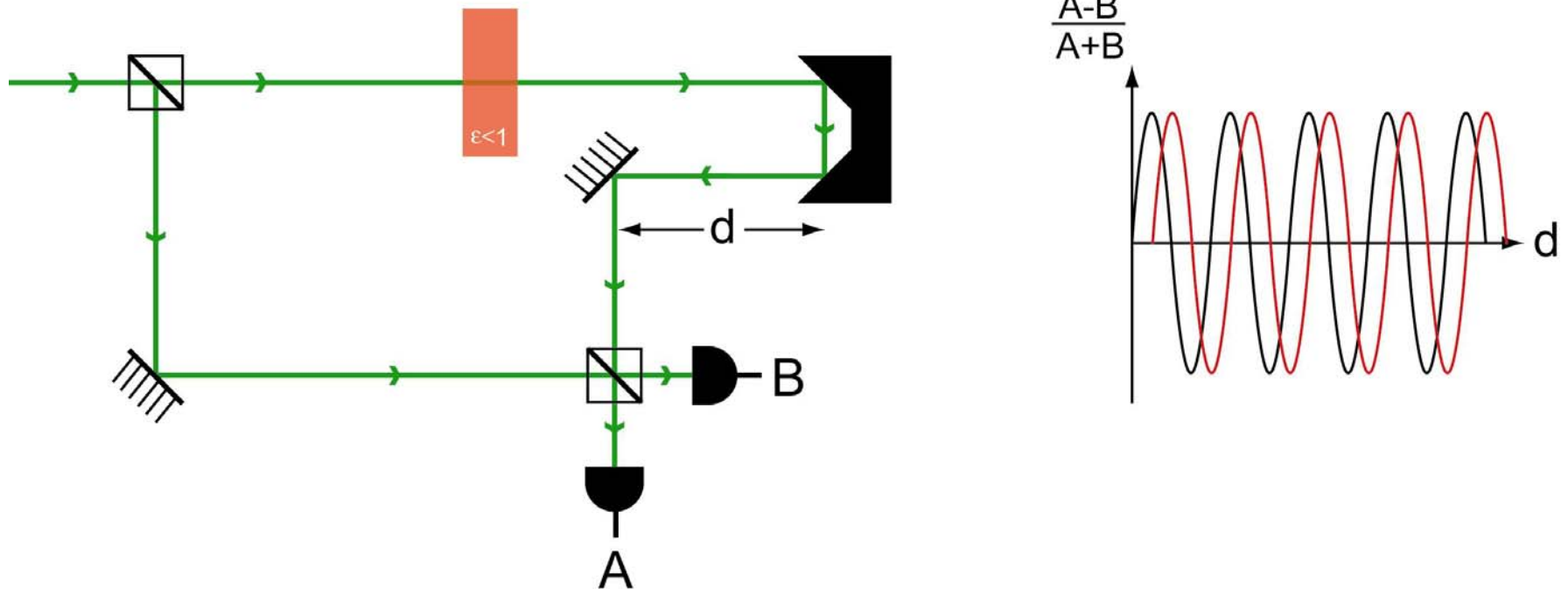
$$\left[\hat{H}_{qubit}, \hat{H}_{int} \right] = 0$$

How to measure without dissipation?



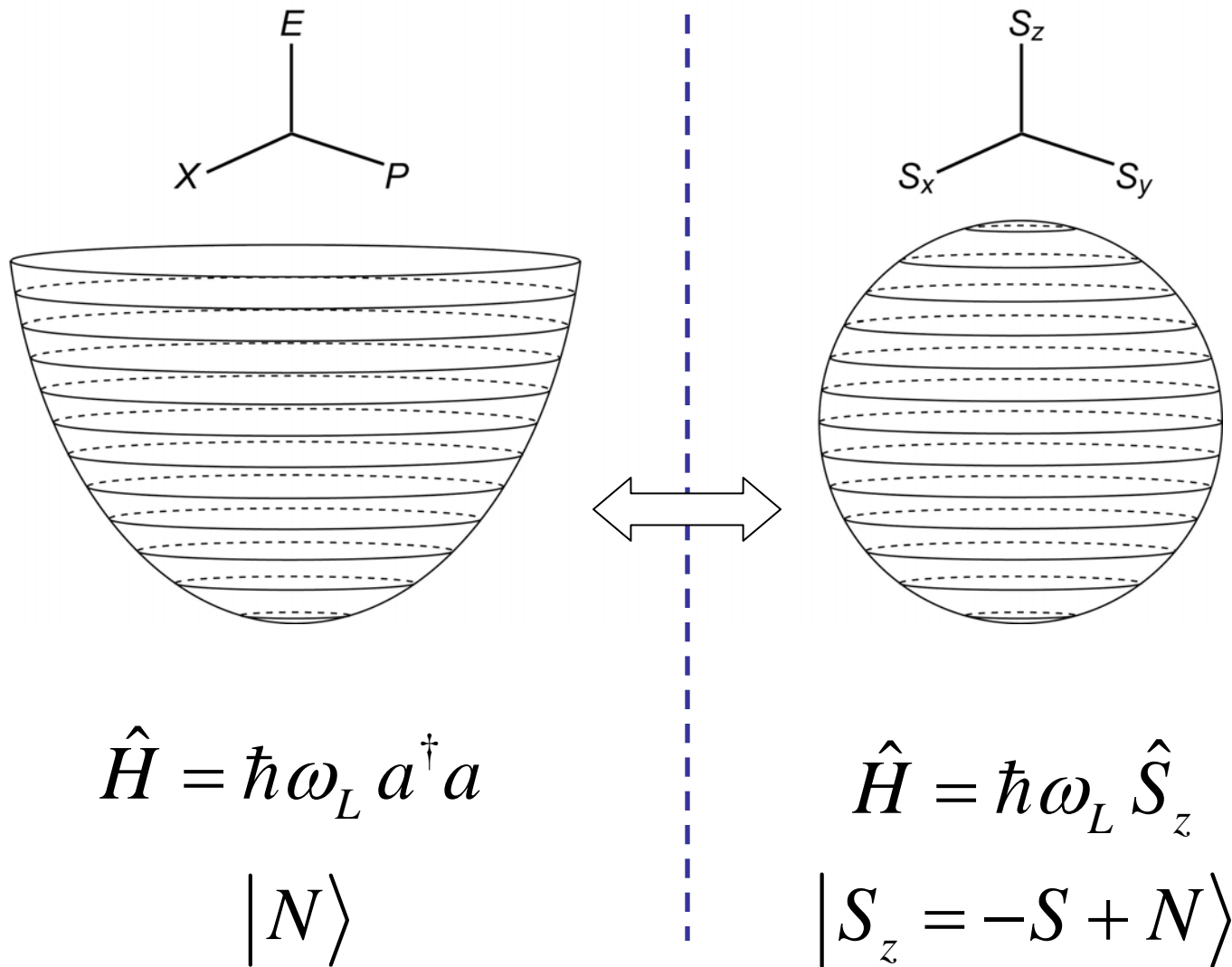
A dispersive measurement – measures susceptibility, not losses
“leave no energy behind !”

How to measure without dissipation?



A dispersive measurement – measures susceptibility, not losses
“leave no energy behind !”

Correspondence between oscillator and spin $S \gg 1$



Possible “natural” qubit-meter interactions

$$\hat{H}_{tot} = \hbar\omega_L \hat{\sigma}_z + \hbar\omega_0 a^\dagger a + \hat{H}_{int}$$

Interaction between spin and oscillator

NO!!! $\hat{H}_{int} = \hbar\omega_{int} (\hat{\sigma}^+ a + \hat{\sigma}^- a^\dagger)$

Interaction between oscillators

NO!!! $\hat{H}_{int} = \hbar\omega_{int} (a_1^\dagger + a_1)(a_2^\dagger + a_2)$

Interaction between spins

NO!!! $\hat{H}_{int} = \hbar\omega_{int} \vec{S}_1 \cdot \vec{S}_2 \quad \hat{H}_{int} = \hbar\omega_{int} (\hat{\sigma}^+ \hat{S}^- + \hat{\sigma}^- \hat{S}^+)$

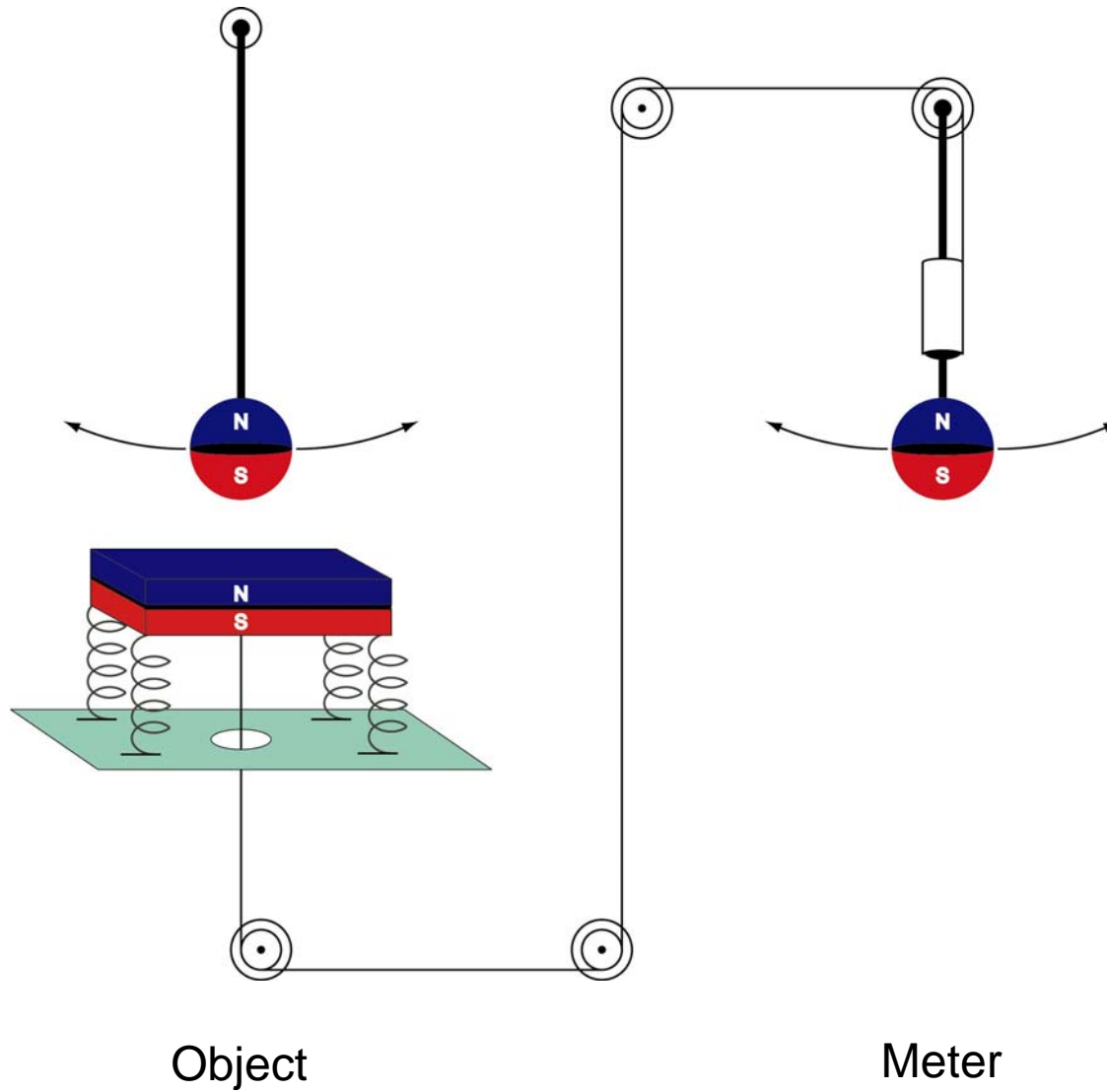
A new QND read-out interaction

$$\hat{H}_{tot} = \hbar\omega_L \hat{\sigma}_z + \hbar\omega_0 a^\dagger a + \hat{H}_{int}$$

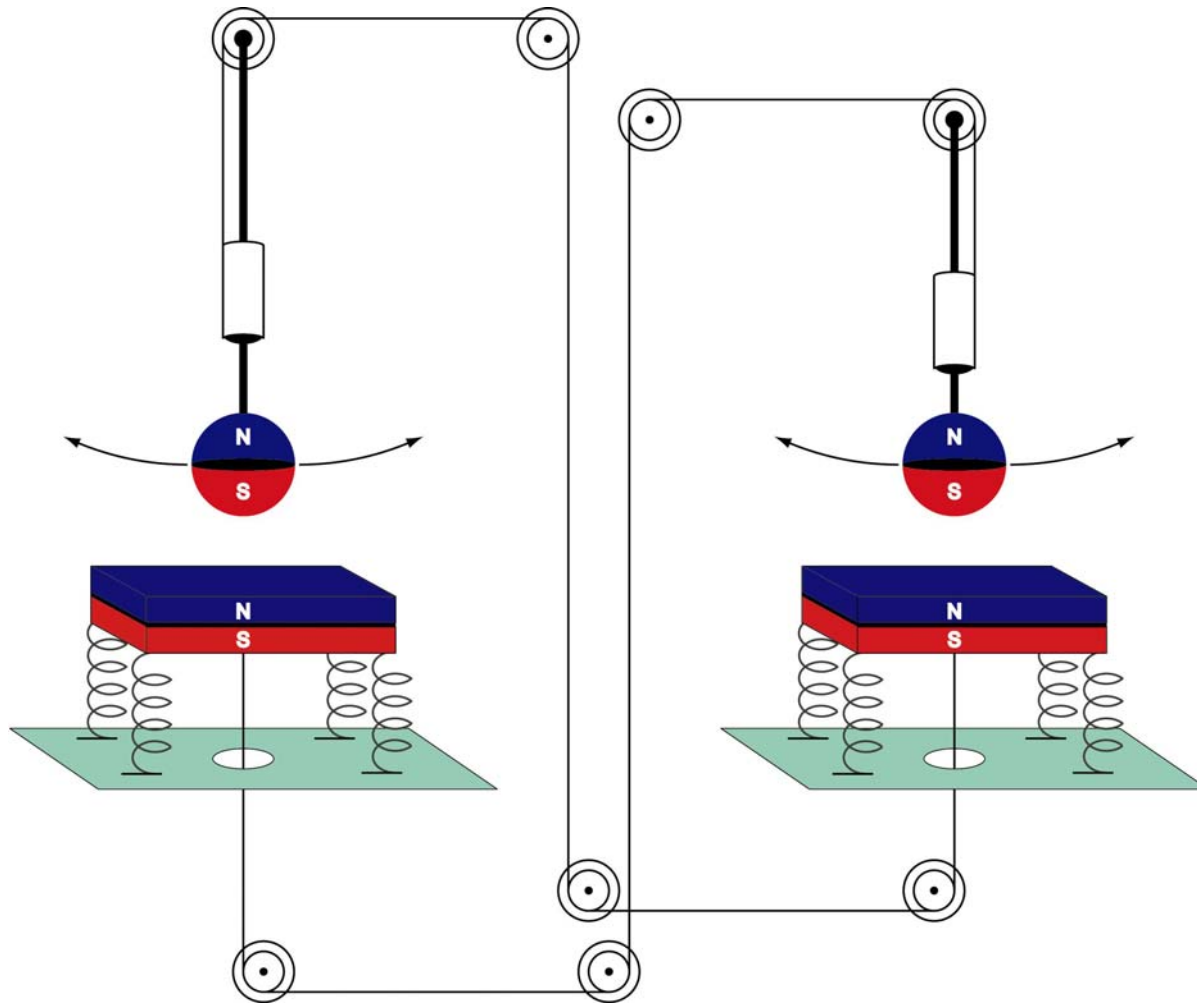
The interaction operator for our QND measurement:

$$\hat{H}_{QND}^{int} = \hbar\omega_0 \lambda \hat{\sigma}_z a^\dagger a$$

Magnetomechanical analog



Magnetomechanical analog



Meter

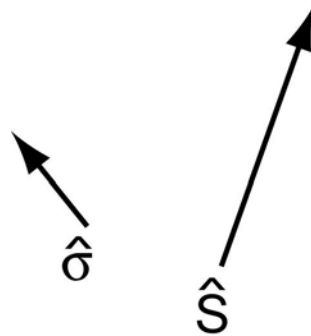
Object

A new symmetric QND read-out interaction

$$\hat{H}_{tot} = \hbar\omega_L \hat{\sigma}_z + \hbar\omega_0 \hat{S}_z + \hat{H}_{int}$$

The interaction operator for our QND measurement:

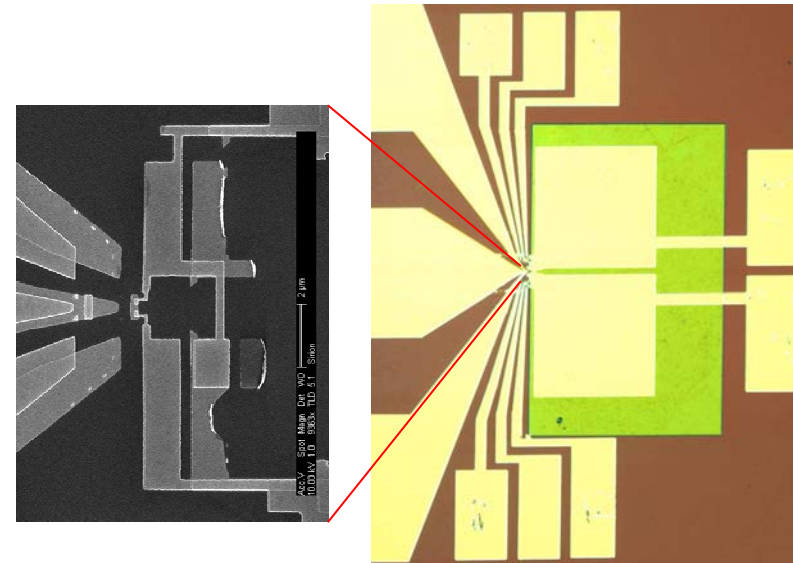
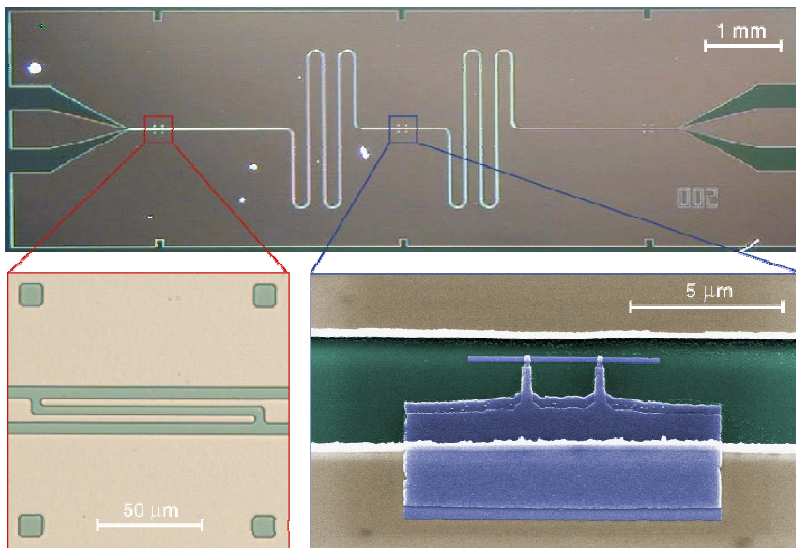
$$\hat{H}_{QND}^{int} = \hbar\omega_0 \lambda \hat{\sigma}_z \hat{S}_z$$



Easy to read formula, but not trivial to realize practically

Fabrication

- No internal dissipation: superconducting electronics
- Non-linearity: easy measurement with anharmonicity
- Control over six orders of magnitude in dimensions

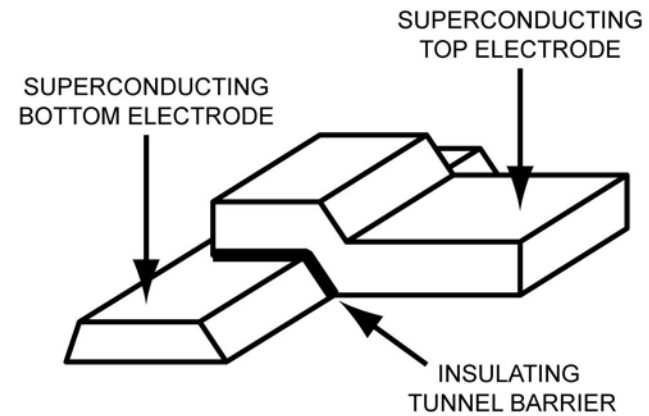
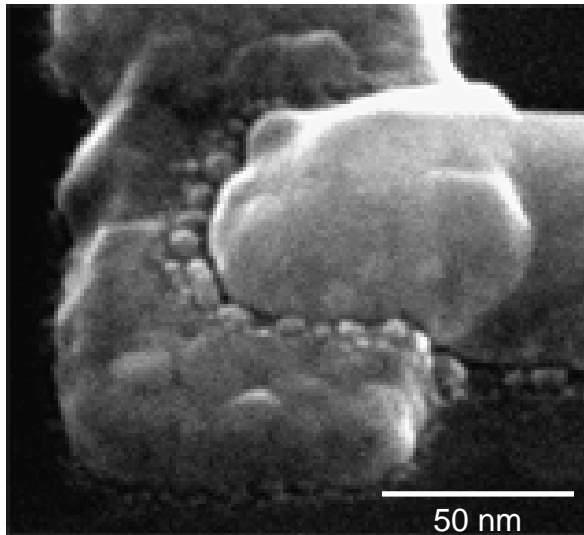


Fabrication

- No internal dissipation: superconducting electronics
- Non-linearity: easy measurement with anharmonicity
- Control over six orders of magnitude in dimensions



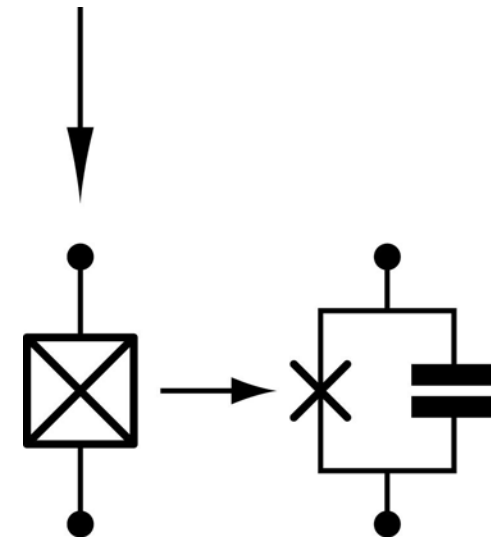
Josephson junction: the only non-linear and non-dissipative component



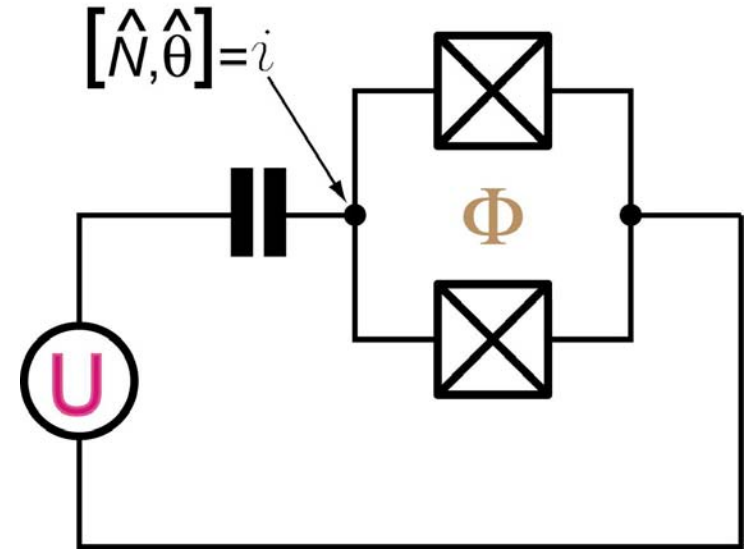
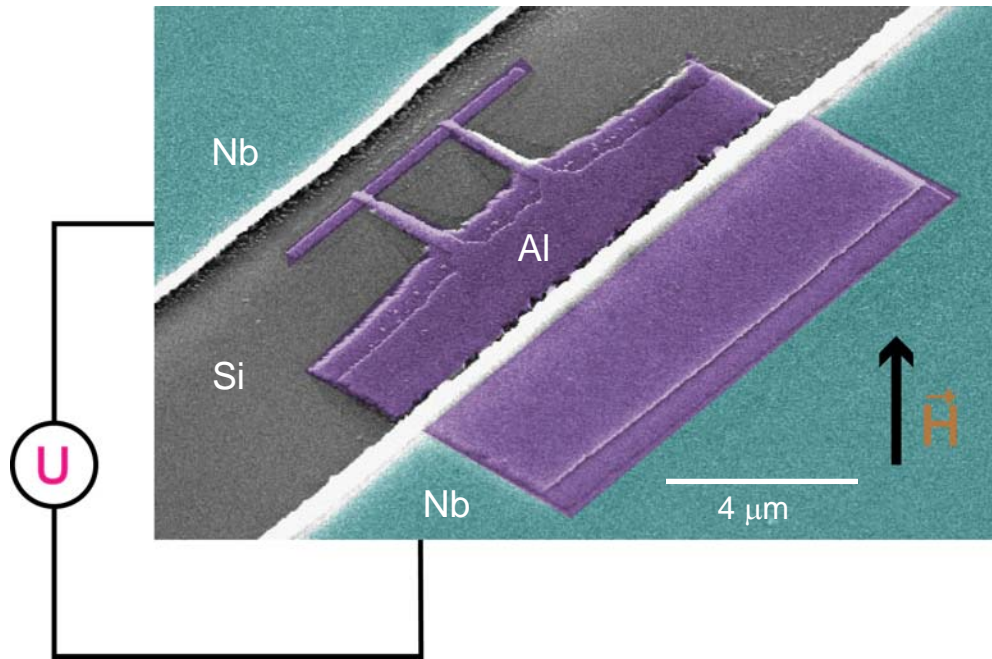
$$I = I_c \sin(2\pi \Phi_J / \Phi_0)$$

$$L_{J0} = \frac{\Phi_0}{2\pi I_c}$$

$$L_J(\Phi_J) = \frac{L_{J0}}{\cos(2\pi \Phi_J / \Phi_0)}$$

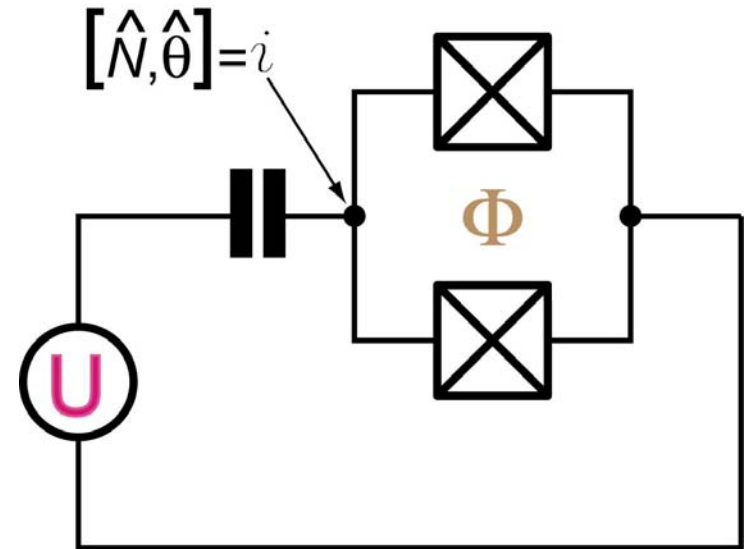
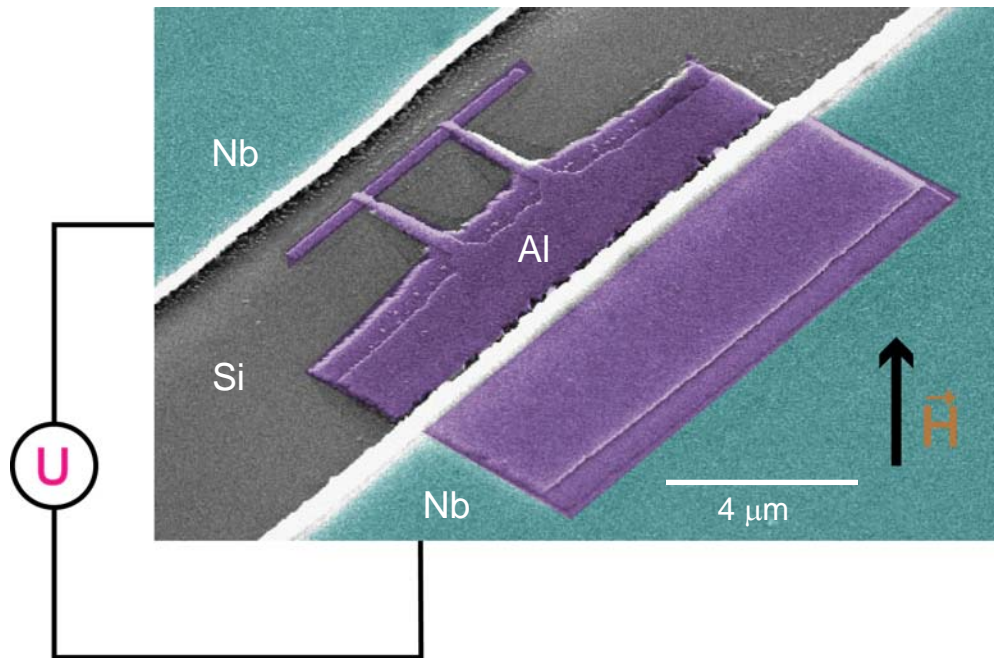


Split Cooper Pair Box Qubit



$$\hat{H}_{sCPB} = E_C \left(\hat{N} - \frac{C_g U}{2e} \right)^2 - E_J \cos \left(\frac{\pi \Phi}{\Phi_0} \right) \cos \hat{\theta}$$

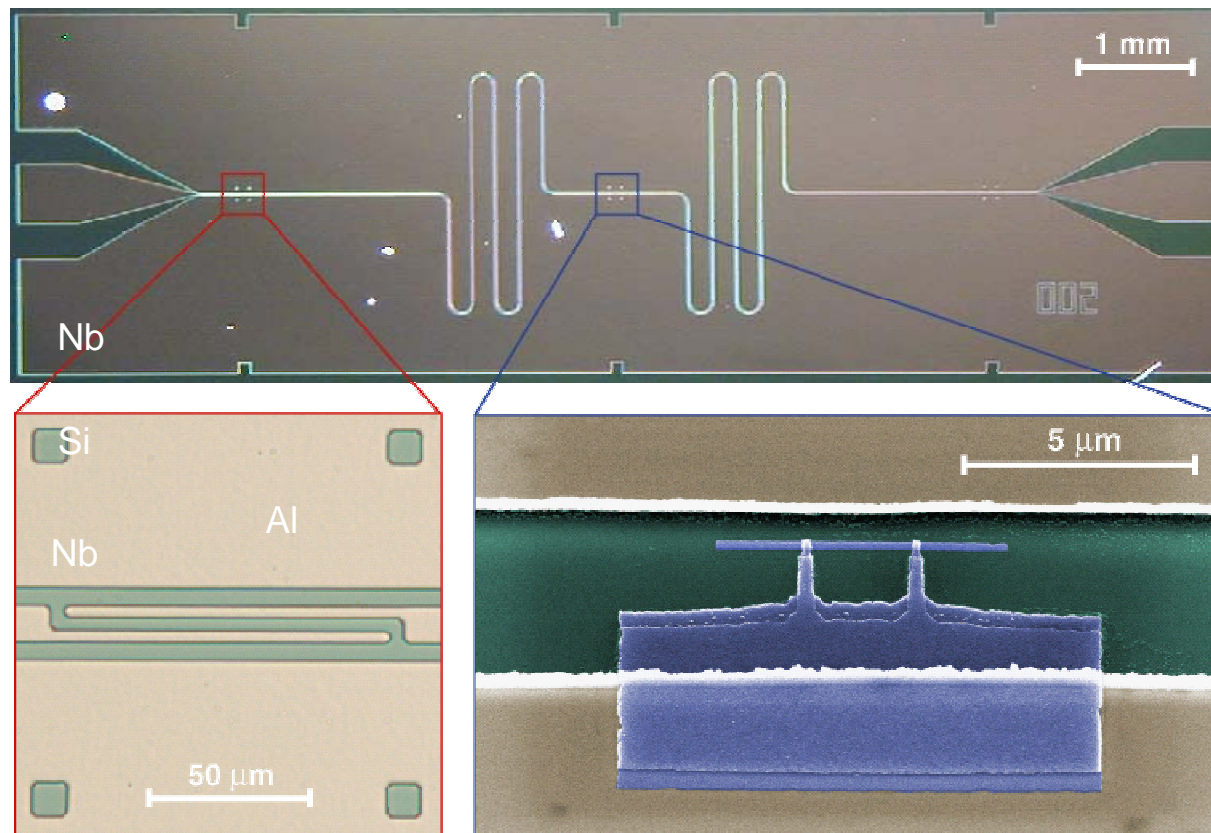
Split Cooper Pair Box Qubit



$$\hat{H}_{sCPB}^* = -\frac{E_J^*}{2} \hat{\sigma}_z$$

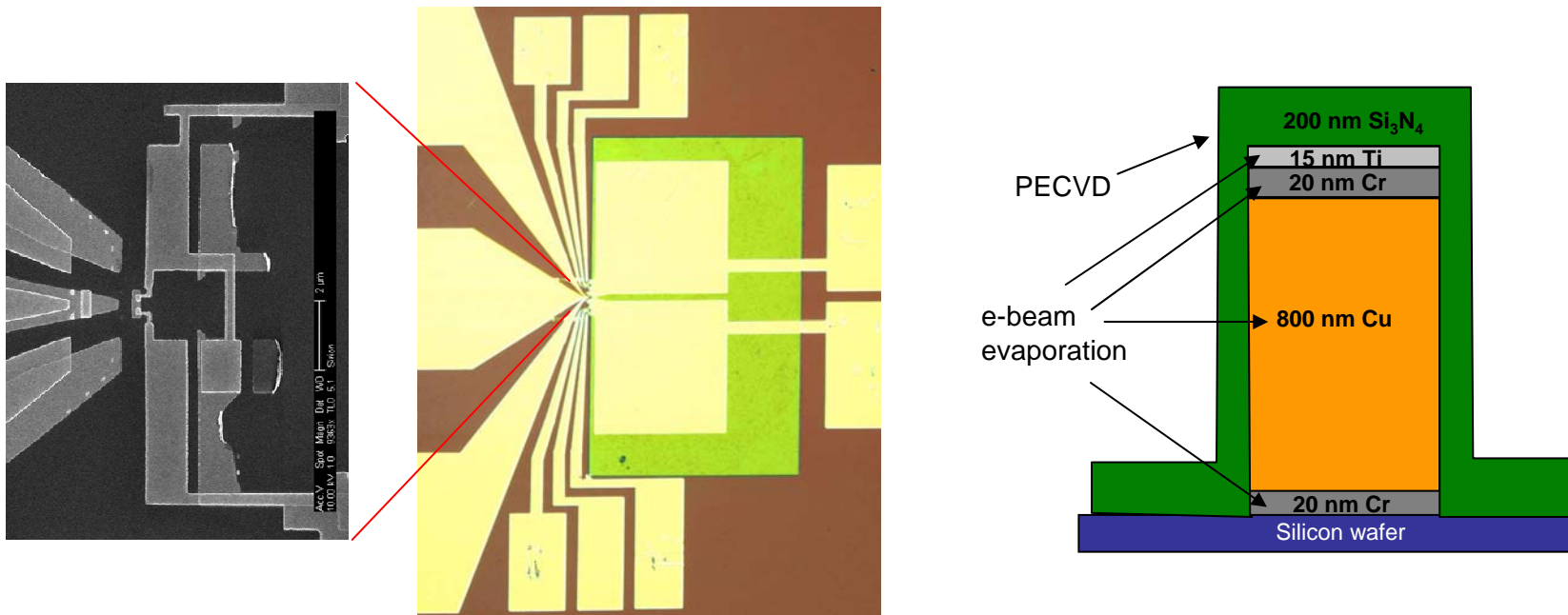
Meter using electrical microwave resonators (1)

Transmission line resonator for “circuit QED”



Meter using electrical microwave resonators (2)

Lumped resonator for “RF-Quantronium”



Two versions of the dispersive read-out strategy

charge

$$Q_k = \frac{\partial E_k}{\partial U}$$

CPB + RF-SET

capacitance

$$C_k = \frac{\partial^2 E_k}{\partial U^2}$$

“Circuit QED”

current

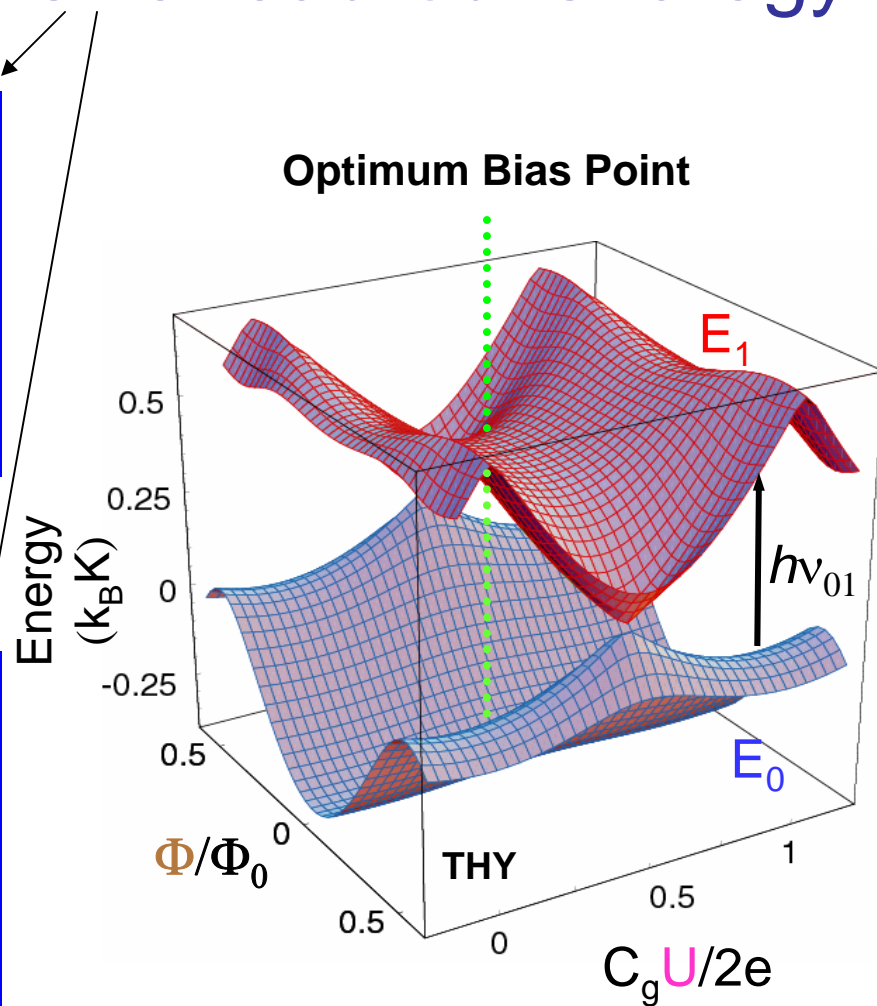
$$I_k = \frac{\partial E_k}{\partial \Phi}$$

CPB + dc JJ
“Quantronium”

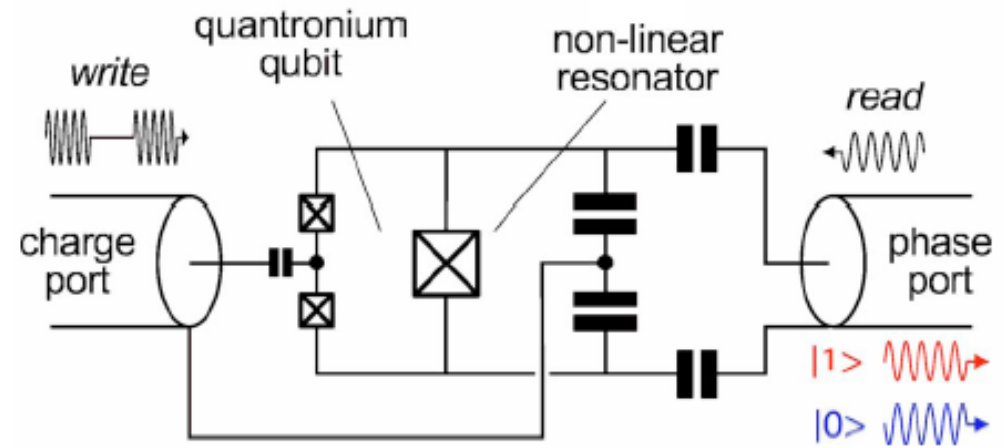
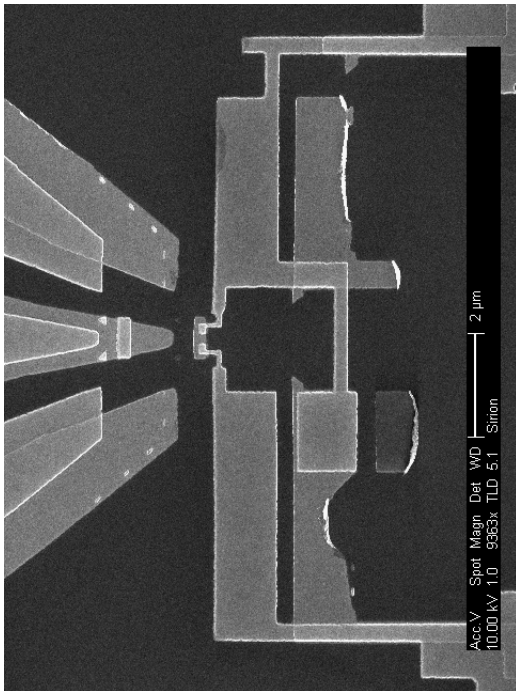
inductance

$$L_k = \left(\frac{\partial^2 E_k}{\partial \Phi^2} \right)^{-1}$$

“RF Quantronium”



Inductively coupling qubit and meter: “RF-Quantronium” architecture



The RF-Quantronium reduced Hamiltonian

$$\hat{H}_{RF-Q}^* = \frac{C_g U(t)}{2e} E_c \hat{\sigma}_x - \frac{E_J}{2} \hat{\sigma}_z + \hbar\omega_p a^\dagger a + \hbar\omega_p \lambda_{RF-Q} \hat{\sigma}_z a^\dagger a - \mu \left(1 + \frac{\lambda_{RF-Q}}{4} \hat{\sigma}_z \right) (a + a^\dagger)^4 - f_\chi (a + a^\dagger) \chi(t)$$

$$\hat{H}_{tot} = \hat{H}_{qubit} + \hat{H}_{meter} + \hat{H}_{int} + \hat{H}_{control} + \hat{H}_{amp}$$

QND interaction operator

$$\hat{H}_{RF-Q}^{int} = \hbar\omega_p \lambda_{RF-Q} \hat{\sigma}_z a^\dagger a$$

$$\lambda_{RF-Q} = \frac{E_J}{4E_J^d}$$

The RF-Quantronium reduced Hamiltonian

$$\hat{H}_{RF-Q}^* = \frac{C_g U(t)}{2e} E_c \hat{\sigma}_x - \frac{E_J}{2} \hat{\sigma}_z + \hbar\omega_p a^\dagger a + \hbar\omega_p \lambda_{RF-Q} \hat{\sigma}_z a^\dagger a - \mu \left(1 + \frac{\lambda_{RF-Q}}{4} \hat{\sigma}_z \right) (a + a^\dagger)^4 - f_\chi (a + a^\dagger) \chi(t)$$

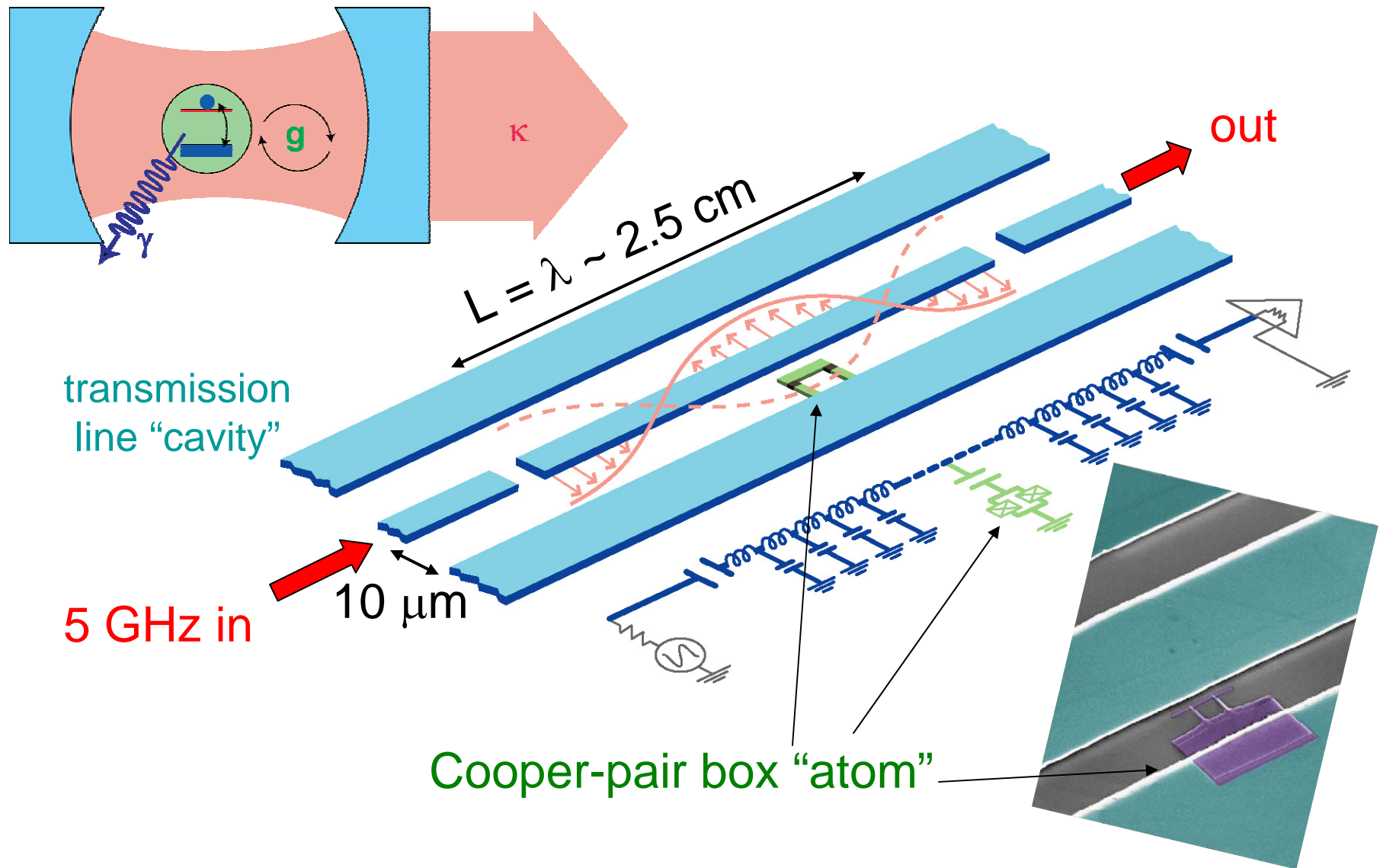
$$\hat{H}_{tot} = \hat{H}_{qubit} + \hat{H}_{meter} + \hat{H}_{int} + \hat{H}_{control} + \hat{H}_{amp}$$

QND interaction operator

$$\hat{H}_{RF-Q}^{int} = \hbar\omega_p \lambda_{RF-Q} \hat{\sigma}_z \hat{S}_z$$

$$\lambda_{RF-Q} = \frac{E_J}{4E_J^d}$$

Capacitively coupling qubit and meter: “circuit QED” architecture



The circuit QED reduced Hamiltonian

$$\hat{H}_{cQED}^* = \frac{C_g U(t)}{2e} \hat{\sigma}_x - \frac{E_J}{2} \hat{\sigma}_z + \hbar\omega_r a^\dagger a - \hbar g (\sigma^+ a + \sigma^- a^\dagger) + f_U U'(t) (a^\dagger + a)$$

for $\Delta = \omega_{01} - \omega_r \gg g$

$$\hat{H}^* = \frac{\hbar\omega_{01}}{2} \left(1 + \lambda_{cQED} \frac{\omega_r}{\omega_{01}} \right) \hat{\sigma}_z + \hbar\omega_r a^\dagger a + \hbar\omega_r \lambda_{cQED} \hat{\sigma}_z a^\dagger a$$

QND probe operator

$$\hat{H}_{cQED}^{\text{int}} = \hbar\omega_r \lambda_{cQED} \hat{\sigma}_z a^\dagger a$$

$$\lambda_{cQED} = \frac{g^2}{\Delta\omega_r}$$

The circuit QED reduced Hamiltonian

$$\hat{H}_{cQED}^* = \frac{C_g U(t)}{2e} \hat{\sigma}_x - \frac{E_J}{2} \hat{\sigma}_z + \hbar\omega_r a^\dagger a - \hbar g (\sigma^+ a + \sigma^- a^\dagger) + f_U U'(t) (a^\dagger + a)$$

for $\Delta = \omega_{01} - \omega_r \gg g$

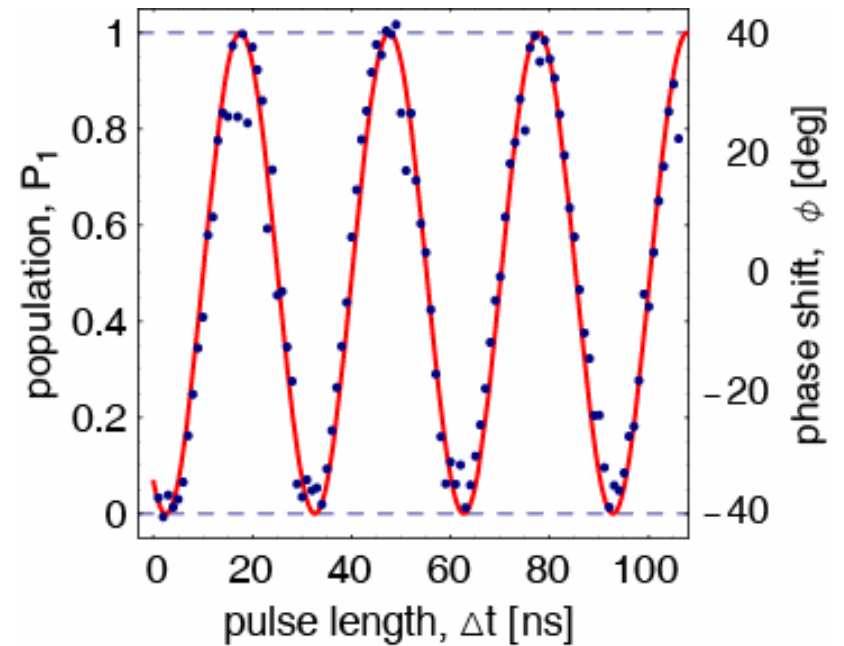
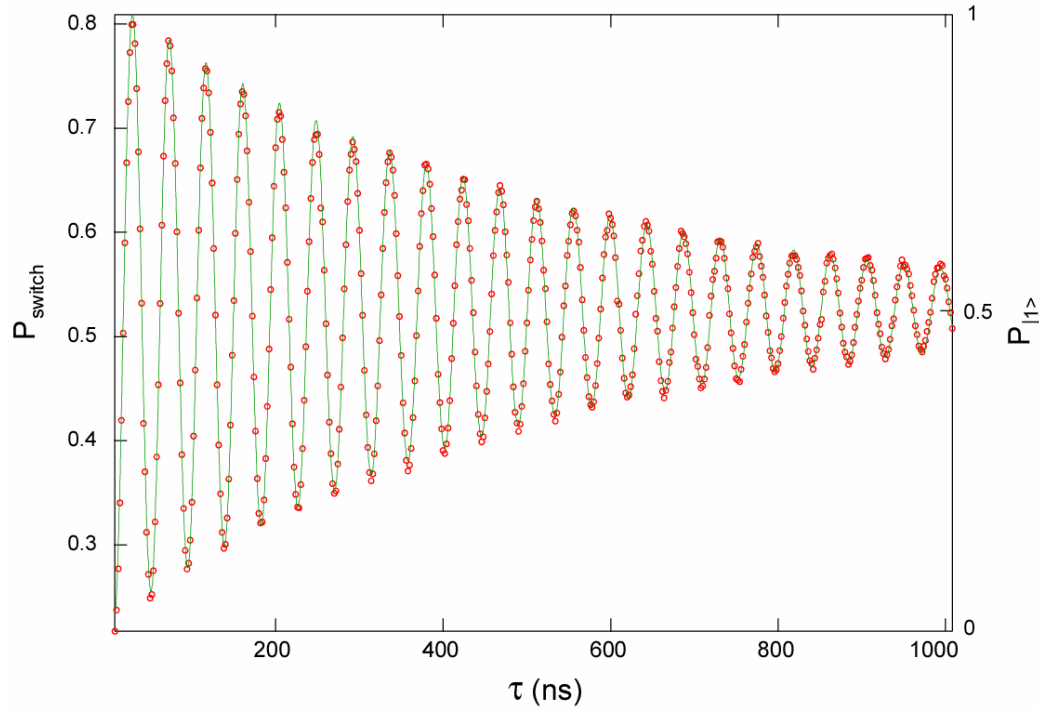
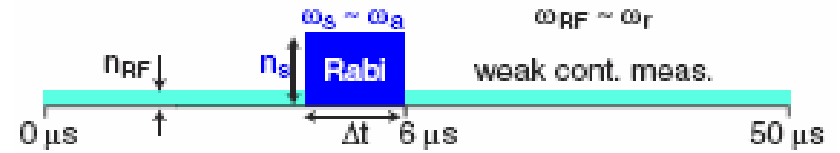
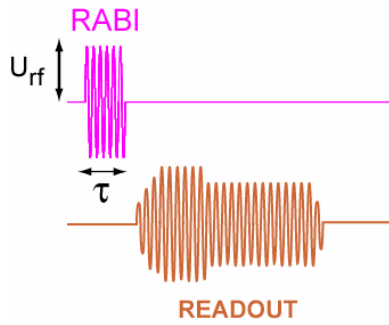
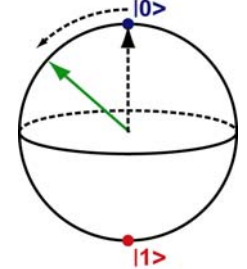
$$\hat{H}^* = \frac{\hbar\omega_{01}}{2} \left(1 + \lambda_{cQED} \frac{\omega_r}{\omega_{01}} \right) \hat{\sigma}_z + \hbar\omega_r a^\dagger a + \hbar\omega_r \lambda_{cQED} \hat{\sigma}_z a^\dagger a$$

QND probe operator

$$\hat{H}_{cQED}^{\text{int}} = \hbar\omega_r \lambda_{cQED} \hat{\sigma}_z \hat{S}_z$$

$$\lambda_{cQED} = \frac{g^2}{\Delta\omega_r}$$

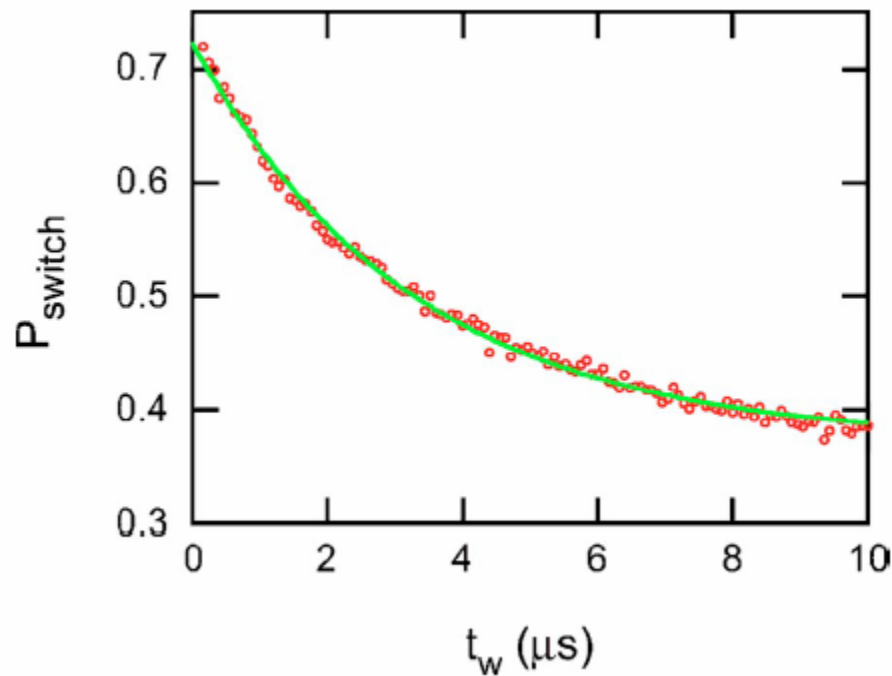
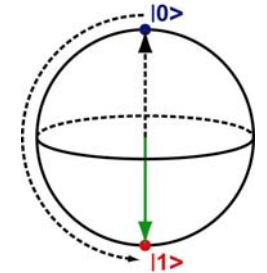
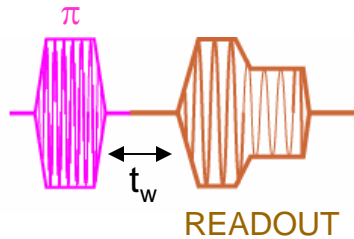
Rabi oscillations: latitude control



“RF-Quantrium”

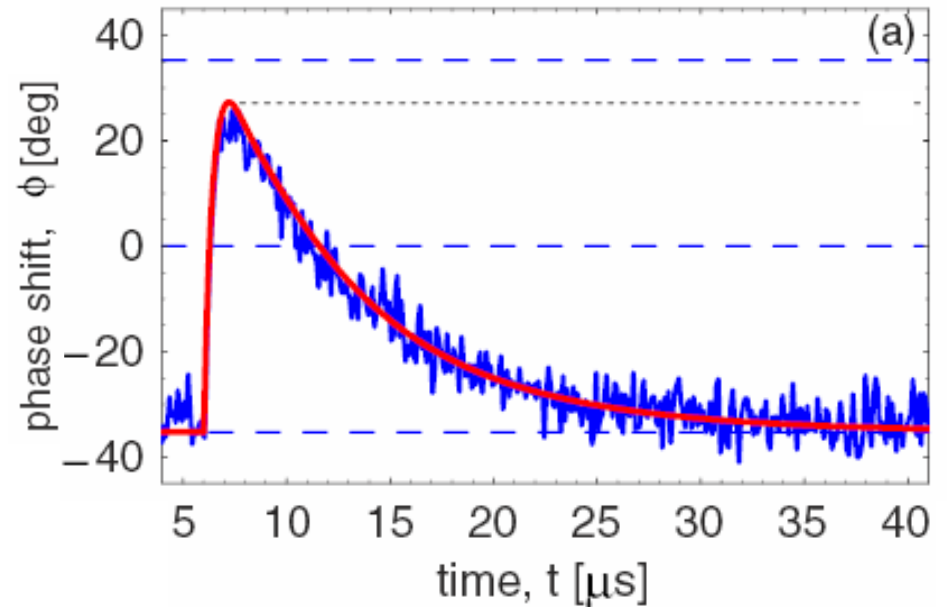
“Circuit QED”

Excited state relaxation: measuring Q_1



“RF-Quantonium”

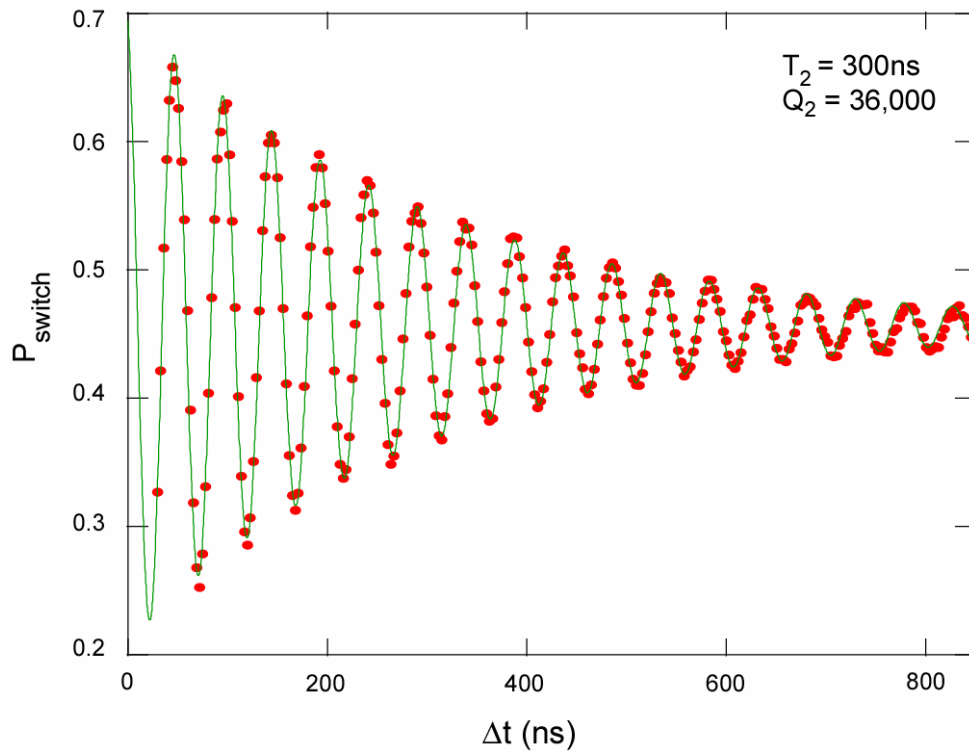
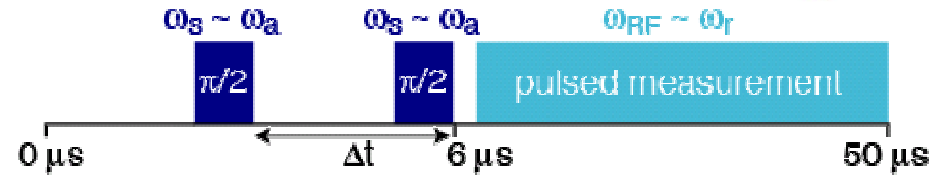
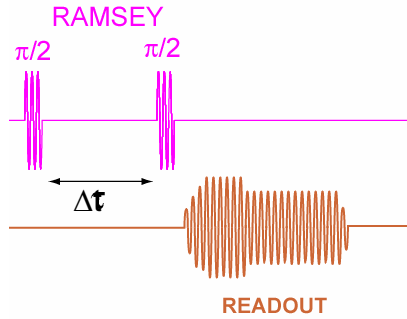
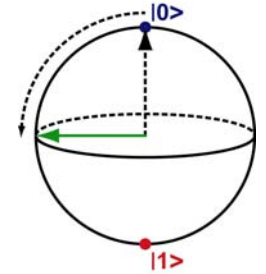
$T_1 = 5.0 \mu\text{s}$ @ $\nu_{01} = 9.5 \text{ GHz}$ $\rightarrow Q_1 = 3.0 \times 10^5$
 $T_1 = 1.3 \mu\text{s}$ @ $\nu_{01} = 19 \text{ GHz}$ $\rightarrow Q_1 = 1.6 \times 10^5$



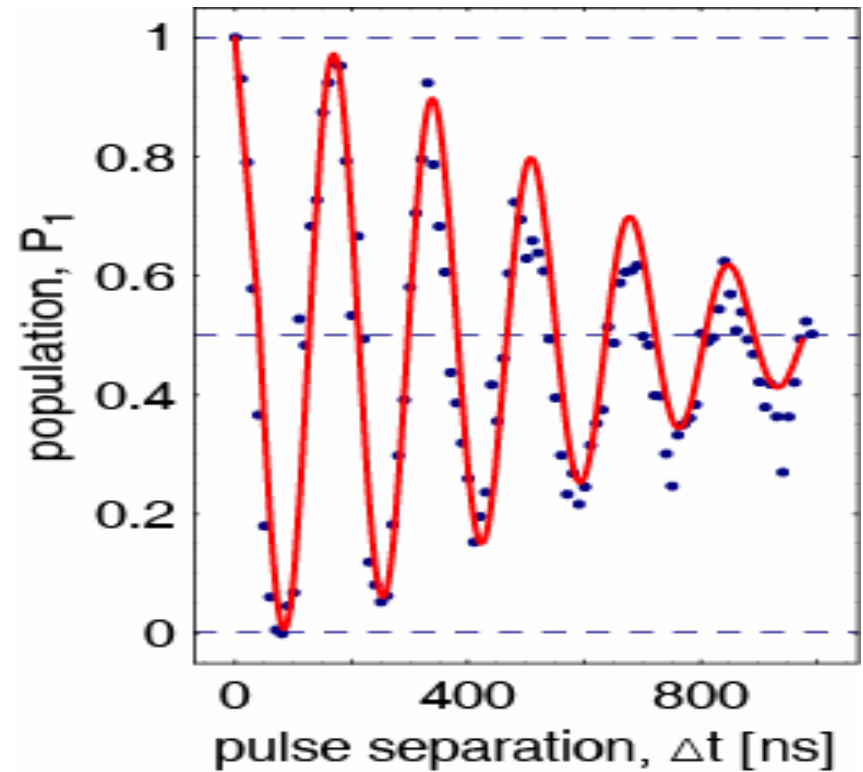
“Circuit QED”

$T_1 = 7.3 \mu\text{s}$ @ $\nu_{01} = 4.3 \text{ GHz}$
 $\rightarrow Q_1 = 2.0 \times 10^5$

Ramsey fringes: longitude control measuring Q_2



RF-Quantrium



Circuit QED

Comparison with published results

Institution	Qubit (write/read)	ν_{01} [GHz]	Q_1 [$\times 10^5$]	Q_2 [$\times 10^4$]	Reference
Yale	Charge/Inductance RF-Quantrium	9.5 19	3.0 1.2	1.9 3.8	Siddiqi et al., PR B73,054510 (2006)
Yale	Charge/Capacitance Circuit QED	4.3	2.0	1.4	Wallraff et al., PRL 95, 060501 (2006)
Saclay	Charge/Phase Quantrium	16.5 16.4	1.9 0.5	5.2 3.1	Vion et al., Science 296, 886 (2002) Collin et al., PRL 93, 157005 (2004)
Helsinki	Charge/Capacitance	11	0.005	0.003	Sillanpää et al., PRL 95, 206806 (2005)
NIST-UCSB	Phase/Flux	4.7	0.14	0.4	Martinis et al., PRL 95, 210503 (2005)
Maryland	Phase/Phase	9.8	0.004	0.006	Xu et al., PR B71, 064512 (2005)
Delft	Flux/Inductance	5.5	1.4	0.7	Bertet et al., PRL 95, 257002 (2005)
UCB	Flux/Flux	4.0	0.1	0.04	Plourde et al., PR B72, 060506 (2005)
NTT	Flux/Flux	4.35	1.3	0.03	Johansson et al., PRL 96, 127006 (2006)
Yale/Chalmers	Charge/Charge	76	6.2	0.016	Lehnert et al., PRL 90, 027002 (2003)
NEC	Charge/Charge	5	0.07	0.0005	Astafiev et al., PRL 96, 137001 (2006) Astafiev et al., PR B69, 180507 (2004)
Chalmers	Charge/Charge	3.6	0.016		Duty et al., PR B69, 140503 (2004)

Perspectives: improving the parts

qubit

- Eliminating the “inactive” junctions
- Improving barrier stoichiometry
- Changing electrode patterning
- Substrate quality

meter

- Resonator quality
- Losses at microwave frequencies
- Coupling to qubit

Perspective: good enough for new experiments

- Controlled two qubits experiments: universal gate set
- Photon number splitting: Fock's states
- Multilayered structures: fully scalable qubit architectures
- Bell's inequalities violation

Quantum Engineer's Holy Grail

Do fully entangled quantum superpositions still exist for complex systems like computers with many hundreds of qubits?



Acknowledgements

W. KECK
FOUNDATION



Michel Devoret
Irfan Siddiqi
R. Vijay
Etienne Boaknin
Mike Metcalfe
Chad Rigetti



Steve Girvin
Alexandre Blais
Ren-Shou Huang



Rob Schoelkopf
Andreas Wallraff
David Schuster
Hannes Majer
Joe Schreier



UNIVERSITE
PARIS-SUD XI

Marc Gabay



Roberto Cristiano
Settimo Termini



ARDA



Bibliography

- [A02] A. Aspect, *Bell's theorem: the naïve view of an experimentalist*, arXiv: quant-ph/0402001.
- [AJW01] A. Aassime, G. Johnsson, G. Wendin, R. J. Schoelkopf, P. Delsing, *Radio-Frequency Single Electron Transistor as Readout Device for Qubits: Charge Sensitivity and Backaction*, Phys. Rev. Lett. **86**, 3376 (2001).
- [B87] J. S. Bell, *Speakable and Unspeakable in Quantum Mechanics. Collected Papers on Quantum Philosophy*, Cambridge University Press (1987).
- [BCB05] P. Bertet, I. Chiorescu, G. Burkard, K. Semba, C. J. P. M. Harmans, J. E. Mooij, *Dephasing of a Superconducting Qubit Induced by Photon Noise*, Phys. Rev. Lett. **95**, 257002 (2005).
- [BK92] V. B. Braginsky, F. Ya. Khalili, *Quantum measurement*, Cambridge University Press (1992).
- [Bo97] V. Bouchiat, *Quantum Fluctuations of the Charge in Single Electron and Single Cooper Pair Devices*, Thesis, Université Paris VI (1997), available in pdf format at http://www-drecam.cea.fr/articles_k2/s02/112/publi.pdf
- [BP92] A. Barone, G. Paternò, *Physics and Applications of the Josephson Effect*, Wiley, New York (1992).
- [BHW04] A. Blais, R.-S. Huang, A. Wallraff, S. M. Girvin, R.J. Schoelkopf, *Cavity quantum electrodynamics for superconducting electrical circuits: An architecture for quantum computation*, Phys. Rev. **A69**, 062320 (2004).
- [BVJ98] V. Bouchiat, D. Vion, P. Joyez, D. Esteve, M. H. Devoret, *Quantum Coherence with a Single Cooper Pair*, Physica Scripta **T76**, 165 (1998).
- [CBS04] I. Chiorescu, P. Berte, K. Semba, Y. Nakamura, C. J. P. M. Harmans, J. E. Mooij, *Coherent dynamics of a flux qubit coupled to a harmonic oscillator*, Nature **431**, 159 (2004).
- [CIA04] E. Collin, G. Ithier, A. Assime, P. Joyez, D. Vion, D. Esteve, *NMR-like Control of a Quantum Bit Superconducting Circuit*, Phys. Rev. Lett. **93**, 157005 (2004).

- [C02] A. Cottet, *Implementation of a quantum bit in a superconducting circuit*, Thesis, Université Paris VI (2002), available in pdf format at http://www-drecam.cea.fr/articles_k2/s02/112/publi.pdf
- [CL83] A. O. Caldeira, A. J. Leggett, *Quantum Tunneling in a Dissipative System*, Ann. Phys, (N.Y.), **149**, 374 (1983).
- [CVJ02] A. Cottet, D. Vion, P. Joyez, D. Esteve, M. H. Devoret, *A Hysteretic Single Cooper Pair Transistor for Single-Shot Reading of a Charge-Qubit*, in *International Workshop on Superconducting Nano-electronic Devices*, p. 73, J. Pekola, B. Ruggiero and P. Silvestrini eds., Kluwer Academic, Plenum Publisher, New York (2002).
- [D85] D. Deutsch, *Quantum Theory, the Church-Turing Principle and the Universal Quantum Computer*, Proc. R. Soc. London Ser. **A400**, 97 (1985).
- [D89] D. Deutsch, *Quantum Computational Networks*, Proc. R. Soc. London Ser. **A425**, 73 (1989).
- [De97] M. H. Devoret, *Quantum Fluctuation in Electrical Circuits*, in *Quantum fluctuations*, S. Reynaud, E. Giacobino and J. Zinn-Justin eds., Elsevier Science (1997).
- [Di95] D. P. DiVincenzo, *Quantum Computation*, Science **270**, 255 (1995).
- [Di00] D. P. DiVincenzo, *The Physical Implementation of Quantum Computation*, Fortschr. Phys. **48**, 771 (2000).
- [DK80] M. I. Dykman, M. A. Krivoglaz, *Fluctuations in nonlinear systems near bifurcations corresponding to the appearance of new stable states*, Physica **A104**, 480 (1980).
- [DM04] M. H. Devoret, J. M. Martinis, *Implementing Qubits with Superconducting Integrated Circuits*, Quantum Information Processing **3**, 163 (2004).
- [DMC85] M. H. Devoret, J. M. Martinis, J. Clarke, *Measurements of macroscopic Quantum Tunneling out of the Zero-Voltage State of a Current-Biased Josephson Junction*, Phys. Rev. Lett. **55**, 1908 (1985).
- [Do77] G. J. Dolan, *Offset masks for lift-off photoprocessing*, Appl. Phys. Lett. **31**, 337 (1977).

- [DS90] M. I. Dykman, V. N. Smelyanski, *Fluctuational transitions between stable states of a nonlinear oscillator driven by random resonant force*, Phys. Rev. **A41**, 3090 (1990).
- [DWM04] M. H. Devoret, A. Wallraff, J. M. Martinis, *Superconducting Qubits: A Short Review*, arXiv: cond-mat/04011174 (2004).
- [F82] R. P. Feynman, *Simulating Physics with Computers*, Int. J. Theor. Phys. **21**, 467 (1982).
- [F85] R. P. Feynman, *Quantum Mechanical computers*, Optics News **11**, 11 (1985).
- [F86] R. P. Feynman, *Quantum Mechanical computers*, Found. Phys. **16**, 507 (1986).
- [F96] R. P. Feynman, *Feynman Lectures on Computation*, J. G. Hey and R. W. Allen eds., Perseus Books (1996).
- [FPC00] J. R. Friedman, V. Patel, W. Chen, S. K. Tolpygo, J. E. Lukens, *Quantum superposition of distinct macroscopic states*, Nature **406**, 43 (2000).
- [FWS05] L. Frunzio, A. Wallraff, D. Schuster, J. Majer, R. J. Schoelkopf, *Fabrication and characterization of superconducting circuit QED devices for quantum computation*, IEEE Trans. on Appl. Superc. **15**, 860 (2005); arXiv: cond-mat/0411708.
- [G40] G. Gamow, *Mr. Tompkins in Wonderland*, Cambridge University Press (1940)
- [G44] G. Gamow, *Mr. Tompkins explores the atom*, Cambridge University Press (1944)
- [Go02] D. Gottesman, *Stabilizer Codes and Quantum Error Correction*, Thesis, California Institute of Technology (2002); arXiv: quant-ph/9705052.
- [GRL03] S. Gulde, M. Riebe, G. P. T. Lancaster, C. Becher, J. Eschner, H. Haffner, F. Schmidt-Kaler, I. Chuang, R. Blatt, *Implementation of the Deutsch-Josza algorithm on an ion-trap quantum computer*, Nature **421**, 48 (2003);
- [ICJ05] G. Ithier, E. Collin, P. Joyez, P. J. Meeson, D. Vion, D. Esteve, F. Chiarello, A. Shnirman, Y. Makhlin, J. Schrieffer, G. Schon, *Decoherence in a superconducting quantum bit circuit*, Phys. Rev. **B72**, 134519 (2005).
- [J62] B. D. Josephson, *Possible New Effects in Superconductive Tunneling*, Phys. Lett. **1**, 251 (1962).

- [K98] B. E. Kane, *A silicon-based nuclear spin quantum computer*, Nature **393**, 133 (1998).
- [L80] A.J. Leggett, *Macroscopic Quantum Systems and the Quantum Theory of Measurement*, Progr. Theor. Phys. (Suppl.) **69**, 80 (1980).
- [LBS03] K. W. Lehnert, K. Bladh, L. F. Spietz, D. Gunnarsson, D. I. Schuster, P. Delsing, R. J. Schoelkopf, *Measurement of the Excited-State Lifetime of a Microelectronic Circuit*, Phys. Rev. Lett. **90**, 027002 (2003).
- [LDi98] D. Loss, D. P. DiVincenzo, *Quantum computation with quantum dots*, Phys. Rev. **A57**, 120 (1998).
- [LKS05] D. Leibfried, E. Knill, S. Seidelin, J. Britton, R. B. Blakestad, J. Chiaverini, D. B. Hume, W. M. Itano, J. D. Jost, C. Langer, R. Ozeri, R. Reichle, D. J. Wineland, *Creation of a six atom “Schrödinger cat” state*, Nature **438**, 639 (2005).
- [MB58] D. C. Mattis, J. Bardeen, *Theory of the Anomalous Skin Effect in Normal and Superconducting Metals*, Phys. Rev. **111**, 412 (1958).
- [MD02] H. Mabuchi, A. Doherty, *Cavity quantum electrodynamics: Coherence in context*, Science **298**, 1372 (2002).
- [MDC85] J. M. Martinis, M. H. Devoret, J. Clarke, *Energy-Level Quantization in the Zero-Voltage State of a Current-Biased Josephson Junction*, Phys. Rev. Lett. **55**, 1543 (1985).
- [MDC87] J. M. Martinis, M. H. Devoret, J. Clarke, *Experimental tests for the quantum behavior of a macroscopic degree of freedom: The phase difference across a Josephson Junction*, Phys. Rev. **B35**, 4682 (1987).
- [MNA03] J. M. Martinis, S. Nam, J. Aumentado, K. M. Lang, C. Urbina, *Decoherence of a superconducting qubit due to bias noise*, Phys. Rev. **B67**, 094510 (2003).
- [NC00] M. Nielsen and I. Chuang, *Quantum Computation and Quantum Information*, Cambridge University Press, Cambridge, UK (2000).
- [NPT99] Y. Nakamura, Yu. A. Pashkin, J. S. Tsai, *Coherent control of macroscopic quantum states in a single-Cooper-pair box*, Nature **398**, 786 (1999).
- [R37] I. Rabi, *Space Quantization in a Gyating Magnetic Field*, Phys. Rev. **51**, 652 (1937).

- [Ra50] N. F. Ramsey, *A Molecular Beam Resonance Method with Separated Oscillating Fields*, Phys. Rev. **78**, 695 (1950).
- [RBD05] C. Rigetti, A. Blais, M. H. Devoret, Protocol for Universal Gates in Optimally Biased Superconducting Qubits, Phys. Rev. Lett. **94**, 240502 (2005).
- [RBH01] J. Raimond, M. Brune, S. Haroche, *Manipulating quantum entanglement with atoms and photons in a cavity*, Rev. Mod. Phys. **73**, 565 (2001).
- [S94] P. W. Shor, *Algorithms for Quantum Computation: Discrete Logarithms and Factoring*, in Proceedings of the 35th Annual Symposium on Foundation of Computer Science, S. Goldwasser ed., p. 124, IEEE Press (1994).
- [S95] P. W. Shor, *Scheme for reducing decoherence in quantum computer memory*, Phys. Rev. **A52**, 2493 (1995).
- [S97] P. W. Shor, *Polynomial time algorithms for prime factorization and discrete logarithms on a quantum computer*, SIAM J. Comput. **26**, 1484 (1997).
- [St96] A. M. Steane, *Error Correcting Codes in Quantum Theory*, Phys. Rev. Lett. **77**, 793 (1996).
- [St98] A. M. Steane, *Quantum computing*, Rep. Prog. Phys. **61**, 117-173 (1998).
- [SVP04] I. Siddiqi, R. Vijay, F. Pierre, C. M. Wilson, M. Metcalfe, C. Rigetti, L. Frunzio, M. H. Devoret, *An RF-driven Josephson bifurcation amplifier for quantum measurements*, Phys. Rev. Lett. **93**, 207002 (2004); arXiv: cond-mat/0312623.
- [SVP05a] I. Siddiqi, R. Vijay, F. Pierre, C. M. Wilson, L. Frunzio, M. Metcalfe, C. Rigetti, R. J. Schoelkopf, M. H. Devoret, D. Vion, D. Esteve, *Direct observation of dynamical switching between two driven oscillation states of a Josephson junction*, Phys. Rev. Lett. **94**, 027005 (2005); arXiv: cond-mat/0312553.
- [SVP05b] I. Siddiqi, R. Vijay, F. Pierre, C. M. Wilson, L. Frunzio, M. Metcalfe, C. Rigetti, M. H. Devoret, *The Josephson bifurcation amplifier for quantum measurements*, Proceeding of the IV International Workshop on Macroscopic Quantum Coherence and Computing, Naples, Italy (2004); arXiv: cond-mat/0507248.

- [SVM06] I. Siddiqi, R. Vijay, M. Metcalfe, E. Boaknin, L. FRUNZIO, R. J. Schoelkopf, M. H. Devoret, *Dispersive measurements of superconducting qubit coherence with a fast, latching readout*, Phys. Rev. **B73**, 054510 (2006); arXiv: cond-mat/0507548.
- [SWB05] D. Schuster, A. Wallraff, A. Blais, L. Frunzio, R.-S. Huang, J. Majer, S. M. Girvin, R. J. Schoelkopf, *AC-Stark shift and dephasing of a superconducting qubit strongly coupled to a cavity field*, Phys. Rev. Lett. **94**, 123602 (2005); arXiv: cond-mat/0408367.
- [TMP05] E. Tan, P. G. Mather, A. C. Perrella, J. C. Read, R. A. Buhrman, *Oxygen stoichiometry in aluminum oxide tunnel barrier layer*, Phys. Rev. **B71**, 161401 (2005).
- [VAC02] D. Vion, A. Aassime, A. Cottet, P. Joyez, H. Pothier, C. Urbina, D. Esteve, M. H. Devoret, *Manipulating the Quantum State of an Electrical Circuit*, Science **296**, 886 (2002).
- [VSB01] L. M. K. Vandersypen, M. Steffen, G. Breyta, C. S. Yannoni, M. H. Sherwood, I. L. Chuang, *Experimental realization of Shor's quantum factoring algorithm using nuclear magnetic resonance*, Nature **414**, 883 (2001).
- [WSB04] A. Wallraff, D. Schuster, A. Blais, L. Frunzio, R.-S. Huang, J. Majer, S. Kumar, S. M. Girvin, R. J. Schoelkopf, *Strong coupling of a single photon to a superconducting qubit using circuit quantum electrodynamics*, Nature. **431**, 162-167 (2004); arXiv: cond-mat/0407325.
- [WSB05] A. Wallraff, D. I. Schuster, A. Blais, L. Frunzio, J. Majer, M. H. Devoret, S. M. Girvin, R. J. Schoelkopf, *Approaching unit visibility for control of a superconducting qubit with dispersive readout*, Phys. Rev. Lett. **95**, 060501 (2005); arXiv: cond-mat/0502645.
- [YD84] B. Yurke, J. S. Denker, *Quantum Network Theory*, Phys. Rev. **A29**, 1419 (1984)